

A Systematic Study of Associations between Supernova Remnants and Molecular Clouds

Xin Zhou¹, Yang Su¹, Ji Yang¹, Xuepeng Chen¹, Yan Sun¹, Zhibo Jiang¹, Min Wang¹, Hongchi Wang¹, Shaobo Zhang¹, Ye Xu¹, Qingzeng Yan¹, Lixia Yuan¹, Zhiwei Chen¹, Yiping Ao¹, Yuehui Ma¹

¹*Purple Mountain Observatory and Key Laboratory of Radio Astronomy, Chinese Academy of Sciences, 10 Yuanhua Road, Nanjing 210033, People's Republic of China; xinzhou@pmo.ac.cn*

ABSTRACT

We universally search for evidence of kinematic and spatial correlation of supernova remnant (SNR) and molecular cloud (MC) associations for nearly all SNRs in the coverage of the MWISP CO survey, i.e. 149 SNRs, 170 SNR candidates, and 18 pure pulsar wind nebulae (PWNe) in $1^\circ < l < 230^\circ$ and $-5.^\circ5 < b < 5.^\circ5$. Based on high-quality and unbiased $^{12}\text{CO}/^{13}\text{CO}/\text{C}^{18}\text{O}$ ($J = 1-0$) survey data, we apply automatic algorithms to identify broad lines and spatial correlations for molecular gas in each SNR region. The 91% of SNR-MC associations detected previously are identified in this paper by CO line emission. Overall, there could be as high as 80% of SNRs associated with MCs. The proportion of SNRs associated with MCs is high within the Galactic longitude less than $\sim 50^\circ$. Kinematic distances of all SNRs that are associated with MCs are estimated based on systemic velocities of associated MCs. The radius of SNRs associated with MCs follows a lognormal distribution, which peaks at ~ 8.1 pc. The progenitor initial mass of these SNRs follows a power-law distribution with an index of ~ -2.3 that is consistent with the Salpeter index of -2.35 . We find that SNR-MC associations are mainly distributed in a thin disk along the Galactic plane, while a small amount distributed in a thick disk. With the height of these SNRs from the Galactic plane below ~ 45 pc, the distribution of the average radius relative to the height of them is roughly flat, and the average radius increases with the height when above ~ 45 pc.

Subject headings: ISM (847) — Supernova remnants (1667) — Molecular clouds (1072) — Galaxy structure (622)

1. Introduction

Supernova remnants (SNRs) release large amounts of momentum, energy, and heavy elements into the interstellar medium (ISM), which modify the physical and chemical properties of the ISM and trigger star formation. Such stellar feedback, affecting the next generation of star formation, primarily characterizes the nonlinear evolution of the ISM. SNRs are also prime candidates of Galactic cosmic ray (CR) sources. Some SNRs have bright γ -ray emission, which may originate from CR particles impacting on the surrounding dense medium (e.g., Aharonian et al. 2008a; Giuliani et al. 2011; Fukui et al. 2021). These sources provide valuable opportunities to study CR acceleration in SNRs. Many SNRs originate from core-collapse supernova explosions of massive stars. Because their progenitor massive stars formed in molecular clouds (MCs) and had relatively short lifetimes, these SNRs are expected to be associated with their parent MCs. In addition, type Ia supernovae may also occur near dense molecular gases (e.g., Lee et al. 2004;

Zhou et al. 2016c; Chen et al. 2017b). It is not clear that how many SNRs are associated with MCs. Supposing half of SNRs originated from core-collapse supernovae (Reynoso & Mangum 2001), there may be more than half of SNRs associated with MCs.

Among different evidences of SNR-MC interaction, i.e. shifted and broadened CO line emission (e.g., Denoyer 1979a; Seta et al. 1998b; Kilpatrick et al. 2016, etc.), OH maser line emission at 1720 MHz (e.g., Goss & Robinson 1968; Frail et al. 1994, 1996; Green et al. 1997; Wardle & Yusef-Zadeh 2002; Yusef-Zadeh et al. 2003; Hewitt & Yusef-Zadeh 2009, etc.), shock excited molecular line emission (e.g., Wootten 1981, etc.), enhanced IR emission (e.g., Arendt 1989; Saken et al. 1992; Reach et al. 2005, 2006; Hewitt et al. 2009, etc.), etc., molecular line emission is widely used in searching associated MC, since it originates from associated molecular gas and provides its local standard-of-rest (LSR) velocity information. To date, about 80 Galactic SNRs have been confirmed or suggested to be associated with MCs, out of about 300 Galac-

tic SNRs (Gaensler et al. 2008; Jiang et al. 2010; Tian et al. 2010; Eger et al. 2011; Jeong et al. 2012; Frail et al. 2013; Chen et al. 2014; Fukuda et al. 2014; Su et al. 2014b; Zhou et al. 2014; Zhu et al. 2014; Zhang et al. 2015; Voisin et al. 2016; Zhou et al. 2016a,c; de Wilt et al. 2017; Lau et al. 2017; Liu et al. 2017; Su et al. 2017b; Liu et al. 2018; Maxted et al. 2018; Su et al. 2018; Ma et al. 2019; Yu et al. 2019; Green 2019; Ranasinghe & Leahy 2022, and references therein). Most of these Galactic SNR-MC associations have been confirmed or suggested through CO or OH maser line emission. In particular, Kilpatrick et al. (2016) performed an effective systematic search for broad ^{12}CO ($J=2-1$) line regions toward 50 SNRs, and confirmed the detection in 19 SNRs including 9 newly identified ones. Sofue et al. (2021) also provided some supplementary morphological search results of CO line emission toward 63 Galactic SNRs in the $10^\circ \leq l \leq 50^\circ$, $|b| \leq 1^\circ$ region. Only a small percentage of SNRs are confirmed to be associated with MCs with clear evidence, e.g., uncontaminated broad CO line emission or OH 1720 MHz maser emission. Many SNRs are located in crowded regions with multiple MCs overlapping each other in the line-of-sight, hence, molecular lines toward these SNRs are overlapping each other. It is difficult to distinguish potential disturbed molecular gases in these SNRs. In addition, physical conditions for the formation of OH 1720 MHz masers are strict, i.e. in regions with moderate temperatures and densities ($T \sim 50-125$ K, $n_{\text{H}_2} \sim 10^5 \text{ cm}^{-3}$) behind slow C-type shocks (Lockett et al. 1999; Hewitt & Yusef-Zadeh 2009), and many SNRs do not have such physical conditions. A large amount of potential SNR-MC associations prohibit general statistical studies of MC environments around SNRs.

Intending to investigate SNR-MC associations, we present in this work a general study of CO line emission toward most SNRs in the northern sky, based on the Milky Way Imaging Scroll Painting (MWISP) unbiased three CO isotope lines survey using the 13.7-meter millimeter wavelength telescope at Qinghai station. The survey data has appropriate spatial resolution, high sensitivity, and large coverage. Both kinematic evidence and spatial correlations are examined, and further statistical analyses of SNRs associated with MCs are performed.

2. Observations

SNRs in the coverage of the Milky Way Imaging Scroll Painting (MWISP¹) project, i.e. nearly all SNRs in $1^\circ < l < 230^\circ$ and $-5.^\circ5 < b < 5.^\circ5$, are investigated. The MWISP project is an unbiased survey of $^{12}\text{CO}/^{13}\text{CO}/\text{C}^{18}\text{O}$ ($J = 1-0$) emission lines

¹<http://www.radioast.nsd.c/mwisp.php>

(see Su et al. 2019; Sun et al. 2020, and references therein, for details), using the Purple Mountain Observatory Delingha (PMODLH) 13.7 m millimeter wavelength telescope (Zuo et al. 2011). The three CO lines were simultaneously observed by a 3×3 multibeam sideband separating superconducting receiver (Shan et al. 2012). The region is mapped via on-the-fly (OTF) observation mode, with a half-power beamwidth (HPBW) of $\sim 51''$. Spectral resolutions of the three CO lines are $\sim 0.16 \text{ km s}^{-1}$ for ^{12}CO ($J = 1-0$), and $\sim 0.17 \text{ km s}^{-1}$ for ^{13}CO and C^{18}O ($J = 1-0$). The typical rms noise level is about 0.5 K for ^{12}CO ($J = 1-0$); and about 0.3 K for ^{13}CO and C^{18}O ($J = 1-0$), corresponding to their spectral resolutions. All data were processed using dedicated pipelines by MWISP working group and the GILDAS/CLASS package². A linear fit was performed in the baseline subtraction. The OTF raw data was meshed with a grid spacing of $30''$, and was corrected for beam efficiency using $T_{mb} = T_A^* / \eta_{mb}$. The data of the full extent of each SNR was extracted, covering an area of 2 to 4 times the size of the remnant. Moreover, for pulsar wind nebulae (PWNe), areas of 16 to 32 times their sizes are covered. SNRs G82.2+5.3 and G93.3+6.9 are not fully covered, nevertheless, more than half of their extents are covered.

Radio continuum emission data at 200 MHz were obtained from the Galactic and Extragalactic All-sky Murchison Widefield Array (GLEAM) survey³ (Wayth et al. 2015; Hurley-Walker et al. 2017, 2019b). 1.4 GHz radio continuum emission data were obtained from the NRAO VLA Sky Survey (NVSS; Condon et al. 1998) and The HI/OH/Recombination line survey (THOR; Beuther et al. 2016; Wang et al. 2020). 4850 MHz radio continuum data were also obtained from the Green Bank 6-cm/Parkes-MIT-NRAO (GB6) survey (Condon et al. 1991, 1993, 1994). 20 cm radio continuum data are from the Multi-Array Galactic Plane Imaging Survey (MAGPIS⁴; Helfand et al. 2006). The information on SNRs in the Green (2019) catalog⁵ and the catalog of high-energy SNRs (SNRcat⁶; Ferrand & Safi-Harb 2012) was used. Based on the radio continuum emission, we define circular regions to designate individual SNRs by visual inspection, mostly along their outermost bright radio continuum shell.

3. Methods

Molecular gases impacted by SNR shock will be disturbed in two respects, i.e. heating and macro-

²<http://www.iram.fr/IRAMFR/GILDAS>

³<https://www.mwatelescope.org/gleam>

⁴<http://third.ucllnl.org/gps>

⁵<http://www.mrao.cam.ac.uk/surveys/snrs/snrs.info.html>

⁶<http://www.physics.umanitoba.ca/snr/SNRcat>

turbulence. Molecular gas behind a transmitted shock in a molecular clump will be accelerated and heated, which is usually detected as broadened line wing in CO line profiles. In addition, molecular gas engulfed by SNR will become cold as the SNR gets old, but still maintains the injected momentum. Hence, relative motion between different parts of molecular gas in SNR, i.e. macro-turbulence, leads to the corresponding CO line profile being broader than that from surrounding quiescent molecular gas. The macro-turbulence in molecular gas injected by SNR could be very general, especially in old SNRs where most of the dense shocked molecular gases become cold. Overall, these effects would result in broadened CO lines from shocked molecular gases. Unlike CO lines from molecular outflows in star-forming regions, these broadened CO lines usually present as extra peaks beside narrow CO lines from surrounding quiescent molecular gases. Such kinematic evidence in SNRs is very useful to confirm SNR-MC associations. It is noteworthy that such broadened CO lines might not be present in some young SNRs that are associated with MCs, because CO molecules nearby can be dissociated by UV radiation from progenitor massive stars or strong shock heating of these young SNRs, and, in general, the kinetic energy of SNR's shock is not sufficiently converted into a molecular cloud (e.g., Inoue et al. 2012; Zhou et al. 2016b; Celli et al. 2019; Sano et al. 2020, and references therein).

An SNR will also reshape nearby MCs, which can destroy less dense molecular gas and leave a cavity, or can accumulate molecular gas and form a shell (e.g., Seta et al. 1998a; Inutsuka et al. 2015). Spatial correlation is commonly used as evidence of SNR-MC association. Many known SNR-MC associations are proposed based on their spatial correlations (see Table 2 in Jiang et al. 2010). In some cases, spatially correlated MCs originate from wind-blown bubbles of the SNR's progenitor, especially for very young SNRs or PWNe, for which kinematic evidence barely exists (Chevalier 1999; Chen et al. 2013, and references therein). Note that the spatial correlation evidence is not as robust as the kinematic evidence, since overlapping of multiple MCs across the Galactic plane through the line of sight would complicate the spatial distribution of molecular gases.

Our goal is to search universally for evidence of kinematic and spatial correlation of SNR-MC association. Thereafter, we also need to settle associated spectral components, by comparing the searching results of broad line and spatial correlation, comparing them with the radio continuum emission of SNRs, and eliminating the contamination of overlaid energetic objects. Finally, we can determine the systemic velocity of MCs associated with SNRs.

In this paper, the velocity of the intensity peak of the associated spectral component, which represents the local standard of rest (LSR) velocity of the main part of molecular gas, is considered as the systemic velocity of MCs associated with SNRs. The detail of searching method is presented in Section 3.1 and 3.2.

3.1. Broad Line Identification

Kinematic evidence of SNR-MC associations would present as broadened lines, and the goal is to search these broadened lines in ^{12}CO ($J=1-0$) data. At the beginning, we smooth all ^{12}CO ($J=1-0$) spectra by bin nearby three channels, to get a high signal-to-noise ratio in broad line searching. The spectral resolution after smoothing is 0.48 km s^{-1} , which is about half of the narrowest ^{12}CO ($J=1-0$) line. Then, we decompose these spectra into individual spectral components, of which the minimum intensity of bottoms is 1σ , the minimum intensity of peak-to-valley differences is 3σ , and the minimum intensity of peaks is 5σ . Broad line identifications are performed based on these spectral components. For these spectral components, we identify broad lines first, then find broader lines in the SNR region than those in the background if exist. Broad lines are identified by following criteria.

- The full width at half maximum (FWHM) of the spectral component be larger than 6 km s^{-1} .
- The kurtosis of the component be larger than 1.1 times that of the best-fitting Gaussian function with the same FWHM in the same velocity range.
- The square rooted variance of channels with intensity greater than the best-fitting Gaussian function be smaller than or equal to the square rooted variance of all channels of the whole component.
- All required values be over three times their σ errors.

As indicated by the Larson's line width-size relationship, the typical FWHM of ^{12}CO ($J=1-0$) lines of normal, parsec scale, quiescent MCs is below $\sim 6 \text{ km s}^{-1}$ (Heyer & Dame 2015). The ^{12}CO ($J=1-0$) line of most shocked molecular gases is with FWHM greater than 6 km s^{-1} (e.g., SNR HB3; Zhou et al. 2016c). The FWHM of the ^{12}CO ($J=1-0$) line of some small shocked molecular clumps can be lower than 6 km s^{-1} ; however, such clumps only occupy a small part of the shocked molecular gas in the SNR in most cases. Therefore, we adopted 6 km s^{-1} as a lower limit of the FWHM of broad lines. Note that, for SNRs adjacent to MCs of much

larger size, a larger FWHM threshold will be applied to identify broad lines associated with SNRs in the following step, which depends on the FWHM of background spectral components. The information on the width of background lines can also help us to eliminate some line overlapping effects.

We use the kurtosis value to characterize the deviation from a Gaussian profile, of which a larger value indicates a distribution with extra wings. Together with the variance of channels with intensity greater than the best-fitting Gaussian function, we can eliminate some line overlapping effects. As shown in Figure 1, components comprising a strong narrow line plus a weak broad wing are mostly selected, and those comprising a strong broad line plus a weak narrow line are eliminated. The CO emission of shocked MC by an SNR usually presents as a strong narrow line plus a broadened line wing, where the narrow line originates from the quiescent matrix MC and the broad wing from shocked molecular gas. Narrow lines of some small molecular clumps in SNRs could be weaker than broad lines, or no narrow line left at all. However, in most cases, such small molecular clumps contribute only a small portion of shocked molecular gas comparing to that from the large matrix MC (e.g., Zhou et al. 2016c), and velocities of these broad lines are usually significantly shifted from that of corresponding narrow lines, which are easily to be distinguished as separate spectral components. Commonly, overlapping CO lines from different MCs in the line-of-sight do not have such features. For instance, in some star-forming regions, central dense molecular gases are mostly disturbed, where broad CO lines are stronger. These criteria are strict, which may eliminate some individual broad lines, but they provide more accurate results for SNRs in complicated backgrounds.

In the following step, we further select broader lines within the SNR region than that in the background. The size of the SNR region is 1.1 times enlarged than that indicated by its radio continuum emission. These broader lines are considered as primary kinematic evidence of the SNR-MC association. The final FWHM threshold for selecting broad lines originating from SNRs satisfies the condition that their FWHM is larger than or equal to the average FWHM of background broad lines. In practice, some SNRs still have many broad lines at different velocities selected. In this case, we add an additional condition to select broad lines for reference. The additional condition requires that the final FWHM threshold be larger than all broad lines in at least one of equally divided sub-regions in the background, which have areas comparable to that of the SNR region. Note that, for SNRs with simple backgrounds, this additional condition does not change the broad line identification results. This

additional condition is hereafter referred to as the clean subbackground region condition. Thereby, we can better identify broad lines originating from SNRs in backgrounds where CO lines are broad, e.g., nearby the Galactic center.

As noted above, full broad line identification criteria are strict, which provide better accuracy but less completeness. Full broad line identification criteria plus the clean subbackground region condition are even more strict. As a complement, a second broad line identification procedure is performed, applying only partial criteria, i.e. FWHM and error criteria, and the final FWHM threshold being larger than or equal to the average FWHM of background broad lines. Broad lines identified only by partial criteria are considered as broad line candidates.

At last, identified broad lines in an SNR are divided into different components, according to their intensity peaks being in each other's velocity range or not. The systemic velocity of broad line groups is determined as the velocity of the overall intensity peak of corresponding ^{13}CO ($J=1-0$) emission. If there is no significant ^{13}CO ($J=1-0$) emission, the systemic velocity is applied as the velocity of the overall intensity peak of ^{12}CO ($J=1-0$) emission. The case that broad lines being adjacent to the associated narrow lines is common, since the SNR shock is slow when it transmitted into a dense cloud. Broad lines are also usually strong near the observed boundary of shocked MCs, where the column density of shocked molecular gas is high, and LSR velocities in the line-of-sight direction of these broad lines are low. The systemic velocity obtained based on broad lines would represent the LSR velocity of most quiescent molecular gases in most cases. Nevertheless, some broad lines can be shifted to velocities far away from associated narrow lines, and are identified as separated broad line components. Therefore, further examination is needed to settle the systemic velocity of associated MCs, e.g., spatial correlation examination that is introduced in Section 3.2.

3.2. Spatial Correlation Coefficient

To examine spatial correlation between SNRs and MCs, we calculate spatial correlation coefficients (abbreviated as SCCs below) between a series of circular rings and channel maps of ^{12}CO ($J=1-0$) emission. Positions and sizes of SNRs, which are used to derive circular rings, are mostly determined by radio continuum emission of SNRs. For preparation, ^{12}CO ($J=1-0$) data is moment masked at first (see Dame 2011, for reference), to eliminate noise that affects the result of weak emission. ^{12}CO ($J=1-0$) channel maps are also linearly interpolated to an 80×80 pixel resolution and normalized to maximum intensity of 1. The 80×80 pixel resolution would simplify the calculation, and enables

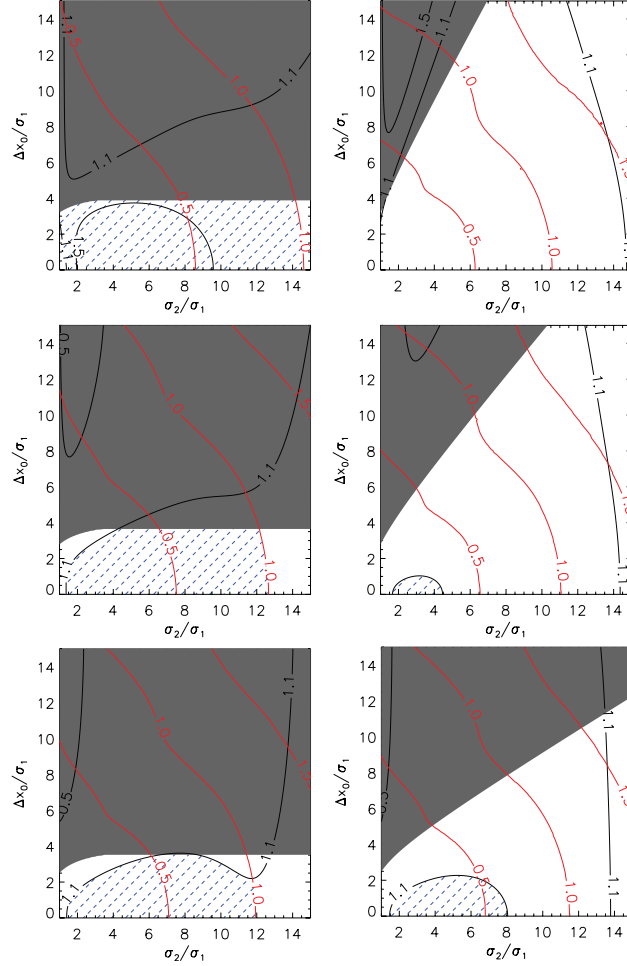


Fig. 1.— Test results of broad line identification. The spectrum comprising two Gaussian components is used for test, with standard deviations of σ_1 and σ_2 and the distance between their peaks of Δx_0 . The FWHM of the first Gaussian component is set to 3, i.e. σ_1 is 1.27. Results are similar for other values of σ_1 . Black contours show the distribution of the kurtosis ratio between the spectrum and a best-fitting Gaussian function. Red contours show the distribution of the square rooted variance ratio between the part of the spectrum larger than the best-fitting Gaussian function and the whole spectrum. Panels in the left column show cases that the broad Gaussian component is weaker than the narrow component, with peak ratios of 0.2, 0.5, and 0.8 from top to bottom, respectively. The right column is opposite, with the ratios of peaks between the broad and narrow components of 5, 2, and 1.2 from top to bottom, respectively. Gray scale regions indicate where two Gaussian components can be resolved. Blue dashed lines denote regions selected by full broad line identification criteria.

the smallest circular ring to be still resolved. The minimum inner radius of circular rings, corresponding to a quarter of the radius of SNRs, is at least 4 pixels, and the maximum inner radius is 20 pixels. The increment of the inner radius of the series of circular rings is 1 pixel. Thicknesses of circular rings are from 2 to 30 pixels at intervals of 2 pixels. The results obtained with these parameters are fully feasible for the following calculations. After these preparations, we calculate Spearman correlation coefficients between ^{12}CO tile images and ring template images, as $\rho = \frac{\sum_i (x_i - \bar{x})(y_i - \bar{y})}{\sqrt{\sum_i (x_i - \bar{x})^2 \sum_i (y_i - \bar{y})^2}}$. This SCC would be large for molecular gases with similar spatial distributions to circular rings. Since the large number of pixels outside the SNR has a large impact on the SCC result, we only consider pixels inside ring templates or within twice the SNR radius. In the following step, we select the largest coefficient for each channel map, and make a coefficient versus velocity channel plot. In the plot, velocity channels with coefficients over 3σ levels usually congregate into different groups that correspond to velocity components in CO spectra. Groups of coefficients with peaks over 5σ confidence level, or over 3σ confidence level and larger than 0.5, are considered as candidates of correlated components. If there is no coefficient over 5σ or larger than 0.5, the maximum coefficient over 3σ will be given for reference. In addition, SCCs that consider pixels inside ring templates or within the SNR radius are also calculated, which can better examine thin molecular shell structures around an SNR. Note that the SCC would be underestimated in some cases, e.g., correlations between partial shells or other irregular shapes, nevertheless, they are still noticeable on the coefficient versus velocity plot in most cases.

3.3. Demonstration

We perform our searching method to several known SNR-MC associations for demonstration at first, and it helps us to optimize the parameters of the algorithm. Among these known SNR-MC associations, SNR IC 443, SNR HB 3, and SNR G16.0–0.5 are representative of SNRs with clear, simple, and complicate CO emission backgrounds, respectively.

3.3.1. IC 443

The association between SNR IC 443 and MCs has been well-established in previous works. The variety of molecular lines studied for this remnant is the most complete, providing a good understanding of the physics of the interaction between the SNR shock and the molecular gas (e.g., van Dishoeck et al. 1993). There are nine shocked molecular clumps in IC 443, which exhibit broad ^{12}CO (J=1–0) line emission (Denoyer 1979a;

Huang et al. 1986; Dickman et al. 1992; Lee et al. 2012a). These clumps are indicated in Figure 2. Eight of them are labeled as A through H, following the nomenclature in Dickman et al. (1992), and the remaining one that is adjacent to clump C is labeled as C', which was named as SC 05 in the study of Lee et al. (2012a). Note that we apply a circular region to denote the remnant in our analysis, which is defined following the northern bright radio continuum shell of the remnant, and there is also radio continuum emission in the south outside the region. As shown in Figure 2, we identify broad lines in five clumps by the full criteria, and in eight clumps by the partial criteria. The broad ^{12}CO (J=1–0) line emission in clump A is too weak, with $T_A^* \sim 0.3$ K (Denoyer 1979a), which is below our detection limit, hence, we found no broad line there. The broad line emission in clump H is also weak, and we only identify broad lines there by partial criteria. In clumps B and C, broad lines are far blue-shifted, separated from the associated narrow line component, which are only identified by partial identification criteria. We evaluate the accuracy of the broad line identification by $(n_{p,SNR} - n_{p,outside}) / (n_{p,SNR} + n_{p,outside})$, where $n_{p,SNR}$ and $n_{p,outside}$ are numbers of broad line points per unit area inside and outside the SNR region, respectively. For IC 443, the broad line identifications using either full or partial criteria have an accuracy of 1. It benefits from the clean MC background toward the SNR in the outer Galactic region. We also evaluate the completeness of the broad line identification by the number ratio between identified broad lines and all lines with FWHM over 6 km s^{-1} . For IC 443, the completeness of broad line identifications using full and partial criteria is ~ 0.20 and 1, respectively. Some broad lines separated from the associated narrow component or stronger than the narrow component are eliminated by full criteria. Since there is no contamination from background line emission, the identification by partial criteria is the most effective.

For SNR IC 443, the SCC has a maximum value of 0.24 at -2.1 km s^{-1} , which is over 3σ but below 5σ levels. The velocity of the maximum SCC is consistent with that of molecular gas associated with the remnant. As seen in Figure 2, associated molecular gas presents some partial shell structures surrounding the remnant. These partial shell structures result in large SCCs. However, central bright CO emission makes the enhancement of the SCC less significant. These associated partial shells were studied by Su et al. (2014a), which are possibly swept up by the stellar wind of the remnant's progenitor.

Both the kinematic evidence and the spatial correlation result indicate that SNR IC 443 is associated with the -3.0 km s^{-1} velocity component. Based on a full distance probability density func-

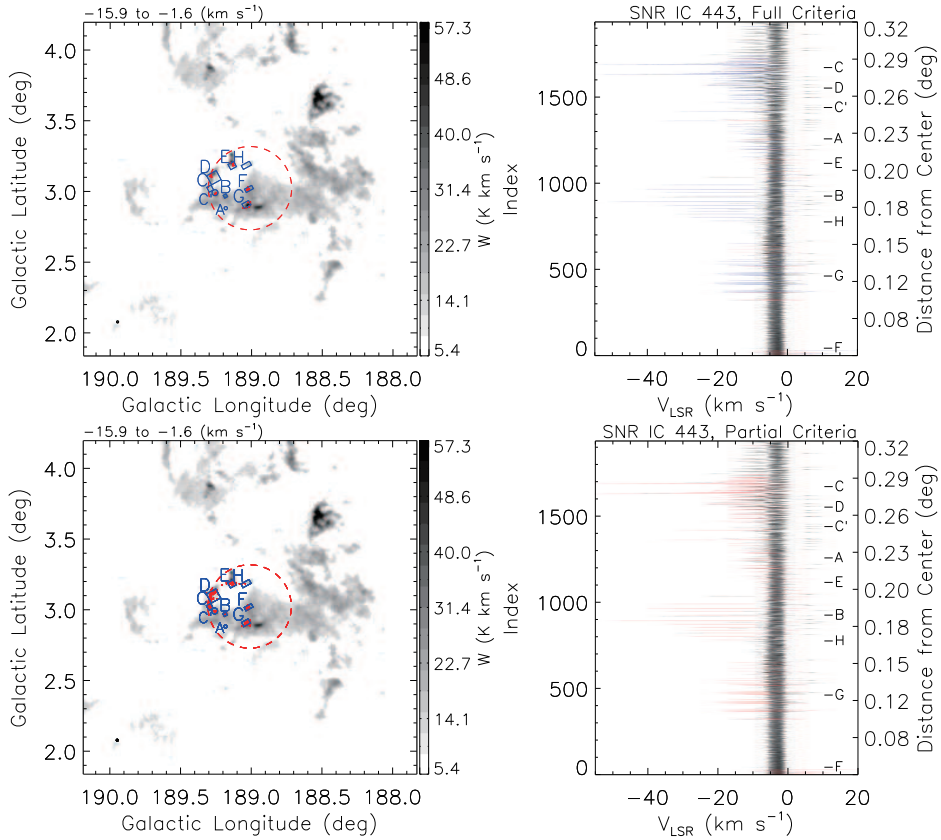


Fig. 2.— Integrated intensity and index-velocity maps of ^{12}CO ($J=1-0$) emission toward SNR IC 443. Both intensity maps in the left column are integrated over the velocity range of -15.9 to -1.6 km s^{-1} , which covers most of the broad lines. The red dashed circle denotes the remnant region, defined by visual inspection according to the bright radio continuum shell of the remnant. Regions A, B, C, D, E, F, G, and H are adopted from Denoyer (1979a), Dickman et al. (1992), where shocked molecular gases were detected by ^{12}CO ($J=1-0$) emission. Region C' is an additional shocked molecular clump, which is adjacent to region C. Locations of broad lines identified by full (*upper*) and partial (*lower*) criteria are denoted by red tiny stars. The minimum value of ^{12}CO emission intensity shown in the colorbar is at 5σ confidence level. The beam is represented by a black circle in the lower left corner. This beam designation is used in all intensity maps in the paper. Index-velocity maps in the right column contain all significant ^{12}CO ($J=1-0$) emission lines in the 1.1 times enlarged remnant region, whose intensity is normalized and logarithmically scaled for better visibility. The index indicates the arrangement of the spectrum at each point, sorted by the distance of the point from the SNR center. Some distances are shown on the right axis. The center of each region adopted from previous works in intensity maps is also shown in index-velocity maps. Broad lines identified by full (*upper*) and partial (*lower*) criteria are in red, and remaining lines with FWHM over 6 km s^{-1} are in blue.

tion⁷ (Reid et al. 2016, 2019), the kinematic distance of the -3.0 km s^{-1} component is estimated as $2.10 \pm 0.03 \text{ kpc}$, which is located in the Perseus spiral arm. Note that Yu et al. (2019) also measured the distance of the associated MC by dust extinction estimation as $1729_{-94}^{+116} \text{ pc}$.

3.3.2. HB 3

SNR HB 3 was initially suggested to be associated with MCs based on their spatial correlations (Landecker et al. 1987; Routledge et al. 1991), and this was further supported by broadened CO lines and H_2 $2.12 \mu\text{m}$ emission detected in later studies (Zhou et al. 2016c; Rho et al. 2021). Note that broadened $^{12}\text{CO}(J=2-1)$ line emission toward this remnant was detected by Kilpatrick et al. (2016), but was suggested to be associated with the H II region W3 (OH) rather than HB 3. SNR HB 3 is associated with the nearby H II region/MC complex W3 (e.g., Zhou et al. 2016c), hence, there is broad line emission in the background. Line overlapping effect in the direction of the outer galaxy toward this SNR is not significant. All shocked molecular clumps found by detailed examination in Zhou et al. (2016c) are also identified here by partial criteria, i.e. in regions a1, a2, b1, b2, c, and d (see Figure 3). Many broad lines outside the SNR region are also identified, and all of them are located in the star-forming region W3 (see Figure 3), possibly associated with H II regions within it. The accuracy and completeness of the broad line identification using partial criteria are 0.98 and 0.61, respectively. Since the broad line identification is barely affected by line overlapping effect for this SNR, the accuracy of using partial criteria is high. There are fewer broad lines identified in the remnant using full criteria, and the corresponding accuracy is evaluated as 0.94. The number ratio between broad lines identified inside and outside the remnant using full criteria is a bit less than that using partial criteria. The completeness of the broad line identification using strict full criteria is as low as 0.11.

In the SCC plot in the upper left panel in Figure 4, when considering pixels inside ring templates or within twice the SNR radius, a component with a peak above the 5σ confidence level indicates a correlation between SNR HB 3 and molecular gas at $\sim -42.2 \text{ km s}^{-1}$. The SCC result considering pixels inside ring templates or within the SNR radius also supports this correlation (see panels in the bottom row in Figure 4). There is a molecular shell at $\sim -42.2 \text{ km s}^{-1}$ spatially correlated with the bright radio continuum shell of the remnant well (also seen in Zhou et al. 2016c). Since the molecular shell occupies only about a quarter of the ring surrounding the remnant (see the right panel in Figure 4), the

peak of the SCC is only 0.22, which is underestimated.

The kinematic evidence and the spatial correlation result indicate that SNR HB 3 is associated with the -44.0 km s^{-1} velocity component. Based on the full distance probability density function, the kinematic distance of the -44.0 km s^{-1} component is estimated as $1.96 \pm 0.04 \text{ kpc}$, which is located in the Perseus spiral arm.

3.3.3. G16.0-0.5

Beaumont et al. (2011) applied Support Vector Machines (SVMs) machine learning algorithm to classify broadened $^{12}\text{CO}(J=3-2)$ lines in SNR G16.0-0.5, and found shocked shell-like molecular gas in a wide velocity range from -5 to $+90 \text{ km s}^{-1}$. Near-infrared H_2 lines at $+51 \text{ km s}^{-1}$ were also detected toward this SNR (Lee et al. 2020). SNR G16.0-0.5 locates in the inner galaxy direction, where line overlapping effect is serious. It needs strict criteria to identify broad lines in such complicated background. Here, applying full criteria, we identify three broad line components in the SNR at velocities of $+43.7$, $+67.9$, and $+87.5 \text{ km s}^{-1}$. The identification accuracy for the $+67.9 \text{ km s}^{-1}$ component is the highest, which is 0.83, and accuracies of other two components are around 0.3. The total completeness is only ~ 0.08 . The high accuracy and low completeness indicate an efficient suppression of line overlapping effect. The $+43.7$ and $+67.9 \text{ km s}^{-1}$ broad line components are also identified when using full criteria plus the clean subbackground region condition. Accordingly, identification accuracies of two components are improved to 0.59 and 0.92, respectively, and the overall completeness drops to 0.03. Overall, broad line identification using partial criteria seems greatly affected by line overlapping effect, with broad line candidates identified at many velocities. Nevertheless, many broad line candidates at $+67.9 \text{ km s}^{-1}$ are identified using partial criteria, and most of them are distributed in the remnant (see Figure 5). There are also many broad line candidates identified at $+43.7 \text{ km s}^{-1}$ by partial criteria, which are widely distributed inside and outside the remnant. As shown in Figure 5, the shocked molecular shell detected by $^{12}\text{CO}(J=3-2)$ emission in the remnant (Beaumont et al. 2011) is mainly composed of gases of the $+67.9 \text{ km s}^{-1}$ velocity component, which also follows the remnant's radio continuum shell peak well. Some molecular gas of the $+43.7 \text{ km s}^{-1}$ velocity component contributes to the shocked molecular shell outside the remnant.

The peak of the SCC for SNR G16.0-0.5 is at $\sim +63.3 \text{ km s}^{-1}$ and above 0.5, which considers pixels inside the ring templates or within twice the radius of the SNR (see the upper left panel in Figure 6). In addition, the $\sim +63.3 \text{ km s}^{-1}$ component

⁷<http://bessel.vlbi-astrometry.org/node/378>

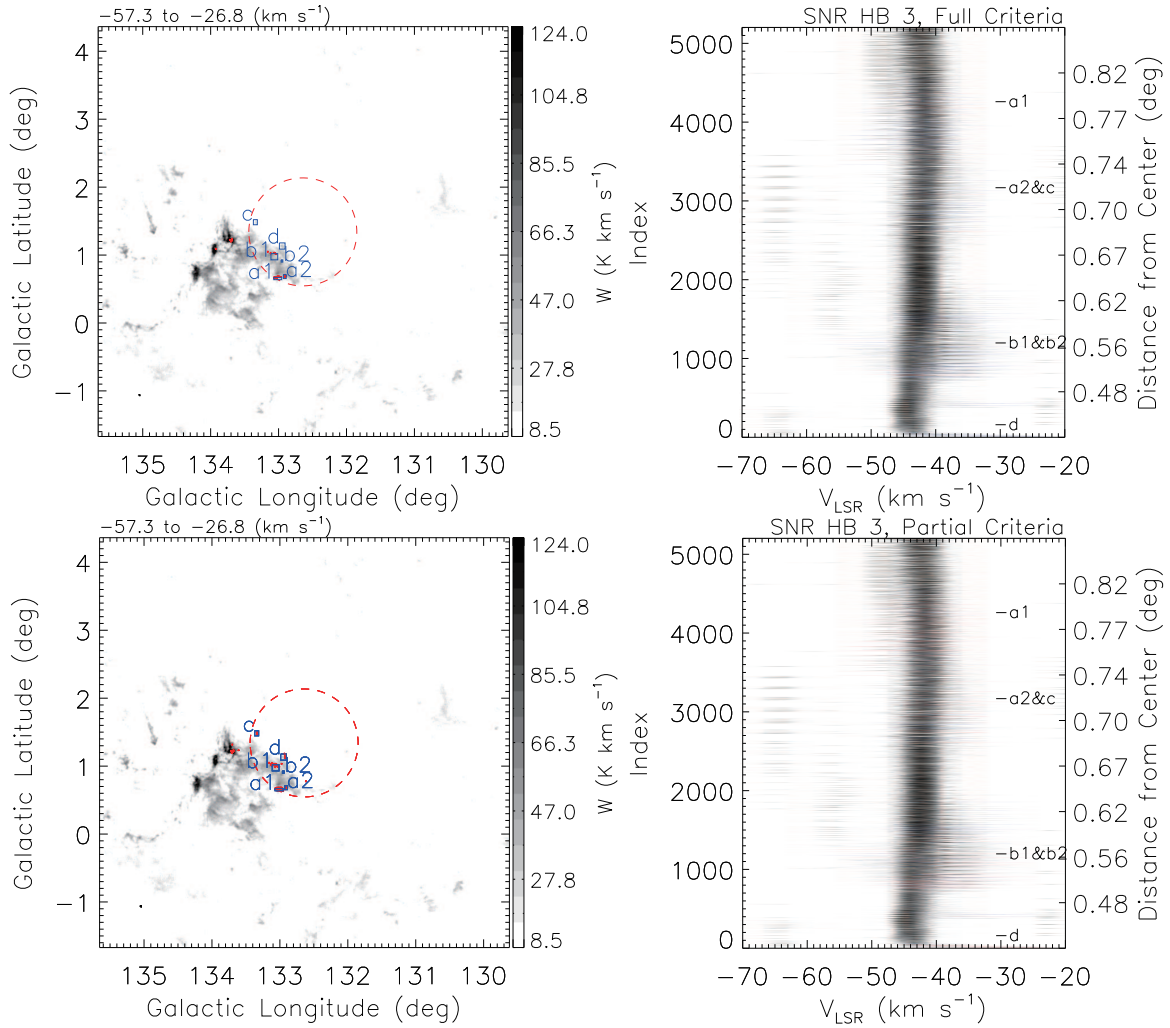


Fig. 3.— Same as Figure 2, but for SNR HB 3. Both integrated intensity maps in the left column are in the velocity range of -57.3 to -26.8 km s^{-1} . Regions a1, a2, b1, b2, c, and d are adopted from Zhou et al. (2016c), which indicate positions of shocked molecular clumps. All broad lines outside the SNR region are located in the star-forming region W3.

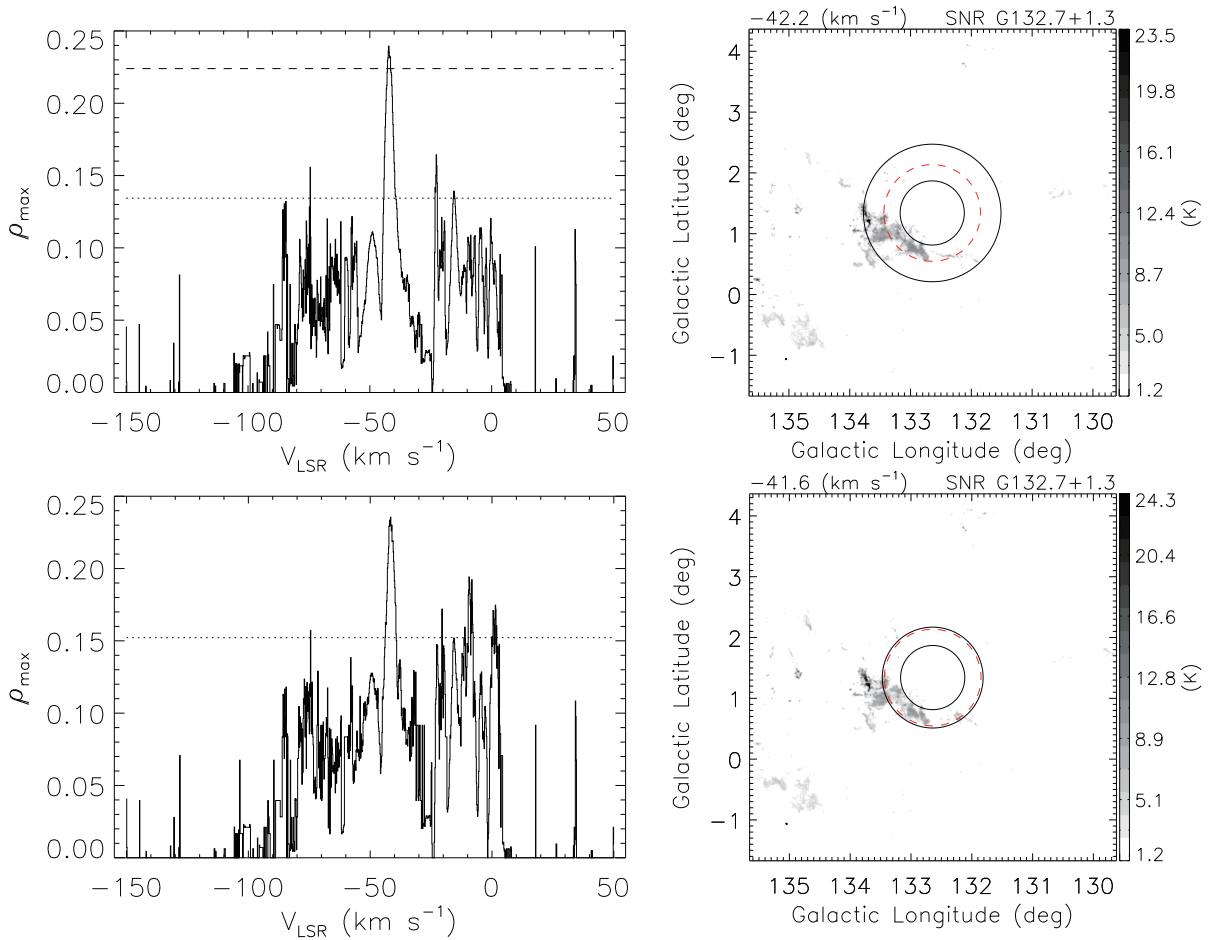


Fig. 4.— Maximum spatial correlation coefficients (SCCs) at each velocity channel and ^{12}CO ($J=1-0$) intensity maps at the corresponding velocity channel at the SCC peak for SNR HB 3. Dashed and dotted lines in panels in the left column denote 5σ and 3σ levels, respectively. Black circles in panels in the right column indicate the annular template applied in the calculation to obtain the maximum SCC. The red dashed circle is the same as in Figure 3. Upper panels show SCC results considering pixels inside the ring template or within twice the SNR radius, which has a significant peak at ~ -42.2 km s^{-1} . For comparison, the peak of the SCC at ~ -41.6 km s^{-1} in lower panels, considering pixels inside the ring template or within the SNR radius, is not above 5σ , however, it distinguishes the molecular shell structure around the SNR more precisely.

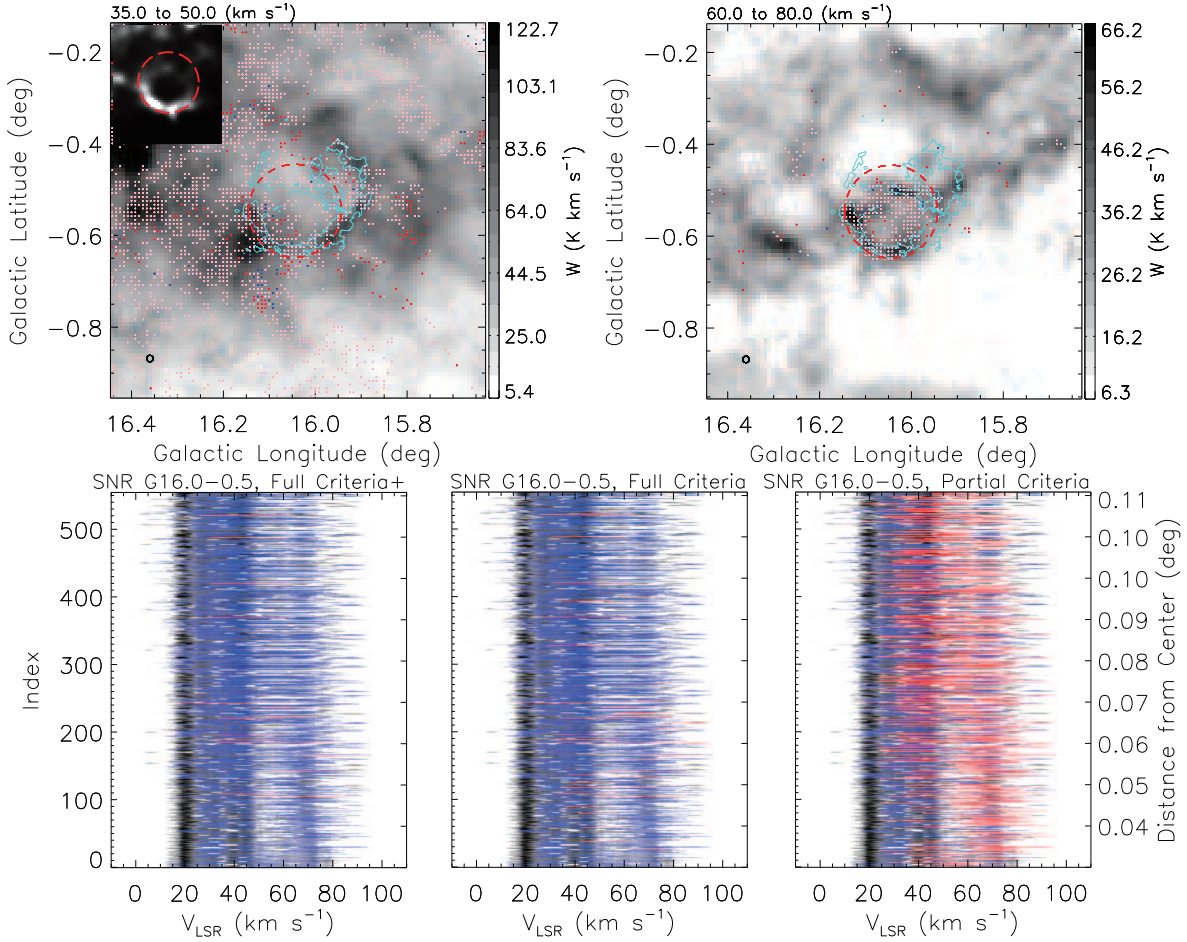


Fig. 5.— Same as Figure 2, but for SNR G16.0–0.5. Two integrate intensity maps of ^{12}CO ($J=1-0$) emission in the upper row are in the velocity ranges of $+35$ to $+50$ km s^{-1} (*left*) and $+60$ to $+80$ km s^{-1} (*right*). Locations of broad lines at velocities of $+43.7$ and $+67.9$ km s^{-1} are denoted by tiny stars on the corresponding *left* and *right* integrated intensity maps, respectively. Broad lines identified by partial criteria are in pink, those by full criteria are in red, and those by full criteria plus the clean subbackground region condition are in blue. Cyan contours in both integrated intensity maps are at half the column density maximum of shocked molecular gas obtained by Beaumont et al. (2011). The GLEAM 200 MHz radio continuum emission map in power-law scale is superimposed on the upper left corner of the *left* integrated intensity map, overlaid with the same red dashed circle as in integrated intensity maps. In the index-velocity maps in the bottom row, broad lines identified by full criteria plus the clean subbackground region condition (*left*), full criteria (*middle*), and partial criteria (*right*) are in red.

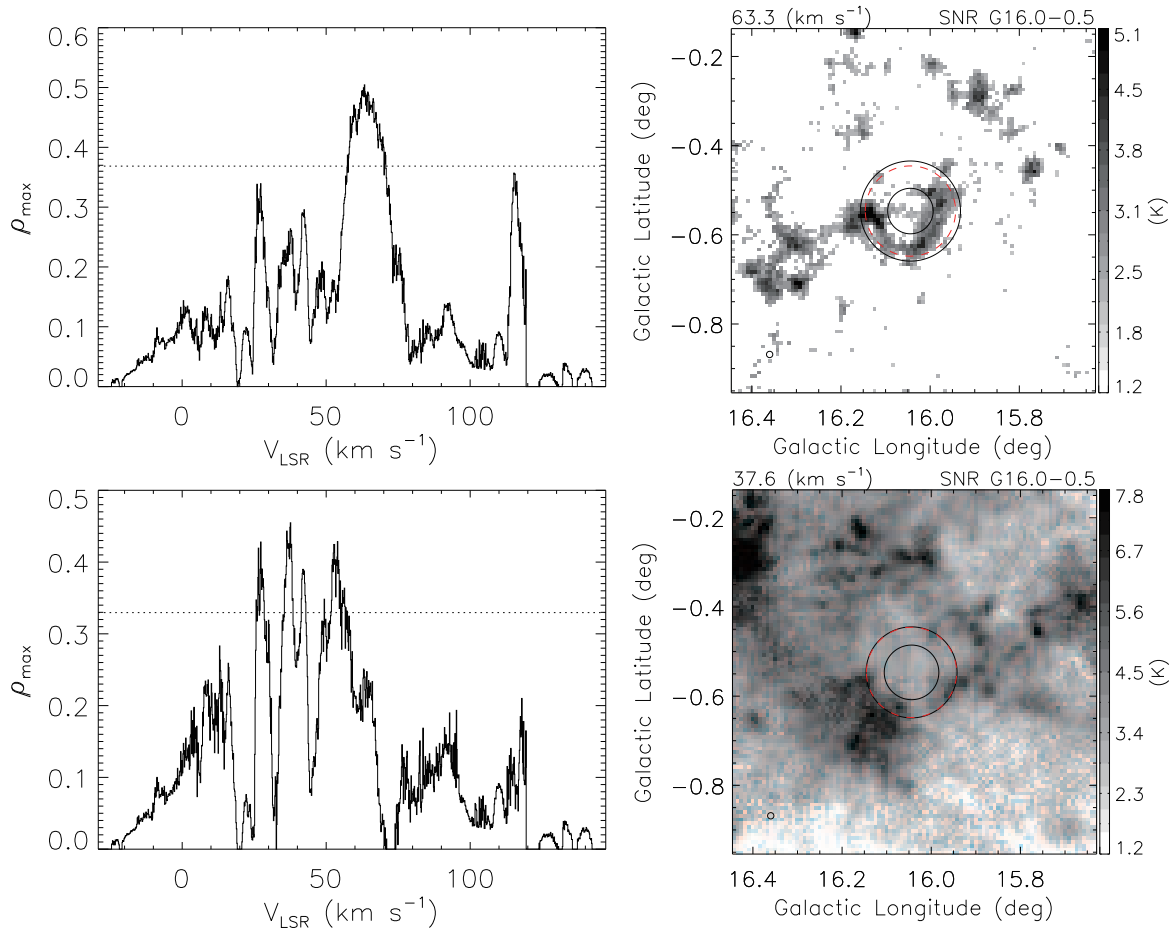


Fig. 6.— Same as Figure 4, but for SNR G16.0–0.5. The red dashed circle in the right panel is the same as in Figure 5. The peak of the SCC at $\sim+63.3$ km s^{-1} in upper panels is above 0.5, nevertheless, the peak of the SCC in lower panels at $\sim+37.6$ km s^{-1} is not so significant.

in the velocity versus SCC plot is wide. There is shell-like molecular gas at $\sim+63.3 \text{ km s}^{-1}$ spatially correlated with the southeastern radio continuum shell of the remnant. It supports the association between the remnant and the 67.9 km s^{-1} broad line component. Nevertheless, when considering pixels inside the ring templates or within the radius of the SNR, the SCC has a nonsignificant peak at $\sim+37.6 \text{ km s}^{-1}$. Molecular gas at $\sim+37.6 \text{ km s}^{-1}$ is distributed around the southeastern and southwestern boundaries, which belongs to the $+43.7 \text{ km s}^{-1}$ broad line component.

There is not much ^{12}CO ($J=3-2$) emission detected around $+67.9 \text{ km s}^{-1}$ as shown by Beaumont et al. (2011). ^{12}CO ($J=3-2$) line emission is efficient to trace hot shocked molecular gas but not cold quiet molecular gas. Based on the spatial correlation result as well as identified broad CO lines with high accuracy, the SNR is probably associated with the $+67.9 \text{ km s}^{-1}$ component. However, we cannot totally rule out the possibility of an association between the SNR and the $+43.7 \text{ km s}^{-1}$ component. Note that a further study of the expanding gas motion suggests that the $+43.7 \text{ km s}^{-1}$ component is associated with another object, which supports the association between SNR G16.0–0.5 and the $+67.9 \text{ km s}^{-1}$ component (Zhou et al. 2023, in preparation). Based on the full distance probability density function, the kinematic distance of the $+67.9 \text{ km s}^{-1}$ velocity component is estimated as $3.9\pm 0.3 \text{ kpc}$, which is located in the Norma spiral arm. Kinematic distances of the $+43.7 \text{ km s}^{-1}$ component are estimated as 3.2 ± 0.3 and $4.0\pm 0.3 \text{ kpc}$. The $+43.7 \text{ km s}^{-1}$ velocity component might be also located in the Norma spiral arm, as indicated by the full distance probability density function.

4. Results

We universally search for evidence of kinematic and spatial correlation of SNR-MC association for 149 SNRs, 170 SNR candidates (SNRCs), and 18 pure PWNe in our coverage. We apply full criteria to identify broad lines associated with SNRs at first, thereafter, apply the partial criteria to those with no broad lines found by full criteria. Broad lines identified by the partial criteria are considered as candidates. In some SNRs, more than one broad line components at different velocities are found. Multiple broad line components found in one SNR might all belong to it, which originate from molecular gases pushed toward and away from us at the near side and far side of the remnant, respectively. However, such multiple components might also originate from contamination of the line overlapping effect or overlaid energetic objects. In particular, in directions perpendicular to the direction of the circular motion of the solar system barycen-

ter around the Galactic center, i.e. around $l\sim 0^\circ$ and $l\sim 180^\circ$, MCs in different spiral arms are with systemic velocities close to each other, where the line overlapping effect is severe. Some lines are intrinsically indistinguishable in observations, which affects broad line identification results. For SNRs with many broad lines at different velocities identified even by full criteria, we use broad lines identified by full criteria plus the clean subbackground region condition as a reference. We greatly eliminate the line overlapping effect in our searching method. Besides, further examination is performed in settling the systemic velocity of MC associated with SNRs. Spatial correlations are also examined to support kinematic evidence, or provided as independent evidence for SNR-MC association candidates. For SNRs and SNRCs within 10° of $l\sim 0^\circ$ or within 5° of $l\sim 180^\circ$, where broad line identifications are affected by serious line overlapping effects, we search spatial correlation evidence first, and then choose those supported by identified broad line candidates. For 18 pure PWNe, to identify candidates of associated MCs, we also search spatial correlation evidence over a large extent at first, and then further examine related broad lines identified by full criteria.

TABLE 1
SNR-MC ASSOCIATIONS IN SURVEY.

SNR (Other Name)	GLon _o	GLat _o	Coverage 'x'	Type ^a	BL V_{LSR}^b km s ⁻¹	SC V_{LSR} (Coefficient) ^c km s ⁻¹	V_{sys}^d km s ⁻¹	Distance ^e kpc	V_{HII}^f km s ⁻¹
G1.4-0.1	1.460	-0.154	41×41	S	+78.9, +127.7	[+57.0 (0.40)]	-4.8?	12.6 (0.23)?	-2.2
G1.9+0.3	1.871	0.324	7×7	S	[-8.7, -2.1, +8.3, +10.0, +49.4]	-	-	-	-
G3.7-0.2	3.775	-0.288	57×57	S	-30.6, +9.3, +17.3, +21.3, +83.5	+19.2 (0.48), +79.4 (0.55)	+9.3?, +83.5?	2.9 (0.47)?, 7.7 (0.66)?	-28.9, +4.1
G3.8+0.3	3.851	0.349	81×81	S	-33.2, -0.6, +12.1, +162.9, +173.2, +185.1	+8.7 (0.38)	+12.1?, +162.9?	2.9 (0.60)?, 8.1 (1.00)?	+7.3
G4.5+6.8 (Kepler)	4.519	6.819	14×14	S	-	[+11.7 (0.29)]	-	-	-
G4.8+6.2	4.776	6.231	65×65	S	-	[+4.8 (0.46)]	+4.8?	1.6 (0.26) or 14.8 (0.26)?	-
G5.2-2.6	5.173	-2.612	55×55	S	-	+7.8 (0.30)	+7.8?	1.5 (0.75)?	-
G5.4-1.2 (Milne 56)	5.363	-1.220	148×148	C	-24.9, -9.7, +0.3, +11.1, +22.1, +187.5	-14.8 (0.27), +8.6 (0.27), +29.7 (0.38)	-24.9	4.2 (0.56) or 12.1 (0.44)	-
G5.5+0.3	5.545	0.368	59×59	S	+10.3	+7.0 (0.55)	+10.3	2.9 (0.54)	-
G6.1+0.5	6.104	0.479	73×73	S	+7.0	+6.0 (0.33)	+7.0	3.0 (0.43)	-
...									

NOTE.—The full table is published in machine-readable format with this paper.

^aType of SNRs, S for shell, C for composite, F for filled center (also known as plerion), and "?" denotes uncertain ones.

^b V_{LSR} of detected broad lines. Those identified only by partial criteria are enclosed by square brackets.

^c V_{LSR} of spatially correlated molecular gas, with the corresponding spatial correlation coefficient enclosed in brackets. Those with coefficients below 5σ confidence level and less than 0.5 are enclosed by square brackets.

^dSystemic velocity of associated MC. "?" denotes possible ones, see text for details.

^eKinematic distance corresponding to V_{sys} . All kinematic distances are estimated by a full distance probability density function (Reid et al. 2016, 2019), and estimated probabilities are enclosed in brackets.

^f V_{LSR} of overlapped H II regions.

TABLE 2
SNR CANDIDATE-MC ASSOCIATIONS IN SURVEY.

SNR candidate	GLon _o	GLat _o	Coverage 'x'	Type	BL V_{LSR} (Accuracy) km s ⁻¹	SC V_{LSR} (Coefficient) km s ⁻¹	V_{sys} km s ⁻¹	Distance kpc	V_{HII} km s ⁻¹
G1.95-0.10	1.929	-0.091	25×25	F	-42.5, +36.7, +44.7, +88.4, +124.9	[+59.5 (0.40)]	+44.7?	8.1 (0.69)?	-
G1.98-0.46	1.975	-0.460	20×20	S	+2.2, +12.6, +157.4	+5.1 (0.40), +8.6 (0.46)	+12.6?	2.8 (0.76)?	-
G2.23+0.06	2.228	0.058	9×9	S	[-23.2, +11.3, +16.6, +23.7, +156.5]	-15.9 (0.54), -6.3 (0.67), -2.9 (0.53), -1.0 (0.55), +6.0 (0.65), +8.3 (0.51), +19.4 (0.52)	-	-	-
G2.28+0.40	2.248	0.385	27×27	S	-66.8, -43.3, +4.8, +13.8, +88.4	+3.2 (0.40), +19.0 (0.40)	+4.8?	2.8 (0.54)?	+4.9
G2.91-0.18	2.910	-0.183	48×48	F	-40.0, -13.3, +4.0, +13.3, +18.6, +52.7, +88.8, +102.6, +160.3 +23.7	+14.3 (0.30), +43.3 (0.27)	-40.0	4.7 (0.92)	-3.5, -2.1, +2.5, +18.1
G3.10-0.09	3.101	-0.093	16×16	C		-18.1 (0.31)	+23.7?, +95.8?	2.9 (0.29) or 12.6 (0.35)?, 8.2 (0.90)?	-
G3.10+0.11	3.103	0.110	9×9	S	[+11.3, +22.7, +58.3, +104.9, +123.9, +135.0, +144.5, +153.6]	+1.7 (0.64), +11.3 (0.55), +17.6 (0.60), +81.9 (0.55), +84.3 (0.61), +87.6 (0.56) [+21.4 (0.37)]	-	-	-
G3.1-0.6	3.100	-0.600	83×83	C	-41.0, -28.4, +6.8, +12.8, +17.4, +19.9, +52.7, +82.2, +102.7 -31.4, +7.1, +15.3	[+0.8 (0.40)]	-41.0?	4.7 (0.71)?	+0.1, +5.1
G4.20-0.30	4.164	-0.333	32×32	C?			-31.4?	4.7 (0.67)?	-
G4.49-0.39	4.482	-0.391	29×29	F	+6.0, +14.1, +20.8, +43.2	+16.3 (0.37), +44.4 (0.41)	+14.1?	2.9 (0.61)?	-
...									

NOTE.—Same as Table 1 but for SNR candidates. The full table is published in machine-readable format with this paper.

Table 3: SNR-MC Associations Studied in Previous Works in Our Coverage.

SNR (Other Name)	OH 1720 MHz Maser V_{LSR}^a km s $^{-1}$	CO BL V_{LSR}^b km s $^{-1}$	CO SC V_{LSR}^c km s $^{-1}$	Other Evidences V_{LSR}^d km s $^{-1}$	Reference e
G1.4-0.1	-2.3 to -2.5	-	-	-32.6 to +29.9 (CH ₃ OH 36 GHz maser)	1, 2, 3
G1.9+0.3	D	-	-	-	1
G5.4-1.2 (Milne 56)	-21	-	-21	-	4, 5
G5.5+0.3	-	-	+12.5	-	5
G6.4-0.1 (W28)	+2.45 to +15.94	+5.8, +7	Y	-2.3 (OH 6035 MHz maser), +6.8 to +8.2 (CH ₃ OH 36 and 44 GHz maser), +6.1 to +13.1 (CS line), +6.3 to +7.4 (HCO+)	1, 10, 11, 12, 13, 14, 3, 6, 7, 8, 9
G8.7-0.1 (W30)	+36	-	-	-	4
G9.7-0.0	+43	-	-	-	4
G9.9-0.8	-	+31	-	+30 (H ₂ line)	15, 16
G11.0-0.0	-	-	+21, +40	+30 (SiO and CO lines, CS and HC ₃ N SC)	17, 18, 19
G11.1+0.1	-	-	+56	-	18
G11.1-0.7	-	-	+33	-	18
G11.2-0.3	D	+32	+33	+45 (H I absorption), +48 (H ₂ line)	1, 15, 16, 18, 20
G11.4-0.1	D	-	+30, +50	-	1, 18
G11.8-0.2	-	-	+49.8	-	18
G12.0-0.1	D	-	+37.4	-	1, 18
G12.2+0.3	-	+50	-	-	15
G13.3-1.3	D	-	-	-	1
G13.5+0.2	-	-	+24	+40 (H ₂ line)	16, 18
G15.4+0.1	-	-	+34, +47.8	+60 (H I SC), +60 (H I absorption)	18, 21, 22
G15.9+0.2	-	-	+29	-	18
G16.0-0.5	-	+40	-	+51 (H ₂ line)	16, 23
G16.7+0.1	+19.92 to +20.0	+25	+25.6, +47, +62	-	1, 15, 18, 24, 7
G17.0-0.0	-	-	+31, +93.4	-	18
G17.4-2.3	D	-	-	-	1
G17.8-2.6	D	-	-	-	1
G18.1-0.1	-	-	+53.1, +49	+100, +102, +103.74 (H I absorption), +73 to +85 (H ₂ line)	16, 18, 25, 26, 27, 28
G18.6-0.2	-	+42	+62, +66	+62 (H I absorption), +62.84 (H I absorption)	15, 18, 25, 26, 29
G18.8+0.3 (Kes 67)	-	-	+19, +21.35	+20 (CO (2-1)/(1-0) ratio of 1.25), +21.35 (H I absorption), +19 (H I SC)	18, 26, 30, 31, 32, 33, 34
G18.9-1.1	-	-	+25.6	+23 (H I absorption), +70 (H ₂ line)	16, 35, 36, 37
G20.0-0.2	-	-	+65, +66, +66.4	+66.4 (H I absorption)	18, 26, 38
G21.5-0.9	D	-	-	~+68 (H I absorption)	1, 26, 39
G21.8-0.6 (Kes 69)	+69.3 to +69.76 (compact), +83.6 to +85.2 (extended)	-	+83, +93.35	+85 (HCO+ line on radio peak), +86 to +93.35 (H I absorption), +61 (H ₂ line)	1, 16, 18, 26, 39, 40, 7
G22.7-0.2	D	+77	+75, +77	+76.63, +76.63 (H I absorption)	1, 18, 26, 41, 42
G23.3-0.3 (W41)	D (at +71)	-	+63, +70, +77, +78.51	+63 (H I SC), +78.51 (H I absorption)	1, 18, 26, 42, 43, 44, 45
G24.7-0.6	D	-	+60, +60.67	-	18, 46, 47
G24.7+0.6	-	-	+112	-	18
G27.4+0.0 (Kes 73, 4C-04.71)	D	+100	+90, +101	+90 (CO (2-1)/(1-0) ~ 1.1), +99.95 (H I absorption), +99 (H ₂ line)	1, 15, 16, 18, 26, 48
G27.8+0.6	D	-	-	-	47
G28.6-0.1	-	-	+86	-	18, 46
G29.6+0.1	-	+94	+99.2	-	15, 18
G29.7-0.3 (Kes 75)	D	+53, +54	+52, +54, +95, +112	+95 to +102 (H I absorption)	1, 15, 18, 26, 49, 50
G31.5-0.6	-	-	+87.5, +97	-	18
G31.9+0.0 (3C 391)	+97.04 to +110.2	+103.9 to +112	+107, +100	+100 (H ₂ line), +104.2 to +108.9 (broad CS line), +111.4 (broad HCO+ line)	1, 15, 16, 18, 47, 51, 52, 53, 54, 55, 7
G32.1-0.9	-	-	+95	+85 (H ₂ line)	16, 18
G32.4+0.1	-	+43	+10.8, +42.6	-	15, 18
G32.8-0.1 (Kes 78)	+86.1	+81	+74, +81, +81.81, +103	+81 (CO (2-1)/(1-0) ratio enhanced), +81.81 (H I absorption), +90 (H ₂ line)	16, 18, 26, 56, 57
G33.2-0.6	-	-	+54, +91	+82 (H ₂ line)	16, 18

Continued on next page

Table 3 – Continued

SNR (Other Name)	OH 1720 MHz Maser V_{LSR}^a km s^{-1}	CO BL V_{LSR}^b km s^{-1}	CO SC V_{LSR}^c km s^{-1}	Other Evidences V_{LSR}^d km s^{-1}	Reference ^e
G33.6+0.1 (Kes 79)	D	$\sim +105$	+70, +80, +103, +105	+80 (CO (3-2)/(1-0) > 0.8 and CO shell in P-V map), +105 (HCO+ line), +95 (H I SC), +57.9 (H I absorp- tion)	1, 15, 18, 26, 58, 59, 60, 61, 62
G34.7-0.4 (W44)	+23.8 to +47.35	+40, +45, +46.6, +47.5, +48	+40, +48, +52	+40 and +45 (high-J CO lines; CO (2- 1)/(1-0) > 1), +40 and +47.5 (HCO+ line), +41 to +49 (H ₂ line), +48 (¹³ CO (1-0)/ ¹² CO (1-0) ~ 0.03 and HCO+ (1-0)/ ¹² CO (1-0) \sim 0.3), +54.4 (OH 6035 MHz maser), +40.9 to +47.1 and +6.7 to +56.9 (CH ₃ OH 36 and 44 GHz maser), +50.48 (H I absorption)	1, 10, 11, 16, 18, 26, 6, 63, 64, 65, 66, 67, 68, 69, 7, 70, 71, 72, 8
G35.6-0.4	-	-	+55, +90	+63.67 (H I absorp- tion)	18, 26, 73, 74
G36.6-0.7	-	-	+57, +79	-	18
G39.2-0.3 (3C 396)	D	+69, +77, +84	+51, +67, +69, +69.39, +84	+56 (H ₂ line), +69.39 (H I absorption)	1, 15, 16, 18, 26, 75, 76, 77
G39.7-2.0 (W50)	-	+53, +77	+32	+53 (CO (2-1)/(1-0) > 0.9, CN (3/1-1/2)), +77 (H I SC)	78, 79, 80
G40.5-0.5	-	-	+55, +58, +67	-	18, 81, 82
G41.1-0.3 (3C 397)	-	+31, +32	+32, +38, +40	-	15, 18, 83, 84
G41.5+0.4	-	-	+58	-	18
G42.0-0.1	-	-	+66	-	18
G43.3-0.2 (W49B)	-	+14	+10, +32, +40, +45, +62	+11 (OH 6035 MHz maser), +63 (HCO+ broad line, high HCO+ (1-0)/CO (1-0) ratio), +12.55 (H I absorp- tion), +40 (H I ab- sorption), +10 (CO high T_{ex} and $\sim +6$ km s^{-1} expanding mo- tion), +64 (H ₂ line)	11, 15, 16, 18, 26, 85, 86, 87, 88
G43.9+1.6	-	+50	Y	-	89
G45.7-0.4	-	-	+26, +48.5	-	18
G46.8-0.3 (HC30)	-	+19	+19, +52	+0 to +40.4 (H I ab- sorption)	18, 90
G49.2-0.7 (W51C)	+68.9 to +72.13	+60	+50, +60	+67.6 (OH 6035 MHz maser), +60 (HCO+ line), +57.6 to +76.2 (CH ₃ OH 36 GHz maser), $\sim +70$ (H I absorption)	1, 11, 18, 63, 7, 91, 92, 93
G53.6-2.2 (3C 400.2)	-	-	-	+27 (H I SC)	94
G54.1+0.3	-	+23	+23, +53, +53.66	+53.66 (H I absorp- tion)	26, 95, 96, 97
G54.4-0.3 (HC40)	-	-	+36.66, +40	+44 (H ₂ line)	16, 52, 98
G57.2+0.8 (4C-21.53)	+30	-	+12, +30	-46 (H I SC)	100, 99
G59.5+0.1	-	+28	Y	+28 (CO (3-2)/(2-1) ~ 1.58)	101
G63.7+1.1	-	-	$\sim +13$, +21	$\sim +13$ (H I SC)	102, 103
G69.0+2.7 (CTB 80)	-	+11.5	+11.5	+13.5 (H I SC)	104
G73.9+0.9	-	-	+3	-	105
G74.9+1.2 (CTB 87)	-	-58	-58, -57.3, -57	-64 (H I SC)	106, 107, 108, 109
G78.2+2.1 (DR4)	-	-	-2 to +13.6	-	110, 111, 112
G84.2-0.8	-	-	-39, -17	-	105, 106, 113
G85.4+0.7	-	-	-41	-	105
G89.0+4.7 (HB 21)	-	-5, +3	-5, -3, ~ -1 (-10 to +8)	+3 (CO (2-1)/(1-0) ratio of 1.6 to 2.3), ~ -1 (H I SC)	114, 115, 116, 117
G93.7-0.2 (CTB 104A)	-	-	-	-6 (H I SC)	118
G94.0+1.0 (3C 434.1)	-	-	-13	-13 (CO (2-1)/(1-0) ratio ~ 1.6)	105, 119
G106.3+2.7	-	-	-6.4	-6.4 (H I SC)	120
G109.1-1.0 (CTB 109)	-	~ -55	-50 to -48	-50 (H I SC)	121, 122, 123, 124
G111.7-2.1 (Cas A)	-	~ -40	Y	-38 (H ₂ CO distance matching), -40 (H I SC and multibands consistency)	125, 126, 127, 128, 129, 15
G116.9+0.2 (CTB 1)	-	-	-	-32 (H I SC)	130

Continued on next page

Table 3 –Continued

SNR (Other Name)	OH 1720 MHz Maser $V_{\text{LSR}}^{\text{a}}$ km s^{-1}	CO BL $V_{\text{LSR}}^{\text{b}}$ km s^{-1}	CO SC $V_{\text{LSR}}^{\text{c}}$ km s^{-1}	Other Evidences $V_{\text{LSR}}^{\text{d}}$ km s^{-1}	Reference ^e
G120.1+1.4 (Tycho)	-	-63.5	-63.5, -62, -61	-61 (high CO (2-1)/(1-0) ratio), -51.5 (H I SC)	131, 132, 133, 134, 135
G127.1+0.5 (R5)	-	$\sim+5$	Y	-	136
G130.7+3.1 (3C 58)	-	-	-	-39.1 to -34.1, ~-38 (H I absorption), ~-36 (H I absorption and SC)	137, 138, 139
G132.7+1.3 (HB 3)	-	-45, -42, -40	-45, -43, -42, -40.5	-30 (H I SC), -42 (high-J CO lines with co-spatial H ₂ emission)	140, 141, 142, 143, 15
G141.2+5.0	-	-	-	-53 (H I SC)	144
G160.9+2.6 (HB 9)	-	-	-	-6 (H I SC)	145
G166.0+4.3 (VRO 42.05.01)	-	-	-22	-6 (H I SC and CO velocity gradient), -34 (H I SC)	106, 146, 147
G180.0-1.7 (S147)	-	-	-	-2.5 (optical extinction SC)	148
G182.4+4.3	-	-	+4	-	105
G189.1+3.0 (IC 443)	-32.0 to -3.5	-40.5 to -3.5, -5, -4.5, -4, -3, -2, +5	-4.5, -4, -3.6, +5	-5 (OH absorption line), -4.5 (high-J CO lines, CO line polarization), +9 (H _{α} line), -2 (CO (2-1)/(1-0) ratio > +3, CO (3-2)/(2-1) \sim 1.58), -4 (H I line with broad wing), -10 (H ₂ line), -5 (HCO+ and HCN self-absorption, CN, SiO, CS, SO, and H ₂ CO lines), -44.2 to -4.2 (CS, HCN, HNC, DCN, HCO+, H ¹³ CO+, H ₂ CO, H ₂ ¹³ CO, CH ₃ OH, CH ₃ CN, HC ₃ N, CO+, C ₂ H, C ₃ H ₂ , HDO, SiO, SO, SO ₂ , H ₂ S, and H ₂ CS lines), -3.5 (H I emission, CO, HCO+, HCN, and H ₂ lines)	1, 149, 15, 150, 151, 152, 153, 154, 155, 156, 157, 158, 159, 160, 161, 162, 163, 164, 165, 6, 68, 7
G205.5+0.5 (Mono-ceros Loop)	-	$\sim+5, \sim+19$	+5, +10, $\sim+11, \sim+15, +19, +20$	-	166, 167, 168, 18
G206.9+2.3 (PKS 0646+06)	-	-	+15	-	166
G213.0-0.6	-	$\sim+9$	+9, +21	-	166, 18
G5.7-0.1	+13	-	+12	-26.4 and -24.4 (CH ₃ OH 36 and 44 GHz maser)	4, 5, 63
G21.8-3.0	-	-	+5.9	-	169
G28.56+0.00	-	-	-	+96.6 (RRL of H II region assumed to be associated by H I absorption)	37
G29.4+0.1	-	-	$\sim+82$	-	170
G44.5-0.2	-	+60	Y	+60 (H I SC)	171
G51.21+0.11 (G51.26+0.11)	-	-	-	+37 to +70 (H I absorption)	172

^a V_{LSR} range of associated OH 1720 MHz maser emission, and 'D' for a detection of OH 1720 MHz line.

^b V_{LSR} of associated broad CO line.

^c V_{LSR} of spatially correlated CO emission, and 'Y' for a detection of spatially correlated CO emission without velocity information.

^d V_{LSR} by other evidence, where 'SC' represents spatial correlation.

^eReferences.– (1) Green et al. (1997); (2) Yusef-Zadeh et al. (1999); (3) Pihlström et al. (2014); (4) Hewitt & Yusef-Zadeh (2009); (5) Liszt (2009); (6) Claussen et al. (1997); (7) Hewitt et al. (2008); (8) Goss & Robinson (1968); (9) Arikawa et al. (1999); (10) Reach et al. (2005); (11) McDonnell et al. (2008); (12) Gusdorf et al. (2012); (13) Nicholas et al. (2012); (14) Wootten (1981); (15) Kilpatrick et al. (2016); (16) Lee et al. (2020); (17) Castelletti et al. (2016); (18) Sofue et al. (2021); (19) Voisin et al. (2019); (20) Green et al. (1988); (21) Castelletti et al. (2013); (22) Supan et al. (2015); (23) Beaumont et al. (2011); (24) Reynoso & Mangum (2000); (25) Johanson & Kerton (2009); (26) Ranasinghe & Leahy (2018b); (27) Paron et al. (2013); (28) Leahy et al. (2014); (29) Voisin et al. (2016); (30) Tian et al. (2007a); (31) Dubner et al. (2004); (32) Dubner et al. (1999); (33) Paron et al. (2012); (34) Paron et al. (2015); (35) Traverso et al. (1999); (36) Furst et al. (1989); (37) Ranasinghe et al. (2020); (38) Petriella et al. (2013); (39) Tian & Leahy (2008); (40) Zhou et al. (2009); (41) Su et al. (2014b); (42) Su et al. (2015); (43) Frail et al. (2013); (44) Tian et al. (2007b); (45) Leahy & Tian (2008b); (46)

Ranasinghe & Leahy (2018a); (47) Frail et al. (1996); (48) Liu et al. (2017); (49) Su et al. (2009); (50) Leahy & Tian (2008a); (51) Reach & Rho (1999); (52) Ranasinghe & Leahy (2017); (53) Reynolds & Moffett (1993); (54) Wilner et al. (1998); (55) Gusdorf et al. (2014); (56) Koralesky et al. (1998); (57) Zhou & Chen (2011); (58) Zhou et al. (2016a); (59) Kuriki et al. (2018); (60) Green & Dewdney (1992); (61) Giacani et al. (2009); (62) Stanimirović et al. (2003); (63) McEwen (2016); (64) Hoffman et al. (2005); (65) Anderl et al. (2014); (66) Sashida et al. (2013); (67) Seta et al. (2004); (68) Seta et al. (1998b); (69) Wootten (1977); (70) Yamada et al. (2017); (71) Yoshiike et al. (2013); (72) Caswell et al. (1975b); (73) Zhu et al. (2013); (74) Paron & Giacani (2010); (75) Su et al. (2011); (76) Lee et al. (2009); (77) de Oña Wilhelmi et al. (2020); (78) Su et al. (2018); (79) Huang et al. (1983); (80) Liu et al. (2020); (81) Yang et al. (2006); (82) Duvidovich et al. (2020); (83) Jiang et al. (2010); (84) Safi-Harb et al. (2005); (85) Chen et al. (2014); (86) Zhu et al. (2014); (87) Sano et al. (2021); (88) Zhou et al. (2022); (89) Zhou et al. (2020b); (90) Supan et al. (2022); (91) Brogan et al. (2000); (92) Koo & Moon (1997); (93) Tian & Leahy (2013); (94) Giacani et al. (1998); (95) Lee et al. (2012b); (96) Koo et al. (2008); (97) Leahy et al. (2008); (98) Junkes et al. (1992); (99) Zhou et al. (2020a); (100) Kothes et al. (2018); (101) Xu & Wang (2012); (102) Wallace et al. (1997); (103) Matheson et al. (2016); (104) Koo et al. (1993); (105) Jeong et al. (2012); (106) Huang & Thaddeus (1986); (107) Cho et al. (1994); (108) Kothes et al. (2003); (109) Liu et al. (2018); (110) Cong (1977); (111) Pollock (1985); (112) Higgs et al. (1983); (113) Feldt & Green (1993); (114) Koo et al. (2001); (115) Byun et al. (2006); (116) Dobashi et al. (2019); (117) Tatematsu et al. (1990b); (118) Uyaniker et al. (2002); (119) Jeong et al. (2013); (120) Kothes et al. (2001); (121) Sasaki et al. (2006); (122) Tatematsu et al. (1987); (123) Tatematsu et al. (1990a); (124) Kothes et al. (2002); (125) Ma et al. (2019); (126) Kilpatrick et al. (2014); (127) Zhou et al. (2018); (128) Reynoso & Goss (2002); (129) Keohane et al. (1996); (130) Willis & Dickel (1971); (131) Cai et al. (2009); (132) Lee et al. (2004); (133) Zhou et al. (2016b); (134) Chen et al. (2017b); (135) Reynoso et al. (1999); (136) Zhou et al. (2014); (137) Green & Gull (1982); (138) Roberts et al. (1993); (139) Kothes (2013); (140) Zhou et al. (2016c); (141) Routledge et al. (1991); (142) Landecker et al. (1987); (143) Rho et al. (2021); (144) Kothes et al. (2014); (145) Leahy & Tian (2007); (146) Arias et al. (2019); (147) Landecker et al. (1989); (148) Chen et al. (2017a); (149) Denoyer (1979a); (150) Denoyer (1979b); (151) Hewitt et al. (2006); (152) Lee et al. (2012a); (153) White et al. (1987); (154) Zhang et al. (2010); (155) Turner et al. (1992); (156) van Dishoeck et al. (1993); (157) Su et al. (2014a); (158) Cornett et al. (1977); (159) Ambrocio-Cruz et al. (2017); (160) Zhang et al. (2013); (161) Rosado et al. (2007); (162) Burton et al. (1988); (163) Dell'Ova et al. (2020); (164) Hezareh et al. (2013); (165) Xu et al. (2011); (166) Su et al. (2017b); (167) Aharonian et al. (2007); (168) Oliver et al. (1996); (169) Gao et al. (2020); (170) Castelletti et al. (2017); (171) Su et al. (2017a); (172) Ranasinghe & Leahy (2022).

Results of SNRs and SNRCs are listed in Table 1 and 2, respectively. We only present short versions of Table 1 and 2 here, and full versions are only available in electronic form. Systemic velocities of MCs associated with SNRs and SNRCs are settled, and corresponding kinematic distances are estimated by the full distance probability density function (Reid et al. 2016, 2019). Note that CO ($J=1-0$) emission is more advantageous in determining the systemic velocity of the associated MC, from which sufficient information about quiet molecular gases can be obtained. The systemic velocity is a directly observed quantity, and the kinematic distance is model dependent. To avoid bias between different models, we uniformly apply the full distance probability density function to estimate kinematic distances here. We also considered available H I absorption results in previous works for some SNRs to discriminate between near and far kinematic distances. For comparison, we also list the results of SNR-MC associations studied in previous works in Table 3 (see also Table 1 in Ranasinghe & Leahy 2022, for a summary of known SNR distances). For known SNRs, about 60% of them were found to be associated with MCs in previous works, however, new SNR-MC associations have still been gradually discovered in recent years. For SNRCs and PWNe, the study of MCs around them is still very limited, of which only about 4 and 11%, respectively, were found to be associated with MCs in previous works. It is worth noting that in some SNRs different evidence gives different velocity results. On the other hand, the interaction details of some SNR-MC associations were very well studied, with shocked molecular gases investigated through multiband observations, e.g., W28, W44, IC 443, etc. (see Table 3 for details).

We present details of searching results of SNRs and SNRCs in Sections 4.1 and 4.2, respectively. In Section 4.3, we discuss searching results for pure PWNe. Corresponding figures of individual objects are available online (Zhou et al. 2023).

4.1. SNRs

SNR-MC association results are summarized in Table 1. In order to better confirm the association evidence, further investigations, e.g., on spatial correlations with partial radio continuum shells or locations of broad lines, are performed on some objects, especially those with more than one broad line components identified. We also make efforts to eliminate contaminations of other energetic sources overlapped, e.g., H II regions. All considered H II regions are introduced from the WISE catalog of Galactic H II regions (Anderson et al. 2014), which is one of the most complete catalogs of H II regions in the Galaxy. Systemic velocities of H II regions overlapping SNRs are listed in Table 1. ^{12}CO or ^{13}CO velocities of H II regions are applied for better comparison with our data, and if they do not exist, velocities of other tracers are used. As noted by Anderson et al. (2014), velocities of most H II regions by different tracers are consistent, the mean of absolute velocity differences between molecular and ionized gas emission is $\sim 4 \text{ km s}^{-1}$.

Among 149 SNRs studied in this paper, 57 of them are found to be associated with MCs, and 70 of them are considered to be possibly associated with MCs. 40 of the 57 SNR-MC associations and 43 of the 70 possible SNR-MC associations were studied in previous works (see Table 3). There are also 7 SNRs with no associated MC found here, but suggested to be associated with surrounding clouds in previous works, mostly based on spatial correlations with H I gases. Few SNR-MC association results in this paper are not the same as those in previous works, including 7 of SNR-MC associations and 4 of possible SNR-MC associations, i.e. G9.9-0.8, G11.1+0.1, G15.4+0.1, G16.0-0.5, G18.9-1.1, G24.7+0.6, G41.5+0.4, G21.5-0.9, G29.7-0.3, G84.2-0.8, and G93.7-0.2. We discuss individual SNRs in Appendix A.

4.2. SNR Candidates

We list all results of SNRC-MC associations in Table 2. Most of SNRCs in our coverage have been recently discovered (Kassim 1988; Gorham 1990; Gray 1994; Trushkin 2001; Brogan et al. 2006; Helfand et al. 2006; Gerbrandt et al. 2014; Anderson et al. 2017; Hurley-Walker et al. 2019a; Gao et al. 2020; Dokara et al. 2021; Ranasinghe et al. 2021), which are not well studied by multiband observations. A similar approach to study SNR-MC associations is performed to investigate associations between SNRCs and MCs. All types of SNRCs are examined in the same way, in particular, no enlargement of coverage is applied for plerionic SNRCs.

170 SNRCs are examined, and 50 of them are suggested to be associated with MCs. There are also 91 of SNRCs considered to be possibly associated with MCs. For all SNRCs, only six of them were studied in previous works, of which five are considered as possible SNRC-MC associations and one as a fixed SNRC-MC association here. The result for one of them is not the same as that in previous works, i.e. G28.56+0.00. We discuss individual SNRCs in Appendix B.

TABLE 4
PWN-MC ASSOCIATION CANDIDATES IN SURVEY.

PWN ^a	PSR ^a	GLon _o	GLat _o	Coverage ′ × ′	SC V_{LSR} (Coefficient) ^b km s ⁻¹	BL Detection ^c	$V_{\text{sys}}^{\text{d}}$ km s ⁻¹	Distance ^e kpc
G18.00−0.69	J1826−1334	18.001	−0.691	28 × 28	+5.4 (0.56)	N	+60.8	3.8 (1.00)
Eel	J1826−1256	18.500	−0.400	500 × 500	[+51.9 (0.45)]	Y	+19.8	1.50 (0.60)
G21.88−0.10	J1831−0952	21.881	−0.102	261 × 261	+40.2 (0.35)	Y	+55.0	3.4 (0.47)
G23.5+0.1?	J1833−0827	23.386	0.063	290 × 290	[+96.2 (0.38)]	Y	+95.8	5.3 (0.84)
G25.24−0.19	J1838−0655	25.246	−0.196	65 × 65	+3.5 (0.47), +9.0 (0.44), +107.1 (0.40)	N, N, Y	+102.1	5.9 (0.95)
G32.64+0.53?	J1849−0001	32.638	0.527	64 × 64	+11.0 (0.44)	N	+98.0	5.2 (0.68)
G36.01+0.06?	J1856+0245	36.008	0.058	74 × 74	[+34.9 (0.45)]	Y	+58.1?	9.5 (1.00)?
G47.38−3.88	J1932+1059	47.382	−3.884	375 × 375	+6.7 (0.33)	N	+6.7?	0.361
G59.20−4.70	J1959+2048	59.197	−4.697	18 × 18	[+13.0 (0.23)]	N	-	-
G63.7+1.1?	3XMM J194753.4+274357 (CXO)	63.781	1.143	215 × 215	[−14.1 (0.28)]	N	+5.6?	7.2 (0.65)?
CTB 87	J194753.3+274351? CXOU J201609.2+371110?	74.944	1.114	236 × 236	+5.4 (0.29)	Y	−51.6?	6.1?
G75.23+0.12	J2021+3651	75.222	0.111	52 × 52	+5.6 (0.46)	[Y]	+6.0?	3.4 (0.99)?
G80.22+1.02	J2032+4127	80.224	1.028	161 × 161	[−2.9 (0.32)]	N	−3.0?	2.6 (0.36)?
3C 58	J0205+6449	130.716	3.080	273 × 273	−7.3 (0.35)	Y	-	-
G141.2+5.0	CXOU J033712.8+615302?	141.180	5.036	113 × 113	[−9.5 (0.32)]	N	-	-
Mushroom	B0355+54	148.190	0.811	47 × 47	[+5.2 (0.30)]	N	-	-
Crab	B0531+21	184.554	−5.786	211 × 211	[+3.2 (0.36)]	N	+3.2?	1.6 (0.58)?
Geminga	J0633+1746	195.134	4.266	100 × 100	−10.8 (0.31)	N	−10.8?	0.25

^a“?” denotes a PWN or pulsar (PSR) candidate.

^b V_{LSR} of spatially correlated (SC) molecular gas, with the corresponding spatial correlation coefficient enclosed in brackets. Those with coefficients below 5σ confidence level and less than 0.5 are enclosed by square brackets.

^cDetection of broad line (BL) emission related to spatially correlated molecular gas. Those identified only by partial criteria are enclosed by squared brackets.

^dSystemic velocity of candidate MC associated with the PWN, and “?” denotes possible ones, see text for details.

^eKinematic distance corresponding to V_{sys} , with the estimated probability enclosed in brackets. The same calculation method as in Table 1 is used, except the distance of CTB 87 estimated by the extinction-distance relation in previous work (Foster & Routledge 2002; Kothes et al. 2003), and the distances of G47.38−3.88 and Geminga estimated by parallax measurements (Chatterjee et al. 2004; Faherty et al. 2007).

4.3. PWNe

We examine MCs around 18 pure PWNe here, to search candidates of associated MCs. Our results of PWN-MC association candidates are presented in Table 4. Kinematic distances of PWN-MC association candidates are estimated. Some of these PWNe have distance estimation results from previous works, which are comparable to the distance results here. Note that most distance measurements in previous works are for associated pulsars. Only two PWNe are with surrounding CO emissions studied in previous works, i.e. G63.7+1.1 and CTB 87, of which possible associations with MCs are found here. There are another two PWNe with surrounding H I emission studied in previous works, i.e. 3C 58 and G141.2+5.0, however, no associated MCs are found here.

We discuss individual PWNe in Appendix C.

5. Discussion

5.1. Proportion of SNRs associated with MCs

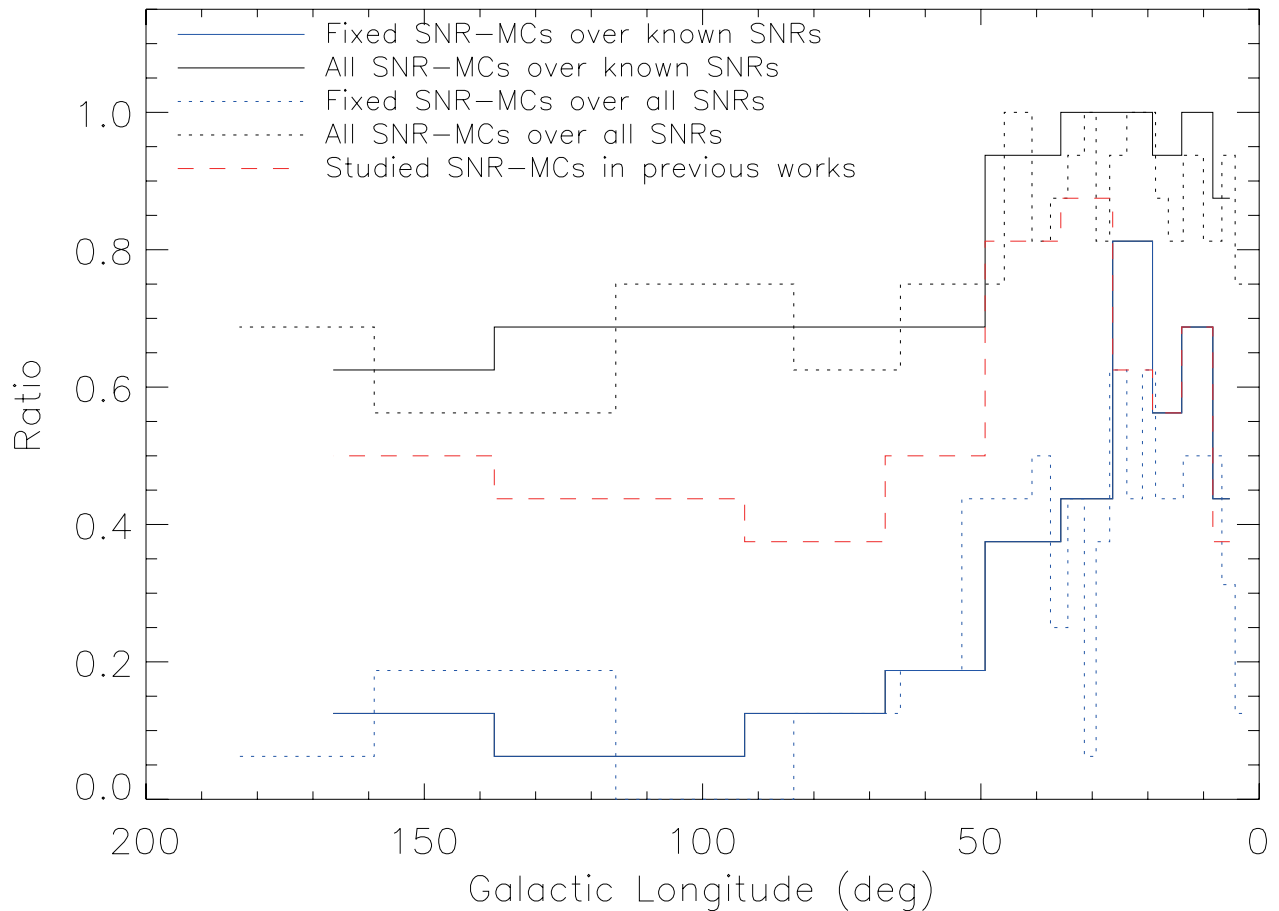


Fig. 7.— Ratios of SNRs associated with MCs along the Galactic longitude. Each histogram is adaptively binned with the number of corresponding SNRs to be sixteen. Black and blue histograms show ratios of all and fixed SNR-MC associations, respectively. Solid lines are for known SNRs, and dotted lines for all known and candidate SNRs. Red dashed line is the ratio of previously detected SNR-MC associations in known SNRs.

Ratios of SNRs associated with MCs along the Galactic longitude are shown in Figure 7, including fixed and all SNR-MC associations in known and all SNRs, respectively. All SNRs include known and candidate SNRs. The ratio of previously detected SNR-MC associations in known SNRs is also shown for reference. All ratios have similar distributions, which are large within the Galactic longitude of $\sim 50^\circ$. It is consistent with the distribution of the ratio of previously detected SNR-MC associations. If all previously detected SNR-MC associations are real, the accuracy of fixed SNR-MC associations suggested in this paper would be at least 70%, and at least 60% for possible SNR-MC associations. Among the previously detected SNR-MC associations, 91% are identified here by ^{12}CO ($J=1-0$) line emission. ^{12}CO ($J=1-0$) line emission of SNR-MC associations can be

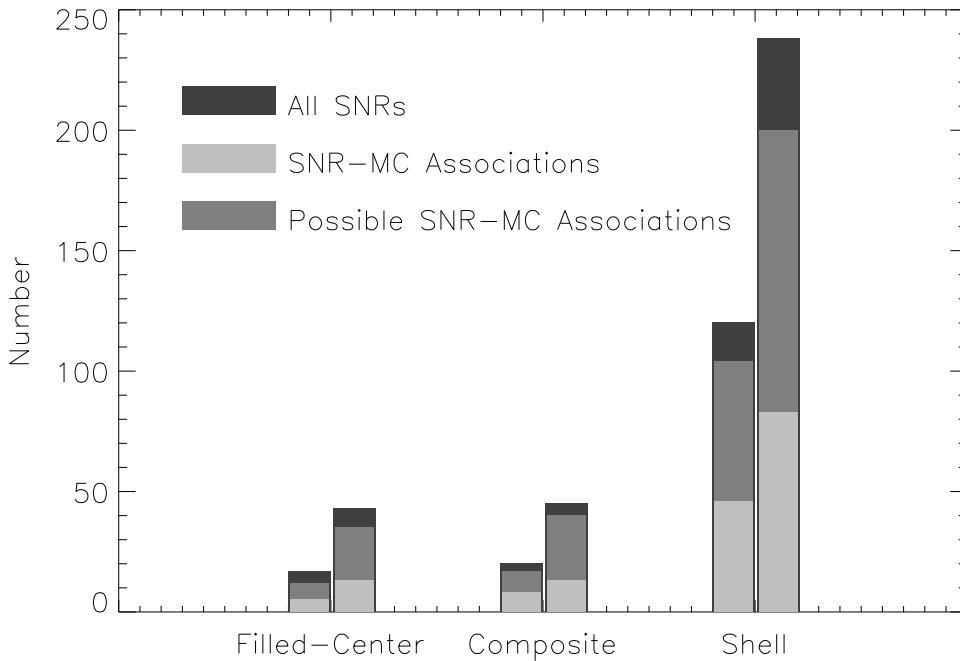


Fig. 8.— Type distributions of SNRs associated with MCs and all SNRs. For each pair of bars, the left one is for SNRs of certain type, and the right one for all SNRs of certain and possible type. The histogram of possible SNR-MC associations (dark gray) is stacked on top of that of fixed SNR-MC associations (light gray), and they are contained in that of all SNRs (black).

contaminated by background emission. However, it is still a good tracer for these associations. Note that there are about 41% of previously detected SNR-MC associations suggested as fixed SNR-MC associations here, and about 50% considered as possible ones.

Figure 8 shows the number of different types of SNRs and that associated with MCs. Except for SNRs of certain composite type, all types of SNRs contain about 30% fixed SNR-MC associations. Considering that only about half of previously detected SNR-MC associations are identified as fixed SNR-MC associations, there is probably more than 60% of SNRs associated with MCs. As indicated by the number of all fixed and possible SNR-MC associations, the percentage of SNRs associated with MCs could be as high as about 80. Among different types of SNRs, composite type SNRs have the highest proportion of being associated with MCs. This is reasonable, since composite SNRs are originated from core-collapse supernovae, and they are interacting with surrounding medium. Filled-center type SNRs are also originated from core-collapse supernovae; however, they have no radio continuum shell indicating effective interactions with surrounding medium. As indicated by the number of all fixed and possible SNR-MC associations for composite type SNRs, there could be close to 90% of core-collapse SNRs interacted with MCs during their lifetime.

5.2. Distribution of SNRs associated with MCs

We estimate radii of SNRs that are associated with MCs, based on their angular sizes and kinematic distances. Angular sizes are estimated from radio continuum emission of SNRs or associated molecular shell-like structures for those with no significant radio continuum emission detected. Kinematic distances of SNRs are estimated based on systemic velocities of their associated MCs by applying the full distance probability density function⁸ (Reid et al. 2016, 2019). We also estimate progenitor initial masses of some SNRs based on their linear relationship with the size of the main-sequence interstellar bubble in a molecular environment, which is reflected by the size of SNRs associated with MCs (see details in Chen et al. 2013). Since this relationship is only valid for stars in the mass range of 8 to 25–30 M_{\odot} , those with estimated progenitor masses outside this range are excluded. The number of SNRs with small-mass progenitors far exceeds the number of SNRs with

⁸<http://bessel.vlbi-astrometry.org/node/378>

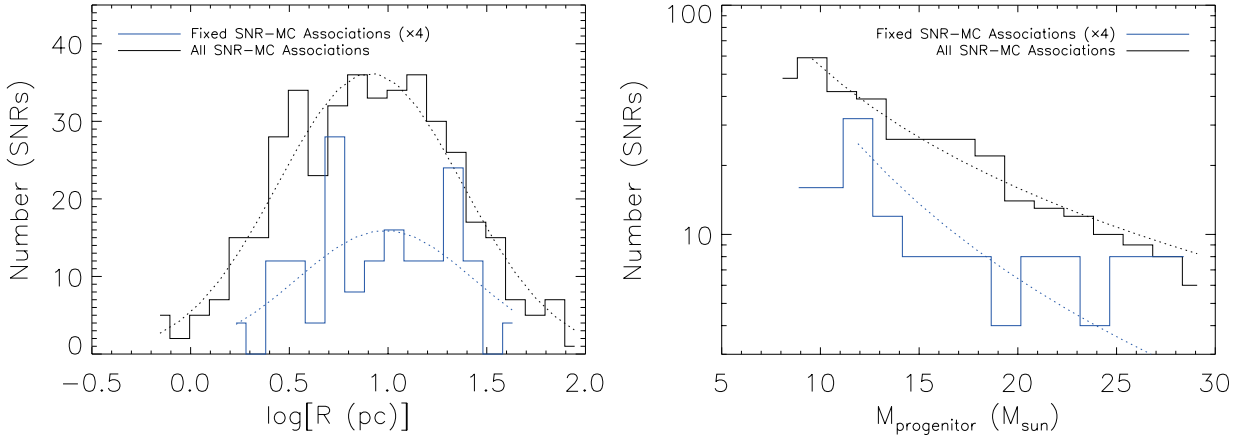


Fig. 9.— Radius (*left*) and progenitor initial mass (*right*) distributions for SNRs associated with MCs. Fixed SNR-MC associations in known SNRs are in blue except for those within 10° of $l \sim 0^\circ$ and within 5° of $l \sim 180^\circ$. All fixed and possible SNR-MC associations in all known and candidate SNRs are in black. The numbers of fixed SNR-MC associations are multiplied by 4 for better visibility. Radii are mostly estimated based on SNRs’ bright radio continuum shells. The progenitor initial mass is estimated based on its linear relationship with the size of the main-sequence interstellar bubble in a molecular environment reflected by the size of SNRs associated with MCs (see details in Chen et al. 2013). Lognormal fitting results of radius distributions and power-law fitting results of progenitor initial mass distributions are shown as dotted lines. SNR radius distributions peak at $9.7^{+2.8}_{-2.2}$ and 8.1 ± 0.5 pc, for the fixed and all SNR-MC associations, respectively. Progenitor initial mass distributions have indices of -2.6 ± 0.6 and -2.3 ± 0.1 , for the fixed and all SNR-MC associations, respectively.

large-mass progenitors. SNRs misidentified at large distances have a large impact on the mass distribution, even though their number is comparable to that of SNRs misidentified at small distances. Therefore, when estimating progenitor masses, we use only the smallest distance of all possible distances for each possible SNR-MC association.

Distributions of the radii and the progenitor initial masses of the SNRs associated with MCs are shown in Figure 9, which are fitted by lognormal and power-law distribution functions, respectively. Fitting of the mass distributions starts at the peak. For both radius and progenitor initial mass distributions, fitting parameters for fixed SNR-MC associations except for those within 10° of $l \sim 0^\circ$ and 5° of $l \sim 180^\circ$ are consistent with that for all fixed and possible SNR-MC associations. It indicates that possible SNR-MC associations do not introduce any significant systematic deviations. The radius distribution of SNRs associated with MCs peaks at ~ 8.1 pc. The progenitor initial mass distribution has an index of ~ -2.3 , which is consistent with the Salpeter index of -2.35 (Salpeter 1955; Bastian et al. 2010, etc.).

The height from the Galactic plane for SNR-MC associations is estimated according to their kinematic distances. Because of the Sun’s vertical displacement from the Galactic midplane, there is a small angle between the Galactic plane and the $b = 0^\circ$ plane. The position of the Galactic midplane is derived from fixed SNR-MC associations in known SNRs except for those within 10° of $l \sim 0^\circ$ and 5° of $l \sim 180^\circ$ by the least squares fitting. Thereby, the height of the Sun above the Galactic midplane is estimated as ~ 15.7 pc. We use the same Galactic plane position to calculate the height of all SNR-MC associations. Distributions of the height from the Galactic plane for SNR-MC associations are shown in Figure 10. The height distribution of all SNR-MC associations has two components, a major narrow component and a minor broad component. Some possible SNR-MC associations with uncertain distances may contribute to the broad component; however, the broad component still exists when we use only the minimum distance among all possible distances for each possible SNR-MC association. The number of fixed SNR-MC associations is limited, of which the height distribution may also have a weak broad component, not significant. It can be fitted well by one Gaussian function. For the height distribution of all SNR-MC associations, the thicknesses (i.e. FWHMs) of two components are estimated as 65 ± 6 and 182 ± 64 pc, respectively. The thickness (i.e. FWHM) is estimated as 90 ± 9 pc for the height distribution of the fixed SNR-MC associations, which is consistent with that of the thin CO disk revealed by Su et al. (2019). However, it may be just an intermediate value between the thicknesses of two components of the distribution of all SNR-MC associations. SNR-MC associations may trace MCs of active star-formation. The thin and thick disks of MCs associated with SNRs found here may be inner layers of the thin and thick CO

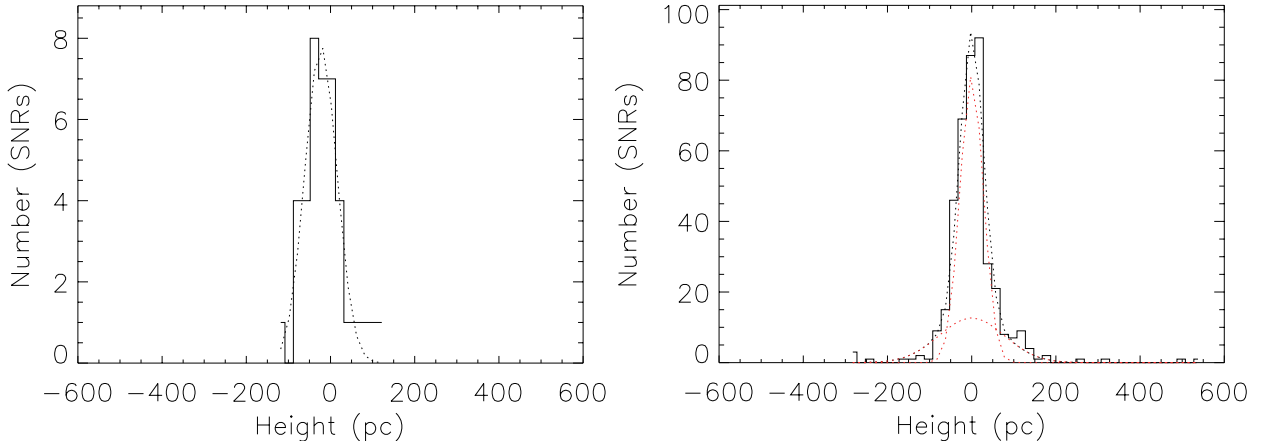


Fig. 10.— Distributions of heights from the Galactic plane for SNR-MC associations. Fixed SNR-MC associations in known SNRs except for those within 10° of $l \sim 0^\circ$ and 5° of $l \sim 180^\circ$ are shown in the left panel. All fixed and possible SNR-MC associations in all known and candidate SNRs are shown in the right panel. The position of the Galactic midplane is derived from the fixed SNR-MC associations by the least squares fitting. The height of the Sun above the Galactic midplane is estimated as ~ 15.7 pc. The same position of the Galactic midplane is also used to calculate heights of all SNR-MC associations. Black dotted lines indicate fitting results by a Gaussian function in the left panel and by two Gaussian functions in the right panel (separated components shown by red dotted lines). Note that all distances estimated for possible SNR-MC associations are used. However, if we use only the smallest distance for each possible SNR-MC association, the height distribution still has two components.

disks revealed by Su et al. (2019), respectively. The ratio of the peak of the thin and thick disks of SNR-MC associations is about 6, which is larger than that of CO disks, i.e. about 2. It indicates that the star-formation may be more efficient in the thin disk.

Figure 11 shows correlations between the radius and the height from the Galactic plane for SNRs associated with MCs. Fixed and all SNR-MC associations selected from known SNRs except for those within 10° of $l \sim 0^\circ$ and 5° of $l \sim 180^\circ$ and all SNR-MC associations, respectively, are considered separately. In the interval where the height is less than ~ 45 pc, the average radius distribution is roughly flat. When the height is greater than ~ 45 pc, the average radius for both fixed and all SNR-MC associations increases with the height. The turning point of the relation between the radius and the height, i.e. at ~ 45 pc, is consistent with the thickness of the thin CO disk revealed by Su et al. (2019). The radius of an SNR is related to its age, its ambient particle density, and the energy of its supernova explosion. The age and supernova explosion energy of SNRs are probably not correlated with their heights from the Galactic midplane. Different ages and explosion energies would make the radius scattered very much in Figure 11. The relationship between the average radius and the height may be caused by a height-dependent density distribution of molecular environments around SNRs. Though, some SNRs associated with MCs are interacting with cavity or shell-like molecular structures that may be relics of wind-blown bubbles created by their progenitor stars, yet, the sizes of these molecular structures are still confined by ambient particle density. As the ambient particle density becomes larger, the radius of SNRs becomes smaller. Therefore, such relation between the average radius and the height probably indicates that the overall density of MCs with active star-formation does not vary much in the thin CO disk. Beyond the thin CO disk, it decreases with increasing height from the Galactic plane. Further investigation on MCs themselves is needed to draw a definite conclusion.

6. Summary

The MWISP project is an unbiased $^{12}\text{CO}/^{13}\text{CO}/\text{C}^{18}\text{O}$ ($J = 1-0$) survey of the Galactic plane in the northern sky. We universally search for evidence of kinematic and spatial correlation of SNR-MC associations for nearly all SNRs in the coverage of the MWISP CO survey, i.e. 149 SNRs, 170 SNRCs, and 18 pure PWNe in $1^\circ < l < 230^\circ$ and $-5.^\circ 5 < b < 5.^\circ 5$. Based on the high-quality CO data obtained from the MWISP survey, we apply automatic algorithms to identify broad lines and spatial correlations for molecular gas in each SNR region. The searching method is demonstrated to be efficient. Among 149 SNRs studied in this paper, 57 of them are found to be associated with MCs, and 70 of them are considered to be possibly associated with MCs. We find 50 SNRCs

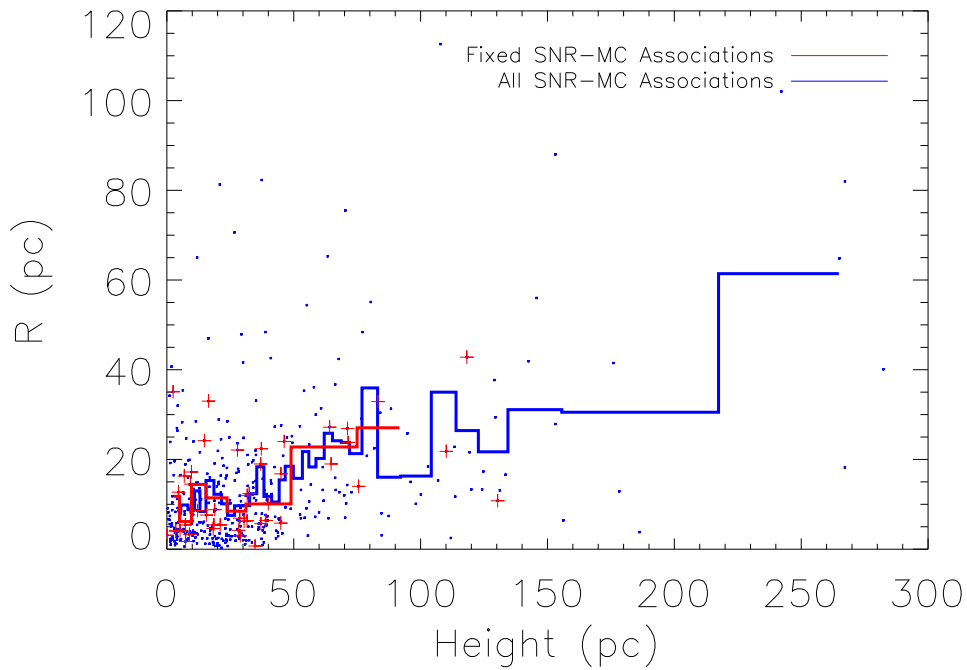


Fig. 11.— Radius vs. height from the Galactic plane for fixed (red pluses) and all (blue tiny stars) SNR-MC associations. Fixed SNR-MC associations are selected from known SNRs except for those within 10° of $l \sim 0^\circ$ and 5° of $l \sim 180^\circ$. All SNR-MC associations, including fixed and possible ones, are selected from all known and candidate SNRs. The position of the Galactic plane is the same as that applied in Figure 10. Two histograms respectively show the average radius of corresponding SNR-MC associations, which are binned with the number of sources to be at least ten and the step of the height to be at least 5 pc.

to be associated with MCs, and 91 SNRCs to be possibly associated with MCs. We also find candidates of associated MCs for 14 pure PWNe. Assuming all SNR-MC associations detected in previous works are real, the accuracy of fixed SNR-MC associations suggested in this paper would be at least 70%, and at least 60% for possible SNR-MC associations. The 91% previously detected SNR-MC associations are identified in this paper by CO line emission, which indicates that CO line emission is efficient for detecting SNR-MC associations. The nine previously detected SNR-cloud associations (about 9%) are not identified here, which are mostly based on spatial correlations with H I gases. We find that the proportion of SNRs associated with MCs is high within the Galactic longitude of $\sim 50^\circ$, with the distribution consistent with that of previously detected SNR-MC associations. Overall, there could be as high as 80% of SNRs associated with MCs.

Based on systemic velocities of associated MCs, kinematic distances of SNRs are estimated. Accordingly, distributions of their radii, progenitor initial masses, and heights from the Galactic plane are studied. We find that the radius and progenitor initial mass distributions of SNRs associated with MCs follow lognormal and power-law distributions, respectively. The radius distribution peaks at ~ 8.1 pc, and the progenitor initial mass distribution has an index of ~ -2.3 that is consistent with the Salpeter index of -2.35 . SNR-MC associations are mainly distributed in a thin disk and also distributed in a faint thick disk along the Galactic plane. For only fixed SNR-MC associations except for those within 10° of $l \sim 0^\circ$ and 5° of $l \sim 180^\circ$, due to their limited number, the thick disk is hard to distinguish, and the overall thickness (FWHM) is estimated as 90 ± 9 pc. For both fixed and possible SNR-MC associations, thicknesses (i.e. FWHMs) of the thin and thick disks are estimated as 65 ± 6 and 182 ± 64 pc, respectively. The thin and thick disks found here may be inner layers of the thin and thick CO disks revealed by Su et al. (2019), respectively. The ratio of peaks of the thin and thick disks of SNR-MC associations is about 5, which is larger than that of CO disks, i.e. about 2. It indicates that star-formation may be more efficient in the thin disk. The Sun's vertical displacement from the Galactic midplane is estimated as ~ 15.7 pc. Radii of SNRs associated with MCs show some correlations with their heights from the Galactic plane, with a turning point at the height of ~ 45 pc. When the height is below ~ 45 pc, the average radius distribution is roughly flat, and the radii of individual SNRs are much scattered. When the height is above ~ 45 pc, the average radius increases with the height. It indicates that the overall density of MCs with active star-formation may not vary much in the thin CO disk, and it decreases with increasing height from the Galactic plane beyond the thin CO disk.

We thank the anonymous referee for providing very helpful comments that improved the paper and its conclusions. This research made use of the data from the Milky Way Imaging Scroll Painting (MWISP) project, which is a multiline survey in $^{12}\text{CO}/^{13}\text{CO}/\text{C}^{18}\text{O}$ along the northern Galactic plane with PMO 13.7m telescope. We are grateful to all the members of the MWISP working group, particularly the staff members at PMO 13.7m telescope, for their long-term support. MWISP was sponsored by National Key R&D Program of China with grant 2017YFA0402701 and CAS Key Research Program of Frontier Sciences with grant QYZDJ-SSW-SLH047. Y.Su and J.Y. are supported by National Natural Science Foundation of China through grants 12173090 and 12041305, respectively. Y.Sun acknowledges support by the Youth Innovation Promotion Association, CAS (Y2022085), and the ‘‘Light of West China’’ Program (No. xbgz-zdsys-202212).

Data Availability Figures of individual objects are available online in <https://www.scidb.cn/en>, at <https://doi.org/10.57760/sciencedb.08076> (Zhou et al. 2023).

REFERENCES

- Aharonian, F., Akhperjanian, A. G., Bazer-Bachi, A. R., et al. 2008a, *A&A*, 481, 401
- Aharonian, F., Akhperjanian, A. G., Barres de Almeida, U., et al. 2008b, *A&A*, 477, 353
- Aharonian, F. A., Akhperjanian, A. G., Bazer-Bachi, A. R., et al. 2007, *A&A*, 469, L1
- Ambrocio-Cruz, P., Rosado, M., de la Fuente, E., Silva, R., & Blanco-Piñon, A. 2017, *MNRAS*, 472, 51
- Anderl, S., Gusdorf, A., & Güsten, R. 2014, *A&A*, 569, A81
- Anderson, L. D., Bania, T. M., Balsler, D. S., et al. 2014, *ApJS*, 212, 1
- Anderson, L. D., Wang, Y., Bihl, S., et al. 2017, *A&A*, 605, A58
- Arendt, R. G. 1989, *ApJS*, 70, 181
- Arias, M., Domček, V., Zhou, P., & Vink, J. 2019, *A&A*, 627, A75

Arikawa, Y., Tatematsu, K., Sekimoto, Y., & Takahashi, T. 1999, PASJ, 51, L7

Bailer-Jones, C. A. L., Rybizki, J., Fouesneau, M., Mantelet, G., & Andrae, R. 2018, AJ, 156, 58

Bastian, N., Covey, K. R., & Meyer, M. R. 2010, ARA&A, 48, 339

Beaumont, C. N., Williams, J. P., & Goodman, A. A. 2011, ApJ, 741, 14

Beuther, H., Bihl, S., Rugel, M., et al. 2016, A&A, 595, A32

Brinkmann, W., Aschenbach, B., & Kawai, N. 1996, A&A, 312, 306

Brogan, C. L., Frail, D. A., Goss, W. M., & Troland, T. H. 2000, ApJ, 537, 875

Brogan, C. L., Gelfand, J. D., Gaensler, B. M., Kassim, N. E., & Lazio, T. J. W. 2006, ApJ, 639, L25

Burton, M. G., Geballe, T. R., Brand, P. W. J. L., & Webster, A. S. 1988, MNRAS, 231, 617

Byun, D.-Y., Koo, B.-C., Tatematsu, K., & Sunada, K. 2006, ApJ, 637, 283

Cai, Z.-Y., Yang, J., & Lu, D.-R. 2009, Chinese Astron. Astrophys., 33, 393

Camilo, F., Ray, P. S., Ransom, S. M., et al. 2009, ApJ, 705, 1

Castelletti, G., Giacani, E., & Petriella, A. 2016, A&A, 587, A71

Castelletti, G., Supan, L., Dubner, G., Joshi, B. C., & Surnis, M. P. 2013, A&A, 557, L15

Castelletti, G., Supan, L., Petriella, A., Giacani, E., & Joshi, B. C. 2017, A&A, 602, A31

Caswell, J. L., Clark, D. H., & Crawford, D. F. 1975a, Australian Journal of Physics Astrophysical Supplement, 37, 39

Caswell, J. L., Murray, J. D., Roger, R. S., Cole, D. J., & Cooke, D. J. 1975b, A&A, 45, 239

Celli, S., Morlino, G., Gabici, S., & Aharonian, F. A. 2019, MNRAS, 487, 3199

Chatterjee, S., Cordes, J. M., Vlemmings, W. H. T., et al. 2004, ApJ, 604, 339

Chen, B. Q., Liu, X. W., Ren, J. J., et al. 2017a, MNRAS, 472, 3924

Chen, X., Xiong, F., & Yang, J. 2017b, A&A, 604, A13

Chen, Y., Jiang, B., Zhou, P., et al. 2014, in IAU Symposium, Vol. 296, Supernova Environmental Impacts, ed. A. Ray & R. A. McCray, 170–177

Chen, Y., Zhou, P., & Chu, Y.-H. 2013, ApJ, 769, L16

Chen, Z., Sefako, R., Yang, Y., et al. 2023, MNRAS, 525, 107

Chevalier, R. A. 1999, ApJ, 511, 798

Cho, S.-H., Kim, K. T., & Fukui, Y. 1994, AJ, 108, 634

Claussen, M. J., Frail, D. A., Goss, W. M., & Gaume, R. A. 1997, ApJ, 489, 143

Condon, J. J., Broderick, J. J., & Seielstad, G. A. 1991, AJ, 102, 2041

Condon, J. J., Broderick, J. J., Seielstad, G. A., Douglas, K., & Gregory, P. C. 1994, AJ, 107, 1829

Condon, J. J., Cotton, W. D., Greisen, E. W., et al. 1998, AJ, 115, 1693

Condon, J. J., Griffith, M. R., & Wright, A. E. 1993, AJ, 106, 1095

Cong, H. I. L. 1977, PhD thesis, Columbia University

Cordes, J. M., & Lazio, T. J. W. 2002, arXiv e-prints, arXiv:0207156

Cornett, R. H., Chin, G., & Knapp, G. R. 1977, A&A, 54, 889

Dame, T. M. 2011, arXiv e-prints, arXiv:1101.1499

de Oña Wilhelmi, E., Sushch, I., Brose, R., et al. 2020, MNRAS, 497, 3581

de Wilt, P., Rowell, G., Walsh, A. J., et al. 2017, MNRAS, 468, 2093

Dell’Ova, P., Gusdorf, A., Gerin, M., et al. 2020, A&A, 644, A64

Denoyer, L. K. 1979a, ApJ, 232, L165

—. 1979b, ApJ, 228, L41

Dickman, R. L., Snell, R. L., Ziurys, L. M., & Huang, Y.-L. 1992, ApJ, 400, 203

Dobashi, K., Shimoikura, T., Endo, N., et al. 2019, PASJ, 71, S11

Dokara, R., Brunthaler, A., Menten, K. M., et al. 2021, A&A, 651, A86

Downes, A. J. B., Pauls, T., & Salter, C. J. 1986, MNRAS, 218, 393

Dubner, G., Giacani, E., Reynoso, E., et al. 1999, AJ, 118, 930

Dubner, G., Giacani, E., Reynoso, E., & Parón, S. 2004, A&A, 426, 201

Dubner, G. M., Holdaway, M., Goss, W. M., & Mirabel, I. F. 1998, AJ, 116, 1842

Duvidovich, L., Petriella, A., & Giacani, E. 2020, MNRAS, 491, 5732

Eger, P., Rowell, G., Kawamura, A., et al. 2011, A&A, 526, A82

Faherty, J., Walter, F. M., & Anderson, J. 2007, Ap&SS, 308, 225

Feldt, C., & Green, D. A. 1993, A&A, 274, 421

Ferrand, G., & Safi-Harb, S. 2012, Advances in Space Research, 49, 1313

Foster, T., & Routledge, D. 2002, in Astronomical Society of the Pacific Conference Series, Vol. 276, Seeing Through the Dust: The Detection of HI and the Exploration of the ISM in Galaxies, ed. A. R. Taylor, T. L. Landecker, & A. G. Willis, 123

Frail, D. A., Claussen, M. J., & Méhault, J. 2013, ApJ, 773, L19

Frail, D. A., Goss, W. M., Reynoso, E. M., et al. 1996, AJ, 111, 1651

Frail, D. A., Goss, W. M., & Slysh, V. I. 1994, ApJ, 424, L111

Fraser, M., & Boubert, D. 2019, ApJ, 871, 92

Fukuda, T., Yoshiike, S., Sano, H., et al. 2014, ApJ, 788, 94

Fukui, Y., Sano, H., Yamane, Y., et al. 2021, ApJ, 915, 84

Furst, E., Hummel, E., Reich, W., et al. 1989, A&A, 209, 361

Gaensler, B. M., Schulz, N. S., Kaspi, V. M., Pivovarov, M. J., & Becker, W. E. 2003, ApJ, 588, 441

Gaensler, B. M., Tanna, A., Slane, P. O., et al. 2008, ApJ, 680, L37

Gao, X. Y., Han, J. L., Reich, W., et al. 2011, A&A, 529, A159

Gao, X. Y., Reich, P., Reich, W., Hou, L. G., & Han, J. L. 2020, MNRAS, 493, 2188

Gerbrandt, S., Foster, T. J., Kothes, R., Geisbüsch, J., & Tung, A. 2014, A&A, 566, A76

Giacani, E., Smith, M. J. S., Dubner, G., et al. 2009, A&A, 507, 841

Giacani, E. B., Dubner, G., Cappa, C., & Testori, J. 1998, A&AS, 133, 61

Giuliani, A., Cardillo, M., Tavani, M., et al. 2011, ApJ, 742, L30

Gorham, P. W. 1990, ApJ, 364, 187

Goss, W. M., & Robinson, B. J. 1968, Astrophys. Lett., 2, 81

Gotthelf, E. V., & Halpern, J. P. 2008, *ApJ*, 681, 515

Gotthelf, E. V., Halpern, J. P., Terrier, R., & Mattana, F. 2011, *ApJ*, 729, L16

Gray, A. D. 1994, *MNRAS*, 270, 847

Green, A. J., Frail, D. A., Goss, W. M., & Otrupcek, R. 1997, *AJ*, 114, 2058

Green, D. A. 2019, *Journal of Astrophysics and Astronomy*, 40, 36

Green, D. A., & Dewdney, P. E. 1992, *MNRAS*, 254, 686

Green, D. A., & Gull, S. F. 1982, *Nature*, 299, 606

Green, D. A., Gull, S. F., Tan, S. M., & Simon, A. J. B. 1988, *MNRAS*, 231, 735

Gusdorf, A., Anderl, S., Güsten, R., et al. 2012, *A&A*, 542, L19

Gusdorf, A., Güsten, R., Anderl, S., Hezareh, T., & Wiesemeyer, H. 2014, in *Supernova Environmental Impacts*, ed. A. Ray & R. A. McCray, Vol. 296, 178–182

Helfand, D. J., Becker, R. H., White, R. L., Fallon, A., & Tuttle, S. 2006, *AJ*, 131, 2525

Hessels, J. W. T., Nice, D. J., Gaensler, B. M., et al. 2008, *ApJ*, 682, L41

Hewitt, J. W., Rho, J., Andersen, M., & Reach, W. T. 2009, *ApJ*, 694, 1266

Hewitt, J. W., & Yusef-Zadeh, F. 2009, *ApJ*, 694, L16

Hewitt, J. W., Yusef-Zadeh, F., & Wardle, M. 2008, *ApJ*, 683, 189

Hewitt, J. W., Yusef-Zadeh, F., Wardle, M., Roberts, D. A., & Kassim, N. E. 2006, *ApJ*, 652, 1288

Heyer, M., & Dame, T. M. 2015, *ARA&A*, 53, 583

Hezareh, T., Wiesemeyer, H., Houde, M., Gusdorf, A., & Siringo, G. 2013, *A&A*, 558, A45

Higgs, L. A., Landecker, T. L., & Roger, R. S. 1983, *AJ*, 88, 97

Hoffman, I. M., Goss, W. M., Brogan, C. L., & Claussen, M. J. 2005, *ApJ*, 627, 803

Huang, R. H. H., Kong, A. K. H., Takata, J., et al. 2012, *ApJ*, 760, 92

Huang, Y. L., Dame, T. M., & Thaddeus, P. 1983, *ApJ*, 272, 609

Huang, Y. L., Dickman, R. L., & Snell, R. L. 1986, *ApJ*, 302, L63

Huang, Y. L., & Thaddeus, P. 1986, *ApJ*, 309, 804

Hurley-Walker, N., Callingham, J. R., Hancock, P. J., et al. 2017, *MNRAS*, 464, 1146

Hurley-Walker, N., Gaensler, B. M., Leahy, D. A., et al. 2019a, *PASA*, 36, e048

Hurley-Walker, N., Hancock, P. J., Franzen, T. M. O., et al. 2019b, *PASA*, 36, e047

Inoue, T., Yamazaki, R., Inutsuka, S.-i., & Fukui, Y. 2012, *ApJ*, 744, 71

Inutsuka, S.-i., Inoue, T., Iwasaki, K., & Hosokawa, T. 2015, *A&A*, 580, A49

Jeong, I.-G., Byun, D.-Y., Koo, B.-C., et al. 2012, *Ap&SS*, 342, 389

Jeong, I.-G., Koo, B.-C., Cho, W.-K., et al. 2013, *ApJ*, 770, 105

Jiang, B., Chen, Y., Wang, J., et al. 2010, *ApJ*, 712, 1147

Johanson, A. K., & Kerton, C. R. 2009, *AJ*, 138, 1615

Junkes, N., Fuerst, E., & Reich, W. 1992, *A&AS*, 96, 1

Kargaltsev, O., Pavlov, G. G., Klingler, N., & Rangelov, B. 2017, *Journal of Plasma Physics*, 83, 635830501

Kassim, N. E. 1988, *ApJ*, 328, L55

Kazes, I., & Caswell, J. L. 1977, *A&A*, 58, 449

Keohane, J. W., Rudnick, L., & Anderson, M. C. 1996, *ApJ*, 466, 309

Kilpatrick, C. D., Biegging, J. H., & Rieke, G. H. 2014, *ApJ*, 796, 144

—. 2016, *ApJ*, 816, 1

Kirichenko, A., Danilenko, A., Shternin, P., et al. 2015, *ApJ*, 802, 17

Koo, B.-C., Kang, J.-h., & Salter, C. J. 2006, *ApJ*, 643, L49

Koo, B.-C., & Moon, D.-S. 1997, *ApJ*, 485, 263

Koo, B.-C., Rho, J., Reach, W. T., Jung, J., & Mangum, J. G. 2001, *ApJ*, 552, 175

Koo, B.-C., Yun, M.-S., Ho, P. T. P., & Lee, Y. 1993, *ApJ*, 417, 196

Koo, B.-C., McKee, C. F., Lee, J.-J., et al. 2008, *ApJ*, 673, L147

Koralesky, B., Frail, D. A., Goss, W. M., Claussen, M. J., & Green, A. J. 1998, *AJ*, 116, 1323

Kothes, R. 2013, *A&A*, 560, A18

Kothes, R., Reich, W., Foster, T., & Byun, D.-Y. 2003, *ApJ*, 588, 852

Kothes, R., Sun, X., Gaensler, B., & Reich, W. 2018, *ApJ*, 852, 54

Kothes, R., Sun, X. H., Reich, W., & Foster, T. J. 2014, *ApJ*, 784, L26

Kothes, R., Uyaniker, B., & Pineault, S. 2001, *ApJ*, 560, 236

Kothes, R., Uyaniker, B., & Yar, A. 2002, *ApJ*, 576, 169

Kuriki, M., Sano, H., Kuno, N., et al. 2018, *ApJ*, 864, 161

Landecker, T. L., Dewdney, P. E., Vaneldik, J. F., & Routledge, D. 1987, *AJ*, 94, 111

Landecker, T. L., Pineault, S., Routledge, D., & Vaneldik, J. F. 1989, *MNRAS*, 237, 277

Lau, J. C., Rowell, G., Burton, M. G., et al. 2017, *MNRAS*, 464, 3757

Leahy, D., Green, K., & Tian, W. 2014, *MNRAS*, 438, 1813

Leahy, D. A., & Ranasinghe, S. 2016, *ApJ*, 817, 74

Leahy, D. A., Tian, W., & Wang, Q. D. 2008, *AJ*, 136, 1477

Leahy, D. A., & Tian, W. W. 2007, *A&A*, 461, 1013

—. 2008a, *A&A*, 480, L25

—. 2008b, *AJ*, 135, 167

Lee, H.-G., Moon, D.-S., Koo, B.-C., Lee, J.-J., & Matthews, K. 2009, *ApJ*, 691, 1042

Lee, J.-J., Koo, B.-C., Snell, R. L., et al. 2012a, *ApJ*, 749, 34

Lee, J.-J., Koo, B.-C., & Tatematsu, K. 2004, *ApJ*, 605, L113

Lee, J.-W., Koo, B.-C., & Lee, J.-E. 2012b, *Journal of Korean Astronomical Society*, 45, 117

Lee, Y.-H., Koo, B.-C., & Lee, J.-J. 2020, *AJ*, 160, 263

Liszt, H. S. 2009, *A&A*, 508, 1331

Liu, B., Chen, Y., Zhang, X., et al. 2017, *ApJ*, 851, 37

Liu, Q.-C., Chen, Y., Chen, B.-Q., et al. 2018, *ApJ*, 859, 173

Liu, Q.-C., Chen, Y., Zhou, P., Zhang, X., & Jiang, B. 2020, *ApJ*, 892, 143

Lockett, P., Gauthier, E., & Elitzur, M. 1999, *ApJ*, 511, 235

Ma, Y., Wang, H., Zhang, M., Li, C., & Yang, J. 2019, *ApJ*, 878, 44

Manchester, R. N., Hobbs, G. B., Teoh, A., & Hobbs, M. 2005, *AJ*, 129, 1993

Matheson, H., Safi-Harb, S., & Kothes, R. 2016, *ApJ*, 825, 134

Maxted, N., Burton, M., Braiding, C., et al. 2018, *MNRAS*, 474, 662

McDonnell, K. E., Wardle, M., & Vaughan, A. E. 2008, *MNRAS*, 390, 49

McEwen, B. C. 2016, PhD thesis, The University of New Mexico

Nicholas, B. P., Rowell, G., Burton, M. G., et al. 2012, *MNRAS*, 419, 251

Oliver, R. J., Masheded, M. R. W., & Thaddeus, P. 1996, *A&A*, 315, 578

Paron, S., Celis Peña, M., Ortega, M. E., et al. 2015, *A&A*, 580, A51

Paron, S., & Giacani, E. 2010, *A&A*, 509, L4

Paron, S., Ortega, M. E., Petriella, A., et al. 2012, *A&A*, 547, A60

Paron, S., Weidmann, W., Ortega, M. E., Albacete Colombo, J. F., & Pichel, A. 2013, *MNRAS*, 433, 1619

Petriella, A., Paron, S. A., & Giacani, E. B. 2013, *A&A*, 554, A73

Pihlström, Y. M., Sjouwerman, L. O., Frail, D. A., et al. 2014, *AJ*, 147, 73

Pollock, A. M. T. 1985, *A&A*, 150, 339

Ranasinghe, S., & Leahy, D. 2022, *ApJ*, 940, 63

Ranasinghe, S., Leahy, D., & Stil, J. 2021, *Universe*, 7, 338

Ranasinghe, S., Leahy, D., & Tian, W. W. 2020, *J. High Energy Phys., Gravitation Cosmol.*, 6, 9

Ranasinghe, S., & Leahy, D. A. 2017, *ApJ*, 843, 119

—. 2018a, *MNRAS*, 477, 2243

—. 2018b, *AJ*, 155, 204

Ranasinghe, S., Leahy, D. A., & Tian, W. 2018, *Open Physics Journal*, 4, 1

Reach, W. T., & Rho, J. 1999, *ApJ*, 511, 836

Reach, W. T., Rho, J., & Jarrett, T. H. 2005, *ApJ*, 618, 297

Reach, W. T., Rho, J., Tappe, A., et al. 2006, *AJ*, 131, 1479

Reich, W., & Sun, X.-H. 2019, *Research in Astronomy and Astrophysics*, 19, 045

Reid, M. J., Dame, T. M., Menten, K. M., & Brunthaler, A. 2016, *ApJ*, 823, 77

Reid, M. J., Menten, K. M., Brunthaler, A., et al. 2019, *ApJ*, 885, 131

Reynolds, S. P., & Moffett, D. A. 1993, *AJ*, 105, 2226

Reynoso, E. M., & Goss, W. M. 2002, *ApJ*, 575, 871

Reynoso, E. M., & Mangum, J. G. 2000, *ApJ*, 545, 874

—. 2001, *AJ*, 121, 347

Reynoso, E. M., Velázquez, P. F., Dubner, G. M., & Goss, W. M. 1999, *AJ*, 117, 1827

Rho, J., Jarrett, T. H., Tram, L. N., et al. 2021, *ApJ*, 917, 47

Roberts, D. A., Goss, W. M., Kalberla, P. M. W., Herbstmeier, U., & Schwarz, U. J. 1993, *A&A*, 274, 427

Roberts, M. S. E., Hessels, J. W. T., Ransom, S. M., et al. 2002, *ApJ*, 577, L19

Rosado, M., Arias, L., & Ambrocio-Cruz, P. 2007, *AJ*, 133, 89

Rousseau, R., Grondin, M. H., Van Etten, A., et al. 2012, *A&A*, 544, A3

Routledge, D., Dewdney, P. E., Landecker, T. L., & Vaneldik, J. F. 1991, *A&A*, 247, 529

Safi-Harb, S., Dubner, G., Petre, R., Holt, S. S., & Durouchoux, P. 2005, *ApJ*, 618, 321

Saken, J. M., Fesen, R. A., & Shull, J. M. 1992, *ApJS*, 81, 715

Salpeter, E. E. 1955, *ApJ*, 121, 161

Sano, H., Inoue, T., Tokuda, K., et al. 2020, *ApJ*, 904, L24

Sano, H., Yoshiike, S., Yamane, Y., et al. 2021, *ApJ*, 919, 123

Sasaki, M., Kothes, R., Plucinsky, P. P., Gaetz, T. J., & Brunt, C. M. 2006, *ApJ*, 642, L149

Sashida, T., Oka, T., Tanaka, K., et al. 2013, *ApJ*, 774, 10

Sato, F. 1979, *Astrophys. Lett.*, 20, 43

Saz Parkinson, P. M., Dormody, M., Ziegler, M., et al. 2010, *ApJ*, 725, 571

Seta, M., Hasegawa, T., Sakamoto, S., et al. 2004, *AJ*, 127, 1098

Seta, M., Winnewisser, G., Hasegawa, T., White, G. J., & Oka, T. 1998a, in *The Central Regions of the Galaxy and Galaxies*, ed. Y. Sofue, Vol. 184, 195

Seta, M., Hasegawa, T., Dame, T. M., et al. 1998b, *ApJ*, 505, 286

Shan, S. S., Zhu, H., Tian, W. W., et al. 2018, *ApJS*, 238, 35

Shan, W. L., Yang, J., Shi, S. C., et al. 2012, *IEEE Transactions on Terahertz Science and Technology*, 2, 593

Sheidaei, F. 2011, in *International Cosmic Ray Conference*, Vol. 7, *International Cosmic Ray Conference*, 244

Sofue, Y., Kohno, M., & Umemoto, T. 2021, *ApJS*, 253, 17

Stanimirović, S., Weisberg, J. M., Dickey, J. M., et al. 2003, *ApJ*, 592, 953

Su, Y., Chen, Y., Yang, J., et al. 2009, *ApJ*, 694, 376

—. 2011, *ApJ*, 727, 43

Su, Y., Fang, M., Yang, J., Zhou, P., & Chen, Y. 2014a, *ApJ*, 788, 122

Su, Y., Yang, J., Zhou, X., Zhou, P., & Chen, Y. 2014b, *ApJ*, 796, 122

Su, Y., Zhang, S., Shao, X., & Yang, J. 2015, *ApJ*, 811, 134

Su, Y., Zhou, X., Yang, J., et al. 2017a, *ApJ*, 845, 48

—. 2018, *ApJ*, 863, 103

—. 2017b, *ApJ*, 836, 211

Su, Y., Yang, J., Zhang, S., et al. 2019, *ApJS*, 240, 9

Sun, L., & Chen, Y. 2019, *ApJ*, 872, 45

Sun, Y., Yang, J., Xu, Y., et al. 2020, *ApJS*, 246, 7

Supan, L., Castelletti, G., Joshi, B. C., Surnis, M. P., & Supanitsky, D. 2015, *A&A*, 576, A81

Supan, L., Fischetto, G., & Castelletti, G. 2022, *A&A*, 664, A89

- Tatematsu, K., Fukui, Y., Iwata, T., Seward, F. D., & Nakano, M. 1990a, *ApJ*, 351, 157
- Tatematsu, K., Fukui, Y., Landecker, T. L., & Roger, R. S. 1990b, *A&A*, 237, 189
- Tatematsu, K., Fukui, Y., Nakano, M., et al. 1987, *A&A*, 184, 279
- Tian, W. W., & Leahy, D. A. 2008, *MNRAS*, 391, L54
- . 2011, *ApJ*, 729, L15
- . 2013, *ApJ*, 769, L17
- Tian, W. W., Leahy, D. A., & Wang, Q. D. 2007a, *A&A*, 474, 541
- Tian, W. W., Li, Z., Leahy, D. A., & Wang, Q. D. 2007b, *ApJ*, 657, L25
- Tian, W. W., Li, Z., Leahy, D. A., et al. 2010, *ApJ*, 712, 790
- Traverso, P. H., Reynoso, E. M., & Dubner, G. M. 1999, *Boletin de la Asociacion Argentina de Astronomia La Plata Argentina*, 43, 50
- Trimble, V. 1968, *AJ*, 73, 535
- Trushkin, S. A. 2001, in *ESA Special Publication, Vol. 459, Exploring the Gamma-Ray Universe*, ed. A. Gimenez, V. Reglero, & C. Winkler, 109–111
- Turner, B. E., Chan, K.-W., Green, S., & Lubowich, D. A. 1992, *ApJ*, 399, 114
- Uyaniker, B., Kothes, R., & Brunt, C. M. 2002, *ApJ*, 565, 1022
- van Dishoeck, E. F., Jansen, D. J., & Phillips, T. G. 1993, *A&A*, 279, 541
- Van Etten, A., Romani, R. W., & Ng, C. Y. 2008, *ApJ*, 680, 1417
- Voisin, F., Rowell, G., Burton, M. G., et al. 2016, *MNRAS*, 458, 2813
- Voisin, F. J., Rowell, G. P., Burton, M. G., et al. 2019, *PASA*, 36, e014
- Wallace, B. J., Landecker, T. L., & Taylor, A. R. 1994, *A&A*, 286, 565
- . 1997, *AJ*, 114, 2068
- Wang, W. 2011, *Research in Astronomy and Astrophysics*, 11, 824
- Wang, Y., Beuther, H., Rugel, M. R., et al. 2020, *A&A*, 634, A83
- Wardle, M., & Yusef-Zadeh, F. 2002, *Science*, 296, 2350
- Wayth, R. B., Lenc, E., Bell, M. E., et al. 2015, *PASA*, 32, e025
- Weisberg, J. M., Siegel, M. H., Frail, D. A., & Johnston, S. 1995, *ApJ*, 447, 204
- White, G. J., Rainey, R., Hayashi, S. S., & Kaifu, N. 1987, *A&A*, 173, 337
- Willis, A. G., & Dickel, J. R. 1971, *Astrophys. Lett.*, 8, 203
- Wilner, D. J., Reynolds, S. P., & Moffett, D. A. 1998, *AJ*, 115, 247
- Wootten, A. 1981, *ApJ*, 245, 105
- Wootten, H. A. 1977, *ApJ*, 216, 440
- Xu, J.-L., & Wang, J.-J. 2012, *A&A*, 543, A24
- Xu, J.-L., Wang, J.-J., & Miller, M. 2011, *ApJ*, 727, 81
- Yamada, M., Oka, T., Takekawa, S., et al. 2017, *ApJ*, 834, L3
- Yang, J., Zhang, J.-L., Cai, Z.-Y., Lu, D.-R., & Tan, Y.-H. 2006, *Chinese J. Astron. Astrophys.*, 6, 210
- Yoshiike, S., Fukuda, T., Sano, H., et al. 2013, *ApJ*, 768, 179

- Yu, B., Chen, B. Q., Jiang, B. W., & Zijlstra, A. 2019, *MNRAS*, 488, 3129
- Yusef-Zadeh, F., Goss, W. M., Roberts, D. A., Robinson, B., & Frail, D. A. 1999, *ApJ*, 527, 172
- Yusef-Zadeh, F., Wardle, M., Rho, J., & Sakano, M. 2003, *ApJ*, 585, 319
- Zhang, G.-Y., Chen, Y., Su, Y., et al. 2015, *ApJ*, 799, 103
- Zhang, X., Chen, Y., Li, H., & Zhou, X. 2013, *MNRAS*, 429, L25
- Zhang, Z., Gao, Y., & Wang, J. 2010, *Science China Physics, Mechanics, and Astronomy*, 53, 1357
- Zhou, P., & Chen, Y. 2011, *ApJ*, 743, 4
- Zhou, P., Chen, Y., Safi-Harb, S., et al. 2016a, *ApJ*, 831, 192
- Zhou, P., Chen, Y., Zhang, Z.-Y., et al. 2016b, *ApJ*, 826, 34
- Zhou, P., Li, J.-T., Zhang, Z.-Y., et al. 2018, *ApJ*, 865, 6
- Zhou, P., Zhou, X., Chen, Y., et al. 2020a, *ApJ*, 905, 99
- Zhou, P., Zhang, G.-Y., Zhou, X., et al. 2022, *ApJ*, 931, 144
- Zhou, X., Chen, Y., Su, Y., & Yang, J. 2009, *ApJ*, 691, 516
- Zhou, X., Su, Y., Yang, J., et al. 2020b, *ApJ*, 900, 155
- Zhou, X., Yang, J., Fang, M., & Su, Y. 2014, *ApJ*, 791, 109
- Zhou, X., Yang, J., Fang, M., et al. 2016c, *ApJ*, 833, 4
- Zhou, X., Su, Y., Yang, J., et al. 2023, A Systematic Study of Associations between Supernova Remnants and Molecular Clouds – Figures of Individual Objects
- Zhu, H., Tian, W. W., Torres, D. F., Pedalletti, G., & Su, H. Q. 2013, *ApJ*, 775, 95
- Zhu, H., Tian, W. W., & Zuo, P. 2014, *ApJ*, 793, 95
- Zuo, Y. X., Li, Y., Sun, J. X., et al. 2011, *Acta Astronomica Sinica*, 52, 152

A. Individual SNRs

G1.4-0.1: This SNR is near the Galactic center, and presents a partial radio continuum shell in the west. As indicated by the SCC, molecular gas at $\sim+3.2$ km s $^{-1}$ is distributed around the remnant. It belongs to the -4.8 km s $^{-1}$ component with broad line candidates identified in the remnant only by partial criteria. The association between the remnant and the -4.8 km s $^{-1}$ component is also supported by OH 1720 MHz masers detected in the SNR at ~-2.4 km s $^{-1}$ (see Table 3). Molecular gas at the nonsignificant peak of the SCC at $\sim+57.0$ km s $^{-1}$ is distributed around the northern boundary of the remnant, which is not well correlated with the remnant's radio continuum emission. There is also molecular gas at $\sim+99.1$ km s $^{-1}$ distributed around the western half of the remnant. It belongs to the $+78.9$ km s $^{-1}$ component with broad line candidates identified in the remnant by full criteria, of which two alternative kinematic distances are estimated as 8.1 ± 2.1 and 11.1 ± 0.3 kpc. However, the association between the remnant and the $+78.9$ km s $^{-1}$ component is not supported by OH 1720 MHz and CH $_3$ OH 36 GHz maser emission detected in previous works (see Table 3). If the remnant is associated with the -4.8 km s $^{-1}$ component, its kinematic distance can be estimated as 12.6 ± 0.3 kpc.

G1.9+0.3: The radius of this SNR is less than the beam size of our observation, which is too small to examine possible spatial correlations. No broad line candidate is identified in it by full criteria.

G3.7-0.2: This SNR presents radio continuum shells in the north and south. Molecular gas at the peak of the SCC at $\sim+19.2$ km s $^{-1}$ is roughly surrounding the SNR. It probably belongs to the $+9.3$ km s $^{-1}$ component, since broad line candidates at $+17.3$ and $+21.3$ km s $^{-1}$ can be attributed to the nearby prominent component at $+9.3$ km s $^{-1}$. Kinematic distances corresponding to these velocities are consistent. In addition, molecular gas at $\sim+2.5$ km s $^{-1}$ belonging to the $+9.3$ km s $^{-1}$ component is distributed around the northern boundary of the remnant. Molecular gas at another peak of the SCC at $\sim+79.4$ km s $^{-1}$ is distributed around and within the northeastern and southeastern boundaries of the remnant, which belongs to the $+83.5$ km s $^{-1}$ component with broad line candidates identified in the remnant. There are also molecular gases at ~-27.1 km s $^{-1}$ distributed around the southern half of the remnant and also inside, which belongs to the -30.6 km s $^{-1}$ component with broad line candidates identified in the remnant by full criteria. Some broad line candidates at -30.6 km s $^{-1}$ are associated with an overlapped H II region in the northwest. Based on kinematic evidence and the spatial correlation result, the SNR is probably associated with the $+9.3$ km s $^{-1}$ component, or may be associated with the $+83.5$ km s $^{-1}$ component. Corresponding kinematic distances are estimated as 2.9 ± 0.2 kpc for the $+9.3$ km s $^{-1}$ component and 7.7 ± 2.1 kpc for the $+83.5$ km s $^{-1}$ component. Note that the association between the SNR and the -30.6 km s $^{-1}$ component cannot be totally ruled out, of which the kinematic distance is estimated as 4.7 ± 0.3 kpc.

G3.8+0.3: As indicated by the SCC, molecular gases at $\sim+8.7$ and $\sim+165.6$ km s $^{-1}$ are roughly surrounding the southeast and southwest of this SNR, respectively. These molecular gases belong to the $+12.1$ km s $^{-1}$ and $+162.9$ km s $^{-1}$ components, respectively, which are with broad line candidates identified in the remnant by full criteria. For the $+12.1$ km s $^{-1}$ component, there is also molecular gas at $\sim+17.5$ km s $^{-1}$ distributed around the northern boundary of the remnant, where radio continuum emission is bright. Note that some broad line candidates at $+12.1$ km s $^{-1}$ are probably originated from a small overlapped H II region in the east, but not all. Based on these evidences, the SNR is probably associated with the $+12.1$ km s $^{-1}$ component, or may be associated with the $+162.9$ km s $^{-1}$ component. Kinematic distances are estimated as 2.9 ± 0.2 kpc for the $+12.1$ km s $^{-1}$ component and 8.1 ± 2.8 kpc for the $+162.9$ km s $^{-1}$ component.

G4.5+6.8 (Kepler): *Kepler's* SNR (SN 1604) is believed to have originated from a Type Ia supernova (Sun & Chen 2019, and references therein). There is very little CO emission detected in the SNR region at velocities of $\sim+4$ and $\sim+12$ km s $^{-1}$. We find no broad line emission and no good spatial correlation result for the SNR.

G4.8+6.2: This SNR is located at a high Galactic latitude nearby *Kepler's* SNR. Molecular gas at the peak of the SCC at $\sim+4.8$ km s $^{-1}$ is roughly surrounding the eastern half of the remnant. No broad line candidate is identified in the remnant even by partial criteria. If the remnant is associated with molecular gas at $\sim+4.8$ km s $^{-1}$, its near and far kinematic distances can be estimated as 1.6 ± 0.3 and 14.8 ± 0.3 kpc, respectively. Considering that the remnant's height from the Galactic plane would be too high at the far kinematic distance, i.e. ~ 1.6 kpc, it is probably located at the near kinematic distance at 1.6 ± 0.3 kpc.

G5.2-2.6: A small amount of molecular gas is detected around this SNR. At the peak of the SCC at $\sim+7.8$ km s $^{-1}$, there are three small molecular clumps distributed on the radio continuum shell of the remnant. There is no broad line candidate identified in the remnant even by partial criteria. If the remnant is associated with molecular gas at $\sim+7.8$ km s $^{-1}$ its kinematic distance can be estimated as 1.5 ± 0.2 kpc.

G5.4-1.2 (Milne 56): This SNR presents bright shell-like radio continuum emission in the northwest. Molecular gas at the peak of the SCC at $\sim+29.7$ km s $^{-1}$ is roughly surrounding the northeast of the remnant but not well correlated with its bright radio continuum shell. Among multiple components with broad line candidates identified in the remnant, only the -24.9 and $+187.5$ km s $^{-1}$ components show some spatial correlations with

the remnant's bright radio continuum shell. Note that broad line candidates at -9.7 km s^{-1} are probably originated from the nearby prominent component at -24.9 km s^{-1} . The association between the remnant and the -24.9 km s^{-1} component is also supported by the detection of the OH 1720 MHz maser at -21 km s^{-1} (see Table 3). Therefore, the remnant is suggested to be associated with the -24.9 km s^{-1} component, of which the near and far kinematic distances are estimated as 4.2 ± 1.1 and 12.1 ± 0.9 kpc, respectively.

G5.5+0.3: As indicated by the SCC, molecular gas at $\sim+7.0 \text{ km s}^{-1}$ is roughly surrounding the southern half of this SNR, where its radio continuum emission is bright. There is also molecular gas at $\sim+7.0 \text{ km s}^{-1}$ distributed around the northern boundary of the remnant. These molecular gases belong to the $+10.3 \text{ km s}^{-1}$ component, which is the only component with broad line candidates identified in the remnant by full criteria. A small part of the remnant in the west overlaps with SNRC G5.38+0.35, nevertheless, identified broad lines are not in this region. These evidences indicate that the remnant is associated with the $+10.3 \text{ km s}^{-1}$ velocity component. This result is consistent with that in a previous work (see Table 3). Accordingly, we estimate the kinematic distance of the remnant as 2.9 ± 0.2 kpc.

G6.1+0.5: Most of this SNR overlaps with SNRC G6.06+0.50 and SNRC G6.12+0.39, and it is also adjacent to SNRC G6.31+0.54. It is difficult to determine the morphology of radio continuum emission from the SNR. Molecular gas at the peak of the SCC at $\sim+6.0 \text{ km s}^{-1}$ seems to be distributed around the northwestern half of the remnant, which belongs to the $+7.0 \text{ km s}^{-1}$ velocity component. The $+7.0 \text{ km s}^{-1}$ component is the only component with broad line candidates identified in the SNR by full criteria. Most of the broad line points are located in the overlapping region with SNRC G6.06+0.50, but not all. Based on these evidences, we suggest that the SNR is associated with the $+7.0 \text{ km s}^{-1}$ component, of which the kinematic distance is estimated as 3.0 ± 0.2 kpc.

G6.1+1.2: This SNR is circled by molecular gas at $\sim+23.2 \text{ km s}^{-1}$ mostly to the east indicated by the SCC. There is also molecular gas at $\sim+13.0 \text{ km s}^{-1}$ distributed around the remnant but not well correlated. These molecular gases may belong to the $+12.2 \text{ km s}^{-1}$ velocity component with broad line candidates identified in the remnant by partial criteria. No broad line candidate is identified in the remnant by full criteria. If the remnant is associated with the $+12.2 \text{ km s}^{-1}$ component, its kinematic distance can be estimated as 1.5 ± 0.2 kpc.

G6.4-0.1 (W28): The association between this SNR and MCs was studied in multiple bands. Wootten (1981) detected broad molecular lines in the remnant, and subsequent studies revealed more details of the interactions between the remnant and surrounding molecular gases (e.g., those in Table 3). We find that two molecular stripes at the minor peak of the SCC at $\sim-5.9 \text{ km s}^{-1}$ spatially correlate well with two inner radio continuum shells, where OH 1720 MHz masers were also detected in previous works (see Table 3). Molecular gas at $\sim-5.9 \text{ km s}^{-1}$ belongs to the $+6.1 \text{ km s}^{-1}$ velocity component. Several groups of broad line candidates at the $+6.1 \text{ km s}^{-1}$ are identified in the remnant by full criteria, which are located on the remnant's radio continuum shells. Molecular gases at other peaks of the SCC at ~-21.1 , $\sim+22.1$, and $\sim+24.3 \text{ km s}^{-1}$ are mostly distributed in the remnant, but not well correlated. These evidences indicate that the SNR is associated with the $+6.1 \text{ km s}^{-1}$ MC, of which the near and far kinematic distances are estimated as 3.0 ± 0.2 and 12.6 ± 0.3 kpc, respectively.

G6.5-0.4: The northwestern half of this SNR overlaps with SNR W28, and it also overlaps with SNRC G6.45-0.56 and SNRC G6.54-0.60 in the south. Molecular gases at minor peaks of the SCC at ~-9.7 and $\sim-16.7 \text{ km s}^{-1}$ are roughly surrounding the northwest and northeast of the remnant, respectively. They belong to the -13.4 km s^{-1} component with broad line candidates identified in the remnant by full criteria. Molecular gas at the peak of the SCC at $\sim+4.0 \text{ km s}^{-1}$ is distributed around the boundary of the remnant but not well correlated, which belongs to the $+6.5 \text{ km s}^{-1}$ component. Note that broad line candidates at $+6.5 \text{ km s}^{-1}$ identified in the remnant are probably originated from SNR W28, and that at $+20.6 \text{ km s}^{-1}$ may be originated from an overlapped H II region. There is no broad line candidate identified in SNRC G6.45-0.56 and SNRC G6.54-0.60 by full criteria. Based on these evidences, we suggest that SNR G6.5-0.4 is associated with the -13.4 km s^{-1} component and locates at a kinematic distance of 4.7 ± 0.3 kpc.

G7.0-0.1: Molecular gas at the peak of the SCC at $\sim+47.3 \text{ km s}^{-1}$ is mostly distributed in this SNR, not well correlated. Molecular gas at the minor peak of the SCC at $\sim+6.5 \text{ km s}^{-1}$ is distributed around the remnant but not well correlated. Corresponding broad line candidates are identified at $+18.3 \text{ km s}^{-1}$ in the remnant by full criteria, and most of the broad line points are distributed around the eastern radio continuum shell of the remnant. These evidences indicate that the remnant is associated with the $+18.3 \text{ km s}^{-1}$ component, accordingly, its kinematic distance can be estimated as 3.6 ± 0.4 kpc.

G7.2+0.2: This SNR presents bright radio continuum emission in the southeast. As indicated by the SCC, molecular gas at $\sim-19.2 \text{ km s}^{-1}$ is roughly surrounding the east of the remnant and distributed around its southwestern boundary, which belongs to the -12.1 km s^{-1} component. The -12.1 km s^{-1} component is with many broad line candidates identified by partial criteria, and all broad line points are located in the remnant.

Some broad line points at -12.1 km s^{-1} are located on the radio continuum shell peak of the remnant. Molecular gases at $\sim+0.2$ and $\sim+13.3 \text{ km s}^{-1}$ are roughly surrounding the southeastern half of the remnant. At the peak of the SCC at $\sim+19.5 \text{ km s}^{-1}$, molecular gas is distributed around the remnant but not well correlated. Broad line candidates corresponding to these molecular gases are identified at $+7.0$ and $+20.4 \text{ km s}^{-1}$ in the remnant by full criteria, respectively. However, all these broad line candidates may belong to the prominent component at $+20.4 \text{ km s}^{-1}$. The remnant may be associated with either the -12.1 or $+20.4 \text{ km s}^{-1}$ components. Kinematic distances are estimated as $18.7\pm 0.5 \text{ kpc}$ for the -12.1 km s^{-1} component and $3.6\pm 0.3 \text{ kpc}$ for the $+20.4 \text{ km s}^{-1}$ component.

G8.7-0.1 (W30): This SNR presents bright radio continuum emission in the southwest. Molecular gas at the nonsignificant peak of the SCC at $\sim+13.0 \text{ km s}^{-1}$ is roughly surrounding the west of the remnant, correlated with its radio continuum emission. It probably belongs to the $+19.3 \text{ km s}^{-1}$ component with broad line candidates identified in the remnant by full criteria. Molecular gas of the $+33.9 \text{ km s}^{-1}$ component is with enhanced CO emission distributed around the southwestern boundary of the remnant, which is best correlated with the remnant's radio continuum emission. Molecular gas at the peak of the SCC at $\sim+30.0 \text{ km s}^{-1}$ is distributed near and within the boundary of the remnant. Molecular gas at the minor peak of the SCC at $\sim+41.1 \text{ km s}^{-1}$ belonging to the $+33.9 \text{ km s}^{-1}$ component is roughly surrounding the south of the remnant. An OH 1720 MHz maser was also detected at $+36 \text{ km s}^{-1}$ in previous work (see Table 3), which also supports the association between the remnant and the $+33.9 \text{ km s}^{-1}$ component. Molecular gas at the minor peak of the SCC at $\sim+181.0 \text{ km s}^{-1}$ is roughly surrounding the north of the remnant but not correlated with its radio continuum emission. Based on these evidences, we suggest that the remnant is associated with the $+33.9 \text{ km s}^{-1}$ component, and corresponding near and far kinematic distances are estimated as 2.9 ± 0.2 and $12.5\pm 0.3 \text{ kpc}$, respectively.

G8.9+0.4: As indicated by the SCC, molecular gas at $\sim+23.5 \text{ km s}^{-1}$ is roughly surrounding the southeastern half of the remnant, which belongs to the $+21.1 \text{ km s}^{-1}$ component. The $+21.1 \text{ km s}^{-1}$ component is with broad line candidates identified in the remnant by full criteria. The spatial correlation result as well as the corresponding broad line candidates indicates the association between the remnant and the $+21.1 \text{ km s}^{-1}$ component, of which the kinematic distance is estimated as $3.7\pm 0.3 \text{ kpc}$. This SNR is close to SNR W30; however, they are probably irrelevant.

G9.7-0.0: The SCC of this SNR has no significant peak. As indicated by the SCC, molecular gas at $\sim+40.2 \text{ km s}^{-1}$ is roughly surrounding the remnant, which belongs to the $+43.0 \text{ km s}^{-1}$ component with broad line candidates identified in the remnant by full criteria. Molecular gas at $\sim+77.5 \text{ km s}^{-1}$ also shows a spatial correlation with the remnant, which is distributed around its southern boundary. It may belong to the $+61.8 \text{ km s}^{-1}$ component with only one broad line candidate identified in the remnant by full criteria. The association between the remnant and the $+43.0 \text{ km s}^{-1}$ component is also supported by OH 1720 MHz maser emission detected at $+43 \text{ km s}^{-1}$ (see Table 3). Based on these evidences, we suggest that the remnant is associated with the $+43.0 \text{ km s}^{-1}$ MC, of which the kinematic distance is estimated as $3.8\pm 0.3 \text{ kpc}$.

G9.8+0.6: The SCC indicates a spatial correlation between this SNR and molecular gas at $\sim+31.3 \text{ km s}^{-1}$, which is roughly surrounding the remnant. It belongs to the $+28.9 \text{ km s}^{-1}$ component with broad line candidates identified in the remnant by full criteria. Therefore, we suggest that the remnant is associated with the $+28.9 \text{ km s}^{-1}$ MC, with the kinematic distance estimated as $2.8\pm 0.2 \text{ kpc}$.

G9.9-0.8: Broad $^{12}\text{CO}(J=2-1)$ lines at $+31 \text{ km s}^{-1}$ and near-infrared H_2 lines at $+30 \text{ km s}^{-1}$ were detected toward this SNR (Kilpatrick et al. 2016; Lee et al. 2020). Here, we find that molecular gas at a peak of the SCC at $\sim+11.3 \text{ km s}^{-1}$ is distributed around the northern boundary of the remnant, which belongs to the $+4.6 \text{ km s}^{-1}$ component with a broad line candidate identified in this SNR by full criteria. Besides, molecular gas at $\sim+16.2 \text{ km s}^{-1}$ may belong to the $+4.6 \text{ km s}^{-1}$ component too, which is roughly surrounding the north of the remnant. No good spatial correlation result is found for other velocity components. Note that broad line candidates at $+28.9 \text{ km s}^{-1}$ identified in the remnant by full criteria seem to be originated from an overlapped H II region. These evidences indicate the association between the remnant and the $+4.6 \text{ km s}^{-1}$ MC, and the corresponding kinematic distance is estimated as $1.5\pm 0.1 \text{ kpc}$.

G11.0-0.0: This SNR presents a partial radio continuum shell in the west. Broad lines at $+12.0$, $+29.7$, and $+38.4 \text{ km s}^{-1}$ are identified in this SNR by full criteria. Several broad line points are at $+38.4 \text{ km s}^{-1}$, which may be originated from the nearby prominent component at $+29.7 \text{ km s}^{-1}$. Molecular gas around $+38.4 \text{ km s}^{-1}$ is distributed around the eastern and southern boundaries of the remnant, however, not well correlated with the remnant's radio continuum shell. Molecular gas at the significant peak of the SCC at $\sim+17.6 \text{ km s}^{-1}$ is distributed around the remnant. Both the $+12.0$ and $+29.7 \text{ km s}^{-1}$ components may contribute to molecular gas at $\sim+17.6 \text{ km s}^{-1}$; however, most of the gas seems to be from the $+29.7 \text{ km s}^{-1}$ component. Therefore, we suggest that the remnant is associated with the $+29.7 \text{ km s}^{-1}$ component, hence, it is probably associated with the nearby filamentary infrared dark cloud G11.11-0.12 (e.g., Chen et al. 2023). The corresponding near and

far kinematic distances are estimated as 2.9 ± 0.3 and 12.4 ± 0.3 kpc, respectively. The near kinematic distance is preferred, if it is associated with the G11.11-0.12.

G11.1+0.1: This SNR was previously called G11.18+0.11. Sofue et al. (2021) found a partial shell structure around it, known as G11.2+0.12, at $+56$ km s⁻¹. The SNR presents bright shell-like radio continuum emission in its southern half. Here, several broad line components are identified in the remnant. Only the $+16.4$ km s⁻¹ component has many broad line points, and most of them are located on the southern radio continuum shell. Molecular gas at $\sim +24.8$ km s⁻¹ is distributed around the southern and eastern boundaries of the remnant. It supports the association between the remnant and the $+16.4$ km s⁻¹ component. Therefore, we suggest that the remnant is associated with the $+16.4$ km s⁻¹ component, of which the near and far kinematic distances are estimated as 3.8 ± 0.3 and 13.4 ± 0.3 kpc, respectively.

G11.1-0.7: Broad lines at three velocities are identified in this SNR; however, only one broad line at $+29.2$ km s⁻¹ and two broad lines at $+41.0$ km s⁻¹ are probably originated from the nearby prominent component at $+37.7$ km s⁻¹. As indicated by the SCC, molecular gas at $\sim +33.7$ km s⁻¹, belonging to the $+37.7$ km s⁻¹ component, is spatially correlated with the remnant's radio continuum emission. These evidences imply an association between the SNR and the $+37.7$ km s⁻¹ velocity component. The corresponding kinematic distance is estimated as 3.0 ± 0.3 kpc.

G11.2-0.3: Broad ¹²CO(J=2-1) lines at $+32$ km s⁻¹ and near-infrared H₂ lines at $+48$ km s⁻¹ were detected toward this SNR (Kilpatrick et al. 2016; Lee et al. 2020, see Table 3 for more information). Here, broad lines at $+0.5$, $+33.4$, and $+40.5$ km s⁻¹ are identified in the SNR by full criteria. Only one broad line at $+40.5$ km s⁻¹ may be originated from the nearby prominent component at $+33.4$ km s⁻¹. The SNR is surrounded by molecular gas at the significant peak of the SCC at $\sim +37.3$ km s⁻¹, which belongs to the $+33.4$ km s⁻¹ component. The $+0.5$ km s⁻¹ broad line component is not well spatially correlated with the remnant. Based on these evidences, we suggest that the remnant is associated with the $+33.4$ km s⁻¹ MC, with the kinematic distance estimated as 2.9 ± 0.3 kpc. The near kinematic distance obtained here is consistent with the H I absorption result in previous work (Green et al. 1988).

G11.4-0.1: Several broad line components are identified in this SNR. As indicated by the SCC, molecular gases at $\sim +16.5$ and $\sim +51.3$ km s⁻¹ are spatially correlated with radio continuum emission of the remnant, especially its radio continuum shell peak in the northeast. These molecular gases belong to the $+12.6$ and $+45.5$ km s⁻¹ broad line components, respectively. The remnant may be associated with either the $+12.6$ or $+45.5$ km s⁻¹ components. Kinematic distances are estimated as 1.25 ± 0.05 and 12.4 ± 0.3 kpc for the $+12.6$ km s⁻¹ component, and 3.8 ± 0.3 kpc for the $+45.5$ km s⁻¹ component.

G11.8-0.2: No broad line is identified in this SNR by full criteria. Three components of broad line candidates are identified in this SNR by partial criteria. Only the $+41.3$ km s⁻¹ component shows some spatial correlation with the remnant. Molecular gas at $\sim +47.9$ km s⁻¹ is roughly surrounding the southeast of the remnant, where radio continuum emission is bright. If the remnant is associated with the $+41.3$ km s⁻¹ MC, its kinematic distance can be estimated as 3.8 ± 0.3 kpc.

G12.0-0.1: There is only one broad line component at $+43.5$ km s⁻¹ identified in this SNR by full criteria. Broad line points are mainly distributed on the radio continuum shell of the remnant in the southeast. The SCC gives no significant spatial correlation results. The $+43.5$ km s⁻¹ MC is mainly distributed in the south, where radio continuum emission is bright. Based on these evidences, we suggest that the remnant is associated with the $+43.5$ km s⁻¹ MC, of which the kinematic distance is estimated as 3.8 ± 0.3 kpc.

G12.2+0.3: This SNR presents a partial radio continuum shell in the southeast (Brogan et al. 2006). Broad ¹²CO(J=2-1) lines at $+50$ km s⁻¹ were detected toward this SNR by Kilpatrick et al. (2016). Here, two broad line components at $+20.3$ and $+30.6$ km s⁻¹ are identified in the SNR by full criteria. As indicated by the SCC, molecular gas at $\sim +7.6$ km s⁻¹ is distributed around the western half of the remnant, not correlated with the southeastern radio continuum shell. It probably belongs to the $+20.3$ km s⁻¹ component. No good spatial correlation result is found for the $+30.6$ km s⁻¹ component. We find that molecular gas at the peak of SCC at $\sim +49.2$ km s⁻¹ is surrounding the southeastern half of the remnant, correlated with the radio continuum shell well. It belongs to the $+54.1$ km s⁻¹ velocity component with broad line candidates identified in the remnant by partial criteria. This broad line component is also detected in previous work (see Table 3). Broad line points at $+54.1$ km s⁻¹ are located on the remnant's radio continuum shell peak in the southeast. Based on these evidences, we suggest that the remnant is associated with the $+54.1$ km s⁻¹ component, with the corresponding kinematic distance estimated as 3.9 ± 0.3 kpc. Note that we cannot totally rule out the possibility of the association between the remnant and the $+20.3$ km s⁻¹ component, of which two alternative kinematic distances are estimated as 1.2 ± 0.2 and 3.9 ± 0.3 kpc.

G12.5+0.2: In this SNR, broad lines at several velocities are identified by full criteria. Two broad lines at $+53.0$ km s⁻¹ may be originated from the nearby prominent component at $+44.6$ km s⁻¹. As indicated by the SCC, molecular gas of the $+30.4$ km s⁻¹ component shows some spatial correlations with the remnant,

which is distributed around the remnant, mostly in the northeast and southwest. Moreover, molecular gas at $\sim+46.5$ km s^{-1} is surrounding the southeast of the remnant and also distributed around its northern and western boundaries, which belongs to the $+44.6$ km s^{-1} broad line component. Therefore, the remnant may be associated with either the $+30.4$ or $+44.6$ km s^{-1} components. Kinematic distances are estimated as 2.9 ± 0.3 kpc for the $+30.4$ km s^{-1} component and 3.8 ± 0.2 kpc for the $+44.6$ km s^{-1} component.

G12.7-0.0: This SNR presents three sections of partial radio continuum shells in the northeast, southeast, and west, and the southeastern one is the longest. There is only one broad line at $+9.1$ km s^{-1} identified in the remnant by full criteria. Molecular gas at a minor peak at $\sim+0.2$ km s^{-1} belonging to the $+9.1$ km s^{-1} component is distributed around the northern boundary of the remnant; however, it is not well correlated with the remnant's radio continuum emission. Molecular gas at the significant peak of the SCC at $\sim+57.8$ km s^{-1} is roughly surrounding the southeastern half of the remnant, following the southeastern radio shell. It belongs to the $+53.0$ km s^{-1} component that is with many broad line candidates identified in the remnant by partial criteria. We find that most of the broad line candidates at $+53.0$ km s^{-1} are distributed within the remnant; furthermore, they are mainly distributed around the southeastern radio continuum shell. For the $+53.0$ km s^{-1} component, both the distribution of molecular gas as well as locations of broad line candidates are correlated with radio continuum emission of the remnant. It strongly indicates that the remnant is associated with the $+53.0$ km s^{-1} MC, of which the kinematic distance is estimated as 3.8 ± 0.3 kpc.

G12.8-0.0: We identify only one broad line at $+11.1$ km s^{-1} in this SNR by full criteria; however, corresponding molecular gas shows no good spatial correlation with the remnant. As indicated by the SCC, molecular gas of the $+21.3$ km s^{-1} component is roughly surrounding the remnant, which is with broad line candidates identified in the remnant by partial criteria. Moreover, molecular gases at $\sim+32.1$ and $\sim+49.5$ km s^{-1} are roughly surrounding the north and east of the remnant but at a distance, respectively. They belong to the $+38.0$ and $+47.2$ km s^{-1} components, respectively, both of which are with broad line candidates identified in the remnant by partial criteria. Based on these evidences, the remnant is probably associated with the $+21.3$ km s^{-1} component with the kinematic distance estimated as 13.4 ± 0.3 kpc. Nevertheless, we cannot exclude the possibility of the association between the remnant and either the $+38.0$ or $+47.2$ km s^{-1} components. The near and far kinematic distances of the $+38.0$ km s^{-1} component are estimated as 3.9 ± 0.3 and 12.4 ± 0.3 kpc, respectively, and the kinematic distance of the $+47.2$ km s^{-1} component is estimated as 3.9 ± 0.3 kpc.

G13.3-1.3: The northwest of this SNR overlaps with SNRC G13.10-0.50. Broad lines at multiple velocities are identified in the remnant by full criteria. Broad lines at $+20.6$ km s^{-1} can be attributed to the nearby prominent component at $+15.4$ km s^{-1} , and broad lines at $+33.7$, $+45.2$, and $+51.8$ km s^{-1} may be originated from the nearby prominent component at $+42.7$ km s^{-1} . As indicated by the SCC, molecular gases at $\sim+14.0$ and $\sim+29.2$ km s^{-1} , belonging to the $+15.4$ km s^{-1} broad line component, are surrounding the north of the remnant. Moreover, molecular gas at the peak of the SCC at $\sim+41.3$ km s^{-1} is roughly surrounding the northwest of the remnant, which belongs to the $+42.7$ km s^{-1} broad line component. Based on these evidences, the remnant may be associated with either the $+15.4$ or $+42.7$ km s^{-1} components. Kinematic distances of them are estimated as 1.25 ± 0.06 and 3.6 ± 0.5 kpc, respectively.

G13.5+0.2: Broad lines at $+17.9$, $+24.9$, and $+38.9$ km s^{-1} are identified in this SNR by full criteria. As indicated by the SCC, molecular gas of the $+17.9$ km s^{-1} component is roughly surrounding the eastern half of the remnant. Molecular gas of the $+38.9$ km s^{-1} component is also distributed around the remnant. No good spatial correlation result is found for the $+24.9$ km s^{-1} component. The remnant may be associated with either the $+17.9$ or $+38.9$ km s^{-1} components, and corresponding kinematic distances are estimated as 1.8 ± 0.1 kpc and 3.8 ± 0.3 kpc, respectively.

G14.1-0.1: This SNR presents bright radio continuum emission in the northwest. Broad lines at $+37.9$ km s^{-1} are identified in the SNR. Some broad lines may be originated from a large overlapped H II region. As indicated by the SCC, molecular gas at $\sim+47.1$ km s^{-1} belonging to the $+37.9$ km s^{-1} component is distributed around the remnant, mostly in the northwest. Molecular gas at the peak of the SCC at $\sim+58.1$ km s^{-1} is distributed around the remnant, however, no corresponding broad line is identified in the remnant even by partial criteria. Based on these evidences, we suggest that the remnant is associated with the $+37.9$ km s^{-1} component, of which the kinematic distance is estimated as 3.9 ± 0.3 kpc.

G15.1-1.6: One broad line at $+62.7$ km s^{-1} is identified in this SNR. As indicated by the SCC, molecular gas of the $+62.7$ km s^{-1} component is roughly surrounding the north of the remnant. Molecular gas at the nonsignificant peak of the SCC at $\sim+19.0$ km s^{-1} is distributed around the northeastern and southwestern boundaries of the remnant; however, there is no corresponding broad line identified in the remnant even by partial criteria. The remnant is probably associated with the $+62.7$ km s^{-1} component, of which the near and far kinematic distances are estimated as 3.8 ± 0.7 and 10.4 ± 1.8 kpc, respectively.

G15.4+0.1: Molecular gases at $+34$ and $+47.8$ km s^{-1} were found to be spatially correlated with this SNR (Castelletti et al. 2013; Sofue et al. 2021), however, H I spatial correlations and absorption results indicate an

association with the $+60 \text{ km s}^{-1}$ cloud (Castelletti et al. 2013; Supan et al. 2015). Here, two components at $+30.9$ and $+46.8 \text{ km s}^{-1}$ are with broad lines identified in the SNR. Some broad lines at $+46.8 \text{ km s}^{-1}$ may be originated from the nearby prominent $+30.9 \text{ km s}^{-1}$ component. As indicated by the SCC, molecular gas at $\sim+34.3 \text{ km s}^{-1}$ is roughly surrounding the southern half of the remnant, which belongs to the $+30.9 \text{ km s}^{-1}$ broad line component. The $+46.8 \text{ km s}^{-1}$ component is not well spatially correlated with the remnant. Therefore, we suggest that the remnant is associated with the $+30.9 \text{ km s}^{-1}$ MC. No H I absorption around the tangent point velocity shown by Castelletti et al. (2013) indicates that the SNR is located at a near kinematic distance. The near kinematic distance of the $+30.9 \text{ km s}^{-1}$ MC is estimated as $3.0\pm 0.4 \text{ kpc}$.

G15.9+0.2: Broad lines at two velocities are identified in this SNR, nevertheless, only one broad line at $+29.1 \text{ km s}^{-1}$ can be attributed to the nearby $+26.4 \text{ km s}^{-1}$ component. As indicated by the SCC, molecular gas of the $+26.4 \text{ km s}^{-1}$ component is roughly surrounding the remnant, correlated with its radio continuum emission. This spatial correlation was also found in previous work (see Table 3). Based on the kinematic evidence as well as the spatial correlation result, we suggest that the remnant is associated with the $+26.4 \text{ km s}^{-1}$ MC, of which the near and far kinematic distances are estimated as 3.1 ± 0.4 and $13.3\pm 0.3 \text{ kpc}$, respectively.

G16.0-0.5: This SNR is discussed in Section 3.3.3.

G16.4-0.5: There are three components with broad lines identified in this SNR by full criteria. Some broad lines at $+39.5 \text{ km s}^{-1}$ may be originated from an overlapped H II region. As indicated by the SCC, molecular gases at $\sim+14.8$ and $\sim+20.2 \text{ km s}^{-1}$, belonging to the $+23.6 \text{ km s}^{-1}$ velocity component, are roughly surrounding the northeast of the remnant and distributed around the remnant, respectively. No good spatial correlation result is found for other velocity components. Based on identified broad lines as well as the spatial correlation result, we suggest that the remnant is associated with the $+23.6 \text{ km s}^{-1}$ MC, of which the kinematic distance is estimated as $3.2\pm 0.4 \text{ kpc}$.

G16.7+0.1: Both OH 1720 MHz maser emission at $\sim+20 \text{ km s}^{-1}$ and broad $^{12}\text{CO}(J=2-1)$ lines at $+25 \text{ km s}^{-1}$ were detected in this SNR (Green et al. 1997; Hewitt et al. 2008; Kilpatrick et al. 2016, see Table 3 for more information). Here, three broad line components are identified in the SNR at $+29.8$, $+43.8$, and $+63.3 \text{ km s}^{-1}$. There are broad line points at $+29.8 \text{ km s}^{-1}$ located near the position of the OH 1720 MHz maser detected by Green et al. (1997). As indicated by the SCC, molecular gas at $\sim+19.5 \text{ km s}^{-1}$ is distributed around the remnant, which belongs to the $+29.8 \text{ km s}^{-1}$ component. For the $+43.8 \text{ km s}^{-1}$ component, molecular gas at $\sim+47.3 \text{ km s}^{-1}$ is roughly surrounding the whole remnant. The $+63.3 \text{ km s}^{-1}$ component shows no good spatial correlation with the remnant. We also find that molecular gas at $\sim+84.3 \text{ km s}^{-1}$ is surrounding the north of the remnant; however, no corresponding broad line is identified in the remnant even by partial criteria. Based on the kinematic and spatial correlation evidences, the remnant is probably associated with the $+29.8 \text{ km s}^{-1}$ component, or may be associated with the $+43.8 \text{ km s}^{-1}$ component. Kinematic distances are estimated as $13.2\pm 0.3 \text{ kpc}$ for the $+29.8 \text{ km s}^{-1}$ component and 4.0 ± 0.3 for the $+43.8 \text{ km s}^{-1}$ component.

G17.0-0.0: Only one broad line component at $+30.4 \text{ km s}^{-1}$ is identified in this SNR by full criteria. As indicated by the SCC, molecular gas of the $+30.4 \text{ km s}^{-1}$ component is distributed around the remnant. Molecular gas at $\sim+94.0 \text{ km s}^{-1}$ is roughly surrounding the southwestern half of the remnant, which is probably a part of a molecular hub-filament structure. Based on the kinematic distance as well as the spatial correlation result, we suggest that the remnant is associated with the $+30.4 \text{ km s}^{-1}$ component, of which the kinematic distance is estimated as $12.1\pm 0.3 \text{ kpc}$.

G17.4-0.1: Two broad line components at $+41.2$ and $+65.6 \text{ km s}^{-1}$ are identified in this SNR. Only one broad line at $+65.6 \text{ km s}^{-1}$ is probably originated from an overlapped H II region. Molecular gas at a minor peak of the SCC at $\sim+39.8 \text{ km s}^{-1}$ is distributed around the northeastern and southwestern boundaries of the remnant, which belongs to the $+41.2 \text{ km s}^{-1}$ component. If the remnant is associated with the $+41.2 \text{ km s}^{-1}$ component, its near and far kinematic distances can be estimated as 3.2 ± 0.3 and $12.0\pm 0.3 \text{ kpc}$, respectively.

G17.4-2.3: This SNR presents a partial radio continuum shell in the southwest. OH 1720 MHz line emission was detected in the SNR (see Table 3). Only one component at $+22.6 \text{ km s}^{-1}$ is with broad lines identified in the remnant by full criteria. Molecular gas at the SCC peak at $\sim+18.4 \text{ km s}^{-1}$ is distributed around the southwestern and northern boundaries of the remnant, which belongs to the $+22.6 \text{ km s}^{-1}$ component. Therefore, we suggest that the remnant is associated with the $+22.6 \text{ km s}^{-1}$ MC, accordingly, its kinematic distance can be estimated as $1.5\pm 0.1 \text{ kpc}$.

G17.8-2.6: There is no broad line identified in this SNR even by partial criteria. At the peak of the SCC at $\sim+7.5 \text{ km s}^{-1}$, there is little molecular gas distributed around the remnant but not well correlated. Considering that OH 1720 MHz line emission was detected in the remnant in a previous work (see Table 3), the remnant may be associated with molecular gas at $\sim+7.5 \text{ km s}^{-1}$ with the kinematic distance estimated as $0.26\pm 0.14 \text{ kpc}$.

G18.1-0.1: Three broad line components at $+50.0$, $+77.0$, and $+94.1 \text{ km s}^{-1}$ are identified in this SNR by full criteria. Molecular gas at the peak of the SCC at $\sim+79.4 \text{ km s}^{-1}$ is distributed around the northeastern and

western boundaries of the remnant, which belongs to the $+77.0 \text{ km s}^{-1}$ component. There is only one broad line identified for the $+77.0 \text{ km s}^{-1}$ component. As indicated by the SCC, molecular gas of the $+50.0 \text{ km s}^{-1}$ component is roughly surrounding the southeastern half of the remnant. For the $+94.1 \text{ km s}^{-1}$ component, nine broad line points are identified in the remnant, and no broad line point is identified outside the remnant. The overall spatial distribution of the $+94.1 \text{ km s}^{-1}$ component is not well correlated with the remnant. However, there is a molecular clump belonging to the $+94.1 \text{ km s}^{-1}$ component that is located on the eastern boundary of the remnant, where radio continuum emission is bright. The association between the remnant and the $+94.1 \text{ km s}^{-1}$ component is also supported by H I absorption results in previous works (see Table 3). Molecular gas at $\sim+14.0 \text{ km s}^{-1}$ is roughly surrounding the southwest of the remnant; however, no corresponding broad line is identified in the remnant even by partial criteria. Therefore, the remnant is probably associated with the $+94.1 \text{ km s}^{-1}$ component, or may be associated with the $+50.0$ or $+77.0 \text{ km s}^{-1}$ components. As shown in previous works, the lack of H I absorption around the tangent point velocity toward the SNR indicates that the SNR is at a near kinematic distance (Leahy et al. 2014; Johanson & Kerton 2009; Ranasinghe & Leahy 2018b). The near kinematic distance of the $+94.1 \text{ km s}^{-1}$ component is estimated as $5.9\pm 1.4 \text{ kpc}$, and that of the $+50.0$ and $+77.0 \text{ km s}^{-1}$ components are estimated as 4.0 ± 0.4 and $4.2\pm 0.4 \text{ kpc}$, respectively.

G18.6-0.2: Broad $^{12}\text{CO}(J=2-1)$ lines at $+42 \text{ km s}^{-1}$ were detected toward this SNR by Kilpatrick et al. (2016). Here, two broad line components at $+46.7$ and $+64.6 \text{ km s}^{-1}$ are identified in the SNR. The SCC peaks at $\sim+49.5 \text{ km s}^{-1}$, where molecular gas is distributed around the remnant. Molecular gas at a minor peak of the SCC at $\sim+66.5 \text{ km s}^{-1}$ is surrounding the remnant except for its northwest side, correlated well with its shell-like radio continuum emission, which belongs to the $+64.6 \text{ km s}^{-1}$ component. Broad lines around $+46.7 \text{ km s}^{-1}$ and the spatial correlation between the remnant and molecular gas at $\sim+66.5 \text{ km s}^{-1}$ were also found in previous work (see Table 3). The association between the remnant and the $+64.6 \text{ km s}^{-1}$ component is also supported by H I absorption results in previous works (see Table 3). Based on these evidences, the remnant is probably associated with the $+64.6 \text{ km s}^{-1}$ component, or may be associated with the $+46.7 \text{ km s}^{-1}$ component. The kinematic distance of the $+46.7 \text{ km s}^{-1}$ component is estimated as $4.1\pm 0.4 \text{ kpc}$, and that of the $+64.6 \text{ km s}^{-1}$ component is estimated as $3.9\pm 0.4 \text{ kpc}$. Note that the lack of H I absorption around the tangent point velocity toward this SNR shown by Johanson & Kerton (2009), Ranasinghe & Leahy (2018b) supports the near kinematic distances obtained here.

G18.8+0.3 (Kes 67): High- J CO lines were detected toward this SNR, which, together with their spatial correlations, indicate that the remnant is in association with $\sim+20 \text{ km s}^{-1}$ MC (e.g., Dubner et al. 2004; Paron et al. 2015, see Table 3 for more information). Here, broad lines at $+20.4$ and $+124.6 \text{ km s}^{-1}$ are identified in the SNR. Most of the broad line points at $+20.4 \text{ km s}^{-1}$ are distributed around the southern boundary of the remnant. Molecular gases at peaks of the SCC at $\sim+11.4$ and $\sim+17.6 \text{ km s}^{-1}$ are distributed around the southwestern boundary of the remnant, which belongs to the $+20.4 \text{ km s}^{-1}$ component. Only one broad line is identified for the $+124.6 \text{ km s}^{-1}$ component, and the $+124.6 \text{ km s}^{-1}$ component shows no good spatial correlation with the remnant. At the peak of the SCC at $\sim+4.6 \text{ km s}^{-1}$, there are two roughly parallel molecular filaments, which extend far beyond the remnant and are partly surrounding the north and south of the remnant. No corresponding broad line around $+4.6 \text{ km s}^{-1}$ is identified in the remnant even by partial criteria. Based on identified broad lines and the spatial correlation result, we suggest that the remnant is associated with the $+20.4 \text{ km s}^{-1}$ MC. This result is consistent with that in previous works, where H I and CO morphologies, H I absorption spectra, and high- J CO lines were studied (see Table 3). Based on H I absorption results, Tian et al. (2007a) indicated that the SNR is at a far kinematic distance. The far kinematic distance of the $+20.4 \text{ km s}^{-1}$ MC is estimated as $13.3\pm 0.3 \text{ kpc}$.

G18.9-1.1: A spatial correlation between this SNR and the MC at $+25.6 \text{ km s}^{-1}$ was found (Traverso et al. 1999), and H I absorption features were detected up to $\sim+23 \text{ km s}^{-1}$ (Furst et al. 1989; Ranasinghe et al. 2020). Nevertheless, near-infrared H_2 lines were detected at $+70 \text{ km s}^{-1}$ by Lee et al. (2020). Here, broad lines at $+44.7$, $+56.0$, and $+64.4 \text{ km s}^{-1}$ are identified in the SNR by full criteria. There is only one broad line at $+56.0 \text{ km s}^{-1}$, which is probably originated from the nearby prominent component at $+64.4 \text{ km s}^{-1}$. As indicated by the SCC, molecular gas of the $+64.4 \text{ km s}^{-1}$ component is roughly surrounding the north of the remnant, where radio continuum emission is bright. Molecular gases at $\sim+6.2$ and $\sim+26.0 \text{ km s}^{-1}$ are distributed around the northwestern and eastern boundaries of the remnant, respectively; however, there is no corresponding broad line identified in the remnant even by partial criteria. We find no good spatial correlation between the remnant and the $+44.7 \text{ km s}^{-1}$ component. Based on these evidences, we suggest that the remnant is associated with the $+64.4 \text{ km s}^{-1}$ MC, with the kinematic distance estimated as $3.8\pm 0.4 \text{ kpc}$. The near kinematic distance obtained here is consistent with the H I absorption result in previous work (Ranasinghe et al. 2020).

G19.1+0.2: Many velocity components have broad lines identified in this SNR by full criteria. As indicated by the SCC, molecular gas of the $+56.8 \text{ km s}^{-1}$ broad line component is distributed around the southwest-

ern half of the remnant, where its radio continuum emission is bright. Molecular gas of the $+112.7 \text{ km s}^{-1}$ broad line component is roughly surrounding the south of the remnant. However, broad lines are identified at $+56.8 \text{ km s}^{-1}$ but not at $+112.7 \text{ km s}^{-1}$ by full criteria plus the clean subbackground region condition. At the peak of the SCC at $\sim+5.4 \text{ km s}^{-1}$, many molecular gases are distributed within the remnant. No good spatial correlation result is found for other broad line components. Based on these evidences, we suggest that the remnant is associated with the $+56.8 \text{ km s}^{-1}$ component, and its kinematic distance is estimated as $4.2\pm 0.5 \text{ kpc}$. Note that we cannot totally rule out the possibility of the association between the remnant and the $+112.7 \text{ km s}^{-1}$ component, of which the kinematic distance is estimated as $9.5\pm 0.4 \text{ kpc}$.

G20.0-0.2: The south of this SNR overlaps with SNRC G19.96-0.33. Three broad line components are identified in the remnant, i.e. $+40.8$, $+65.8$, and $+88.5 \text{ km s}^{-1}$. There is only one broad line at $+40.8 \text{ km s}^{-1}$, which may be associated with overlapped H II regions. There are many broad lines at $+65.8 \text{ km s}^{-1}$ outside the overlapping regions with H II regions and the SNRC. Molecular gas at a peak of the SCC at $\sim+73.2 \text{ km s}^{-1}$, which belongs to the $+65.8 \text{ km s}^{-1}$ component, is roughly surrounding the northwestern half of the remnant. In addition, at the peak of the SCC at $\sim+65.6 \text{ km s}^{-1}$, an elongated molecular clump is roughly distributed along the western boundary of the remnant. Molecular gases of other broad line components show no good spatial correlation with the remnant. The kinematic evidence as well as the spatial correlation result indicates an association between the remnant and the $+65.8 \text{ km s}^{-1}$ MC. The result here is consistent with CO morphology and H I absorption results from previous studies (see Table 3). Considering the presence of H I absorption at the tangent point velocity shown by Ranasinghe & Leahy (2018b), the kinematic distance of the SNR is estimated as $10.6\pm 1.3 \text{ kpc}$.

G21.0-0.4: There is only one component at $+41.2 \text{ km s}^{-1}$ with broad lines identified in this SNR. Note that some broad lines may be originated from a large overlapped H II region. Broad line points are mainly distributed around the remnant. Molecular gas at a minor peak of the SCC at $\sim+49.8 \text{ km s}^{-1}$, which belongs to the $+41.2 \text{ km s}^{-1}$ component, is distributed around the southeastern and northern boundaries of the remnant. Based on these evidences, we suggest that the remnant is associated with the $+41.2 \text{ km s}^{-1}$ MC with the kinematic distance estimated as $3.4\pm 0.4 \text{ kpc}$.

G21.5-0.9: Ranasinghe & Leahy (2018b), Tian & Leahy (2008) suggest an association between this SNR and the $\sim+68 \text{ km s}^{-1}$ cloud, based on H I absorption results (see Table 3 for more information). Here, no broad line is identified in the SNR by full criteria. As indicated by the SCC, molecular gases at $\sim+54.6$ and $\sim+58.6 \text{ km s}^{-1}$ are roughly surrounding the remnant. It supports the association between the remnant and the $+56.0 \text{ km s}^{-1}$ component that is with broad line candidates identified in the remnant by partial criteria. If the remnant is associated with the $+56.0 \text{ km s}^{-1}$ MC, its kinematic distance can be estimated as $3.4\pm 0.3 \text{ kpc}$. The near kinematic distance obtained here is consistent with the H I absorption result in previous works (Tian & Leahy 2008; Ranasinghe & Leahy 2018b, and references therein).

G21.6-0.8: Broad lines at three velocities are identified in this SNR. As indicated by the SCC, molecular gases at $\sim+49.5$ and $\sim+63.5 \text{ km s}^{-1}$ are distributed around the remnant, which belong to the $+52.5 \text{ km s}^{-1}$ broad line component. No good spatial correlation is found for other broad line components. Therefore, we suggest that the remnant is associated with the $+52.5 \text{ km s}^{-1}$ MC and locates at a kinematic distance of $3.4\pm 0.3 \text{ kpc}$.

G21.8-0.6 (Kes 69): Several components are with broad lines identified in this SNR. Broad lines at $+71.7 \text{ km s}^{-1}$ can be attributed to the nearby prominent component at $+83.2 \text{ km s}^{-1}$. Only the $+83.2 \text{ km s}^{-1}$ component is with broad line points distributed on radio continuum shells of the remnant in the northeast and southwest. Extended OH 1720 MHz maser emission at $\sim+84 \text{ km s}^{-1}$ was also detected around the southwestern radio continuum shell (see Table 3). Molecular gas at $\sim+66.5 \text{ km s}^{-1}$ is roughly surrounding the southwest of the remnant, which seems to belong to the $+83.2 \text{ km s}^{-1}$ component. There is molecular gas of the $+83.2 \text{ km s}^{-1}$ component distributed along radio continuum shells and also inside the remnant. No good spatial correlation result is found for other velocity components. The SCC peaks at $+44.8 \text{ km s}^{-1}$, where filamentary molecular gas is distributed inside the remnant. These evidences indicate an association between the remnant and the $+83.2 \text{ km s}^{-1}$ MC, of which the kinematic distance is estimated as $4.4\pm 0.7 \text{ kpc}$. The result here is consistent with previous multiband studies (see Table 3).

G22.7-0.2: Broad CO lines were detected in this SNR, indicating its association with the $+77 \text{ km s}^{-1}$ MC (Su et al. 2014b, see Table 3 for more information). Here, we identify numerous broad line components in the SNR by full criteria. Some broad lines are probably originated from overlapped H II regions. When using full criteria plus the clean subbackground region condition, only two broad line components at $+73.1$ and $+106.4 \text{ km s}^{-1}$ are identified in the SNR. As indicated by the SCC, molecular gas at $\sim+77.1 \text{ km s}^{-1}$, belonging to the $+73.1 \text{ km s}^{-1}$ broad line component, is surrounding radio continuum emission of the remnant in the southeast very well. Molecular gas at the peak of the SCC at $\sim+6.3 \text{ km s}^{-1}$ is distributed around the eastern boundary of the remnant but not well correlated. No good spatial correlation is found for other velocity components. Therefore, we suggest that the remnant is associated with the $+73.1 \text{ km s}^{-1}$ MC with the kinematic

distance estimated as 4.6 ± 0.5 kpc. This is consistent with results in previous works (see Table 3).

G23.3-0.3 (W41): Many broad line components are identified in this SNR even by full criteria plus the clean subbackground region condition. Broad lines at $+52.8$ and $+77.5$ km s^{-1} can be attributed to nearby prominent components at $+56.6$ and $+74.1$ km s^{-1} , respectively. More than two hundreds points in the remnant are with broad lines identified at $+74.1$ km s^{-1} , but very few outside the remnant. Most of these broad line points are located on radio continuum shells of the remnant, and some of them are located in overlapped H II regions. Furthermore, OH 1720 MHz line emission at $+71$ km s^{-1} was detected in this remnant (see Table 3). The $+74.1$ km s^{-1} component is not well spatially correlated with the remnant. There is molecular gas of the $+74.1$ km s^{-1} component distributed around radio continuum shells of the remnant, nevertheless, there is also a lot of molecular gas of the component distributed in the remnant, which is associated with overlapped H II regions. As indicated by the SCC, molecular gas at $\sim +52.1$ km s^{-1} , belonging to the $+56.6$ km s^{-1} component, is distributed along two bright radio continuum filaments of the remnant in the west. Molecular gas at the nonsignificant peak of the SCC at $\sim +8.7$ km s^{-1} is roughly surrounding the southeast of the remnant; however, it is not well correlated with radio continuum emission of the remnant. No good spatial correlation result is found for other broad line components. Based on these evidences, the remnant may be associated with either the $+56.6$ or $+74.1$ km s^{-1} components. Kinematic distances are estimated as 3.5 ± 0.4 kpc for the $+56.6$ km s^{-1} component and 4.8 ± 0.6 kpc for the $+74.1$ km s^{-1} component. The near kinematic distances obtained here are consistent with the H I absorption result in previous works (Ranasinghe & Leahy 2018b, and references therein).

G24.7-0.6: Broad lines at $+57.9$ and $+97.3$ km s^{-1} are identified in this SNR. The $+97.3$ km s^{-1} component is with only one broad line point identified, and shows no good spatial correlation with the remnant. As indicated by the SCC, the remnant is spatially correlated with molecular gas at $\sim +51.4$ km s^{-1} , which is roughly surrounding the remnant. It supports the association between the remnant and the $+57.9$ km s^{-1} component. Therefore, we suggest that the remnant is associated with the $+57.9$ km s^{-1} MC with the kinematic distance estimated as 3.7 ± 0.4 kpc. The near kinematic distance obtained here is consistent with the H I absorption result in previous work (Ranasinghe & Leahy 2018a).

G24.7+0.6: Sofue et al. (2021) found a spatial correlation between this SNR and molecular gas at $+112$ km s^{-1} . Here, there are several broad line components identified in the SNR even by full criteria plus the clean subbackground region condition. Some broad lines at $+102.6$ km s^{-1} are originated from overlapped H II regions. At peaks of the SCC at $\sim +7.0$ and $\sim +43.2$ km s^{-1} , molecular gases are distributed around the remnant and also inside it, which are not well correlated with the remnant. As indicated by the SCC, the $+17.5$ and $+114.9$ km s^{-1} broad line components also show some spatial correlations with the remnant. For the $+17.5$ km s^{-1} component, broad line points are located on the remnant's partial radio shells in the east and west. Molecular gas at $\sim +16.3$ km s^{-1} belonging to the $+17.5$ km s^{-1} component is also distributed around the remnant's radio continuum shells. Molecular gas at $\sim +113.0$ km s^{-1} is distributed around the southern boundary of the remnant but not well correlated with the remnant's radio continuum emission. Broad lines at $+114.9$ and $+106.8$ km s^{-1} are probably originated from a molecular hub-filament structure overlapping the south of the remnant. Therefore, we suggest that the remnant is associated with the $+17.5$ km s^{-1} MC, and the corresponding kinematic distance is estimated as 1.6 ± 0.3 kpc. The near kinematic distance obtained here is consistent with the H I absorption result in previous work (Ranasinghe et al. 2018).

G25.1-2.3: Only one component at $+53.1$ km s^{-1} is with broad lines identified in this SNR. At a peak of the SCC at $\sim +53.8$ km s^{-1} , molecular gas is distributed around the northern shell-like radio continuum emission of the remnant. Molecular gas at the peak of the SCC at $\sim +10.0$ km s^{-1} is roughly surrounding the southwestern radio continuum shell of the remnant; however, no corresponding broad line is identified in the remnant even by partial criteria. Therefore, we suggest that the remnant is associated with the $+53.1$ km s^{-1} MC with the kinematic distance estimated as 3.9 ± 0.8 kpc.

G27.4+0.0 (Kes 73, 4C-04.71): Broad $^{12}\text{CO}(J=2-1)$ lines at $+100$ km s^{-1} and near-infrared H_2 lines at $+99$ km s^{-1} were detected toward this SNR (Kilpatrick et al. 2016; Lee et al. 2020, see Table 3 for more information). We find only one component at $+99.3$ km s^{-1} with broad lines identified in the SNR by full criteria. Molecular gas at a peak of the SCC at $\sim +103.3$ km s^{-1} is surrounding the northeast of the remnant, which belongs to the $+99.3$ km s^{-1} component. At the peak of the SCC at $\sim +76.4$ km s^{-1} , there are several molecular clumps distributed around the remnant but not well correlated. Based on these evidences, the remnant is probably associated with the $+99.3$ km s^{-1} MC. Ranasinghe & Leahy (2018b) find no H I absorption around the tangent point velocity, indicating that the SNR is at a near kinematic distance. The near kinematic distance of the $+99.3$ km s^{-1} MC is estimated as 6.0 ± 0.6 kpc.

G27.8+0.6: Multiple broad line components are identified in this SNR even by full criteria plus the clean subbackground region condition. Broad lines at $+99.8$ and $+105.1$ km s^{-1} can be attributed to the nearby prominent component at $+97.0$ km s^{-1} . Some broad lines at $+35.7$ and few at $+97.0$ km s^{-1} are probably

originated from two overlapped H II regions. As indicated by the SCC, the $+97.0 \text{ km s}^{-1}$ component is spatially correlated with the southern radio continuum emission of the remnant well. Molecular gases at $\sim+10.0$ and $\sim+41.0 \text{ km s}^{-1}$ are distributed around the northeastern and southern boundaries of the remnant, respectively. However, these molecular gases are not correlated with the southern radio continuum emission of the remnant. There are also molecular clumps at $\sim+68.9 \text{ km s}^{-1}$ distributed around the eastern boundary of the remnant but mostly inside it. No good spatial correlation is found for other velocity components. Therefore, we suggest that the remnant is associated with the $+97.0 \text{ km s}^{-1}$ MC, and the near and far kinematic distances are estimated as 5.3 ± 1.0 and 8.1 ± 0.5 kpc, respectively.

G28.6-0.1: Broad lines at $+74.9$ and $+94.3 \text{ km s}^{-1}$ are identified in this SNR by full criteria. Some broad lines at $+74.9 \text{ km s}^{-1}$ are probably originated from the nearby $+94.3 \text{ km s}^{-1}$ component. As indicated by the SCC, molecular gas of the $+94.3 \text{ km s}^{-1}$ component is distributed around the remnant, mostly surrounding the southwestern half of it. No good spatial correlation result is found for the $+74.9 \text{ km s}^{-1}$ component. These evidences indicate an association between the remnant and the $+94.3 \text{ km s}^{-1}$ component, of which the kinematic distance is estimated as 8.1 ± 0.5 kpc. The far kinematic distance obtained here is consistent with the H I absorption result in previous work (Ranasinghe & Leahy 2018a).

G28.8+1.5: There is only one component at $+11.7 \text{ km s}^{-1}$ with broad lines identified in this SNR by full criteria. As indicated by the SCC, molecular gas at $\sim+5.7 \text{ km s}^{-1}$ is distributed around the remnant, which belongs to the $+11.7 \text{ km s}^{-1}$ component. These evidences indicate that the remnant is associated with the $+11.7 \text{ km s}^{-1}$ MC, and the corresponding kinematic distance is estimated as 0.4 ± 2.2 or 1.6 ± 0.3 kpc.

G29.6+0.1: Broad $^{12}\text{CO}(J=2-1)$ lines at $+94 \text{ km s}^{-1}$ were detected toward this SNR by Kilpatrick et al. (2016) (see Table 3 for more information). We identify three broad line components in the SNR by full criteria. There are more points with broad lines identified for the $+80.4 \text{ km s}^{-1}$ component than the other two components. As indicated by the SCC, the $+80.4$ and $+97.0 \text{ km s}^{-1}$ components show some spatial correlations with the remnant. Molecular gas at $\sim+86.0 \text{ km s}^{-1}$ belonging to the $+80.4 \text{ km s}^{-1}$ component is roughly surrounding the eastern half of the remnant. Molecular gas of the $+97.0 \text{ km s}^{-1}$ component is distributed around the remnant except for its northwest side. Note that molecular gas at the peak of the SCC at $\sim+65.1 \text{ km s}^{-1}$ is roughly surrounding the whole remnant except for its east side; however, no corresponding broad line is identified even by partial criteria. Molecular gas at another peak of the SCC at $\sim+42.2 \text{ km s}^{-1}$ is mainly distributed in the remnant but not well correlated. Therefore, the remnant may be associated with either the $+80.4$ or $+97.0 \text{ km s}^{-1}$ components. As shown by Ranasinghe et al. (2018), there is no H I absorption at the tangent point velocity, indicating that the SNR is at a near kinematic distance. The kinematic distance of the $+80.4 \text{ km s}^{-1}$ component is estimated as 4.5 ± 0.5 kpc, of which the near kinematic distance is consistent with the H I absorption result. For the $+97.0 \text{ km s}^{-1}$ component, the near kinematic distance is estimated as 4.8 ± 0.5 kpc, consistent with that of the $+80.4 \text{ km s}^{-1}$ component.

G29.7-0.3 (Kes 75): Su et al. (2009), Kilpatrick et al. (2016) studied CO line emission toward this SNR, and found broad line features around $+54 \text{ km s}^{-1}$. On the other hand, Leahy & Tian (2008a), Ranasinghe & Leahy (2018b) analyzed H I absorption spectra toward the SNR, and found no significant H I absorption feature for a ^{13}CO velocity component at $\sim+102 \text{ km s}^{-1}$. Together with a significant H I absorption feature at $\sim+95 \text{ km s}^{-1}$, they suggest an LSR velocity range of $\sim 95\text{--}102 \text{ km s}^{-1}$. Nevertheless, the H I absorption at $\sim+102 \text{ km s}^{-1}$ is not strong but still exists as suggested by Su et al. (2009), hence, H I absorption features no longer provide strong constrains on the LSR velocity of the SNR. These indicate complicated ISM distributions toward the remnant (see Table 3 for more information). Here, there is only one broad line component at $+87.3 \text{ km s}^{-1}$ identified in the SNR by full criteria. As indicated by the SCC, the $+87.3 \text{ km s}^{-1}$ component also shows some spatial correlations with the remnant, of which molecular gas is roughly surrounding the remnant. Note that multiple components are with broad line candidates identified in the remnant by partial criteria, e.g., at $+53.7 \text{ km s}^{-1}$. Based on evidences we found here, the remnant is probably associated with the $+87.3 \text{ km s}^{-1}$ component, of which the kinematic distance is estimated as 4.6 ± 0.6 kpc.

G30.7+1.0: Three velocity components at $+29.9$, $+51.1$, and $+80.5 \text{ km s}^{-1}$ are with broad lines identified in this SNR. As indicated by the SCC, the $+51.1$ and $+80.5 \text{ km s}^{-1}$ components are spatially correlated with the remnant. Molecular gas at $\sim+49.2 \text{ km s}^{-1}$ is roughly surrounding the remnant. Molecular gas at $\sim+80.8 \text{ km s}^{-1}$ is surrounding the south of the remnant. If the remnant is associated with the $+51.1 \text{ km s}^{-1}$ component, the near and far kinematic distances are estimated as 3.4 ± 1.0 and 10.7 ± 0.9 kpc, respectively. If associated with the $+80.5 \text{ km s}^{-1}$ component, the near and far kinematic distances are estimated as 3.7 ± 0.5 and 7.6 ± 3.3 kpc, respectively.

G30.7-2.0: There is only one broad line component at $+80.3 \text{ km s}^{-1}$ identified in this SNR by full criteria. Molecular gas at the peak of the SCC at $\sim+8.7 \text{ km s}^{-1}$ is roughly surrounding the remnant except for its east side, which belongs to the $+7.5 \text{ km s}^{-1}$ component with broad line candidates identified in the remnant by partial criteria. Molecular gas of the $+80.3 \text{ km s}^{-1}$ component is mainly distributed in the east of the remnant

but not well correlated. The remnant is probably associated with the $+7.5 \text{ km s}^{-1}$ component, or may be associated with the $+80.3 \text{ km s}^{-1}$ component. Corresponding kinematic distances are estimated as 0.24 ± 0.02 and $7.8 \pm 2.2 \text{ kpc}$, respectively.

G31.5-0.6: Two broad line components at $+81.7$ and $+95.8 \text{ km s}^{-1}$ are identified in this SNR by full criteria. As indicated by the SCC, molecular gas at $\sim +79.4 \text{ km s}^{-1}$ is roughly surrounding the north of the remnant, which belongs to the $+81.7 \text{ km s}^{-1}$ component. Molecular gas at $\sim +106.5 \text{ km s}^{-1}$ component is distributed around the eastern boundary of the remnant, which belongs to the $+95.8 \text{ km s}^{-1}$ component. The remnant may be associated with either the $+81.7$ or $+95.8 \text{ km s}^{-1}$ components, of which kinematic distances are estimated as 4.2 ± 0.7 and $5.5 \pm 1.5 \text{ kpc}$, respectively. Both velocity components are probably in the near Scutum spiral arm.

G31.9+0.0 (3C 391): Both OH 1720 MHz maser emission and different kinds of broadened molecular lines were detected in this SNR at around $+105 \text{ km s}^{-1}$ (Green et al. 1997; Frail et al. 1996; Wilner et al. 1998; Reach & Rho 1999; Hewitt et al. 2008; Gusdorf et al. 2014; Kilpatrick et al. 2016, see Table 3 for more information). Lee et al. (2020) also detected near-infrared H_2 lines at $+100 \text{ km s}^{-1}$ toward the SNR. Here, only one broad line component at $+104.1 \text{ km s}^{-1}$ is identified in the SNR by full criteria. As indicated by the SCC, the $+104.1 \text{ km s}^{-1}$ component is also spatially correlated with the remnant. Molecular gas at $\sim +107.1 \text{ km s}^{-1}$ is roughly surrounding the remnant. These evidences indicate that the remnant is associated with the $+104.1 \text{ km s}^{-1}$ MC, and the corresponding kinematic distance is estimated as $7.2 \pm 0.8 \text{ kpc}$. Note that the result here is consistent with the H I absorption result in previous work (Ranasinghe & Leahy 2017).

G32.0-4.9 (3C 396.1): There is no broad line identified in this SNR even by partial criteria. Molecular gas at the peak of the SCC at $\sim +0.6 \text{ km s}^{-1}$ is distributed around the southwestern boundary of the remnant. In addition, molecular gas at an adjacent peak of the SCC at $\sim +3.8 \text{ km s}^{-1}$ is roughly surrounding the northeast of the remnant. If the remnant is associated with molecular gas at $\sim +0.6 \text{ km s}^{-1}$, its kinematic distance can be estimated as $0.24 \pm 0.02 \text{ kpc}$.

G32.1-0.9: This SNR is adjacent to SNRC G32.37-0.51 to the northeast. There is only one component at $+91.3 \text{ km s}^{-1}$ with broad lines identified in the northeast of the remnant. Molecular gas at a peak of the SCC at $\sim +100.8 \text{ km s}^{-1}$ is distributed around the northeastern boundary of the remnant, which belongs to the $+91.3 \text{ km s}^{-1}$ component. The remnant is probably associated with the $+91.3 \text{ km s}^{-1}$ component with the corresponding kinematic distance estimated as $5.0 \pm 0.9 \text{ kpc}$.

G32.4+0.1: Broad $^{12}\text{CO}(J=2-1)$ lines at $+43 \text{ km s}^{-1}$ were detected toward this SNR by Kilpatrick et al. (2016) (see Table 3 for more information). Here, only one component at $+42.0 \text{ km s}^{-1}$ is with broad lines identified in the SNR. Broad line points are located in the southeastern overlapping H II regions and around the northeastern boundary of the remnant. Molecular gas at a peak of the SCC at $\sim +48.3 \text{ km s}^{-1}$ is surrounding the north and west of the remnant, which belongs to the $+42.0 \text{ km s}^{-1}$ broad line component. Therefore, we suggest that the remnant is associated with the $+42.0 \text{ km s}^{-1}$ MC. The corresponding kinematic distance is estimated as $10.1 \pm 0.4 \text{ kpc}$.

G32.8-0.1 (Kes 78): This SNR presents shell-like radio continuum emission in the southeast (Caswell et al. 1975a). The north of the SNR overlaps with the small SNRC G32.73+0.15. OH 1720 MHz maser emission at $+86.1 \text{ km s}^{-1}$, broad CO lines at $+81 \text{ km s}^{-1}$, and near-infrared H_2 lines at $+90 \text{ km s}^{-1}$ were detected in the SNR (Koralesky et al. 1998; Zhou & Chen 2011; Lee et al. 2020, see Table 3 for more information). Here, multiple broad line components are identified in the SNR by full criteria. Some broad lines are probably originated from overlapped H II regions. As indicated by the SCC, the $+64.1 \text{ km s}^{-1}$ broad line component shows some spatial correlations with the remnant, of which a part of a long molecular filament is roughly surrounding its southeast. The SCC peaks at $\sim +92.7 \text{ km s}^{-1}$, where molecular gas is mainly distributed in the remnant. There is also a molecular filament at $\sim +91.4 \text{ km s}^{-1}$ surrounding the south of the remnant but at a distance. These molecular gases belong to the $+94.5 \text{ km s}^{-1}$ broad line component. Broad line points of two components, i.e. at $+64.1$ and $+94.5 \text{ km s}^{-1}$, are outside the overlapping region with SNRC G32.73+0.15. Nevertheless, only the $+94.5 \text{ km s}^{-1}$ component is with broad lines identified in the SNR by full criteria plus the clean subbackground region condition. The highest velocity of H I absorption features is $\sim +90 \text{ km s}^{-1}$ (e.g., Zhou & Chen 2011), indicating that the remnant is in front of the tangent point and behind the MC at $\sim +90 \text{ km s}^{-1}$. It favors the $+94.5 \text{ km s}^{-1}$ MC being associated with the remnant. Based on these evidences, we suggest that the remnant is associated with the $+94.5 \text{ km s}^{-1}$ component, of which the kinematic distance is estimated as $5.1 \pm 0.5 \text{ kpc}$. The near kinematic distance obtained is consistent with the H I absorption result in previous works (Ranasinghe & Leahy 2018b, and references therein).

G33.2-0.6: No broad line is identified in this SNR by full criteria. Only one component at $+78.9 \text{ km s}^{-1}$ is with broad line candidates identified in the remnant by partial criteria. Molecular gas of the $+78.9 \text{ km s}^{-1}$ component is distributed around the northern radio continuum shell of the remnant. The remnant is probably associated with the $+78.9 \text{ km s}^{-1}$ component, of which the kinematic distance is estimated as $4.7 \pm 0.8 \text{ kpc}$.

G33.6+0.1 (Kes 79): Broad CO lines at $\sim+105 \text{ km s}^{-1}$ were detected toward this SNR (Kilpatrick et al. 2016; Zhou et al. 2016a, see Table 3 for more information). Here, several broad line components are identified in the SNR by full criteria. No significant spatial correlation result is found through the SCC. Some molecular gas of the $+71.6 \text{ km s}^{-1}$ broad line component is surrounding the western radio continuum shell of the remnant; however, there is also some molecular gas inside the remnant. There is molecular gas of the $+105.3 \text{ km s}^{-1}$ component distributed around the radio continuum shell of the remnant in the southeast, especially, matching a radio continuum protrusion. Some broad line points at $+105.3 \text{ km s}^{-1}$ are also distributed on the top and in the wings of the radio continuum protrusion. No good spatial correlation result is found for other broad line components. The remnant is probably associated with the $+105.3 \text{ km s}^{-1}$ component, or may be associated with the $+71.6 \text{ km s}^{-1}$ component. Kinematic distances are estimated as $5.1\pm 0.6 \text{ kpc}$ for the $+71.6 \text{ km s}^{-1}$ component and $6.7\pm 0.6 \text{ kpc}$ for the $+105.3 \text{ km s}^{-1}$ component.

G34.7-0.4 (W44): The association between this SNR and MCs was confirmed by multiband observations of shocked molecular gases, e.g., OH masers, CH_3OH masers, CO lines, HCO^+ lines, near-infrared H_2 lines, etc. (Caswell et al. 1975b; Wootten 1977; Green et al. 1997; Claussen et al. 1997; Seta et al. 2004; Hewitt et al. 2008; McDonnell et al. 2008; Sashida et al. 2013; Yoshiike et al. 2013; Anderl et al. 2014; McEwen 2016; Yamada et al. 2017; Lee et al. 2020, see Table 3 for more information). As a well-established case of SNR-MC association, the interaction details were further studied as well, which also explains the hadronic γ -ray production in the remnant (Yoshiike et al. 2013). Note that a small part of the SNR in the northeast overlaps with SNRC G34.93-0.24. Here, broad lines at several velocities are identified in the remnant even by full criteria plus the clean subbackground region condition. Broad lines at $+42.7$ and $+46.8 \text{ km s}^{-1}$ can be attributed to the nearby prominent component at $+46.0 \text{ km s}^{-1}$. Most of the broad line points at $+46.0 \text{ km s}^{-1}$ are distributed around the southeastern radio continuum shell of the remnant. Molecular gas at the peak of the SCC at $\sim+48.9 \text{ km s}^{-1}$ is also roughly surrounding the southeastern radio shell, which belongs to the $+46.0 \text{ km s}^{-1}$ broad line component. We find no good spatial correlation between the remnant and other broad line components. Note that a large portion of broad lines at $+81.9 \text{ km s}^{-1}$ is probably originated from an overlapped H II region in the northwest. Based on the kinematic evidence and the spatial correlation result, we suggest that the remnant is associated with the $+46.0 \text{ km s}^{-1}$ MC with the kinematic distance estimated as $2.5\pm 0.2 \text{ kpc}$. The near kinematic distance obtained here is consistent with the H I absorption result in previous works (Ranasinghe & Leahy 2018b, and references therein).

G35.6-0.4: We identified several broad line components in this SNR by full criteria. As indicated by the SCC, molecular gas at $\sim+11.9 \text{ km s}^{-1}$ is spatially correlated with the radio continuum emission of the remnant well; however, no corresponding broad line is identified in the remnant even by partial criteria. Molecular gases at minor peaks of the SCC at $\sim+26.0$ and $\sim+37.5 \text{ km s}^{-1}$, which probably belong to the $+27.4 \text{ km s}^{-1}$ broad line component, are roughly surrounding the northwest and east of the remnant, respectively. Molecular gas of the $+54.6 \text{ km s}^{-1}$ component is distributed around the northern boundary of the remnant. In addition, broad line points of the $+54.6 \text{ km s}^{-1}$ component are distributed around the radio continuum emission of the remnant. No spatial correlation is found for other broad line components. The remnant may be associated with either the $+27.4$ or $+54.6 \text{ km s}^{-1}$ components. H I absorption results in previous works favor the SNR at a near kinematic distance (Zhu et al. 2013; Ranasinghe & Leahy 2018b). The kinematic distance is estimated as $2.1\pm 0.2 \text{ kpc}$ for the $+27.4 \text{ km s}^{-1}$ component. The near kinematic distance of the $+54.6 \text{ km s}^{-1}$ component is estimated as $2.9\pm 0.4 \text{ kpc}$.

G36.6-0.7: The northeast of this SNR overlaps with SNRC G36.66-0.50, and there is an H II region at $+54.1 \text{ km s}^{-1}$ located in the overlapping region. There are two broad line components identified in the remnant by full criteria, i.e. at $+56.6$ and $+78.7 \text{ km s}^{-1}$. Broad line points at $+56.6 \text{ km s}^{-1}$ are located in the overlapping region with the SNRC and the H II region. As indicated by the SCC, molecular gas at $\sim+54.4 \text{ km s}^{-1}$ belonging to the $+56.6 \text{ km s}^{-1}$ component is distributed around the northeastern half of the remnant. One broad line point is at $+78.7 \text{ km s}^{-1}$, which is outside the overlapping region with the SNRC and the H II region. Molecular gas of the $+78.7 \text{ km s}^{-1}$ component is distributed around the northeastern boundary of the remnant. The remnant may be associated with either the $+56.6$ or $+78.7 \text{ km s}^{-1}$ components. Kinematic distances are estimated as $3.0\pm 0.5 \text{ kpc}$ for the $+56.6 \text{ km s}^{-1}$ component and $4.2\pm 0.5 \text{ kpc}$ for the $+78.7 \text{ km s}^{-1}$ component.

G36.6+2.6: This SNR presents radio continuum shells in the northwest and south. No broad line is identified in this SNR even by partial criteria. The SCC peaks at $\sim+19.5 \text{ km s}^{-1}$, where molecular gas is distributed around the southern and western boundaries of the remnant. If the remnant is associated with molecular gas at $\sim+19.5 \text{ km s}^{-1}$, its kinematic distance can be estimated as $0.5\pm 0.4 \text{ kpc}$.

G38.7-1.3: The northeast of this SNR overlaps with SNRC G38.72-0.87. Only one broad line component at $+75.1 \text{ km s}^{-1}$ is identified in the remnant by full criteria. Note that many broad line points are in the overlapping region with the SNRC. The SCC also supports the association between the remnant and the $+75.1 \text{ km s}^{-1}$ component, of which molecular gas is roughly surrounding the northeastern radio continuum shell. We suggest

that the remnant is associated with the $+75.1 \text{ km s}^{-1}$ component, and the corresponding kinematic distance is estimated as $4.2 \pm 0.6 \text{ kpc}$.

G39.2-0.3 (3C 396): Broad CO lines at $+69$, $+77$, and $+84 \text{ km s}^{-1}$ and near-infrared H_2 lines at $+56 \text{ km s}^{-1}$ were detected toward this SNR in previous works (Su et al. 2011; Kilpatrick et al. 2016; Lee et al. 2020, see Table 3 for more information). Here, two broad lines at $+44.1$ and $+61.4 \text{ km s}^{-1}$ are identified in this SNR by full criteria. The SCC peaks at $\sim +56.4 \text{ km s}^{-1}$, where molecular gas is roughly surrounding the remnant. It supports the association between the remnant and the $+61.4 \text{ km s}^{-1}$ component. No spatial correlation is found between the remnant and the $+44.1 \text{ km s}^{-1}$ component. Molecular gas at a minor peak of the SCC at $\sim +12.7 \text{ km s}^{-1}$ is roughly surrounding the remnant except for its southwest side, but no corresponding broad line is identified in the remnant even by partial criteria. At another minor peak of the SCC at $\sim +86.2 \text{ km s}^{-1}$, molecular gas is also roughly surrounding the whole remnant except for its southwest side. It belongs to the $+84.2 \text{ km s}^{-1}$ component with broad line candidates identified in the remnant by partial criteria. The remnant may be associated with either the $+61.4$ or $+84.2 \text{ km s}^{-1}$ components. Su et al. (2011), Ranasinghe & Leahy (2018b) showed H I absorption up to the tangent point velocity, indicating that the SNR is at a far kinematic distance. The kinematic distance of the $+61.4 \text{ km s}^{-1}$ component is estimated as $8.7 \pm 0.5 \text{ kpc}$, and the far kinematic distance of the $+84.2 \text{ km s}^{-1}$ component is estimated as $7.4 \pm 0.9 \text{ kpc}$.

G39.7-2.0 (W50): The radio continuum emission of this SNR is bipolar spindle shape, hosting the X-ray binary system SS 433 with relativistic jets precessing around the major axis of W50 (e.g., Downes et al. 1986; Brinkmann et al. 1996; Dubner et al. 1998; Gao et al. 2011). Broad CO lines at $+77$ and $+53 \text{ km s}^{-1}$ were detected toward this SNR by Su et al. (2018), Liu et al. (2020), respectively (see Table 3 for more information). However, broad CO lines at $+77 \text{ km s}^{-1}$ are outside the SNR region we examined, probably due to jet-ISM interactions (Su et al. 2018), and the width of asymmetric broad CO lines at $+53 \text{ km s}^{-1}$ is $\lesssim 6 \text{ km s}^{-1}$ (Liu et al. 2020). Here, we identify no broad line in the SNR by full criteria. We also find no good spatial correlation between the remnant and molecular gas at different velocities.

G40.5-0.5: We identify several broad line components in this SNR by full criteria. Only one broad line is at $+65.3 \text{ km s}^{-1}$, which can be attributed to the nearby component at $+67.7 \text{ km s}^{-1}$. As indicated by the SCC, only the $+67.7 \text{ km s}^{-1}$ broad line component is spatially correlated with the remnant. Molecular gas at the peak of the SCC at $\sim +53.0 \text{ km s}^{-1}$ is roughly surrounding the northeastern half of the remnant, where radio continuum emission is bright. Based on these evidences, we suggest that the remnant is associated with the $+65.3 \text{ km s}^{-1}$ component. The corresponding kinematic distance is estimated as $8.4 \pm 0.4 \text{ kpc}$.

G41.1-0.3 (3C 397): Broad CO lines at $\sim +32 \text{ km s}^{-1}$ were detected toward this SNR (Jiang et al. 2010; Kilpatrick et al. 2016, see Table 3 for more information). Here, two broad line components at $+35.7$ and $+60.4 \text{ km s}^{-1}$ are identified in the SNR by full criteria. Broad lines at $+60.4 \text{ km s}^{-1}$ may be originated from an overlapped H II region. The SCC peaks at $\sim +43.0 \text{ km s}^{-1}$, where molecular gas is roughly surrounding the remnant. It belongs to the $+35.7 \text{ km s}^{-1}$ component. Both the kinematic evidence and the spatial correlation result indicate that the remnant is associated with the $+35.7 \text{ km s}^{-1}$ component. As shown by Leahy & Ranasinghe (2016), the presence of H I absorption up to the tangent point velocity indicates that the SNR is at a far kinematic distance. The far kinematic distance of the $+35.7 \text{ km s}^{-1}$ component is estimated as $8.8 \pm 1.7 \text{ kpc}$.

G41.5+0.4: Sofue et al. (2021) found a spatial correlation between this SNR and molecular gas at $+58 \text{ km s}^{-1}$. Here, there are two broad line components at $+41.0$ and $+57.1 \text{ km s}^{-1}$ identified in the SNR by full criteria. As indicated by the SCC, molecular gas at $\sim +35.4 \text{ km s}^{-1}$ is roughly surrounding the remnant, which belongs to the $+41.0 \text{ km s}^{-1}$ component. No good spatial correlation result is found for the $+57.1 \text{ km s}^{-1}$ component. Therefore, we suggest that the remnant is associated with the $+41.0 \text{ km s}^{-1}$ component, of which the kinematic distance is estimated as $2.6 \pm 0.5 \text{ kpc}$. The near kinematic distance obtained here is consistent with the H I absorption result in previous work (Ranasinghe et al. 2018).

G42.0-0.1: The south of this SNR overlaps with SNRC G41.95-0.18. Three broad line components are identified in the remnant by full criteria, i.e. at $+19.8$, $+56.6$, and $+65.6 \text{ km s}^{-1}$. There are also many broad lines at $+56.6 \text{ km s}^{-1}$ identified outside the remnant, which are unrelated to the remnant. We also find no good spatial correlation between the remnant and the $+56.6 \text{ km s}^{-1}$ component. Broad line points at $+19.8 \text{ km s}^{-1}$ are located in the overlapping region with an H II region in the northwest. However, there are also many broad line candidates at $+19.8 \text{ km s}^{-1}$ identified in the remnant but outside the overlapping region with the H II region by partial criteria. Molecular gas at a minor peak of the SCC at $\sim +16.2 \text{ km s}^{-1}$ is surrounding the east of the remnant and distributed in the northwest of the remnant, which belongs to the $+19.8 \text{ km s}^{-1}$ component. There is only one broad line at $+65.6 \text{ km s}^{-1}$, which locates in the overlapping region with SNRC G41.95-0.18. Three molecular clumps at the nonsignificant peak of the SCC at $\sim +73.3 \text{ km s}^{-1}$ are distributed around the remnant, which belongs to the $+65.6 \text{ km s}^{-1}$ component. The remnant may be associated with either the $+19.8$ or $+65.6 \text{ km s}^{-1}$ components. Kinematic distances are estimated as $11.0 \pm 0.4 \text{ kpc}$ for the $+19.8 \text{ km s}^{-1}$

component and as 7.9 ± 0.5 kpc for the $+65.6 \text{ km s}^{-1}$ component.

G42.8+0.6: A small part of this SNR in the east overlaps with SNRC G43.02+0.73. No broad line is identified in this SNR by full criteria. Broad line candidates at two velocities are identified in the remnant by partial criteria. There is only one broad line candidate at $+25.6 \text{ km s}^{-1}$, which can be attributed to the nearby $+23.7 \text{ km s}^{-1}$ component. Most of the broad line candidate points are outside the overlapping region with SNRC G43.02+0.73. Molecular gases at minor peaks of the SCC at $\sim +26.5$ and $\sim +33.3 \text{ km s}^{-1}$ are roughly surrounding the northwest and southeast of the remnant, respectively, which belong to the $+23.7 \text{ km s}^{-1}$ component. The remnant may be associated with the $+23.7 \text{ km s}^{-1}$ component, and the corresponding kinematic distance is estimated as 10.8 ± 0.3 kpc.

G43.3-0.2 (W49B): More or less spatial correlations were found for all three major velocity components in the direction of this SNR, i.e. at about $+10$, $+45$, and $+60 \text{ km s}^{-1}$ (Chen et al. 2014; Zhu et al. 2014; Sano et al. 2021; Sofue et al. 2021). Broad $^{12}\text{CO}(J=2-1)$ lines at $+14 \text{ km s}^{-1}$ were detected toward the SNR by Kilpatrick et al. (2016), and warm molecular gases at $\sim +10 \text{ km s}^{-1}$ and the expanding gas motion at $\sim +10$ and $\sim +40 \text{ km s}^{-1}$ were detected by Sano et al. (2021). Nevertheless, Zhou et al. (2022) detected very broad HCO+ lines in the SNR, providing strong evidence for the association between the remnant and the $\sim +63 \text{ km s}^{-1}$ velocity component. Lee et al. (2020) also detected near-infrared H_2 lines at $+64 \text{ km s}^{-1}$ toward the remnant. The SNR was also studied by other spectral lines supporting one or the other of the three components (see Table 3 for more information). Here, two broad line components at $+39.8$ and $+60.1 \text{ km s}^{-1}$ are identified in the SNR by full criteria. There is only one broad line identified for the $+39.8 \text{ km s}^{-1}$ component, which locates in the northwestern radio bright region of the remnant. Some broad lines of the $+60.1 \text{ km s}^{-1}$ component are in an overlapped H II region in the southeast. The SCC has two significant peaks at $\sim +15.6$ and $\sim +43.3 \text{ km s}^{-1}$. Molecular gas at $\sim +43.3 \text{ km s}^{-1}$ that belongs to the $+39.8 \text{ km s}^{-1}$ component is surrounding the whole remnant except for its northwest side. A minor peak at $\sim +56.5 \text{ km s}^{-1}$ also indicates a roughly spatial correlation between the remnant the $+60.1 \text{ km s}^{-1}$ component, where molecular gas is distributed around the remnant's boundary. Based on these evidences, either the $+39.8$ or $+60.1 \text{ km s}^{-1}$ components may be associated with the remnant. As shown by Ranasinghe & Leahy (2018b), the presence of H I absorption up to the tangent point velocity indicates that the SNR is at a far kinematic distance. The far kinematic distance of the $+39.8 \text{ km s}^{-1}$ component is estimated as 9.3 ± 0.8 kpc, and the kinematic distance of the $+60.1 \text{ km s}^{-1}$ component is estimated as 7.7 ± 0.6 kpc.

G43.9+1.6: Broad CO lines at $+50 \text{ km s}^{-1}$ were detected toward this SNR by Zhou et al. (2020b). Here, no broad line is identified in the SNR by full criteria. One broad line candidate at $+47.9 \text{ km s}^{-1}$ is identified in the SNR by partial criteria. As indicated by the SCC, there are several molecular clumps belonging to the $+47.9 \text{ km s}^{-1}$ component distributed around the eastern half of the remnant. These evidences indicate that the remnant may be associated with the $+47.9 \text{ km s}^{-1}$ component. This association is consistent with the result in previous work (see Table 3). Corresponding near and far kinematic distances are estimated as 2.8 ± 0.6 and 8.9 ± 0.6 kpc, respectively.

G45.7-0.4: This SNR is adjacent to SNRC G45.35-0.37 to the west. Broad lines at several velocities are identified in the remnant by full criteria, nevertheless, only the $+59.6 \text{ km s}^{-1}$ component is with more than one broad line identified. Besides, we also find spatial correlation between the remnant and the $+59.6 \text{ km s}^{-1}$ component. Molecular gas at the peak of the SCC at $\sim +71.4 \text{ km s}^{-1}$ is surrounding the southeast and northwest of the remnant, where partial radio continuum shells are present. No good spatial correlation is found for other velocity components. These evidences indicate that the remnant is associated with the $+59.6 \text{ km s}^{-1}$ MC with the kinematic distance estimated as 7.0 ± 0.6 kpc.

G46.8-0.3 (HC30): Three broad line components are identified in this SNR by full criteria. Two of them at $+19.4$ and $+59.3 \text{ km s}^{-1}$ are found to be spatially associated with the remnant, as indicated by the SCC. For the $+19.4 \text{ km s}^{-1}$ component, molecular gas at $\sim +21.4 \text{ km s}^{-1}$ is roughly surrounding the north of the remnant. For the $+59.3 \text{ km s}^{-1}$ component, molecular gas at $\sim +56.4 \text{ km s}^{-1}$ presents as a cavity-like structure enclosing the remnant. Therefore, the remnant may be associated with either the $+19.4$ or $+59.3 \text{ km s}^{-1}$ components. Note that there is H I absorption at the tangent point velocity toward this SNR detected by Sato (1979), Ranasinghe & Leahy (2018b), and Supan et al. (2022), indicating that the SNR is at a far kinematic distance. The far kinematic distance of the $+19.4 \text{ km s}^{-1}$ component is estimated as 10.1 ± 0.6 kpc, and the kinematic distance of the $+59.3 \text{ km s}^{-1}$ component is estimated as 6.9 ± 0.5 kpc.

G49.2-0.7 (W51C): Both OH 1720 MHz maser emission with velocities from $+68.9$ to $+72.13 \text{ km s}^{-1}$ and broad $^{12}\text{CO}(J=2-1)$ lines at $+60 \text{ km s}^{-1}$ were detected in this SNR (Green et al. 1997; Koo & Moon 1997; Brogan et al. 2000; Hewitt et al. 2008, see Table 3 for more information). Here, broad lines at three velocities are identified in the SNR by full criteria. All of these broad lines are probably originated from the same component at $+61.1 \text{ km s}^{-1}$. Note that part of broad lines may be associated with overlapped H II regions. As indicated by the SCC, the $+61.1 \text{ km s}^{-1}$ component is spatially correlated with the remnant, and most

of its gas is surrounding the north of the remnant. As indicated by the kinematic evidence and the spatial correlation result, the remnant is associated with the $+61.1 \text{ km s}^{-1}$ MC with the corresponding kinematic distance estimated as $5.5 \pm 0.3 \text{ kpc}$. This is consistent with multiband results in previous works (see Table 3).

G53.6-2.2 (3C 400.2): We identify no broad line and find no good spatial correlation result for this SNR. The SCC peaks at $\sim +18.3 \text{ km s}^{-1}$, where a molecular clump is located around the eastern boundary of the remnant. It may support the spatial correlation between the remnant and H I gas revealed in previous work (see Table 3).

G54.1+0.3: Toward this SNR, broad $^{12}\text{CO}(J=2-1)$ lines were detected at $+23 \text{ km s}^{-1}$ with widths (FWHM) $\lesssim 7 \text{ km s}^{-1}$ (Lee et al. 2012b, see Table 3 for more information). Here, no broad line is identified in the SNR even by partial criteria. The SCC peaks at $\sim +51.3 \text{ km s}^{-1}$, where molecular gas is roughly surrounding the northwest of the remnant and also distributed around the southeastern boundary. If the remnant is associated with molecular gas at $\sim +51.3 \text{ km s}^{-1}$, its kinematic distance can be estimated as $4.4 \pm 0.6 \text{ kpc}$.

G54.4-0.3 (HC40): This SNR presents a bright radio continuum shell in the north. The northwest of this SNR is adjacent to two H II regions at about $+38$ and $+42 \text{ km s}^{-1}$. Broad lines associated with these H II regions are identified, which are outside the remnant. Broad lines at velocities of $+35.5$, $+40.2$, and $+51.5 \text{ km s}^{-1}$ in the remnant are identified by full criteria. Two broad lines at $+40.2 \text{ km s}^{-1}$ component can be attributed to the nearby $+35.5 \text{ km s}^{-1}$ component. At the minor peak of the SCC at $\sim +39.8 \text{ km s}^{-1}$, molecular gas is distributed around the northern boundary of the remnant but not well correlated, which belongs to the $+35.5 \text{ km s}^{-1}$ component. We find no good spatial correlation between the remnant and the $+51.5 \text{ km s}^{-1}$ component. Therefore, we suggest that the remnant and the $+35.5 \text{ km s}^{-1}$ component are associated. Considering that H I absorption is present up to the tangent point velocity shown by Ranasinghe & Leahy (2017), the kinematic distance of the $+35.5 \text{ km s}^{-1}$ component is estimated as $5.1 \pm 0.3 \text{ kpc}$.

G55.0+0.3: The south of this SNR is adjacent to an H II region at about $+31 \text{ km s}^{-1}$. Two broad line components at $+10.5$ and $+28.4 \text{ km s}^{-1}$ are identified in the remnant. No good spatial correlation is found between the remnant and the $+10.5 \text{ km s}^{-1}$ component. Molecular gas at the peak of the SCC at $\sim +38.9 \text{ km s}^{-1}$ is roughly surrounding the east and south of the remnant, which belongs to the $+28.4 \text{ km s}^{-1}$ broad line component. Therefore, we suggest that the remnant is associated with the $+28.4 \text{ km s}^{-1}$ component with the kinematic distance estimated as $4.3 \pm 0.7 \text{ kpc}$.

G55.7+3.4: This SNR presents shell-like radio continuum emission around its southwestern half. No broad line is identified in this SNR even by partial criteria. Molecular gas at the peak of the SCC at $\sim +6.8 \text{ km s}^{-1}$ is roughly surrounding the south of the remnant. The remnant may be associated with molecular gas at $\sim +6.8 \text{ km s}^{-1}$, of which the near and far kinematic distances are estimated as 0.1 ± 0.6 and $9.0 \pm 0.6 \text{ kpc}$, respectively. If the remnant locates at the far distance of 9.0 kpc , its height from the Galactic plane would be as high as $\sim 540 \text{ pc}$.

G57.2+0.8 (4C-21.53): No broad line is identified in this SNR even by partial criteria. As indicated by the SCC, molecular gases at $\sim +13.0$ and $\sim +30.0 \text{ km s}^{-1}$ show some spatial correlations with the remnant. Molecular gas at $\sim +13.0 \text{ km s}^{-1}$ is roughly surrounding the south of the remnant. Molecular gas at $\sim +30.0 \text{ km s}^{-1}$ presents as a short filament connected to a shell-like structure located in the south of the remnant. The remnant may be associated with molecular gases at $\sim +13.0$ or $\sim +30.0 \text{ km s}^{-1}$. The presence of H I absorption up to the tangent point velocity shown by Ranasinghe et al. (2018) indicates that the SNR is at the far side of the tangent point. For molecular gas at $\sim +13.0 \text{ km s}^{-1}$, the kinematic distance is estimated as $8.3 \pm 0.7 \text{ kpc}$. For molecular gas at $\sim +30.0 \text{ km s}^{-1}$, the far kinematic distance is estimated as $6.3 \pm 1.4 \text{ kpc}$.

G59.5+0.1: Broad CO lines at $+28 \text{ km s}^{-1}$ were detected toward this SNR by (Xu & Wang 2012, see Table 3 for more information). The SNR is close to H II regions at about -3 and $+29 \text{ km s}^{-1}$. Here, three broad line components at $+0.7$, $+21.8$, and $+28.9 \text{ km s}^{-1}$ are identified in the SNR by full criteria. There are two broad lines identified at $+28.9 \text{ km s}^{-1}$, which can be attributed to the nearby $+21.8 \text{ km s}^{-1}$ component. Broad line points of the $+0.7 \text{ km s}^{-1}$ component are beside the nearby H II region at about -3 km s^{-1} . Molecular gas at the peak of the SCC at $\sim +1.9 \text{ km s}^{-1}$ is distributed around the northern boundary of the remnant, however, not well correlated. Molecular gas of the $+21.8 \text{ km s}^{-1}$ component is distributed around the eastern half of the remnant, which is also not well correlated. The remnant may be associated with either the $+0.7$ or $+21.8 \text{ km s}^{-1}$ components. Kinematic distances are estimated as $8.3 \pm 0.4 \text{ kpc}$ for the $+0.7 \text{ km s}^{-1}$ component and $2.2 \pm 0.1 \text{ kpc}$ for the $+21.8 \text{ km s}^{-1}$ component.

G65.1+0.6: This SNR presents a bright radio continuum shell in the southwest and some radio continuum emission in the northeast. Broad lines at several velocities are identified in the SNR by full criteria. Broad lines at -3.5 and $+11.3 \text{ km s}^{-1}$ are probably originated from nearby components at -16.4 and $+16.0 \text{ km s}^{-1}$, respectively. As indicated by the SCC, molecular gas at $\sim -15.2 \text{ km s}^{-1}$ shows some spatial correlations with the remnant, which is distributed around the southwestern radio continuum shell of the remnant. It belongs to the -16.4 km s^{-1} broad line component. Molecular gas at $\sim +18.6 \text{ km s}^{-1}$ belonging to the $+16.0 \text{ km s}^{-1}$

broad line component is distributed around the southwestern and northeastern boundaries of the remnant. The remnant may be associated with either the -16.4 or $+16.0$ km s^{-1} components. The kinematic distance of the -16.4 km s^{-1} component is estimated as 7.9 ± 0.5 kpc. The near and far kinematic distances of the $+16.0$ km s^{-1} component are estimated as 1.6 ± 1.1 and 5.7 ± 0.9 kpc, respectively.

G66.0-0.0: No broad line is identified in this SNR by full criteria; however, broad line candidates at velocities of $+1.7$, $+9.1$, and $+15.6$ km s^{-1} are identified in this SNR by partial criteria. Broad lines at $+9.1$ km s^{-1} can be attributed to the nearby prominent component at $+15.6$ km s^{-1} . Molecular gases of both the $+1.7$ and $+15.6$ km s^{-1} components are roughly surrounding the remnant. The remnant may be associated with either of these two components. Kinematic distances are estimated as 7.1 ± 0.4 kpc for the $+1.7$ km s^{-1} component and 4.4 ± 0.5 kpc for the $+15.6$ km s^{-1} component.

G67.6+0.9: Only one broad line component at -21.3 km s^{-1} is identified in this SNR by full criteria. However, the -21.3 km s^{-1} component shows no good spatial correlation with the remnant. At the peak of the SCC at $\sim +1.7$ km s^{-1} , there are molecular clumps roughly surrounding the remnant, mainly in the southeast, which belongs to the $+9.8$ km s^{-1} component with a broad line candidate identified in the remnant by partial criteria. The remnant is probably associated with the $+9.8$ km s^{-1} component, or may be associated with the -21.3 km s^{-1} component. Kinematic distances are estimated as 4.3 ± 0.7 kpc for the $+9.8$ km s^{-1} component and 7.7 ± 0.6 for the -21.3 km s^{-1} component.

G67.8+0.5: No broad line is identified in this SNR even by partial criteria. Molecular gas at the peak of the SCC at ~ -1.7 km s^{-1} is distributed around the northern and western boundaries of the remnant. If the remnant is associated with molecular gas at ~ -1.7 km s^{-1} , its kinematic distance can be estimated as 6.9 ± 0.5 kpc.

G68.6-1.2: Only one broad line component at $+10.0$ km s^{-1} is identified in this SNR, with broad line points distributed in the north. As indicated by the SCC, molecular gas at $\sim +11.9$ km s^{-1} is roughly surrounding the remnant, which belongs to the $+10.0$ km s^{-1} component. Based on these results, we suggest that the remnant is associated with the $+10.0$ km s^{-1} component with the corresponding kinematic distance estimated as 4.2 ± 0.6 kpc.

G69.7+1.0: No broad line is identified in this SNR even by partial criteria. We also find no good spatial correlation result. However, there are several peaks of the SCC. Molecular gas at ~ -64.3 km s^{-1} is distributed around the southeastern boundary of the remnant, and molecular gas at ~ -48.9 km s^{-1} is distributed around the northeastern boundary. There is more molecular gas at $\sim +13.7$ km s^{-1} , which is widely distributed around the east of the remnant.

G73.9+0.9: We only identify one broad line candidate at $+0.3$ km s^{-1} in this SNR by partial criteria. Molecular gas at a peak of the SCC at $\sim +6.0$ km s^{-1} is distributed around the southern boundary of the remnant, which belongs to the $+0.3$ km s^{-1} component. The remnant may be associated with the $+0.3$ km s^{-1} component, of which the kinematic distance is estimated as 3.5 ± 0.6 kpc.

G78.2+2.1 (DR4): One broad line component at -0.8 km s^{-1} is identified in this SNR by full criteria. Molecular gas at the peak of the SCC at $\sim +1.3$ km s^{-1} is roughly surrounding the remnant, which belongs to the -0.8 km s^{-1} component. These evidences indicate that the remnant is associated with the -0.8 km s^{-1} component. The corresponding kinematic distance is estimated as 2.5 ± 0.8 kpc.

G82.2+5.3 (W63): A small part of this SNR in the north is not covered in our observation. No broad line is identified in the SNR even by partial criteria. Molecular gas at the nonsignificant peak of the SCC at ~ -18.7 km s^{-1} is distributed around the southwestern boundary of the remnant, where the remnant's radio continuum emission is bright. If the remnant is associated with molecular gas at ~ -18.7 km s^{-1} , its kinematic distance can be estimated as 5.1 ± 0.8 kpc.

G83.0-0.3: Only one broad line candidate at $+12.2$ km s^{-1} is identified in this SNR by partial criteria. No significant spatial correlation result is found through the SCC. Nevertheless, molecular gas at a peak of the SCC at $\sim +12.4$ km s^{-1} is distributed around the northeastern and western boundary of the remnant, which belongs to the $+12.2$ km s^{-1} component. The remnant may be associated with the $+12.2$ km s^{-1} component, and the corresponding kinematic distance is estimated as 1.9 ± 0.5 kpc.

G84.2-0.8: Spatial correlations between this SNR and MCs at -39 and -17 km s^{-1} were found (Huang & Thaddeus 1986; Feldt & Green 1993; Jeong et al. 2012). Here, no broad line is identified in the SNR even by partial criteria. The SCC peaks at ~ -17.5 km s^{-1} where molecular gas is mainly distributed in the remnant, not well correlated. Molecular gas at a peak of the SCC at $\sim +6.0$ km s^{-1} is roughly cavity-like, surrounding the remnant. If the remnant is associated with molecular gas at $\sim +6.0$ km s^{-1} , its kinematic distance can be estimated as 1.4 ± 0.2 kpc.

G85.4+0.7: Broad line candidates are identified in this SNR by partial criteria. No broad line is identified in the SNR by full criteria. As indicated by the SCC, the remnant is spatially correlated with the -41.7 and -0.6 km s^{-1} components. The -41.7 km s^{-1} component is well surrounding the east and southwest of the

remnant, and the -0.6 km s^{-1} component is roughly surrounding its south and northwest. The remnant may be associated with the -41.7 or -0.6 km s^{-1} components. Kinematic distances are estimated as $5.1 \pm 0.6 \text{ kpc}$ for the -41.7 km s^{-1} component and $1.7 \pm 0.4 \text{ kpc}$ for the -0.6 km s^{-1} component.

G89.0+4.7 (HB 21): Broad CO lines at -5 and $+3 \text{ km s}^{-1}$ were detected toward this SNR (Koo et al. 2001; Byun et al. 2006, see Table 3 for more information). Here, only one broad line component at -16.3 km s^{-1} is identified in the remnant by full criteria; however, it shows no good spatial correlation with the remnant. As indicated by the SCC, molecular gas at $\sim -8.3 \text{ km s}^{-1}$ is spatially correlated with the remnant, which is distributed around the remnant. It belongs to the -4.9 km s^{-1} component with broad lines identified in the remnant by partial criteria. Based on these evidences, the remnant is probably associated with the -4.9 km s^{-1} component, or may be associated with the -16.3 km s^{-1} component. We estimate kinematic distances to be $3.7 \pm 0.9 \text{ kpc}$ for the -16.3 km s^{-1} component and $1.6 \pm 0.2 \text{ kpc}$ for the -4.9 km s^{-1} component. The association with the -4.9 km s^{-1} component is consistent with multiband results in previous works (see Table 3).

G93.3+6.9 (DA 530): Part of this SNR in the east is not covered in our observation. No broad line is identified in the remnant even by partial criteria. We also find no good spatial correlation result for this remnant.

G93.7-0.2 (CTB 104A): Uyaniker et al. (2002) found a spatial correlation between this SNR and H I gas at -6 km s^{-1} . Here, only one broad line candidate at $+19.4 \text{ km s}^{-1}$ is identified in the SNR by partial criteria. The SCC peaks at $\sim +11.3 \text{ km s}^{-1}$, where molecular gas is surrounding the northwest of the remnant. It belongs to the $+19.4 \text{ km s}^{-1}$ component. The remnant may be associated with the $+19.4 \text{ km s}^{-1}$ component. In the direction of this remnant, the velocity of $+19.4 \text{ km s}^{-1}$ is beyond the Galactic rotation curve; hence, no corresponding kinematic distance is obtained.

G94.0+1.0 (3C 434.1): No broad line is identified in this SNR even by partial criteria. Molecular gas at the peak of the SCC at $\sim -13.3 \text{ km s}^{-1}$ is roughly surrounding the northwest of the remnant. No good spatial correlation result is found for molecular gases at other velocities. The spatial correlation result indicates a possible association between the remnant and molecular gas at $\sim -13.3 \text{ km s}^{-1}$. The corresponding kinematic distance is estimated as $2.9 \pm 0.8 \text{ kpc}$.

G96.0+2.0: This SNR presents shell-like radio continuum emission in the southwest. Only one component at -18.6 km s^{-1} is with broad line candidates identified in the SNR by partial criteria, while no broad line is identified in it by full criteria. Molecular gas at the peak of the SCC at $\sim -15.7 \text{ km s}^{-1}$ is distributed around the northwestern boundary but not correlated well, which belongs to the -18.6 km s^{-1} component. The SNR may be associated with the -18.6 km s^{-1} component, of which the kinematic distance is estimated as $3.0 \pm 0.8 \text{ kpc}$.

G106.3+2.7: We identify no broad line in this SNR even by partial criteria. The SCC peaks at $\sim -6.7 \text{ km s}^{-1}$, where molecular gas is roughly surrounding the north of the remnant. If the remnant is associated with molecular gas at $\sim -6.7 \text{ km s}^{-1}$, its kinematic distance can be estimated as $0.8 \pm 0.1 \text{ kpc}$.

G108.2-0.6: No broad line is identified in this SNR even by partial criteria. There are many molecular clumps at the peak of the SCC at $\sim -49.5 \text{ km s}^{-1}$ roughly surrounding the east of the remnant. The remnant may be associated with molecular gas at $\sim -49.5 \text{ km s}^{-1}$, of which the kinematic distance is estimated as $2.9 \pm 0.3 \text{ kpc}$.

G109.1-1.0 (CTB 109): An anticorrelation between the CO and X-ray distributions was found and studied in detail by Tatematsu et al. (1987, 1990a), and an association between this SNR and MCs was suggested (see Table 3 for more information). Sasaki et al. (2006) detected an asymmetric CO line profile at $\sim -55 \text{ km s}^{-1}$ but only broadened by $\lesssim 3 \text{ km s}^{-1}$. No broad CO emission above 0.4 K was detected by Tatematsu et al. (1990a). We identify no broad line in the SNR even by partial criteria. Molecular gas at the peak of the SCC at $\sim -51.1 \text{ km s}^{-1}$ shows some spatial correlations with the remnant, which is surrounding the west of it. If the remnant is associated with molecular gas at $\sim -51.1 \text{ km s}^{-1}$, we can estimate its kinematic distance as $2.8 \pm 0.3 \text{ kpc}$.

G111.7-2.1 (Cas A): Broad CO lines at $\sim -40 \text{ km s}^{-1}$ were detected toward this SNR (Kilpatrick et al. 2014, 2016; Ma et al. 2019, see Table 3 for more information). Nevertheless, no broad CO lines with widths greater than 7 km s^{-1} were detected by Zhou et al. (2018). We identify broad line candidates in only one component at -39.0 km s^{-1} in the SNR by partial criteria. Molecular gas of the -39.0 km s^{-1} component is mainly distributed in the east and south of the remnant. If the remnant is associated with the -39.0 km s^{-1} component, its kinematic distance can be estimated as $3.5 \pm 0.3 \text{ kpc}$.

G120.1+1.4 (Tycho): Broad $^{12}\text{CO}(J=1-0)$ lines ($> 5 \text{ km s}^{-1}$) at -63.5 km s^{-1} were detected toward this SNR by Cai et al. (2009) (see Table 3 for more information). Here, no broad line is identified in the SNR even by partial criteria. The SCC peaks at $\sim -63.0 \text{ km s}^{-1}$, where molecular gas is surrounding the northeast of the remnant and also distributed around its southwestern boundary. The remnant may be associated with molecular gas at $\sim -63.0 \text{ km s}^{-1}$, of which near and far kinematic distances are estimated as 2.7 ± 0.7 and $5.5 \pm 0.8 \text{ kpc}$, respectively. Note that the absence of H I absorption feature within the velocity range of -46 to -41 km s^{-1} favors the near kinematic distance (Tian & Leahy 2011).

G126.2+1.6: One broad line component at $+3.7 \text{ km s}^{-1}$ is identified in this SNR by full criteria. As indicated by the SCC, molecular gas at $\sim -3.8 \text{ km s}^{-1}$ is surrounding the northeast and northwest of the remnant, spatially correlated with the partial radio continuum shell in the northwest. In addition, molecular gas at $\sim +6.7 \text{ km s}^{-1}$ is distributed around the southeastern and western boundary of the remnant. These molecular gases belong to the $+3.7 \text{ km s}^{-1}$ component. The kinematic evidence as well as the spatial correlation result indicates an association between the remnant and the $+3.7 \text{ km s}^{-1}$ component, of which two alternative kinematic distances are estimated as 0.1 ± 0.2 and 1.3 ± 0.1 kpc.

G127.1+0.5 (R5): Broad CO lines at $\sim +5 \text{ km s}^{-1}$ were detected toward this SNR by Zhou et al. (2014). Here, only one component at $+2.7 \text{ km s}^{-1}$ is with broad line candidates identified in the SNR by partial criteria. Molecular gas at a peak of the SCC at $\sim +6.0 \text{ km s}^{-1}$, as part of a long filament near the remnant, is surrounding the northeast of the remnant, which belongs to the $+2.7 \text{ km s}^{-1}$ component. It is spatially correlated with the radio continuum shell of the remnant. Based on these evidences, the remnant is probably associated with the $+2.7 \text{ km s}^{-1}$ component, and the corresponding kinematic distance is estimated as 0.23 ± 0.02 kpc.

G132.7+1.3 (HB 3): This SNR is discussed in Section 3.3.2.

G150.3+4.5: The middle and southwest of this SNR overlap with two SNRCs, i.e. G150.8+3.8 and G149.5+3.2. No broad line is identified in the remnant even by partial criteria. The SCC indicates a roughly spatial correlation between the remnant and molecular gas at $\sim +1.6 \text{ km s}^{-1}$, which distributes around eastern and southern boundaries of the remnant. If the remnant is associated with molecular gas at $\sim +1.6 \text{ km s}^{-1}$, its kinematic distance can be estimated as 0.27 ± 0.01 kpc.

G152.4-2.1: Only one broad line candidate at -16.3 km s^{-1} is identified in this SNR by partial criteria. As indicated by minor peaks of the SCC, molecular gas of the -16.3 km s^{-1} component is distributed around eastern and northern boundaries of the remnant. However, they are not spatially correlated very well. If the remnant is associated with the -16.3 km s^{-1} component, its kinematic distance can be estimated as 1.9 ± 0.4 kpc.

G160.9+2.6 (HB 9): We identify only one broad line component in this SNR at -21.6 km s^{-1} ; however, it shows no good spatial correlation with the remnant. The SCC peaks at $\sim -2.5 \text{ km s}^{-1}$, where molecular gas is surrounding the northeast of the remnant. The remnant may be associated with either the -21.6 km s^{-1} component or molecular gas at $\sim -2.5 \text{ km s}^{-1}$. Kinematic distances are estimated as 2.1 ± 0.4 kpc for the -21.6 km s^{-1} component and 0.5 ± 0.2 kpc for molecular gas at $\sim -2.5 \text{ km s}^{-1}$.

G180.0-1.7 (S147): The peak of the SCC for this SNR is not significant, where molecular gas at $\sim +6.5 \text{ km s}^{-1}$ is distributed around the remnant. Part of the molecular gas belongs to the $+1.7 \text{ km s}^{-1}$ component that is the only component with a broad line candidate identified in the remnant by partial criteria. We identify no broad line in the remnant by full criteria. If the remnant is associated with the $+1.7 \text{ km s}^{-1}$ component, its kinematic distance can be estimated as 1.59 ± 0.03 or 4.3 ± 0.5 kpc.

G182.4+4.3: Molecular gas at the peak of the SCC at $\sim +5.6 \text{ km s}^{-1}$ is surrounding the north and northwest of this SNR. However, we identify no broad line in the remnant even by partial criteria. If the remnant is associated with molecular gas at $\sim +5.6 \text{ km s}^{-1}$, its kinematic distance can be estimated as 0.23 ± 0.02 kpc.

G189.1+3.0 (IC 443): This SNR is discussed in Section 3.3.1.

G190.9-2.2: We identify one broad line component at $+1.0 \text{ km s}^{-1}$ in this SNR by full criteria. At the peak of the SCC at $\sim -4.1 \text{ km s}^{-1}$, there is a filamentary shape MC located in the northern part of the remnant but not correlated well. Additionally, molecular gas at another peak of the SCC at $\sim +5.1 \text{ km s}^{-1}$ is distributed around the southeastern and western boundaries of the remnant. These molecular gases belong to the $+1.0 \text{ km s}^{-1}$ component. Therefore, the remnant is probably associated with the $+1.0 \text{ km s}^{-1}$ component, with the corresponding kinematic distance estimated as 1.6 ± 0.2 kpc.

G205.5+0.5 (Monoceros Loop): Broad CO lines at $\sim +5$ and $\sim +19 \text{ km s}^{-1}$ were detected toward this SNR with widths of several kilometers per second (Su et al. 2017b, see Table 3 for more information). Here, we identify one broad line component at $+21.3 \text{ km s}^{-1}$ in the SNR only by partial criteria. Broad line points are located near an overlapped H II region at $+18.1 \text{ km s}^{-1}$ in the south. Molecular gas at the peak of the SCC at $\sim +13.3 \text{ km s}^{-1}$ is around northern and southern boundaries of the remnant, which belongs to the $+21.3 \text{ km s}^{-1}$ component. The remnant may be associated with the $+21.3 \text{ km s}^{-1}$ component, of which the kinematic distance is estimated as 2.3 ± 0.4 kpc.

G206.9+2.3 (PKS 0646+06): No broad line is identified in this SNR. The SCC indicates a spatial correlation between the remnant and molecular gas at $\sim +13.7 \text{ km s}^{-1}$, which surrounds the south of the remnant. If the remnant is associated with molecular gas at $\sim +13.7 \text{ km s}^{-1}$, its kinematic distance can be estimated as 2.3 ± 0.4 kpc.

G213.0-0.6: Broad CO lines at $\sim +9 \text{ km s}^{-1}$ were detected toward this SNR with widths of several kilometers per second (Su et al. 2017b, see Table 3 for more information). Here, we identify no broad line in the SNR and find no good spatial correlation result. Molecular gas at the peak of the SCC at $\sim +22.9 \text{ km s}^{-1}$ is distributed

within the remnant.

B. Individual SNR Candidates

G1.95-0.10: The SCC peaks at $\sim+59.5 \text{ km s}^{-1}$, where molecular gas is roughly surrounding the west of this SNRC. It belongs to the $+44.7 \text{ km s}^{-1}$ component with a broad line candidate identified in the SNRC by full criteria. These evidences indicate a possible association between the SNRC and the $+44.7 \text{ km s}^{-1}$ component. The corresponding kinematic distance is estimated as $8.1\pm 2.9 \text{ kpc}$.

G1.98-0.46: Molecular gas at the peak of the SCC at $\sim+8.6 \text{ km s}^{-1}$ is distributed around this SNRC, which belongs to the $+12.6 \text{ km s}^{-1}$ velocity component. Identified broad line candidates in the SNRC also support the association between the SNRC and the $+12.6 \text{ km s}^{-1}$ component. If the SNRC is associated with the $+12.6 \text{ km s}^{-1}$ component, its kinematic distance can be estimated as $2.8\pm 0.3 \text{ kpc}$.

G2.23+0.06: This SNRC is classified as the plerion type, and it is small. We find no good spatial correlation result and identify no broad line candidate in it by full criteria.

G2.28+0.40: Molecular gas at the peak of the SCC at $\sim+3.2 \text{ km s}^{-1}$ is roughly surrounding this SNRC, which belongs to the $+4.8 \text{ km s}^{-1}$ velocity component with many broad line candidates identified in the SNRC's west by full criteria. The SNRC may be associated with the $+4.8 \text{ km s}^{-1}$ component, of which the kinematic distance is estimated as $2.8\pm 0.3 \text{ kpc}$.

G2.91-0.18 and G3.1-0.6: The southeast of SNRC G2.91-0.18 is adjacent to SNRC G3.1-0.6. For SNRC G2.91-0.18, molecular gas at a peak of the SCC at $\sim-42.7 \text{ km s}^{-1}$ is surrounding the south and southwest of the SNRC, where shell-like radio continuum emission is present. It belongs to the -40.0 km s^{-1} velocity component that is with broad line candidates identified in the SNRC by full criteria. These evidences indicate that SNRC G2.91-0.18 is associated with the -40.0 km s^{-1} component, of which the kinematic distance is estimated as $4.7\pm 0.3 \text{ kpc}$. For SNRC G3.1-0.6, molecular gas at a minor peak of the SCC at $\sim-32.2 \text{ km s}^{-1}$ is roughly surrounding the north of the SNRC, which belongs to the -41.0 km s^{-1} component with broad line candidates identified in the SNRC by full criteria. SNRC G3.1-0.6 may be associated with the -41.0 km s^{-1} component with the corresponding kinematic distance estimated as $4.7\pm 0.3 \text{ kpc}$. Therefore, these two SNRCs may be related to each other.

G3.10-0.09: This SNRC overlaps with SNRC G2.91-0.18. Molecular gases at minor peaks of the SCC at $\sim+33.3$ and $\sim+92.9 \text{ km s}^{-1}$ are roughly surrounding the shell-like radio continuum emission of the SNRC in the west. Molecular gas at $\sim+33.3 \text{ km s}^{-1}$ probably belongs to the $+23.7 \text{ km s}^{-1}$ component, which is with a broad line candidate identified in the SNRC by full criteria. Molecular gas at $\sim+92.9 \text{ km s}^{-1}$ belongs to the $+95.8 \text{ km s}^{-1}$ component with broad line candidates identified in the SNRC only by partial criteria. Based on these evidences, either the $+23.7$ or $+95.8 \text{ km s}^{-1}$ components may be associated with the SNRC. Near and far kinematic distances are estimated as 2.9 ± 0.3 and $12.6\pm 0.3 \text{ kpc}$ for the $+23.7 \text{ km s}^{-1}$ component, respectively. For the $+95.8 \text{ km s}^{-1}$ component, the kinematic distance is estimated as $8.2\pm 2.9 \text{ kpc}$. This SNRC is not likely to be associated with SNRC G2.91-0.18.

G3.10+0.11: This SNRC is classified as the plerion type. No good spatial correlation result is found for the SNRC, because of its small size. We also identify no broad line candidate in it by full criteria.

G4.20-0.30: Molecular gas at a peak of the SCC at $\sim-27.8 \text{ km s}^{-1}$ is roughly surrounding the northern radio continuum shell of this SNRC, which belongs to the -31.4 km s^{-1} component with broad line candidates identified in the SNRC by full criteria. As supported by the spatial correlation result and identified broad line candidates, the SNRC is probably associated with the -31.4 km s^{-1} component, of which the kinematic distance is estimated as $4.7\pm 0.3 \text{ kpc}$.

G4.49-0.39 and G4.57-0.24: The northeast of SNRC G4.49-0.39 is adjacent to SNRC G4.57-0.24. For SNRC G4.49-0.39, molecular gas at a peak of the SCC at $\sim+16.3 \text{ km s}^{-1}$ shows some spatial correlations with radio continuum emission of the SNRC, which is roughly surrounding the east and south of the SNRC. It belongs to the $+14.1 \text{ km s}^{-1}$ velocity component that is with broad line candidates identified in the SNRC by full criteria. If SNRC G4.49-0.39 and the $+14.1 \text{ km s}^{-1}$ component are associated, the kinematic distance of the SNRC can be estimated as $2.9\pm 0.2 \text{ kpc}$. For SNRC G4.57-0.24, molecular gas at $\sim+17.0 \text{ km s}^{-1}$ is roughly surrounding its east and northwest, as indicated by the SCC, which belongs to the $+12.3 \text{ km s}^{-1}$ velocity component. There is only one broad line candidate identified in the SNRC by full criteria, which is at $+12.3 \text{ km s}^{-1}$. These evidences indicate that SNRC G4.57-0.24 is associated with the $+12.3 \text{ km s}^{-1}$ component, and the corresponding kinematic distance is estimated as $2.9\pm 0.2 \text{ kpc}$. These two SNRCs may be related to each other.

G5.11+0.33: This SNRC presents a radio continuum shell in the west. Molecular gas at the peak of the SCC at $\sim-28.6 \text{ km s}^{-1}$ is roughly surrounding the north and southeast of the SNRC; however, it is with no broad line candidate identified in the SNRC even by partial criteria. The distribution of molecular gas at $\sim+11.7 \text{ km s}^{-1}$ roughly follows the western radio continuum shell. It belongs to the only velocity component

with broad line candidates identified in the SNRC by full criteria, which is at $+13.8 \text{ km s}^{-1}$. Note that part of broad line candidates may be originated from an overlapped H II region at $+12.0 \text{ km s}^{-1}$. The SNRC is probably associated with the $+13.8 \text{ km s}^{-1}$ component with the kinematic distance estimated as $2.9 \pm 0.2 \text{ kpc}$. Accordingly, the SNRC may be related to the overlapped H II region.

G5.16-0.32: Molecular gas at the peak of the SCC at $\sim +5.4 \text{ km s}^{-1}$ is distributed around this SNRC but not correlated well, which belongs to the $+7.6 \text{ km s}^{-1}$ component with a broad line candidate identified in the SNRC by full criteria. Moreover, molecular gas at a minor peak of the SCC at $\sim +59.5 \text{ km s}^{-1}$ shows good spatial correlation with the SNRC, which is surrounding its southern half. It belongs to the $+58.9 \text{ km s}^{-1}$ component that is with broad line candidates identified only by partial criteria. Based on these evidences, either the $+7.6$ or $+58.9 \text{ km s}^{-1}$ components may be associated with the SNRC. Corresponding kinematic distances are estimated as 2.9 ± 0.2 and $10.9 \pm 0.3 \text{ kpc}$ for the $+7.6$ and $+58.9 \text{ km s}^{-1}$ components, respectively.

G5.36-0.71: Molecular gas at a peak of the SCC at $\sim +21.0 \text{ km s}^{-1}$ is roughly surrounding this SNRC. It belongs to the $+13.0 \text{ km s}^{-1}$ component that is with broad line candidates identified in the SNRC by full criteria. The SNRC is probably associated with the $+13.0 \text{ km s}^{-1}$ component, and the corresponding kinematic distance is estimated as $2.9 \pm 0.2 \text{ kpc}$.

G5.38-0.28: This SNRC is classified as the plerion type. Since the SNRC is small, no good spatial correlation result is found. No broad line candidate is identified in it by full criteria too.

G5.38+0.35: The east of this SNRC overlaps with SNR G5.5+0.3, and it presents a partial radio continuum shell in the northwest. As indicated by minor peaks of the SCC, the $+8.5 \text{ km s}^{-1}$ component shows a coarse spatial correlation with the SNRC, of which a portion of molecular gas is distributed around the SNRC's radio continuum shell. The $+8.5 \text{ km s}^{-1}$ component is the only component with broad line candidates identified in the SNRC by full criteria. If the SNRC is associated with the $+8.5 \text{ km s}^{-1}$ component, its kinematic distance can be estimated as $2.9 \pm 0.2 \text{ kpc}$.

G5.7-0.1 (also known as G5.67-0.12): We consider SNRC G5.7-0.1 and SNRC G005.673-0.118 (see Dokara et al. 2021) as one SNRC. For this SNRC, we find no prominent spatial correlation result. Two components at velocities of -26.1 and $+8.3 \text{ km s}^{-1}$ are with broad line candidates identified in the SNRC by full criteria. Molecular gases at minor peaks of the SCC belonging to these two components are roughly surrounding the southwest and northeast of the SNRC, respectively. We cannot determine which of the velocity components at -26.1 or $+8.3 \text{ km s}^{-1}$ is associated with the SNRC. In previous works, OH 1720 MHz maser and broad CO emission were detected at $\sim +12 \text{ km s}^{-1}$, and the CH₃OH 36 and 44 GHz masers were detected at $\sim -25 \text{ km s}^{-1}$ (see Table 3). We estimate the kinematic distance of the -26.1 km s^{-1} component to be $4.7 \pm 0.3 \text{ kpc}$, and the near and far kinematic distances of the $+8.3 \text{ km s}^{-1}$ component to be 2.9 ± 0.2 and $12.6 \pm 0.3 \text{ kpc}$, respectively.

G5.76+0.52: Molecular gas at a peak of the SCC at $\sim +11.7 \text{ km s}^{-1}$ is roughly surrounding this SNRC. It belongs to the $+6.6 \text{ km s}^{-1}$ velocity component with broad line candidates identified in the SNRC. The SNRC may be associated with the $+6.6 \text{ km s}^{-1}$ component with the kinematic distance estimated as $2.9 \pm 0.2 \text{ kpc}$.

G5.99+0.02: The east of this SNRC is adjacent to SNR W28. As indicated by minor peaks of the SCC, the spatial distribution of the $+8.0 \text{ km s}^{-1}$ velocity component is roughly correlated with the SNRC, which is distributed around the SNRC. It is also with broad line candidates identified in the SNRC. If the SNRC is associated with the $+8.0 \text{ km s}^{-1}$ component, its near and far kinematic distances can be estimated as 3.0 ± 0.2 and $13.4 \pm 0.3 \text{ kpc}$, respectively.

G6.06+0.50, G6.12+0.39 and G6.31+0.54: All of these three SNRCs overlap with SNR G6.1+0.5. For SNRC G6.06+0.50, molecular gas at the peak of the SCC at $\sim +8.7 \text{ km s}^{-1}$ is roughly surrounding it, which belongs to the $+6.8 \text{ km s}^{-1}$ velocity component with broad line candidates identified in it. These evidences indicate that SNRC G6.06+0.50 is associated with the $+6.8 \text{ km s}^{-1}$ component with the corresponding kinematic distance estimated as $3.0 \pm 0.2 \text{ kpc}$. This SNRC seems to be at the same distance as SNR G6.1+0.5. For SNRC G6.12+0.39, the SCC indicates a spatial correlation with molecular gas at $\sim +10.8 \text{ km s}^{-1}$, which is surrounding the whole SNRC except for its west side. Its spatial distribution is consistent with that of the $+21.8 \text{ km s}^{-1}$ component that is with a broad line candidate identified in the SNRC. The $+7.0 \text{ km s}^{-1}$ component is also with broad line candidates identified in the SNRC, which are probably originated from SNR G6.1+0.5 or SNRC G6.06+0.50. Therefore, we suggest that SNRC G6.12+0.39 is associated with the $+21.8 \text{ km s}^{-1}$ MC and locates at a kinematic distance of $3.6 \pm 0.3 \text{ kpc}$. SNRC G6.31+0.54 presents a flat radio continuum shell in the northeast. For SNRC G6.31+0.54, we find no good spatial correlation result and identify no broad line candidate in it by full criteria, hence, no associated MC settled.

G6.45-0.56 and G6.54-0.60: These two SNRCs overlap with the south and southwest of SNR G6.5-0.4, respectively. We find no good spatial correlation result and identify no broad line candidate in these two SNRCs by full criteria.

G7.4+0.3: Molecular gas at a peak of the SCC at $\sim +13.7 \text{ km s}^{-1}$ is roughly surrounding this SNRC. It belongs to the $+16.4 \text{ km s}^{-1}$ velocity component, which is with broad line candidates identified in the SNRC by full

criteria. The SNRC may be associated with the $+16.4 \text{ km s}^{-1}$ component, of which the kinematic distance is estimated as $3.6 \pm 0.4 \text{ kpc}$.

G7.5-1.7: This SNRC exhibits shell-like radio continuum emission in the north. We find that velocity components at $+10.5$ and $+136.2 \text{ km s}^{-1}$ show some spatial correlations with the SNRC, of which broad line candidates are also identified in the SNRC. For the $+10.5 \text{ km s}^{-1}$ component, there are shell-like molecular filaments roughly surrounding the southwest and north of the SNRC. Molecular gas of the $+136.2 \text{ km s}^{-1}$ component is distributed around the northern radio continuum shell of the SNRC, correlated not so well. Based on these evidences, the SNRC is probably associated with the $+10.5 \text{ km s}^{-1}$ component, or may be associated with the $+136.2 \text{ km s}^{-1}$ component. Kinematic distances of the $+10.5$ and $+136.2 \text{ km s}^{-1}$ components are estimated as 1.5 ± 0.1 and $8.1 \pm 1.9 \text{ kpc}$, respectively.

G8.04+0.57: Molecular gas at the peak of the SCC at $\sim +20.3 \text{ km s}^{-1}$ distributes around the southeast of this SNRC, where its radio continuum emission is bright. It supports the association between the SNRC and the $+12.3 \text{ km s}^{-1}$ component that is the only component with broad line candidates identified in the SNRC by full criteria. If the SNRC is associated with the $+12.3 \text{ km s}^{-1}$ component, its kinematic distance can be estimated as $1.6 \pm 0.1 \text{ kpc}$.

G8.86-0.26: The south side of this SNRC is adjacent to an H II region at $+31.0 \text{ km s}^{-1}$, and it also overlaps with large SNR W30. The SCC peaks at $\sim +20.0 \text{ km s}^{-1}$, where molecular gas is distributed around the SNRC. It belongs to the $+18.4 \text{ km s}^{-1}$ component, which is with broad line candidates identified by full criteria. If the SNRC is associated with the $+18.4 \text{ km s}^{-1}$ component, its kinematic distance can be estimated as $3.7 \pm 0.3 \text{ kpc}$.

G11.55+0.33: Broad lines at three velocities, i.e. -3.0 , $+11.8$, and $+29.9 \text{ km s}^{-1}$, are identified in this SNRC. As indicated by the SCC, molecular gas at $\sim +18.6 \text{ km s}^{-1}$ belonging to the $+11.8 \text{ km s}^{-1}$ broad line component shows some spatial correlations with the SNRC, which is roughly surrounding the southwest of it and also distributed around its northern boundary. There is also molecular gas at $\sim +31.9 \text{ km s}^{-1}$ distributed around the western half of the SNRC, which belongs to the $+29.9 \text{ km s}^{-1}$ broad line component. No good spatial correlation is found between the SNRC and the -3.0 km s^{-1} component. Based on these evidences, the SNRC is probably associated with the $+11.8 \text{ km s}^{-1}$ component, or may be associated with the $+29.9 \text{ km s}^{-1}$ component. Kinematic distances are estimated as $1.25 \pm 0.05 \text{ kpc}$ for the $+11.8 \text{ km s}^{-1}$ component and $2.9 \pm 0.3 \text{ kpc}$ for the $+29.9 \text{ km s}^{-1}$ component.

G13.10-0.50: The southeast of this SNRC overlaps with SNR G13.3-1.3. There are several broad line components identified in the SNRC. Nevertheless, there is only one broad line at both $+53.5$ and $+56.5 \text{ km s}^{-1}$, which are probably originated from the nearby $+50.6 \text{ km s}^{-1}$ component. Molecular gas at a peak of the SCC at $\sim +53.3 \text{ km s}^{-1}$ is surrounding the bright radio continuum shell of the SNRC in the north, which belongs to the $+50.6 \text{ km s}^{-1}$ broad line component. Both the kinematic evidence and the spatial correlation result indicate that the SNRC is associated with the $+50.6 \text{ km s}^{-1}$ component. The corresponding kinematic distance is estimated as $3.9 \pm 0.3 \text{ kpc}$. At the peak of the SCC at $\sim +18.4 \text{ km s}^{-1}$, there are molecular clumps distributed around the eastern and southern boundaries of the SNRC. It belongs to the $+19.9 \text{ km s}^{-1}$ velocity component, with only one broad line identified in the south. The $+19.9 \text{ km s}^{-1}$ component and the SNRC do not seem to be associated. We find no spatial correlation between the SNRC and other broad line components.

G13.50+0.07: This SNRC is a plerion type. We find no good spatial correlation result for the SNRC, because of its small size. We also identify no broad line in it by full criteria. Based on our observation, we cannot determine if the SNRC is associated with an MC.

G13.55+0.35, G13.63+0.30, and G13.65+0.26: SNRCs G13.55+0.35 and G13.65+0.26 overlap with SNRC G13.63+0.30. Several broad line components are identified in SNRC G13.55+0.35 by full criteria. As indicated by the SCC, molecular gas at $\sim +9.4 \text{ km s}^{-1}$ that belongs to the $+16.9 \text{ km s}^{-1}$ broad line component is spatially correlated with the SNRC, which is roughly surrounding the southwestern radio continuum shell of the SNRC. No good spatial correlation is found between the SNRC and other broad line components. Therefore, SNRC G13.55+0.35 is probably associated with the $+16.9 \text{ km s}^{-1}$ component, with the corresponding kinematic distance estimated as $1.8 \pm 0.1 \text{ kpc}$. For SNRC G13.63+0.30, only one broad line component at $+22.2 \text{ km s}^{-1}$ is identified in it. The $+22.2 \text{ km s}^{-1}$ component is also spatially correlated with the SNRC, as indicated by the SCC, of which molecular gas is roughly surrounding the SNRC. We suggest that SNRC G13.63+0.30 is associated with the $+22.2 \text{ km s}^{-1}$ component, and its kinematic distance can be estimated as $3.0 \pm 0.4 \text{ kpc}$. For SNRC G13.65+0.26, no broad line is identified in it by full criteria. As indicated by the SCC, molecular gas at $\sim +26.2 \text{ km s}^{-1}$ is distributed around the southeastern boundary of the SNRC, which belongs to the $+25.1 \text{ km s}^{-1}$ component with broad line candidates identified by partial criteria. SNRC G13.65+0.26 may be associated with the $+25.1 \text{ km s}^{-1}$ component, of which the kinematic distance is estimated as $3.0 \pm 0.4 \text{ kpc}$. SNRCs G13.63+0.30 and G13.65+0.26 may be in the same neighborhood, but SNRC G13.55+0.35 is not likely.

G13.66-0.24: There are multiple broad line components identified in this SNRC. Broad lines at $+43.5$ and $+50.1 \text{ km s}^{-1}$ can be attributed to the nearby prominent component at $+43.2 \text{ km s}^{-1}$. Some broad lines at

other velocities are probably originated from an overlapped H II region in the east. As indicated by the SCC, only the $+43.2 \text{ km s}^{-1}$ broad line component shows some spatial correlations with the SNRC, of which molecular gas is roughly surrounding the SNRC. The kinematic evidence and the spatial correlation result indicate that the SNRC is associated with the $+43.2 \text{ km s}^{-1}$ component. The corresponding kinematic distance is estimated as $3.9 \pm 0.3 \text{ kpc}$.

G14.52+0.14: This SNRC presents bright radio continuum emission in the southeast and shell-like radio continuum emission around its southern half. Several broad line components are identified in this SNRC. Three of them at velocities of $+26.2$, $+38.2$, and $+136.0 \text{ km s}^{-1}$ show some spatial correlations with the SNRC. The $+26.2 \text{ km s}^{-1}$ component is with some molecular clumps distributed around the northeastern boundary of the SNRC. Molecular gas at $\sim +53.0 \text{ km s}^{-1}$ that probably belongs to the $+38.2 \text{ km s}^{-1}$ component is roughly surrounding the south of the SNRC. Molecular gas of the $+136.0 \text{ km s}^{-1}$ component is roughly surrounding the southeast of the SNRC. Any of these three components may be associated with the SNRC. The near and far kinematic distances of the $+26.2 \text{ km s}^{-1}$ component are estimated as 3.0 ± 0.4 and $13.3 \pm 0.3 \text{ kpc}$, respectively. Kinematic distances of the $+38.2$ and $+136.0 \text{ km s}^{-1}$ components are estimated as 3.9 ± 0.3 and $7.9 \pm 1.9 \text{ kpc}$, respectively.

G15.51-0.15: Only one broad line component at $+50.6 \text{ km s}^{-1}$ is identified in this SNRC. At a peak of the SCC at $\sim +58.3 \text{ km s}^{-1}$, molecular gas is roughly surrounding the SNRC, which supports the association between the SNRC and the $+50.6 \text{ km s}^{-1}$ broad line component. Therefore, we suggest that the SNRC is associated with the $+50.6 \text{ km s}^{-1}$ component with the corresponding kinematic distance estimated as $3.9 \pm 0.3 \text{ kpc}$.

G15.86+0.52, G16.02+0.75, and G16.13+0.69: Both SNRCs G15.86+0.52 and G16.02+0.75 overlap with SNRC G16.13+0.69. No broad line is identified in SNRC G15.86+0.52 even by partial criteria. Molecular gas at a nonsignificant peak of the SCC at $\sim +33.2 \text{ km s}^{-1}$ is distributed around the eastern boundary of it but not well correlated. For SNRC G16.02+0.75, two broad line components are identified in it. As indicated by the SCC, molecular gases at $\sim +15.7$ and $\sim +27.5 \text{ km s}^{-1}$ show spatial correlation with it. Molecular gas at $\sim +15.7 \text{ km s}^{-1}$ is surrounding its southern half, which belongs to the $+14.6 \text{ km s}^{-1}$ component with a broad line candidate identified in the SNRC by partial criteria. Molecular gas at $\sim +27.5 \text{ km s}^{-1}$ is surrounding its east and south, which belongs to the $+30.1 \text{ km s}^{-1}$ broad line component. The other broad line component at $+42.7 \text{ km s}^{-1}$ shows no spatial correlation with the SNRC. Therefore, SNRC G16.02+0.75 may be associated with the $+14.6$ or $+30.1 \text{ km s}^{-1}$ components, of which corresponding kinematic distances are estimated as 1.4 ± 0.3 and $1.50 \pm 0.04 \text{ kpc}$. Kinematic distances of both velocity components are consistent, both of which are probably located at the near side of the Sagittarius spiral arm. SNRC G16.13+0.69 is large, and its radio continuum emission is weak. Several broad line components are identified in it. As indicated by the SCC, the $+19.9$ and $+52.6 \text{ km s}^{-1}$ broad line components show some spatial correlations with the SNRC. Molecular gas at $\sim +23.5 \text{ km s}^{-1}$ is roughly surrounding the north of the SNRC, and some molecular clumps at $\sim +50.2 \text{ km s}^{-1}$ are distributed around the boundary of the SNRC's southern half. When using full criteria plus the clean subbackground region condition, two broad line components at $+27.6$ and $+36.4 \text{ km s}^{-1}$ are identified in the SNRC. The $+27.6 \text{ km s}^{-1}$ component has substantial molecular gas distributed in the remnant, which seems not correlated with the remnant. The $+36.4 \text{ km s}^{-1}$ component has a shell-like structure surrounding the southeastern boundary of the remnant, nevertheless, it also has molecular gas distributed in the SNRC. Note that some molecular gases of the $+52.6 \text{ km s}^{-1}$ component seems to originate from the $+36.4 \text{ km s}^{-1}$ component. These spatial correlation results are undetermined, since the weak radio continuum emission of the SNRC has no clear spatial structure. The $+19.9$, $+36.4$, or $+52.6 \text{ km s}^{-1}$ components may be associated with SNRC G16.13+0.69, and their kinematic distances are estimated as 1.8 ± 0.1 , 3.3 ± 0.9 , and $3.6 \pm 0.4 \text{ kpc}$, respectively.

G16.36-0.18: We identify no broad line in this SNRC by full criteria. We also find no good spatial correlation result for the SNRC, because of its small size.

G16.96-0.93: Broad lines are identified in this SNRC at $+40.3$ and $+45.0 \text{ km s}^{-1}$. Broad lines at $+40.3 \text{ km s}^{-1}$ are probably originated from the nearby $+45.0 \text{ km s}^{-1}$ component. Molecular gas at a peak of the SCC at $\sim +28.6 \text{ km s}^{-1}$ is distributed along the southern radio continuum shell of the SNRC, which probably originated from the $+45.0 \text{ km s}^{-1}$ component. Based on these evidences, we suggest that the SNRC is associated with the $+45.0 \text{ km s}^{-1}$ component, and its kinematic distance can be estimated as $3.3 \pm 0.3 \text{ kpc}$.

G17.34-0.14: No broad line is identified in this SNRC by full criteria. Only one broad line candidate at -8.7 km s^{-1} is identified in it by partial criteria, which is probably originated from an overlapped H II region. We also find no good spatial correlation result for the SNRC because of its small size.

G17.43+0.27: No broad line is identified in this SNRC by full criteria. The SCC peaks at $\sim +21.7 \text{ km s}^{-1}$, where molecular gas is roughly surrounding the northeast of the SNRC; however, no corresponding broad line candidate is identified even by partial criteria.

G17.59+0.24: No broad line is identified in this SNRC by full criteria. The SNRC is a bit small, nevertheless, possible spatial correlations are found between it and molecular gas at $\sim +21.3$ and $\sim +46.2 \text{ km s}^{-1}$, both of

which are roughly surrounding the south and east of the SNRC. They belong to the $+24.4$ and $+46.5$ km s^{-1} components, respectively, which are with broad line candidates identified in the SNRC by partial criteria. The SNRC may be associated with the $+24.4$ or $+46.5$ km s^{-1} components, of which kinematic distances are estimated as 1.50 ± 0.05 and 3.2 ± 0.3 kpc, respectively.

G17.62+0.09: This SNRC presents shell-like radio continuum emission in the west, and it overlaps multiple H II regions around $+17$ km s^{-1} . Several broad line components are identified in the SNRC. As indicated by the SCC, only the $+16.9$ km s^{-1} broad line component is spatially correlated with the radio continuum shell of the SNRC, of which molecular gas at $\sim +20.6$ km s^{-1} is roughly surrounding the west half of it. These evidences indicate that the SNRC is associated with the $+16.9$ km s^{-1} component, hence, associated with overlapped H II regions. The corresponding near and far kinematic distances are estimated as 1.5 ± 0.1 and 13.3 ± 0.4 kpc, respectively.

G17.80-0.02: Several broad line components are identified in this SNRC. As indicated by the SCC, molecular gas at $\sim +35.2$ km s^{-1} , belonging to the $+47.0$ km s^{-1} broad line component, presents a cavity-like structure around the SNRC. No spatial correlation is found for other broad line components. These evidences indicate that the SNRC is associated with the $+47.0$ km s^{-1} component, and the corresponding near and far kinematic distances are estimated as 4.0 ± 0.4 and 12.0 ± 0.3 kpc, respectively.

G18.39-0.82 and G18.53-0.86: These two SNRC overlap each other. Broad lines are identified in SNRC G18.39-0.82 at $+48.8$ and $+51.6$ km s^{-1} . Broad lines at $+51.6$ km s^{-1} can be attributed to the nearby component at $+48.8$ km s^{-1} . Molecular gas at a minor peak of the SCC at $\sim +61.7$ km s^{-1} is surrounding the northern half of the SNRC, which belongs to the $+48.8$ km s^{-1} broad line component. Based on these evidences, SNRC G18.39-0.82 is probably associated with the $+48.8$ km s^{-1} component, with the corresponding kinematic distance estimated as 3.3 ± 0.3 kpc. SNRC G18.53-0.86 presents bright shell-like radio continuum emission in the southeast. Three broad line components are identified in this SNRC. However, broad line points at $+48.8$ and $+51.6$ km s^{-1} are in the overlapping region with SNRC G18.39-0.82, all of which are probably originated from the $+48.8$ km s^{-1} component. As indicated by the SCC, molecular gas at $\sim +39.7$ km s^{-1} is distributed around the SNRC, but not well correlated with its radio continuum shell. It belongs to the $+48.8$ km s^{-1} broad line component. Moreover, molecular gas at $\sim +71.7$ km s^{-1} , belonging to the $+65.6$ km s^{-1} broad line component, is surrounding the northeast of the SNRC. SNRC G18.53-0.86 may be associated with either the $+48.8$ or $+65.6$ km s^{-1} components. Kinematic distances are estimated as 3.3 ± 0.3 kpc for the $+48.8$ km s^{-1} component and 3.9 ± 0.4 kpc for the $+65.6$ km s^{-1} component.

G19.1-3.1: Only one broad line component at $+6.0$ km s^{-1} is identified in this SNRC. Molecular gas at the peak of the SCC at $\sim +8.3$ km s^{-1} is surrounding the eastern half of the SNRC, which belongs to the $+6.0$ km s^{-1} component. These evidences indicate that the SNRC is associated with the $+6.0$ km s^{-1} component, and the corresponding kinematic distance is estimated as 0.25 ± 0.14 kpc.

G19.48-0.11: We identify several broad line components in this SNRC even by full criteria plus the clean sub-background region condition. Molecular gas at a nonsignificant peak of the SCC at $\sim +72.9$ km s^{-1} is roughly surrounding the SNRC, which belongs to the $+66.6$ km s^{-1} broad line component. Moreover, molecular gas at $\sim +32.1$ km s^{-1} is also distributed around the boundary of the SNRC, which belongs to the $+26.1$ km s^{-1} broad line component. The SNRC may be associated with either the $+26.1$ or $+66.6$ km s^{-1} components. The near and far kinematic distances of the $+26.1$ km s^{-1} component are estimated as 1.5 ± 0.05 and 11.8 ± 0.3 kpc, respectively. The kinematic distance of the $+66.6$ km s^{-1} component is estimated as 4.1 ± 0.5 kpc.

G19.7-0.7: Two broad line components at $+44.0$ and $+64.6$ km s^{-1} are identified in this SNRC. As indicated by the SCC, molecular gas at $\sim +67.1$ km s^{-1} is distributed around the SNRC but not correlated well. No good spatial correlation is found between the SNRC and the $+44.0$ km s^{-1} broad line component. These evidences indicate a possible association between the SNRC and the $+64.6$ km s^{-1} component, of which the kinematic distance is estimated as 4.1 ± 0.4 kpc.

G19.75+0.20: Several broad line components are identified in this SNRC. A broad line at $+108.9$ km s^{-1} can be attributed to the nearby prominent component at $+123.5$ km s^{-1} . Molecular gas at the peak of the SCC at $\sim +109.8$ km s^{-1} is roughly surrounding the southeast of the SNRC. In addition, molecular gas at $\sim +125.4$ km s^{-1} is roughly surrounding the southwest of the SNRC. These molecular gases belong to the $+123.5$ km s^{-1} broad line component. The SNRC may be associated with the $+123.5$ km s^{-1} component with the corresponding kinematic distance estimated as 9.4 ± 0.4 kpc.

G19.96-0.33: The north of this SNRC overlaps with SNR G20.0-0.2, and the east of it overlaps with an H II region at $+67.3$ km s^{-1} . Three broad line components are identified in the SNRC. Only one broad line is identified at $+57.5$ km s^{-1} , which is probably originated from the nearby prominent component at $+65.8$ km s^{-1} . The SCC indicates a spatial correlation between the SNRC and the $+65.8$ km s^{-1} broad line component, of which molecular gas at $\sim +58.3$ km s^{-1} is roughly surrounding the SNRC. No spatial correlation is found between the SNRC and the $+28.9$ km s^{-1} broad line component. Therefore, we suggest that the SNRC is associated with

the $+65.8 \text{ km s}^{-1}$ MC, and the kinematic distance can be estimated as $4.0 \pm 0.6 \text{ kpc}$. SNRC G19.96-0.33, SNR G20.0-0.2, and the overlapped H II region are probably in the same neighborhood.

G20.20+0.03: Three broad line components are identified in this SNRC. However, only one broad line is identified at $+71.1 \text{ km s}^{-1}$, which can be attributed to the nearby prominent component at $+77.5 \text{ km s}^{-1}$. As indicated by the SCC, the $+77.5 \text{ km s}^{-1}$ broad line component is spatially correlated with the SNRC, of which molecular gas at $\sim +64.8 \text{ km s}^{-1}$ is roughly surrounding the whole SNRC except for its southeast side. The $+25.6 \text{ km s}^{-1}$ broad line component shows no spatial correlation with the SNRC. These evidences indicate that the SNRC is associated with the $+77.5 \text{ km s}^{-1}$ component, and its kinematic distance can be estimated as $4.4 \pm 0.5 \text{ kpc}$.

G20.26-0.86: Among three broad line components identified in this SNRC, only that at $+40.0 \text{ km s}^{-1}$ shows some spatial correlations with the SNRC. Molecular gas at the peak of the SCC at $\sim +48.7 \text{ km s}^{-1}$ is distributed around the SNRC. Therefore, we suggest that the SNRC is associated with the $+40.0 \text{ km s}^{-1}$ component with the corresponding kinematic distance estimated as $3.3 \pm 0.3 \text{ kpc}$.

G20.30-0.06: Two broad line components are identified in this SNRC. No significant spatial correlation result is found. Molecular gas of the $+50.5 \text{ km s}^{-1}$ broad line component is distributed around the northeastern and southwestern boundaries of the SNRC, and molecular gas of the $+73.2 \text{ km s}^{-1}$ broad line component is mostly distributed in the eastern half of it. The SNRC may be associated with either the $+50.5$ or $+73.2 \text{ km s}^{-1}$ components. Kinematic distances are estimated as $4.2 \pm 0.5 \text{ kpc}$ for the $+50.5 \text{ km s}^{-1}$ component and $4.4 \pm 0.4 \text{ kpc}$ for the $+73.2 \text{ km s}^{-1}$ component. Both components are probably located at the near side of the Norma spiral arm.

G21.49-0.01 and G21.60-0.18: A small part of SNRC G21.49-0.01 overlaps with the northwest of SNRC G21.60-0.18. Several broad line components are identified in SNRC G21.49-0.01. As indicated by the SCC, the $+67.2$ and $+91.2 \text{ km s}^{-1}$ broad line components show some spatial correlations with the SNRC. Molecular gas at $\sim +72.1 \text{ km s}^{-1}$ belonging to the $+67.2 \text{ km s}^{-1}$ component is surrounding the northwest and southeast of the SNRC, and molecular gases at $\sim +91.6$ and $\sim +102.5 \text{ km s}^{-1}$ belonging to the $+91.2 \text{ km s}^{-1}$ component are roughly surrounding the north and southeast of the SNRC, respectively. The $+91.2 \text{ km s}^{-1}$ component is also with broad lines identified by full criteria plus the clean subbackground region condition. SNRC G21.49-0.01 may be associated with either the $+67.2$ or $+91.2 \text{ km s}^{-1}$ components. The kinematic distance of the $+67.2 \text{ km s}^{-1}$ component is estimated as $4.7 \pm 0.4 \text{ kpc}$, and the near and far kinematic distances of the $+91.2 \text{ km s}^{-1}$ component are estimated as 4.6 ± 0.6 and $8.7 \pm 2.3 \text{ kpc}$, respectively. For SNRC G21.60-0.18, multiple broad line components are identified in it by full criteria. Broad lines at $+61.3$ and $+93.3 \text{ km s}^{-1}$ are probably originated from the nearby prominent components at $+69.7$ and $+85.0 \text{ km s}^{-1}$, respectively. When using full criteria plus the clean subbackground region condition, only one broad line at $+69.7 \text{ km s}^{-1}$ is identified in the SNRC. Shell-like radio continuum emission is present in the southeastern half of the SNRC. Molecular gas of the $+45.3 \text{ km s}^{-1}$ broad line component is surrounding the southeastern half of the SNRC, which shows good spatial correlation with its radio continuum shell. Molecular clumps of the $+85.0 \text{ km s}^{-1}$ broad line component are also distributed around the southeastern boundary of the SNRC. SNRC G21.60-0.18 may be associated with either the $+45.3$ or $+85.0 \text{ km s}^{-1}$ components. Kinematic distances are estimated as $3.3 \pm 0.4 \text{ kpc}$ for the $+45.3 \text{ km s}^{-1}$ component and $4.6 \pm 0.5 \text{ kpc}$ for the $+85.0 \text{ km s}^{-1}$ component. Note that molecular gases of the $+6.1$ and $+69.7 \text{ km s}^{-1}$ broad line components are not spatially correlated with the radio continuum shell of the SNRC; however, some molecular gases of them at minor peaks of the SCC are distributed around the SNRC. The association between SNRC G21.60-0.18 and either of these two components is not totally ruled out. Kinematic distances of the $+6.1$ and $+69.7 \text{ km s}^{-1}$ components are estimated as 15.0 ± 0.4 and $4.6 \pm 0.5 \text{ kpc}$, respectively.

G21.68+0.13: Several broad line components are identified in this SNRC. As indicated by the SCC, molecular gas at $\sim +76.0 \text{ km s}^{-1}$ is surrounding the south of the SNRC and is also distributed around its northern boundary, which belongs to the $+78.2 \text{ km s}^{-1}$ broad line component. The $+113.7 \text{ km s}^{-1}$ broad line component also shows some spatial correlations with the SNRC, with molecular gas at $\sim +108.6 \text{ km s}^{-1}$ roughly surrounding its east and molecular gas at $\sim +112.1 \text{ km s}^{-1}$ distributed around its northern boundary. The SNRC may be associated with either the $+78.2$ or $+113.7 \text{ km s}^{-1}$ components. Their kinematic distances are estimated as 4.7 ± 0.4 and $8.0 \pm 1.3 \text{ kpc}$, respectively.

G21.8-3.0: No broad line is identified in this SNRC by full criteria. The SCC indicates that molecular gas at $\sim +6.7 \text{ km s}^{-1}$ is distributed around the SNRC, mostly around its western half, which belongs to the $+3.2 \text{ km s}^{-1}$ component with broad lines identified in the SNRC by partial criteria. The SNRC may be associated with the $+3.2 \text{ km s}^{-1}$ component with the corresponding kinematic distance estimated as $0.24 \pm 0.13 \text{ kpc}$.

G21.86+0.17: Several broad line components are identified in this SNRC. As indicated by the SCC, molecular gas of the $+47.8 \text{ km s}^{-1}$ broad line component is roughly surrounding the east and south of the SNRC, where a partial radio continuum shell is present. Therefore, we suggest that the SNRC is associated with the $+47.8 \text{ km s}^{-1}$ component, of which the kinematic distance can be estimated as $3.3 \pm 0.4 \text{ kpc}$.

G22.05-0.03: We identify two broad components in this SNRC at $+74.6$ and $+91.7$ km s^{-1} . Both broad line components have molecular gases roughly distributed around the SNRC. The SNRC may be associated with the $+74.6$ or $+91.7$ km s^{-1} components, of which kinematic distances are estimated 4.7 ± 0.4 and 4.7 ± 0.5 kpc, respectively. Both of the two components are probably located at the near side of the Norma spiral arm.

G22.18+0.31 and G22.32+0.11: These two SNRCs are adjacent to each other. SNRC G22.18+0.31 is relatively large, and its radio continuum emission is weak. We identify multiple broad line components in it by full criteria. Broad lines at $+13.3$ km s^{-1} are probably originated from the nearby prominent component at $+7.0$ km s^{-1} . Three broad line components, i.e. at $+7.0$, $+54.6$, and $+85.2$ km s^{-1} , are with molecular gases roughly surrounding parts of the SNRC. The $+85.2$ km s^{-1} component is also with one broad line identified in the SNRC by full criteria plus the clean subbackground region condition. Any of these three components may be associated with SNRC G22.18+0.31. Kinematic distances are estimated as 15.0 ± 0.4 , 3.3 ± 0.4 , and 4.7 ± 0.5 kpc, respectively. For SNRC G22.32+0.11, we identify multiple broad line components in it by full criteria too. Only one broad line is identified at $+55.1$ km s^{-1} , which is probably originated from the nearby $+50.3$ km s^{-1} component. The $+50.3$ km s^{-1} component also has a broad line identified in the SNRC by full criteria plus the clean subbackground region condition. As indicated by the SCC, both the $+15.8$ and $+50.3$ km s^{-1} components are with molecular gases roughly surrounding parts of the SNRC. SNRC G22.32+0.11 may be associated with the $+15.8$ or $+50.3$ km s^{-1} components. Their kinematic distances are estimated as 1.5 ± 0.04 and 3.3 ± 0.4 kpc, respectively.

G22.95-0.31: Two broad line components are identified in this SNRC at $+31.5$ and $+75.1$ km s^{-1} . As indicated by the SCC, only the $+75.1$ km s^{-1} broad line component shows some spatial correlations with the SNRC, of which molecular gas is roughly surrounding the SNRC. Therefore, we suggest that the SNRC is associated with the $+75.1$ km s^{-1} component with the kinematic distance estimated as 4.8 ± 0.5 kpc.

G23.1+0.1: There are several H II regions adjacent to this SNRC at velocities of about $+78$, $+90$, and $+108$ km s^{-1} . We identify multiple broad line components in the SNRC by full criteria. However, only the $+92.7$ km s^{-1} component is with broad lines identified in the SNRC by full criteria plus the clean subbackground region condition. Broad lines at $+75.1$ km s^{-1} have wide velocity ranges, which can be attributed to nearby prominent component at $+92.7$ km s^{-1} . Kinematic distances estimated for the $+75.1$ and $+92.7$ km s^{-1} components are consistent. Some broad lines at $+105.6$ km s^{-1} are probably originated from the $+92.7$ km s^{-1} component too. The SCC indicates a spatial correlation between the SNRC and molecular gas at $\sim +83.5$ km s^{-1} , which is roughly surrounding radio continuum bright parts of the SNRC, i.e. the southeastern half and northwest. It supports the association between the SNRC and the $+92.7$ km s^{-1} component. The SNRC is probably associated with the $+92.7$ km s^{-1} component. However, the $+4.8$ and $+65.1$ km s^{-1} broad line components also show some spatial correlations with the SNRC, of which molecular gases are roughly surrounding the south of it. It is also possible that the SNRC is associated with the $+4.8$ or $+65.1$ km s^{-1} components. The kinematic distance estimated for the $+92.7$ km s^{-1} component is 5.1 ± 0.6 kpc. For the $+4.8$ and $+65.1$ km s^{-1} components, kinematic distances are estimated as 15.0 ± 0.4 and 4.9 ± 0.5 kpc, respectively.

G23.85-0.18 and G24.0-0.3: These two SNRCs overlap each other. SNRC G24.0-0.3 is much larger than SNRC G23.85-0.18. Two broad line components are identified in SNRC G23.85-0.18 at $+44.8$ and $+57.3$ km s^{-1} . As indicated by the SCC, both show some spatial correlations with the SNRC. Molecular gas of the $+44.8$ km s^{-1} component is roughly surrounding the north and south of the SNRC, and molecular gas of the $+57.3$ km s^{-1} component roughly surrounding the east of it. SNRC G23.85-0.18 may be associated with the $+44.8$ or $+57.3$ km s^{-1} components. Their kinematic distances are estimated as 3.7 ± 0.4 and 3.5 ± 0.4 kpc, respectively, which are consistent. Both of the two components are probably located at the near side of the Scutum spiral arm. SNRC G24.0-0.3 presents shell-like radio continuum emission in its northern half. There are multiple broad line components identified in this SNRC by full criteria. The $+55.3$ km s^{-1} broad line component presents a bubble-like structure with inward protrusions, which has the same center as the SNRC but has a smaller radius. In addition, the $+55.3$ km s^{-1} component is also with a broad line identified by full criteria plus the clean subbackground region condition. Molecular gas at a minor peak of the SCC at $\sim +110.6$ km s^{-1} also shows a spatial correlation with the SNRC, which is roughly surrounding the bright radio continuum shell in the northeast. It belongs to the $+111.6$ km s^{-1} broad line component. We find no good spatial correlation between the SNRC and other broad line components. Therefore, SNRC G24.0-0.3 may be associated with the $+55.3$ or $+111.6$ km s^{-1} components. Their kinematic distances are estimated as 3.6 ± 0.4 and 7.1 ± 0.9 kpc, respectively.

G23.97+0.51: Three broad line components are identified in this SNRC at $+94.5$, $+110.1$, and $+110.3$ km s^{-1} . Only one broad line is identified at $+110.3$ km s^{-1} , which can be attributed to the nearby $+110.1$ km s^{-1} component. As indicated by the SCC, both the $+94.5$ and $+110.1$ km s^{-1} components show some spatial correlations with the SNRC. Molecular gas at $\sim +99.4$ km s^{-1} is distributed around the northern boundary of the SNRC, and molecular gas at $\sim +106.2$ km s^{-1} is roughly surrounding the south of it. Therefore, the SNRC may be associated with the $+94.5$ or $+110.1$ km s^{-1} components. The near and far kinematic distances of the

+94.5 km s⁻¹ component are estimated as 5.2±0.7 and 7.7±2.2 kpc, respectively. The kinematic distance of the +110.1 km s⁻¹ component is estimated as 6.2±1.1 kpc.

G24.06-0.81: This SNRC is small, and classified as the plerion type. We find no good spatial correlation result, and identify no broad line in it by full criteria.

G24.19+0.28: We identify two broad line components in this SNRC at +50.8 and +114.1 km s⁻¹. As indicated by the SCC, molecular gas at ~+115.9 km s⁻¹ belonging to the +114.1 km s⁻¹ component is roughly surrounding the south of the SNRC. No good spatial correlation is found between the SNRC and the +50.8 km s⁻¹ component. Therefore, we suggest that the SNRC is associated with the +114.1 km s⁻¹ component, and its kinematic distance can be estimated as 6.9±1.1 kpc.

G25.49+0.01: Multiple broad line components are identified in this SNRC. As indicated by the SCC, molecular gases at ~+55.1 and ~+94.0 km s⁻¹ are distributed around the SNRC, which belong to the +54.3 and +94.5 km s⁻¹ broad line components, respectively. These evidences indicate that the SNRC may be associated with the +54.3 or +94.5 km s⁻¹ components. The near and far kinematic distances of the +54.3 km s⁻¹ component are estimated as 3.8±0.5 and 11.1±0.3 kpc, respectively. For the +94.5 km s⁻¹ component, the near and far kinematic distances are estimated as 5.7±0.8 and 8.9±0.4 kpc, respectively.

G26.04-0.42: Several broad line components are identified in this SNRC. Broad lines at +93.5 and +112.7 km s⁻¹ are probably originated from the nearby prominent component at +104.6 km s⁻¹. Their kinematic distance estimation results are also consistent, all at the near side of the Norma spiral arm. Only the +104.6 km s⁻¹ component shows some spatial correlations with the SNRC, with molecular gases distributed around the northern boundary of it. Therefore, we suggest that the SNRC is associated with the +104.6 km s⁻¹ component, accordingly, its kinematic distance can be estimated as 5.6±0.6 kpc.

G26.13+0.13: This SNRC overlaps with multiple H II regions, and many broad line components are identified in it by full criteria. When using full criteria plus the clean subbackground region condition, two broad lines at +70.7 and +97.1 km s⁻¹ are identified in the SNRC by full criteria plus the clean subbackground region condition. Molecular gas at ~+102.2 km s⁻¹ belonging to the +97.1 km s⁻¹ component presents a shell-like structure surrounding the southeastern radio continuum shell of the SNRC, which also has some inward protrusions. Based on these evidences, we suggest that the SNRC is associated with the +97.1 km s⁻¹ component, of which the near and far kinematic distances are estimated as 5.8±0.6 and 8.8±0.4 kpc, respectively.

G26.53+0.07: We consider SNRC G26.6-0.1 as a southeastern part of SNRC G26.53+0.07. This SNRC presents bright shell-like radio continuum emission in its eastern half. We identify many broad lines in the SNRC by full criteria. Only one broad line is identified at +113.2 km s⁻¹, which can be attributed to the nearby +103.1 km s⁻¹ component. When using full criteria plus the clean subbackground region condition, the +34.5 and +103.1 km s⁻¹ components each have a broad line identified in the SNRC. The SCC indicates a spatial correlation between the SNRC and the +103.1 km s⁻¹ component, of which molecular gas is distributed around the SNRC. The +34.5 km s⁻¹ broad line component also shows a spatial correlation with the SNRC, with molecular gas roughly surrounding the northeast of it and a molecular clump located in the southeast of the SNRC. No spatial correlation is found for other broad line components. Based on these evidences, the SNRC is probably associated with the +103.1 km s⁻¹ component, or may be associated with the +34.5 km s⁻¹ component. Kinematic distances are estimated as 6.1±0.6 and 8.7±0.4 kpc for the +103.1 km s⁻¹ component, and 12.5±0.3 for the +34.5 km s⁻¹ component.

G26.75+0.73: Radio continuum emission of this SNRC is bright in the north. We identify only one broad line component in the SNRC at +86.5 km s⁻¹. As indicated by the SCC, molecular gas at ~+89.2 km s⁻¹ is distributed around the southern boundary and a small section of the northern boundary. It supports the association between the SNRC and the +86.5 km s⁻¹ broad line component. Note that molecular gas at the peak of the SCC at ~+46.7 km s⁻¹ is roughly surrounding the north of the SNRC; however, no corresponding broad line is identified even by partial criteria. Based on these evidences, we suggest that the SNRC is associated with the +86.5 km s⁻¹ component with the near and far kinematic distances estimated as 4.5±0.5 and 7.9±2.4 kpc, respectively.

G27.06+0.04: This SNRC presents a bright radio continuum shell in the east, and some weak radio continuum emission in the west. Multiple broad line components are identified in the SNRC. As indicated by the SCC, the +63.3 km s⁻¹ component is spatially correlated with the SNRC well. Molecular gas at ~+66.7 km s⁻¹ is surrounding the eastern radio continuum shell and distributed around the southern and western boundaries. Molecular gas at ~+61.0 km s⁻¹ is distributed along the southwestern boundary of the SNRC, and there is also a half cavity-like structure around the east of the SNRC in large scale. No good spatial correlation result is found for other broad line components. Therefore, we suggest that the SNRC is associated with the +63.3 km s⁻¹ component. Johanson & Kerton (2009) showed H I absorption up to the tangent point, indicating that the SNR is at the far side of the tangent point. The far kinematic distance of the +63.3 km s⁻¹ component is estimated as 10.9±0.4 kpc.

G27.18+0.30: This SNRC is small, and has diffuse and elongated radio continuum emission. Only one broad line is identified in the SNRC at $+73.1 \text{ km s}^{-1}$. As indicated by the SCC, the $+73.1 \text{ km s}^{-1}$ component shows a minor spatial correlation with the SNRC, of which molecular gas is roughly surrounding the east of it. Therefore, the SNRC is probably associated with the $+73.1 \text{ km s}^{-1}$ component, of which the kinematic distance is estimated as $4.3 \pm 0.3 \text{ kpc}$.

G27.78-0.33: This SNRC presents a bright radio continuum shell in the northeast. Two broad line components are identified in this SNRC at $+45.8$ and $+88.5 \text{ km s}^{-1}$. The $+45.8 \text{ km s}^{-1}$ component shows good spatial correlation with the SNRC. Molecular gas at $\sim +42.7 \text{ km s}^{-1}$ is surrounding the northeastern radio continuum shell of the SNRC, and molecular gas at $\sim +45.1 \text{ km s}^{-1}$ is roughly surrounding the whole SNRC. These evidences strongly support the association between the SNRC and the $+45.8 \text{ km s}^{-1}$ component. Nevertheless, the $+88.5 \text{ km s}^{-1}$ component also shows minor spatial correlation with the SNRC, of which molecular gas at $\sim +93.8 \text{ km s}^{-1}$ is roughly surrounding the northeastern radio continuum shell of it. It is also possible that the SNRC is associated with the $+88.5 \text{ km s}^{-1}$ component. The kinematic distance of the $+45.8 \text{ km s}^{-1}$ component is estimated as $4.1 \pm 0.7 \text{ kpc}$, and $4.4 \pm 0.4 \text{ kpc}$ for the $+88.5 \text{ km s}^{-1}$ component. With consistent distances estimated, both velocity components are probably located at the near side of the Scutum spiral arm.

G28.21+0.02: This SNRC is classified as the plerion type. The SCC indicates a good spatial correlation between the SNRC and molecular gas at $\sim +101.0 \text{ km s}^{-1}$, which is shell-like and surrounding the SNRC. It belongs to the $+98.8 \text{ km s}^{-1}$ component with broad lines identified in the SNRC by full criteria. These evidences indicate that the SNRC is associated with the $+98.8 \text{ km s}^{-1}$ component with the kinematic distance estimated as $8.2 \pm 0.5 \text{ kpc}$.

G28.22-0.09: This SNRC is a plerion type but uncertain. Since the SNRC is small, we find no significant spatial correlation result, and no broad line is identified in it by full criteria. Note that molecular gas at the peak of the SCC at $\sim +82.5 \text{ km s}^{-1}$ is roughly surrounding the southeast of the SNRC.

G28.3+0.2 and G28.33+0.06: These two SNRCs are adjacent to each other. SNRC G28.3+0.2 presents shell-like radio continuum emission in the southeast. Several broad line components are identified in this SNRC. We find that the SNRC is spatially correlated with the $+47.9 \text{ km s}^{-1}$ broad line component, of which molecular gas is distributed along the radio continuum shell. The SCC also indicates that molecular gases at $\sim +73.7$ and $\sim +106.0 \text{ km s}^{-1}$ are roughly surrounding the south of the SNRC, which belong to the $+80.0$ and $+97.8 \text{ km s}^{-1}$ broad line components, respectively. SNRC G28.3+0.2 is probably associated with the $+47.9 \text{ km s}^{-1}$ component; however, it may be associated with either the $+80.0$ or $+97.8 \text{ km s}^{-1}$ components too. Kinematic distances are estimated as $10.8 \pm 0.5 \text{ kpc}$ for the $+47.9 \text{ km s}^{-1}$ component, 4.4 ± 0.4 for the $+80.0 \text{ km s}^{-1}$ component, and 5.6 ± 0.9 or $8.2 \pm 0.5 \text{ kpc}$ for the $+97.8 \text{ km s}^{-1}$ component. SNRC G28.33+0.06 is classified as the plerion type. There are several H II regions located around this SNRC at velocities of about $+46$, $+76$, and $+81 \text{ km s}^{-1}$. Molecular gas at the peak of the SCC at $\sim +97.3 \text{ km s}^{-1}$ is distributed around the SNRC, which belongs to the $+100.6 \text{ km s}^{-1}$ component with broad lines identified in the SNRC by full criteria. SNRC G28.33+0.06 may be associated with the $+100.6 \text{ km s}^{-1}$ component with the near and kinematic distances estimated as 5.8 ± 0.9 and $8.2 \pm 0.5 \text{ kpc}$, respectively.

G28.56+0.00: This SNRC was considered to be related to a nearby H II region at $+96.6 \text{ km s}^{-1}$, based on their very similar H I absorption spectra (Ranasinghe et al. 2020). The east of the SNRC is adjacent to an H II region at $+43 \text{ km s}^{-1}$. Two broad line components are identified in this SNRC at $+43.3$ and $+75.7 \text{ km s}^{-1}$. As indicated by the SCC, both show some spatial correlations with the SNRC. Molecular gas at $\sim +34.8 \text{ km s}^{-1}$ is distributed around the northern boundary of the SNRC, and molecular gas at $\sim +70.6 \text{ km s}^{-1}$ is roughly surrounding the south of the SNRC. Since the SNRC is small, the spatial correlation result is indefinite. The SNRC may be associated with the $+43.3$ or $+75.7 \text{ km s}^{-1}$ components. The presence of H I absorption up to the tangent point shown by Ranasinghe et al. (2020) indicates that the SNR is at a far kinematic distance. The kinematic distance of the $+43.3 \text{ km s}^{-1}$ component is estimated as $10.8 \pm 0.4 \text{ kpc}$, and the far kinematic distance of the $+75.7 \text{ km s}^{-1}$ component is estimated as $8.2 \pm 0.6 \text{ kpc}$.

G28.52+0.27 and G28.64+0.20: These two SNRCs overlap each other. Several broad line components are identified in SNRC G28.52+0.27. As indicated by the SCC, two broad line components at $+82.2$ and $+100.3 \text{ km s}^{-1}$ show some spatial correlations with the SNRC. Molecular gas at $\sim +72.7 \text{ km s}^{-1}$ is roughly distributed around the SNRC, and molecular gas at $\sim +98.1 \text{ km s}^{-1}$ is roughly surrounding the south of the SNRC. SNRC G28.52+0.27 may be associated with the $+82.2$ or $+100.3 \text{ km s}^{-1}$ components. Kinematic distances of these two components are estimated as 4.4 ± 0.4 and $5.5 \pm 0.9 \text{ kpc}$, respectively. SNRC G28.64+0.20 is larger, and several broad line components are identified in it too. When using full criteria plus the clean subbackground region condition, broad lines are identified at $+81.2$ and $+104.4 \text{ km s}^{-1}$ in the SNRC. Three broad line components at $+52.1$, $+81.2$, and $+104.4 \text{ km s}^{-1}$ show roughly spatial correlations with the SNRC, of which molecular gases are distributed around the SNRC. SNRC G28.64+0.20 may be associated with any of these three components. As shown by Johanson & Kerton (2009), there is H I absorption up to the tangent

point, indicating that SNRC G28.64+0.20 is at a far kinematic distance. Far kinematic distances are estimated as 10.8 ± 0.5 kpc for the $+52.1$ km s^{-1} component, 8.1 ± 0.6 kpc for the $+81.2$ km s^{-1} component, and 8.1 ± 0.5 kpc for the $+104.4$ km s^{-1} component.

G28.7-0.4: Several broad line components are identified in this SNRC. Broad lines at $+81.9$ km s^{-1} are probably originated from the nearby prominent component at $+73.9$ km s^{-1} . As indicated by the SCC, molecular gas of the $+73.9$ km s^{-1} broad line component is distributed around the SNRC. These evidences indicate that the SNRC is associated with the $+73.9$ km s^{-1} component with the corresponding kinematic distance estimated as 4.3 ± 0.3 kpc.

G28.87+0.62: This SNRC is small. We find no good spatial correlation result for it, and identify no broad line in it by full criteria.

G28.88+0.24, G28.88+0.41, and G28.93+0.25: SNRC G28.93+0.25 is adjacent to the other two SNRCs, and SNRC G28.88+0.41 is also adjacent to SNRC G28.64+0.20. There are several H II regions at $\sim +108$ km s^{-1} located near the junction between SNRCs G28.88+0.41 and G28.64+0.20. Since SNRC G28.88+0.24 is small, we find no good spatial correlation result for it, and no broad line is identified in it by full criteria. SNRC G28.88+0.41 presents shell-like radio continuum emission in the southwest. Several broad line components are identified in it. Note that only one broad line is identified at $+73.7$ km s^{-1} , which can be attributed to the nearby prominent component at $+84.3$ km s^{-1} . As indicated by the SCC, molecular gas at $\sim +73.8$ km s^{-1} is surrounding the southwestern radio continuum shell of the SNRC. It supports the associated between the SNRC and the $+84.3$ km s^{-1} broad line component. The $+53.7$ and $+96.1$ km s^{-1} broad line components also have some molecular gases distributed around the radio continuum shell; however, they are not well spatially correlated with it. Therefore, we suggest that SNRC G28.88+0.41 is associated with the $+84.3$ km s^{-1} component with the corresponding kinematic distance estimated as 4.4 ± 0.5 kpc. For SNRC G28.93+0.25, we identify only one broad line at $+83.2$ km s^{-1} in it. Molecular gas of the $+83.2$ km s^{-1} component is mainly distributed in the northwestern half of the SNRC, where its radio continuum emission is bright; however, they are not spatially correlated well. If SNRC G28.93+0.25 is associated with the $+83.2$ km s^{-1} component, its kinematic distance can be estimated as 4.5 ± 0.4 kpc. SNRCs G28.88+0.41 and G28.93+0.25 may be related to each other and located at the near side of the Scutum spiral arm.

G29.33+0.28: Only one broad line is identified in this SNRC at $+91.5$ km s^{-1} . The SCC indicates that the broad line component is spatially correlated with the SNRC, with molecular gas at $\sim +95.7$ and $\sim +100.2$ km s^{-1} surrounding the southern half of the SNRC. The southern half of the SNRC is radio continuum bright. Based on these evidences, we suggest that the SNRC is associated with the $+91.5$ km s^{-1} component with the kinematic distance estimated as 4.7 ± 0.5 kpc.

G29.4+0.1: This SNRC presents bright filamentary radio continuum emission in its central region, and there is also a faint radio continuum shell in the southeast. Several broad line components are identified in this SNRC. Only one broad line is identified at $+97.8$ km s^{-1} , which can be attributed to the nearby prominent component at $+91.0$ km s^{-1} . When applying the additional clean subbackground region condition, only the $+80.4$ km s^{-1} component is with a broad line identified in the SNRC. As indicated by the SCC, molecular gas at $\sim +28.4$ and $\sim +46.0$ km s^{-1} , belonging to the $+36.4$ km s^{-1} broad line component, is distributed around the eastern and southern boundaries, respectively. Molecular gas of the $+58.9$ km s^{-1} broad line component has an elongated molecular clump distributed along the southeastern boundary of the SNRC, and a molecular filament distributed along the bright filamentary radio continuum emission in the northwest of the SNRC. Molecular gas at $\sim +75.2$ km s^{-1} is surrounding the southeastern radio continuum shell of the SNRC, which belongs to the $+80.4$ km s^{-1} broad line component. Molecular gas at $\sim +96.5$ km s^{-1} , belonging to the $+91.0$ km s^{-1} component, is roughly distributed around the southeastern and northwestern boundaries of the SNRC. Based on these evidences, the SNRC is probably associated with the $+58.9$ or $+80.4$ km s^{-1} components; however, it may be associated with the $+36.4$ or $+91.0$ km s^{-1} components too. The presence of H I absorption up to the tangent point shown by Castelletti et al. (2017); Johanson & Kerton (2009) indicates that the SNRC is at a far kinematic distance. If the SNRC is associated with the $+58.9$ km s^{-1} component, its kinematic distance can be estimated as 10.6 ± 0.4 kpc, and if it is associated with the $+80.4$ km s^{-1} component, its kinematic distance can be estimated as 7.9 ± 0.6 kpc. Kinematic distances of the $+36.4$ and $+91.0$ km s^{-1} components are estimated as 12.2 ± 0.3 and 7.9 ± 0.6 kpc, respectively. Both the $+80.4$ and $+91.0$ km s^{-1} components are probably located at the near side of the Scutum spiral arm.

G29.41-0.18: Multiple broad line components are identified in this SNRC. Broad lines at $+59.8$ and $+93.8$ km s^{-1} may be originated from the nearby prominent components at $+77.5$ and $+93.1$ km s^{-1} , respectively. When applying the additional clean subbackground region condition, only the $+77.5$ km s^{-1} component is with broad lines identified in the SNRC. As indicated by the SCC, there are molecular gases of the $+77.5$ and $+93.1$ km s^{-1} components roughly distributed around the SNRC. These spatial correlations are not significant. The SNRC may be associated with the $+77.5$ or $+93.1$ km s^{-1} components. Kinematic distances are estimated

as 4.4 ± 0.4 for the $+77.5 \text{ km s}^{-1}$ component, and 4.7 ± 0.5 or 7.9 ± 0.6 for the $+93.1 \text{ km s}^{-1}$ component.

G29.92+0.21: This SNRC is classified as the plerion type. As indicated by the SCC, molecular gas at $\sim +37.5 \text{ km s}^{-1}$ is roughly surrounding the north and east of the SNRC, which belongs to the $+38.0 \text{ km s}^{-1}$ component with broad lines identified. Molecular gas at $\sim +97.6 \text{ km s}^{-1}$ is surrounding the eastern half of the SNRC, and molecular gas at $\sim +106.0 \text{ km s}^{-1}$ is distributed around the eastern and western boundaries. They belong to the $+90.3 \text{ km s}^{-1}$ component that is with broad lines identified. The SNRC is most likely to be associated with the $+90.3 \text{ km s}^{-1}$ component; however, it may be associated with the $+38.0 \text{ km s}^{-1}$ component too. Kinematic distances are estimated as $4.7\pm 0.3 \text{ kpc}$ for the $+90.3 \text{ km s}^{-1}$ component, and 2.1 ± 0.3 or $12.0\pm 0.3 \text{ kpc}$ for the $+38.0 \text{ km s}^{-1}$ component.

G30.30+0.13: This SNRC is classified as the plerion type. Since the SNRC is small, no significant spatial correlation result is found. Nevertheless, molecular gas at $\sim +86.4 \text{ km s}^{-1}$ is roughly distributed around the SNRC, which belongs to the $+84.8 \text{ km s}^{-1}$ component with a broad line identified in the SNRC. If the SNRC is associated with the $+84.8 \text{ km s}^{-1}$ component, its kinematic distance can be estimated as $4.9\pm 0.8 \text{ kpc}$.

G30.36+0.62 and G30.51+0.57: These two SNRCs are overlapping each other. Three broad line components are identified in SNRC G30.36+0.62. Only the $+47.0$ and $+88.7 \text{ km s}^{-1}$ broad line components show some spatial correlations with the SNRC, of which molecular gases are mostly distributed around the southeastern boundary of the SNRC. SNRC G30.36+0.62 may be associated with the $+47.0$ or $+88.7 \text{ km s}^{-1}$ components. Kinematic distances of these two components are estimated as 10.6 ± 0.5 and $5.0\pm 0.8 \text{ kpc}$, respectively. For SNRC G30.51+0.57, two broad line components at $+72.9$ and $+88.3 \text{ km s}^{-1}$ are identified in it by full criteria. As indicated by the SCC, molecular gases at $\sim +69.2$ and $\sim +82.7 \text{ km s}^{-1}$ are surrounding the southwest and east of the SNRC, respectively. Molecular gas at the peak of the SCC at $\sim +16.8 \text{ km s}^{-1}$ is surrounding the southeastern half of the SNRC, which belongs to the $+16.6 \text{ km s}^{-1}$ component with broad line candidates identified in the SNRC only by partial criteria. SNRC G30.51+0.57 may be associated with the $+16.6$, $+72.9$, or $+88.3 \text{ km s}^{-1}$ components. Kinematic distances of them are estimated as 12.4 ± 0.3 , 3.5 ± 0.3 , and $4.4\pm 0.5 \text{ kpc}$, respectively. Both the $+72.9$ and $+88.3 \text{ km s}^{-1}$ components are probably located at the near side of the Scutum spiral arm.

G30.38+0.42: This SNRC presents a partial radio continuum shell in the southwest. Three broad line components are identified in this SNRC. As indicated by the SCC, only the $+17.9$ and $+93.0 \text{ km s}^{-1}$ components show roughly spatial correlations with the SNRC. Molecular gas at $\sim +15.4 \text{ km s}^{-1}$ is surrounding the eastern half of the SNRC, and molecular gas at $\sim +89.2 \text{ km s}^{-1}$ is distributed around the SNRC. The SNRC may be associated with the $+17.9$ or $+93.0 \text{ km s}^{-1}$ components, and their corresponding kinematic distances are estimated as 12.5 ± 0.3 and $4.9\pm 0.7 \text{ kpc}$, respectively.

G31.22-0.02 and G31.26-0.04: These two SNRCs overlap each other. Several broad line components are identified in both of the two SNRCs. Since many broad line points are located in the overlapping region between two SNRCs, the identification of broad lines for each SNRC is not very clear. In SNRC G31.22-0.02, only one broad line is identified at $+84.7 \text{ km s}^{-1}$, which can be attributed to the nearby prominent component at $+78.2 \text{ km s}^{-1}$. Almost all of broad line points in the SNRC are located in the overlapping region between two SNRCs, except for one at $+25.6 \text{ km s}^{-1}$. As indicated by the SCC, the $+44.3$ and $+78.2 \text{ km s}^{-1}$ broad line components show some spatial correlations with the SNRC. At $\sim +48.4 \text{ km s}^{-1}$, a molecular bar and a molecular clump are distributed around the eastern and western of the SNRC, respectively. In addition, molecular gas at $\sim +34.3 \text{ km s}^{-1}$ is distributed around the northeastern and western boundaries of the SNRC. Molecular gas at $\sim +82.5 \text{ km s}^{-1}$ is distributed around the SNRC, and molecular gas at $\sim +91.9 \text{ km s}^{-1}$ is surrounding the southeast of the SNRC. These evidences indicate that SNRC G31.22-0.02 is probably associated with the $+78.2 \text{ km s}^{-1}$ component, or may be associated with the $+44.3 \text{ km s}^{-1}$ component. Kinematic distances are estimated as $4.9\pm 0.8 \text{ kpc}$ for the $+78.2 \text{ km s}^{-1}$ component and $10.2\pm 0.4 \text{ kpc}$ for the $+44.3 \text{ km s}^{-1}$ component. For SNRC G31.26-0.04, as indicated by the SCC, molecular gas at $\sim +38.3 \text{ km s}^{-1}$ belonging to the $+44.3 \text{ km s}^{-1}$ broad line component is surrounding the whole SNRC except for its southeast side, and molecular gas at $\sim +95.2 \text{ km s}^{-1}$ belonging to the $+98.8 \text{ km s}^{-1}$ broad line component is roughly surrounding the eastern half of the SNRC. There is also some molecular gas at $\sim +84.1 \text{ km s}^{-1}$ distributed around the southwestern and southeastern boundaries of the SNRC, which belongs to the $+78.7 \text{ km s}^{-1}$ component; however, it seems to be a part of a molecular hub-filament structure located in the southwest. In addition, most of the broad line points at $+78.7 \text{ km s}^{-1}$ are located in the overlapping region with SNRC G31.22-0.02. SNRC G31.26-0.04 is probably associated with the $+44.3 \text{ km s}^{-1}$ component, or may be associated with the $+98.8 \text{ km s}^{-1}$ component. We also cannot rule out the possibility of the association with $+78.7 \text{ km s}^{-1}$ component. Kinematic distances are estimated as $10.2\pm 0.4 \text{ kpc}$ for the $+44.3 \text{ km s}^{-1}$ component, $4.9\pm 0.8 \text{ kpc}$ for the $+78.7 \text{ km s}^{-1}$ component, and $7.1\pm 0.8 \text{ kpc}$ for the $+98.8 \text{ km s}^{-1}$ component. Based on these results, these two SNRCs are probably unrelated.

G31.44+0.36: Broad lines are identified in this SNRC at four velocities. However, there is only one broad line at $+97.5 \text{ km s}^{-1}$, and it can be attributed to the nearby prominent component at $+96.0 \text{ km s}^{-1}$. All three

broad line components at $+23.2$, $+74.6$, and $+96.0$ km s^{-1} show more or less spatial correlations with the SNRC, as indicated by the SCC. Molecular gas at ~ 22.7 is roughly surrounding the whole SNRC except for its southwest side, and molecular gas at $\sim +77.6$ km s^{-1} is roughly surrounding the south and northwest of the SNRC. Molecular gas at $\sim +109.5$ km s^{-1} is surrounding the SNRC and also has a small amount inside. The $+23.2$, $+74.6$, or $+96.0$ km s^{-1} components may be associated with the SNRC. Their kinematic distances are estimated as 12.3 ± 0.4 , 5.0 ± 0.7 , and 5.1 ± 0.6 kpc, respectively.

G31.93+0.16: Two broad line components are identified in this SNRC at $+44.7$ and $+102.1$ km s^{-1} . As indicated by the SCC, molecular gas at $\sim +110.2$ km s^{-1} is roughly surrounding the northwest of the SNRC, which belongs to the $+102.1$ km s^{-1} broad line component. The $+44.7$ km s^{-1} component shows no good spatial correlation with the SNRC. These evidences indicate that the SNRC is probably associated with the $+102.1$ km s^{-1} component, with the corresponding kinematic distance estimated as 6.8 ± 0.8 kpc. Accordingly, this SNRC could be related to an overlapped H II region in its northwest.

G32.22-0.21: This SNRC is a plerion type. Molecular gas at a minor peak of the SCC at $\sim +91.9$ km s^{-1} is distributed around the northern boundary of the SNRC and surrounding the southwest of the SNRC at a far distance, which belongs to the $+80.9$ km s^{-1} component with broad lines identified. The SNRC may be associated with the $+80.9$ km s^{-1} component, of which the kinematic distance is estimated as 4.9 ± 0.8 kpc.

G32.37-0.51: The southwest of this SNR is adjacent to SNR G32.1-0.9. No broad line is identified in this SNRC by full criteria. The SCC indicates that the SNRC is spatially correlated with molecular gas at $\sim +45.9$ km s^{-1} , which is roughly surrounding the whole SNRC except for its west side. It belongs to the $+42.2$ km s^{-1} component that is with a broad line candidate identified in the SNRC by partial criteria. Therefore, the SNRC may be associated with the $+42.2$ km s^{-1} component with the corresponding kinematic distance estimated as 2.4 ± 0.2 kpc.

G32.46-0.11: Two broad line components are identified in this SNRC at $+81.5$ and $+100.3$ km s^{-1} . As indicated by the SCC, molecular gas at $\sim +83.7$ km s^{-1} , belonging to the $+81.5$ km s^{-1} broad line component, is surrounding the east of the SNRC and also distributed around the southwestern boundary of it. We find no good spatial correlation between the SNRC and the $+100.3$ km s^{-1} component. Since this SNRC is a bit small, the spatial correlation result is indefinite. The kinematic evidence and the spatial correlation result indicate that the SNRC is associated with the $+81.5$ km s^{-1} component with the kinematic distance estimated as 5.0 ± 0.8 kpc.

G32.73+0.15: This SNRC is located around the northern boundary of SNR Kes 78, and its north is adjacent to an H II region at $+19$ km s^{-1} . Three broad line components are identified in this SNRC. As indicated by the SCC, only the $+74.1$ km s^{-1} broad line component shows some spatial correlations with the SNRC, of which molecular gas is distributed around the eastern and southern boundaries of the SNRC. These evidences indicate that the SNRC is associated with the $+74.1$ km s^{-1} component with the kinematic distance estimated as 5.1 ± 0.8 kpc.

G33.62-0.23: We identify two broad line components at $+60.3$ and $+74.4$ km s^{-1} in this SNRC. As indicated by the SCC, molecular gas at $\sim +73.5$ km s^{-1} is distributed around the eastern boundary of the SNRC, which belongs to the $+74.4$ km s^{-1} component. No good spatial correlation result is found for the $+60.3$ km s^{-1} component. Therefore, we suggest that the SNRC is associated with the $+74.4$ km s^{-1} component with the kinematic distance estimated as 5.2 ± 0.6 kpc.

G34.52-0.76: The north of this SNRC is adjacent to SNR W44. No broad line is identified in this SNRC by full criteria. The SCC indicates a spatial correlation between the SNRC and molecular gas at $\sim +11.4$ km s^{-1} , which is roughly surrounding the SNRC. However, there is no corresponding broad line identified even by partial criteria.

G34.62+0.24: This SNRC is classified as the plerion type. The SCC indicates that the SNRC is spatially correlated with molecular gas at $\sim +43.3$ km s^{-1} , which is distributed around the SNRC mostly on its eastern half. It belongs to the $+44.8$ km s^{-1} component that is with broad line candidates identified in the SNRC by partial criteria. No broad line is identified in the SNRC by full criteria. The SNRC may be associated with the $+44.8$ km s^{-1} component with the kinematic distance estimated as 2.5 ± 0.2 kpc.

G34.93-0.24: The west of this SNRC overlaps with SNR W44. Several broad line components are identified in this SNRC. Only one broad line identified at $+42.8$ km s^{-1} and some of broad lines at $+51.1$ km s^{-1} can be attributed to the nearby prominent component at $+44.8$ km s^{-1} . When applying the additional clean sub-background region condition, only the $+83.2$ km s^{-1} component is with a broad line identified in the SNRC. As indicated by the SCC, molecular gas at $\sim +41.0$ km s^{-1} is roughly surrounding the northeast of the SNRC and distributed around the southwestern boundary of it, which belongs to the $+44.8$ km s^{-1} broad line component. Molecular gas at $\sim +72.2$ km s^{-1} , belonging to the $+83.2$ km s^{-1} broad line component, is distributed around the eastern and western boundaries of the SNRC. No good spatial correlation is found between the SNRC and other broad line components. Therefore, the SNRC may be associated with the $+44.8$ or $+83.2$ km s^{-1} com-

ponents, and corresponding kinematic distances are estimated as 2.5 ± 0.2 kpc and 5.0 ± 0.6 kpc, respectively. If this SNRC is associated with the $+44.8$ km s^{-1} component, it is probably related to SNR W44 and a northern overlapped H II region.

G35.13-0.34: Two broad line components are identified at $+43.7$ and $+76.0$ km s^{-1} in this SNRC. As indicated by the SCC, molecular gas of the $+43.7$ km s^{-1} component is roughly surrounding the northeast of the SNRC. The $+76.0$ km s^{-1} component shows no good spatial correlation with the SNRC. Since this SNRC is small, the spatial correlation result is indefinite. The SNRC may be associated with the $+43.7$ km s^{-1} component with the kinematic distance estimated as 2.5 ± 0.2 kpc.

G35.3-0.0: We identify several broad line components in this SNRC. Some broad lines at $+53.1$ km s^{-1} are originated from overlapped H II regions, especially those in the east of the SNRC. Broad lines at $+42.7$ km s^{-1} may be originated from the $+53.1$ km s^{-1} component that has a wide velocity range. When applying the additional clean subbackground region condition, only the $+53.1$ km s^{-1} component is with a broad line identified in the SNRC. As indicated by the SCC, molecular gases at $\sim +40.5$ and $\sim +66.4$ km s^{-1} are surrounding the west and south of the SNRC, which support the associated between the SNRC and the $+53.1$ km s^{-1} component. No good spatial correlation is found for other broad line components. Therefore, we suggest that the SNRC is associated with the $+53.1$ km s^{-1} component, of which the kinematic distance can be estimated as 9.6 ± 0.5 kpc.

G36.66-0.50: The southwest of this SNRC overlaps with SNR G36.6-0.7. Three broad line components are identified in this SNRC. Only the $+56.6$ and $+78.9$ km s^{-1} components show some spatial correlations with the SNRC, as indicated by the SCC. Note that part of broad lines at $+56.6$ km s^{-1} may be originated from an overlapped H II region in the southwest of the SNRC. Molecular gas at $\sim +52.7$ km s^{-1} is distributed around the northeastern and southwestern boundaries of the SNRC, and molecular gas at $\sim +85.6$ km s^{-1} is distributed around the northern and southwestern boundaries of the SNRC. Therefore, the SNRC may be associated with the $+56.6$ or $+78.9$ km s^{-1} components, with corresponding kinematic distances estimated as 9.2 ± 0.4 and 4.3 ± 0.5 kpc, respectively.

G36.68-0.14: Three broad line components are identified in this SNRC. The $+54.6$ and $+78.2$ km s^{-1} components show some spatial correlations with the SNRC. Molecular gases at $\sim +49.2$ and $\sim +89.5$ km s^{-1} are both distributed around the SNRC and have a small amount inside. The SNRC may be associated with the $+54.6$ or $+78.2$ km s^{-1} components, of which kinematic distances are estimated as 9.3 ± 0.5 and 4.5 ± 0.6 kpc, respectively.

G36.84-0.43: This SNRC is classified as the plerion type, and its southeast is adjacent to an H II region at about $+61$ km s^{-1} . The SCC indicates that the SNRC is spatially correlated with molecular gas at $\sim +80.5$ km s^{-1} , which is surrounding the whole SNRC except for its southwest side. It belongs to the $+80.7$ km s^{-1} component with a broad line identified in the SNRC by full criteria. These evidences indicate that the SNRC is associated with the $+80.7$ km s^{-1} component, and its kinematic distance can be estimated as 4.4 ± 0.6 kpc.

G36.85-0.25: Two broad line components are identified at $+55.1$ and $+79.7$ km s^{-1} . As indicated by the SCC, molecular gas at $\sim +57.1$ km s^{-1} is roughly surrounding the SNRC, and molecular gas at $\sim +78.3$ km s^{-1} is surrounding the northwest and southeast of the SNRC. These molecular gases belong to the $+55.1$ and $+79.7$ km s^{-1} broad line components, respectively. The spatial correlation result is indefinite, since the SNRC is a bit small. The SNRC may be associated with the $+55.1$ or $+79.7$ km s^{-1} components with kinematic distances estimated as 9.3 ± 0.5 and 4.5 ± 0.6 kpc, respectively.

G36.90+0.49: We identify no broad line in this SNRC by full criteria. The SCC peaks at $\sim +12.4$ km s^{-1} ; however, no corresponding broad line is identified in the SNRC even by partial criteria.

G37.34+0.42: Only one broad line is identified at $+90.8$ km s^{-1} in this SNRC, of which molecular gas is distributed around the southern boundary of the SNRC. Therefore, we suggest that the SNRC is associated with the $+90.8$ km s^{-1} component with the kinematic distance estimated as 4.7 ± 0.6 kpc.

G37.51+0.78: This SNRC is small and classified as the plerion type. We find no good spatial correlation result and identify no broad line in it even by partial criteria.

G37.62-0.22: Two broad line components are identified at $+18.8$ and $+48.2$ km s^{-1} in this SNRC. The SNRC is small, and we find no good spatial correlation result. If the SNRC is associated with the $+18.8$ km s^{-1} component, its kinematic distance can be estimated as 2.2 ± 0.3 kpc, and if it is associated with the $+48.2$ km s^{-1} component, its kinematic distance can be estimated as 9.1 ± 0.6 kpc.

G37.67-0.50: Two broad lines at $+51.7$ and $+74.6$ km s^{-1} are identified in this SNRC. As indicated by the SCC, the $+74.6$ km s^{-1} component shows some spatial correlations with the SNRC, of which molecular gases at $\sim +65.1$ and $\sim +77.8$ km s^{-1} are roughly surrounding the SNRC. No good spatial correlation is found for the $+51.7$ km s^{-1} component. These evidences indicate that the SNRC is associated with the $+74.6$ km s^{-1} component with the kinematic distance estimated as 4.4 ± 0.5 kpc. Additionally, there are broad line candidates at $+45.5$ km s^{-1} identified by partial criteria, concentrated in a molecular clump in the southern region of the

SNRC, which are probably unrelated to the SNRC.

G37.88+0.32 and G38.17+0.09: These two SNRCs are adjacent to each other. Several broad line components are identified in SNRC G37.88+0.32. As indicated by the SCC, molecular gas at $\sim+1.1$ km s $^{-1}$ is distributed around the northeastern boundary of the SNRC, and molecular gas at $\sim+9.4$ km s $^{-1}$ is roughly surrounding the northwest of the SNRC, which belong to the $+3.0$ km s $^{-1}$ broad line component. Molecular gas at $\sim+81.7$ km s $^{-1}$ belonging to the $+85.5$ km s $^{-1}$ broad line component is distributed around the SNRC. SNRC G37.88+0.32 may be associated with the $+3.0$ or $+85.5$ km s $^{-1}$ components, of which kinematic distances are estimated as 12.8 ± 0.6 and 4.5 ± 0.6 kpc, respectively. For SNRC G38.17+0.09, multiple broad line components are identified in it. Some broad lines at $+62.1$ km s $^{-1}$ are probably originated from an overlapped H II region in the southwest of the SNRC, nevertheless, there are still more broad line points at this velocity than at other velocities. When applying the additional clean subbackground region condition, only the $+82.2$ km s $^{-1}$ component is with broad lines identified in the SNRC. However, it shows no good spatial correlation with the SNRC. As indicated by minor peaks of the SCC, the $+2.7$, $+17.8$, and $+62.1$ km s $^{-1}$ broad line components show some spatial correlations with the SNRC. Molecular gas at $\sim+0.2$ km s $^{-1}$ is distributed around the western boundary of the SNRC. Molecular gas at $\sim+16.0$ km s $^{-1}$ is distributed around the northern and southeastern boundaries of the SNRC, and molecular gas at $\sim+21.9$ km s $^{-1}$ is surrounding its southwest. Molecular gas at $\sim+64.3$ km s $^{-1}$ is roughly surrounding the south of the SNRC and also distributed around its northern boundary. SNRC G38.17+0.09 is most likely to be associated with the $+62.1$ km s $^{-1}$ component; however, it may be associated with either the $+2.7$ or $+17.8$ km s $^{-1}$ components too. Kinematic distances are estimated as 4.1 ± 0.7 kpc for the $+62.1$ km s $^{-1}$ component, 11.5 ± 0.5 kpc for the $+2.7$ km s $^{-1}$ component, and 11.5 ± 0.4 kpc for the $+17.8$ km s $^{-1}$ component.

G38.62-0.24: Two broad line components are identified in this SNRC at $+44.0$ and $+67.9$ km s $^{-1}$. Molecular gas at a minor peak of the SCC at $\sim+47.0$ km s $^{-1}$ is roughly surrounding the east of the SNRC and also distributed around its western boundary, which belongs to the $+44.0$ km s $^{-1}$ broad line component. These evidences support the association between the SNRC and the $+44.0$ km s $^{-1}$ component, of which the kinematic distance is estimated as 2.5 ± 0.5 kpc.

G38.68-0.43: This SNRC is classified as the plerion type. As indicated by the SCC, molecular gas at $\sim+20.3$ km s $^{-1}$ is roughly surrounding the north the SNRC. It belongs to the $+18.9$ km s $^{-1}$ component that is with broad lines identified. These evidences indicate an association between the SNRC and the $+18.9$ km s $^{-1}$ component, with the corresponding kinematic distance estimated as 2.2 ± 0.2 kpc.

G38.72-0.87: This SNRC is classified as the plerion type and overlaps with SNR G38.7-1.3. As indicated by the SCC, molecular gases at $\sim+42.7$ and $\sim+80.0$ km s $^{-1}$ are roughly surrounding the northeast of the SNRC. However, molecular gas at $\sim+42.7$ km s $^{-1}$ is with no corresponding broad line identified. Molecular gas at $\sim+80.0$ km s $^{-1}$ is with broad lines identified in the SNRC at $+74.4$ km s $^{-1}$. There is also a broad line identified at $+79.8$ km s $^{-1}$, which can be attributed to the prominent component at $+74.4$ km s $^{-1}$ too. Therefore, we suggest that the SNRC is associated with the $+74.4$ km s $^{-1}$ component, and the corresponding kinematic distance is estimated as 4.3 ± 0.4 kpc.

G38.83-0.01: No broad line is identified in this SNRC even by partial criteria. We also find no significant spatial correlation result, since this SNRC is small. Note that molecular gas at a peak of the SCC at $\sim+41.1$ km s $^{-1}$ is distributed around the SNRC except for its southwest side.

G39.19+0.52: Two broad line components are identified in this SNRC at $+20.6$ and $+28.2$ km s $^{-1}$. The SCC indicates that the SNRC is spatially correlated with molecular gas at $\sim+45.6$ km s $^{-1}$, which is surrounding the northwestern half of the SNRC well. It supports the association between the SNRC and the $+28.2$ km s $^{-1}$ component. Nevertheless, there is also molecular gas at $\sim+12.5$ km s $^{-1}$ roughly surrounding the southwest of the SNRC, which may belong to the $+20.6$ km s $^{-1}$ component. Therefore, the SNRC is probably associated with the $+28.2$ km s $^{-1}$ component with the kinematic distance estimated as 1.90 ± 0.08 kpc. However, it is also possible that the SNRC is associated with the $+20.6$ km s $^{-1}$ component, of which the kinematic distance is estimated as 11.5 ± 0.3 kpc.

G39.20+0.81: No broad line is identified in this SNRC even by partial criteria. Since the SNRC is a bit small, we also find no good spatial correlation result.

G39.54+0.37: Only one broad line component is identified in this SNRC at $+36.2$ km s $^{-1}$, which is spatially correlated with the SNRC indicated by the SCC. Molecular gas at $\sim+42.2$ km s $^{-1}$ is roughly surrounding the southwest and northwest of the SNRC. We suggest that the SNRC is associated with the $+36.2$ km s $^{-1}$ component with the kinematic distance estimated as 1.91 ± 0.07 kpc.

G39.56-0.32: This SNRC overlaps a small H II region at $+55.2$ km s $^{-1}$, and is also adjacent to several H II regions at velocities of about $+14$, $+27$, $+51$, $+53$, and $+58$ km s $^{-1}$. We identify only one broad line component in this SNRC at $+57.9$ km s $^{-1}$, which is also spatially correlated with the SNRC. One of many broad line points seems to be originated from the overlapped H II region in the southern region of the SNRC. Molecular gas

at $\sim+52.9 \text{ km s}^{-1}$ is roughly surrounding the northern half of the SNRC. The SCC also indicates a spatial correlation between the SNRC and molecular gas at $\sim+15.2 \text{ km s}^{-1}$, which is surrounding the eastern half of the SNRC; however, no corresponding broad line is identified by full criteria. Therefore, we suggest that the SNRC is associated with the $+57.9 \text{ km s}^{-1}$ component and may be related to the overlapped and adjacent H II regions. The corresponding kinematic distance is estimated as $8.7\pm 0.5 \text{ kpc}$.

G41.51-0.53: Several broad line components are identified in this SNRC. Only the $+37.4 \text{ km s}^{-1}$ component shows some spatial correlations with the SNRC, as indicated by the SCC. Molecular gas at $\sim+37.6 \text{ km s}^{-1}$ is roughly surrounding the northwestern half of the SNRC. Based on these evidences, we suggest that the SNRC is associated with the $+37.4 \text{ km s}^{-1}$ component with the kinematic distance estimated as $1.92\pm 0.08 \text{ kpc}$.

G41.63+0.26: The northwest of this SNRC is adjacent to SNR G41.5+0.4. Only one broad line component is identified in this SNRC at $+36.5 \text{ km s}^{-1}$, and as indicated by the SCC, molecular gas at $\sim+34.3 \text{ km s}^{-1}$ belonging to it is roughly surrounding the SNRC. These evidences indicate that the SNRC is associated with the $+36.5 \text{ km s}^{-1}$ component with the kinematic distance estimated as $2.5\pm 0.5 \text{ kpc}$. Both SNRC G41.63+0.26 and SNR G41.5+0.4 are located at the near side of the Sagittarius spiral arm, and they may be related.

G41.95-0.18: The north of this SNRC overlaps with SNR G42.0-0.1. We identify only one broad line component in this SNRC at $+65.6 \text{ km s}^{-1}$, which is not well spatially correlated with the SNRC. Molecular gas at a minor peak of the SCC at $\sim+73.7 \text{ km s}^{-1}$ is distributed around the southeastern boundary and also in the northwest of the SNRC. In addition, as indicated by the SCC, molecular gas at $\sim+17.5 \text{ km s}^{-1}$ is surrounding the eastern half of the SNRC, and molecular gas at $\sim+29.5 \text{ km s}^{-1}$ is surrounding the southeast and northwest of the SNRC. These molecular gases belong to the $+15.8$ and $+27.1 \text{ km s}^{-1}$ components, which are with broad line candidates identified in the SNRC by partial criteria. The SNRC may be associated with the $+65.6 \text{ km s}^{-1}$ component, or with either the $+15.8$ or $+27.1 \text{ km s}^{-1}$ components. Kinematic distances are estimated as $7.9\pm 0.5 \text{ kpc}$ for the $+65.6 \text{ km s}^{-1}$ component, $11.1\pm 0.4 \text{ kpc}$ for the $+15.8 \text{ km s}^{-1}$ component, and $3.0\pm 1.0 \text{ kpc}$ for the $+27.1 \text{ km s}^{-1}$ component.

G42.62+0.14: We identify only one broad line at $+64.3 \text{ km s}^{-1}$ in this SNRC. As indicated by the SCC, molecular gas at $\sim+57.5 \text{ km s}^{-1}$, belonging to the $+64.3 \text{ km s}^{-1}$ component, is roughly surrounding the southeast of the SNRC and also distributed around its northern boundary. Therefore, we suggest that the SNRC is associated with the $+64.3 \text{ km s}^{-1}$ component with the near and far kinematic distances estimated as 3.6 ± 0.4 and $7.2\pm 1.1 \text{ kpc}$, respectively.

G42.71-0.27: Several broad line components are identified in this SNRC. Nevertheless, there is only one broad line identified at $+60.1$ and $+69.4 \text{ km s}^{-1}$, which can be attributed to the nearby prominent component at $+60.4 \text{ km s}^{-1}$. The SCC indicates that the $+60.4 \text{ km s}^{-1}$ component is spatially correlated with the SNRC, with molecular gas at $\sim+55.9 \text{ km s}^{-1}$ surrounding the whole SNRC except for its southwest side. Based on these evidences, the SNRC is associated with the $+60.4 \text{ km s}^{-1}$ component with the kinematic distance estimated as $7.8\pm 0.5 \text{ kpc}$.

G43.02+0.73: This SNRC is adjacent to SNR G42.8+0.6 in the west. No broad line is identified in this SNRC by full criteria. The SCC indicates a roughly spatial correlation between the SNRC and molecular gas at $\sim+59.4 \text{ km s}^{-1}$, which is surrounding the northeast of the SNRC and also distributed in the southeast of it. There is also molecular gas at $\sim+67.1 \text{ km s}^{-1}$ roughly surrounding the southeast of the SNRC. These molecular gases belong to the $+59.4 \text{ km s}^{-1}$ component with broad line candidates identified in the SNRC by partial criteria. The SNRC may be associated with the $+59.4 \text{ km s}^{-1}$ component with the near and far kinematic distances estimated as 3.8 ± 0.9 and $8.1\pm 0.9 \text{ kpc}$, respectively.

G43.07+0.56: This SNRC presents a bright partial radio continuum shell in the south and weak diffuse radio continuum emission elsewhere. No broad line is identified in this SNRC by full criteria. Molecular gas at the peak of the SCC at $\sim+42.4 \text{ km s}^{-1}$ is roughly surrounding the north of the SNRC, which belongs to the $+40.3 \text{ km s}^{-1}$ component with a broad line candidate identified in the SNRC by partial criteria. Molecular gas at a peak of the SCC at $\sim+1.3 \text{ km s}^{-1}$ roughly is surrounding the south of the SNRC; however, no corresponding broad line candidate is identified in it. If the SNRC is associated with the $+40.3 \text{ km s}^{-1}$ component, its kinematic distance can be estimated as $2.7\pm 0.4 \text{ kpc}$.

G44.08+0.13 and G44.5-0.2: These two SNRCs are overlapping each other. Among broad lines identified in SNRC G44.08+0.13, one broad line is at $+12.0 \text{ km s}^{-1}$, and three broad lines at $+59.1 \text{ km s}^{-1}$ can be attributed to the nearby $+55.1 \text{ km s}^{-1}$ component. As indicated by the SCC, the $+55.1 \text{ km s}^{-1}$ component shows spatial correlations with the SNRC, with molecular gases at $\sim+45.1$ and $\sim+67.6 \text{ km s}^{-1}$ surrounding the southeast and southern half of the SNRC, respectively. Additionally, molecular gases at $\sim+8.4$ and $\sim+21.1 \text{ km s}^{-1}$, belonging to the $+12.0 \text{ km s}^{-1}$ component, are surrounding the northeast and southeast of the SNRC, respectively. SNRC G44.08+0.13 is most likely to be associated with the $+55.1 \text{ km s}^{-1}$ component; however, it is also possible that it is associated with the $+12.0 \text{ km s}^{-1}$ component. Kinematic distances are estimated as 3.6 ± 0.6 and $8.0\pm 0.5 \text{ kpc}$ for the $+55.1 \text{ km s}^{-1}$ component and $10.7\pm 0.4 \text{ kpc}$ for the $+12.0 \text{ km s}^{-1}$ component. SNRC G44.5-0.2 was

suggested to be a counterpart of the shell-type TeV source HESS J1912+101, with broad CO lines detected at $+60 \text{ km s}^{-1}$ (Su et al. 2017a; Reich & Sun 2019, see Table 3 for more information). It is large and overlaps multiple H II regions. Here, many broad lines are identified in this SNRC, and some of them are probably originated from overlapped H II regions. Most of the broad lines are at $+59.8 \text{ km s}^{-1}$, and that at $+44.5$ and $+68.1 \text{ km s}^{-1}$ can be attributed to the $+59.8 \text{ km s}^{-1}$ component too. Few broad lines are identified at $+24.4 \text{ km s}^{-1}$, and some of them are located in the overlapping region with SNRC G44.08+0.13. No significant spatial correlation result is found for SNRC G44.5-0.2. Molecular gases at $\sim+15.1$ and $\sim+51.3 \text{ km s}^{-1}$ are roughly distributed around the SNRC, which belong to the $+24.4$ and $+59.8 \text{ km s}^{-1}$ components, respectively. SNRC G44.5-0.2 is probably associated with the $+59.8 \text{ km s}^{-1}$ component; however, it may be associated with the $+24.4 \text{ km s}^{-1}$ component too. Kinematic distances are estimated as $7.6\pm 0.4 \text{ kpc}$ for the $+59.8 \text{ km s}^{-1}$ component and $4.0\pm 0.7 \text{ kpc}$ for the $+24.4 \text{ km s}^{-1}$ component. It is possible that SNRCs G44.08+0.13 and G44.5-0.2 are related to each other.

G45.35-0.37: The east of this SNRC is adjacent to SNR G45.7-0.4. Broad lines are identified in this SNRC at $+56.1$ and $+66.5 \text{ km s}^{-1}$. However, only one broad line is identified at $+66.5 \text{ km s}^{-1}$, which can be attributed to the nearby prominent component at $+56.1 \text{ km s}^{-1}$. As indicated by the SCC, molecular gas at $\sim+46.0 \text{ km s}^{-1}$, belonging to the $+56.1 \text{ km s}^{-1}$ component, is distributed around the SNRC. Based on these evidences, we suggest that the SNRC is associated with the $+56.1 \text{ km s}^{-1}$ component with the kinematic distance estimated as $7.3\pm 0.6 \text{ kpc}$. Both SNRC G45.35-0.37 and SNR G45.7-0.4 seem located at the far side of the Sagittarius spiral arm, and may be related to each other.

G45.51-0.03: Two broad line components are identified in this SNRC at $+11.3$ and $+59.6 \text{ km s}^{-1}$. As indicated by the SCC, molecular gas at $\sim+51.6 \text{ km s}^{-1}$ is surrounding the western half of the SNRC and also distributed around its eastern boundary. In addition, molecular gas at $\sim+67.0 \text{ km s}^{-1}$ is distributed around the SNRC. These spatial correlations support the association between the SNRC and the $+59.6 \text{ km s}^{-1}$ component. No spatial correlation is found for the $+11.3 \text{ km s}^{-1}$ component. Associated with the $+59.6 \text{ km s}^{-1}$ component, we can estimate the kinematic distance of the SNRC as $7.3\pm 0.5 \text{ kpc}$.

G46.18-0.02: This SNRC presents shell-like structures in radio continuum emission. It overlaps with H II regions at $+15 \text{ km s}^{-1}$ in the south, and is also adjacent to an H II region at $+63 \text{ km s}^{-1}$ in the southwest. Molecular gases at $\sim+50.5$ and $\sim+54.8 \text{ km s}^{-1}$ are roughly surrounding the southern half of the SNRC, indicated by the SCC. These molecular gases belong to the $+56.0 \text{ km s}^{-1}$ component that is the only broad line component identified in the SNRC. Therefore, we suggest that the SNRC is associated with the $+56.0 \text{ km s}^{-1}$ component with the kinematic distance estimated as $7.0\pm 0.7 \text{ kpc}$.

G46.54-0.03: Two broad line components are identified in this SNRC at $+15.8$ and $+57.5 \text{ km s}^{-1}$. Molecular gas at the peak of the SCC at $\sim+16.0 \text{ km s}^{-1}$ is roughly surrounding the SNRC, which belongs to the $+15.8 \text{ km s}^{-1}$ broad line component. Molecular gas of the $+57.5 \text{ km s}^{-1}$ component shows no significant spatial correlation with the SNRC. Based on these evidences, we suggest that the SNRC is associated with the $+15.8 \text{ km s}^{-1}$ component, and the corresponding kinematic distance is estimated as $10.3\pm 0.4 \text{ kpc}$.

G47.15+0.73: The radius of this SNRC is less than the beam size of our observation, which is too small to examine possible spatial correlations. There is no broad line identified in this SNRC even by partial criteria.

G47.36-0.09: Three broad line components are identified in this SNRC. However, broad lines at $+64.3 \text{ km s}^{-1}$ can be attributed to the nearby prominent component at $+55.1 \text{ km s}^{-1}$. Molecular gases at $\sim+34.9$ and $\sim+53.5 \text{ km s}^{-1}$ are distributed around the SNRC, which probably belong to the $+41.5$ and $+55.1 \text{ km s}^{-1}$ broad line components. The SNRC may be associated with the $+41.5$ or $+55.1 \text{ km s}^{-1}$ components. Kinematic distances are estimated as $4.0\pm 0.8 \text{ kpc}$ for the $+41.5 \text{ km s}^{-1}$ component and $4.1\pm 0.5 \text{ kpc}$ for the $+55.1 \text{ km s}^{-1}$ component. Kinematic distances of these two velocity components are consistent, and both are probably located at the near side of the Sagittarius spiral arm.

G47.74-0.97: Only one broad line component is identified in this SNRC at $+50.3 \text{ km s}^{-1}$. As indicated by the SCC, molecular gas at $\sim+50.0 \text{ km s}^{-1}$ is distributed around the northern boundary of the SNRC, which belongs to the $+50.3 \text{ km s}^{-1}$ component. These evidences indicate that the SNRC is associated with the $+50.3 \text{ km s}^{-1}$ component, of which the near and far kinematic distances are estimated as 3.2 ± 0.7 and $7.7\pm 0.7 \text{ kpc}$, respectively.

G48.88+0.17: Broad lines at three velocities are identified in this SNRC. There are two broad lines at $+55.0 \text{ km s}^{-1}$, which can be attributed to the nearby component at $+49.6 \text{ km s}^{-1}$. This SNRC presents shell-like radio continuum emission in its eastern half. As indicated by the SCC, molecular gas at $\sim+16.8 \text{ km s}^{-1}$, belonging to the $+8.5 \text{ km s}^{-1}$ broad line component, is surrounding the northwestern half of the SNRC. Molecular gas at $\sim+58.4 \text{ km s}^{-1}$, belonging to the $+49.6 \text{ km s}^{-1}$ broad line component, is roughly surrounding the southeastern half of the SNRC. Based on these evidences, the SNRC is probably associated with the $+49.6 \text{ km s}^{-1}$ component, and the corresponding kinematic distance is estimated as $5.3\pm 0.7 \text{ kpc}$. It is also possible that the SNRC is associated with the $+8.5 \text{ km s}^{-1}$ component, of which the kinematic distance is estimated as 10.1 ± 0.4

kpc.

G51.06+0.56: No broad line is identified in this SNRC even by partial criteria. We also find no significant spatial correlation result by the SCC. Nevertheless, molecular gas at a peak of the SCC at $\sim+37.9$ km s $^{-1}$ is roughly surrounding the west of the SNRC, where shell-like radio continuum emission is present. If the SNRC is associated with molecular gas at $\sim+37.9$ km s $^{-1}$, its kinematic distance can be estimated as 8.0 ± 0.8 kpc.

G51.21+0.11 (G51.26+0.11): Two broad line components are identified in this SNRC. Nevertheless, only one broad line is identified at $+51.3$ km s $^{-1}$, and it can be attributed to the nearby prominent broad line component at $+54.6$ km s $^{-1}$. As indicated by the SCC, molecular gas at $\sim+62.9$ km s $^{-1}$ is distributed around the southeastern boundary of the SNRC, which belongs to the $+54.6$ km s $^{-1}$ component. Therefore, we suggest that the SNRC is associated with the $+54.6$ km s $^{-1}$ component. Considering the presence of H I absorption up to the tangent point velocity shown by Ranasinghe & Leahy (2022), its kinematic distance is estimated as 5.8 ± 0.5 kpc.

G53.07+0.49: No broad line is identified in this SNRC even by partial criteria. Because of its small size, no good spatial correlation result is found for it too.

G53.84-0.75: Two broad lines are identified in this SNRC at $+25.1$ and $+37.9$ km s $^{-1}$. As indicated by the SCC, molecular gas at $\sim+23.7$ km s $^{-1}$ is spatially correlated with radio continuum bright regions of the SNRC, which is roughly surrounding the west of the SNRC and also distributed around its eastern boundary. It belongs to the $+25.1$ km s $^{-1}$ broad line component. No spatial correlation is found between the SNRC and the $+37.9$ km s $^{-1}$ component. Based on these evidences, the SNRC is associated with the $+25.1$ km s $^{-1}$ component, of which the kinematic distance is estimated as 1.6 ± 0.7 kpc.

G56.56-0.75: This SNRC is classified as the plerion type. Molecular gas at the peak of the SCC at $\sim+31.9$ km s $^{-1}$ is surrounding the northwest of the SNRC. It belongs to the only component with broad line candidates identified in the SNRC by partial criteria, at $+32.0$ km s $^{-1}$. No broad line is identified in the SNRC by full criteria. The SNRC is probably associated with the $+32.0$ km s $^{-1}$ component with the kinematic distance estimated as 2.8 ± 0.7 kpc.

G57.12+0.35: Two broad line components are identified in this SNRC at -1.1 and $+10.3$ km s $^{-1}$. We find no significant spatial correlation result by the SCC, nevertheless, molecular gas at $\sim+7.6$ km s $^{-1}$ is roughly surrounding the east of the SNRC and distributed around its northwestern boundary, which belongs to the $+10.3$ km s $^{-1}$ component. There is also molecular gas at ~-8.7 km s $^{-1}$ roughly surrounding the southwest of the SNRC and also distributed around its northern boundary, which belongs to the -1.1 km s $^{-1}$ component, however, it is not well correlated with radio continuum emission in the northeastern half. The SNRC may be associated with the -1.1 or $+10.3$ km s $^{-1}$ components, with kinematic distances estimated as 8.9 ± 0.4 and 8.5 ± 0.5 kpc, respectively. Kinematic distances of two components are consistent, and both are located in the Perseus spiral arm.

G58.70-0.31: This SNRC is classified as the plerion type. Molecular gas at the peak of the SCC at ~-5.6 km s $^{-1}$ is surrounding the east of the SNRC. However, no broad line is identified in the SNRC even by partial criteria. The SNRC might be associated with molecular gas at ~-5.6 km s $^{-1}$, of which the kinematic distance is estimated as 8.6 ± 0.5 kpc.

G59.46+0.83: This SNRC is classified as the plerion type. Molecular gas at the peak of the SCC at $\sim+24.3$ km s $^{-1}$ is distributed around the SNRC, but not correlated well. Moreover, no broad line is identified in the SNRC even by partial criteria.

G59.68+1.25: The east of this SNRC overlaps with SNR G59.8+1.2. We identify no broad line in this SNRC even by partial criteria. The SCC indicates that molecular gas at $\sim+9.5$ km s $^{-1}$ is spatially correlated with the SNRC, which is roughly surrounding the southwestern half of the SNRC. The SNRC might be associated with molecular gas at $\sim+9.5$ km s $^{-1}$ with the near and far kinematic distances estimated as 0.5 ± 0.7 and 7.8 ± 0.7 kpc, respectively.

G59.83-0.41: Only one broad line candidate at $+55.1$ km s $^{-1}$ is identified in this SNRC by partial criteria. However, we find no good spatial correlation result for the $+55.1$ km s $^{-1}$ component or other velocity components.

G128.5+2.6: This SNRC presents shell-like radio continuum emission in the south. Only one broad line is identified in the SNRC at -7.6 km s $^{-1}$. The SCC indicates a spatial correlation between the SNRC and the -7.6 km s $^{-1}$ component, of which molecular gas at ~-2.9 km s $^{-1}$ is roughly surrounding the south of the SNRC and also distributed around its northeastern boundary. Based on these evidences, we suggest that the SNRC is associated with the -7.6 km s $^{-1}$ component, and its kinematic distance can be estimated as 0.6 ± 0.2 kpc.

G149.5+3.2, G150.8+3.8, and G151.2+2.9: SNRCs G149.5+3.2 and G151.2+2.9 are adjacent to SNRC G150.8+3.8, and all of them overlap with SNR G150.3+4.5. No broad line is identified in these three SNRCs even by partial criteria. For SNRC G149.5+3.2, molecular gas at the peak of the SCC at $\sim+1.3$ km s $^{-1}$ is

roughly surrounding its southeast, however, not correlated with bright radio continuum emission of the SNRC. Molecular gas at $\sim+6.2$ km s $^{-1}$ is roughly surrounding the northwest of the SNRC, where there is bright radio continuum emission. If the SNRC G149.5+3.2 is associated with molecular gas at $\sim+6.2$ km s $^{-1}$, its near and far kinematic distances can be estimated as 0.25 ± 0.05 and 2.05 ± 0.07 kpc, respectively. SNRC G150.8+3.8 presents shell-like radio continuum emission in its southeast. As indicated by the SCC, there is a molecular shell at $\sim+1.7$ km s $^{-1}$ roughly surrounding its radio continuum shell, which also has some protrusions pointing toward its center. Therefore, SNRC G150.8+3.8 may be associated with molecular gas at $\sim+1.7$ km s $^{-1}$ with kinematic distance estimated as 0.4 ± 0.2 kpc, and it may be related to SNR G150.3+4.5. For SNRC G151.2+2.9, molecular gases at nonsignificant peaks of the SCC at ~-9.4 and $\sim+4.0$ km s $^{-1}$ are mainly distributed in the northwest, not correlated with shell-like radio continuum emission in the southeast of the SNRC.

G172.8+1.5: Three broad line components at -16.4 , -9.0 , and -2.3 km s $^{-1}$ are identified in this SNRC. Only one broad line is identified at -9.0 km s $^{-1}$, which can be attributed to the nearby prominent component at -16.4 km s $^{-1}$. No significant spatial correlation is found through the SCC. There is molecular gas at ~-22.7 km s $^{-1}$ distributed around the northern boundary of the SNRC, which belongs to the -16.4 km s $^{-1}$ broad line component. If the SNRC is associated with the -16.4 km s $^{-1}$ component, its kinematic distance can be estimated as 1.7 ± 0.04 kpc.

G189.6+3.3: The southwest of this SNRC overlaps with SNR IC 443. All broad lines identified in this SNRC are in the overlapping region with SNR IC 443, which are probably originated from SNR IC 443. Molecular gas at the peak of the SCC at ~-3.0 km s $^{-1}$ is distributed around the northwestern and southwestern boundaries of the SNRC, but not correlated well. We cannot determine which MC is associated with the SNRC.

G190.2+1.1: This SNRC is revealed as a rapidly expanding H I shell observed by H I 21 cm line emission (Koo et al. 2006). No broad line is identified in the SNRC by full criteria. Molecular gas at the peak of the SCC at $\sim+5.1$ km s $^{-1}$ shows some spatial correlations with the SNRC, which is roughly surrounding its southern half. It belongs to the $+7.5$ km s $^{-1}$ component with broad line candidates identified by partial criteria. The SNRC may be associated with the $+7.5$ km s $^{-1}$ component, of which the kinematic distance is estimated as 2.1 ± 0.03 kpc.

C. Individual PWNe

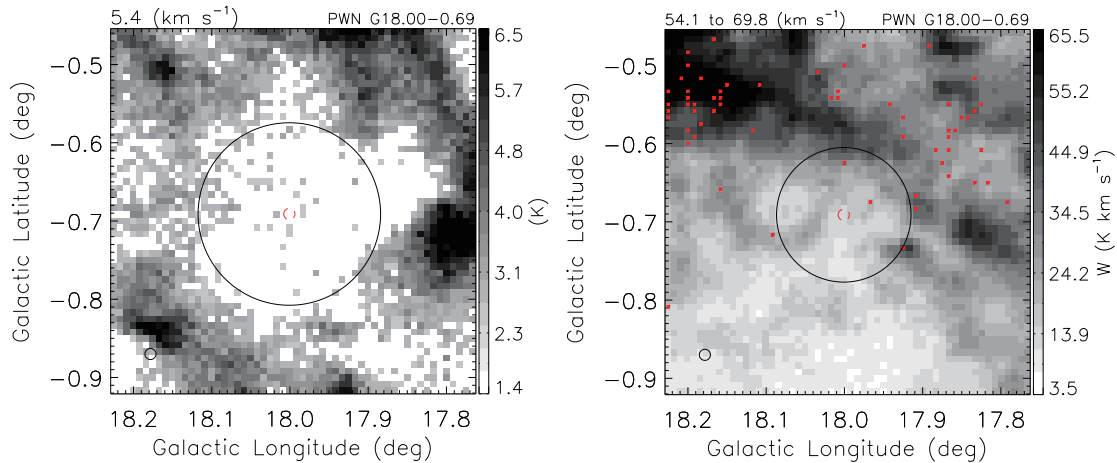


Fig. 12.— ^{12}CO ($J=1-0$) intensity maps of PWN G18.00-0.69, at the $+5.4$ km s $^{-1}$ velocity channel (left) and integrated over the velocity range of $+54.1$ to $+69.8$ km s $^{-1}$ (right). Minimum values of ^{12}CO emission intensity shown in colorbars are at 3σ confidence level. Red tiny stars denote locations of broad lines identified by full criteria. Red dashed circles denote the extent of the PWN. Black solid circles delineate the cavity edge (left) and the surrounding shell (right).

G18.00-0.69: As inferred from the radio dispersion measurement, the distance of the associated pulsar was estimated as 3.9 ± 0.4 kpc (Cordes & Lazio 2002; Gaensler et al. 2003), while, the extinction-distance relation of red clump stars toward this PWN derived a distance of 3.1 ± 0.2 kpc (Shan et al. 2018). The SCC peaks at $\sim+5.4$ km s $^{-1}$, where molecular gas presents a cavity-like structure around the PWN, as shown in the left panel in Figure 12. The corresponding kinematic distance is estimated as 1.26 ± 0.05 kpc. However, no corresponding broad line is identified even by partial criteria. Both a minor peak of the SCC and the detection of associated

broad line emission indicate that the PWN is associated with the $+60.8 \text{ km s}^{-1}$ velocity component. As shown in Figure 12, molecular gas of the $+60.8 \text{ km s}^{-1}$ component is surrounding the PWN in the west. In addition, there is also a shell-like molecular structure besides the PWN in the east, which seems unrelated. Therefore, we suggest that the PWN is associated with the $+60.8 \text{ km s}^{-1}$ component, with the corresponding kinematic distance estimated as $3.8 \pm 0.4 \text{ kpc}$. The radius of the western shell-like structure is $\sim 5.7 \text{ pc}$.

Eel: This PWN might be associated with the TeV source HESS J1825-137 (Voisin et al. 2016). The dis-

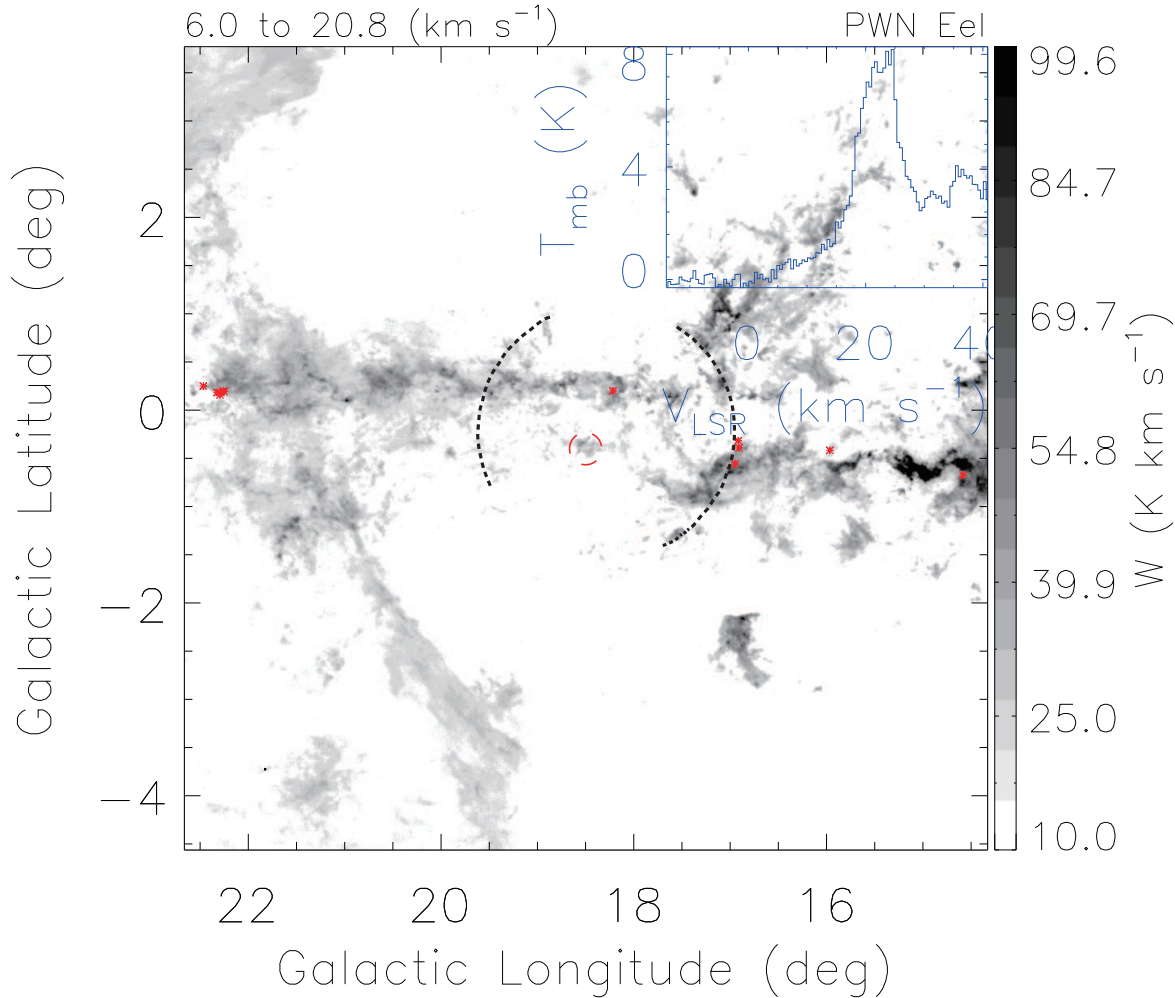


Fig. 13.— ^{12}CO ($J=1-0$) intensity map of PWN Eel, integrated over the velocity range of $+6.0$ to $+20.8 \text{ km s}^{-1}$. The minimum value of ^{12}CO emission intensity shown in the colorbar is at 5σ level. Red tiny stars denote locations of broad lines identified by full criteria. The extent of the PWN is denoted by a red dashed circle. Two shell-like structures are sketched by two black dotted lines. The average ^{12}CO ($J=1-0$) spectrum of three broad line points on the western shell-like structure is shown in the upper right corner.

persion measure of the accompany pulsar is unknown; however, distance estimations were performed based on pulsar’s properties, which give possible distances of $\sim 1.3 \text{ kpc}$ (Wang 2011) and $\sim 3.9 \text{ kpc}$ (Kargaltsev et al. 2017). The SCC for the PWN has no significant peak. In this direction, there presents a large bubble in local MCs at $\sim +6 \text{ km s}^{-1}$, and the PWN locates near the southeastern boundary of it. Nevertheless, two shell-like CO structures of the $+19.8 \text{ km s}^{-1}$ component seem correlated, which circulate the PWN, and broad lines are also identified on them by full criteria (see Figure 13). Note that there are some background MCs near these shell-like structures, which are distributed near the Galactic plane and probably at a far kinematic distance. Therefore, we suggest that the PWN is associated with the $+19.8 \text{ km s}^{-1}$ MC, hence, locates at a kinematic distance of $1.50 \pm 0.04 \text{ kpc}$. The radius of these shell-like structures is $\sim 35 \text{ pc}$.

G21.88-0.10: The dispersion measure distance of PSR J1831-0952 was estimated as 4.3 kpc (Manchester et al. 2005; Sheidaei 2011). Here, the SCC indicates an association between the PWN and molecular gas at $\sim +40.2 \text{ km s}^{-1}$, which is distributed around the PWN. It belongs to the $+55.0 \text{ km s}^{-1}$ component with broad

lines identified. The corresponding kinematic distance is estimated as 3.4 ± 0.4 kpc.

G23.5+0.1: Molecular gas at the peak of the SCC at $\sim +96.2$ km s^{-1} is roughly surrounding this PWN candidate, which belongs to the $+95.8$ km s^{-1} component with broad lines identified. We suggest that the PWN candidate is associated with the $+95.8$ km s^{-1} component, with the corresponding kinematic distance estimated as 5.3 ± 0.7 kpc. It is consistent with the H I absorption result toward PSR J1833-0827 (Weisberg et al. 1995). The radius of the surrounding shell-like structure is ~ 15 pc.

G25.24-0.19: A distance of 6.6 kpc was adopted for this PWN by assuming an association with an adjacent cluster of red supergiant stars (Gotthelf & Halpern 2008). The SCC peaks at $\sim +3.5$, $\sim +9.0$, and $\sim +107.1$ km s^{-1} . There is no clear shell-like or cavity-like structure found for molecular gases at $\sim +3.5$ and $\sim +9.0$ km s^{-1} . Molecular gas at $\sim +107.1$ km s^{-1} is roughly surrounding the PWN in the northeast, which belongs to the $+102.1$ km s^{-1} component with corresponding broad lines identified. Note that there is also a small shell-like structure at $\sim +62.5$ km s^{-1} roughly surrounding the PWN; however, it is probably related to a large-scale hub-filament structure but not the PWN. Therefore, we suggest that the PWN is associated with the $+102.1$ km s^{-1} component, with the kinematic distance estimated as 5.9 ± 0.7 kpc. Correspondingly, the radius of the surrounding shell-like structure is ~ 24 pc. Note that, the derived distance is consistent with that adopted by Gotthelf & Halpern (2008).

G32.64+0.53: Considering the large X-ray absorbing column density toward this source, a distance of 7 kpc,

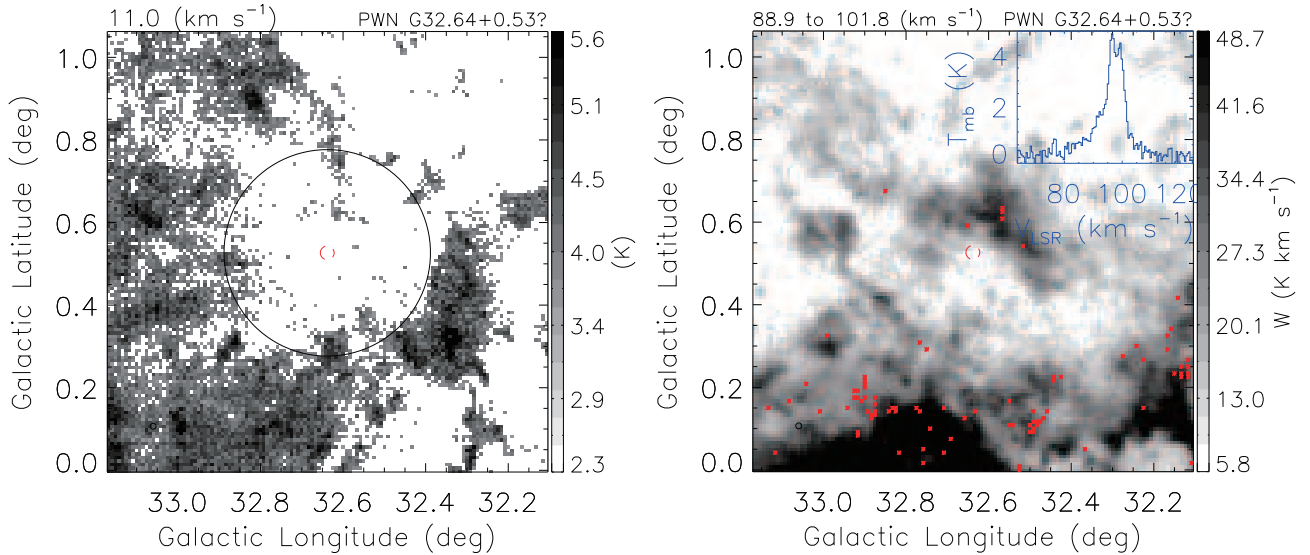


Fig. 14.— ^{12}CO ($J=1-0$) intensity maps of PWN candidate G32.64+0.53, at the $+11.0$ km s^{-1} velocity channel (left) and integrated over the velocity range of $+88.9$ to $+101.8$ km s^{-1} (right). Minimum values of ^{12}CO emission intensity shown in colorbars are at 5σ confidence level. Red tiny stars denote locations of broad lines identified by full criteria. Red dashed circles denote the extent of the PWN. Black solid circles delineate the cavity edge (left) and the surrounding shell (right). The average ^{12}CO ($J=1-0$) spectrum of broad line emission from the surrounding shell is shown in the upper right corner of the right panel.

located at the tangent point of the Scutum arm, was assumed (Gotthelf et al. 2011). As indicated by the SCC, there is a cavity-like structure at $\sim +11.0$ km s^{-1} distributed around this PWN candidate (see Figure 14); however, no corresponding broad line emission is detected. Molecular gas at a minor peak of the SCC at $\sim +97.8$ km s^{-1} also shows possible spatial correlation with the PWN candidate, which is roughly surrounding it in the north. It belongs to the $+98.0$ km s^{-1} component, which is the only broad line component identified in the nearby region by full criteria (see Figure 14). Based on the spatial correlation as well as the kinematic evidence, we suggest that the PWN candidate is associated with the $+98.0$ km s^{-1} MC, hence, locates at a kinematic distance of 5.2 ± 0.5 kpc. The radius of the surrounding shell-like structure is ~ 9 pc.

G36.01+0.06: This PWN candidate was detected as spatially extended γ -ray source, i.e. HESS J1857+026 (Aharonian et al. 2008b), powered by PSR J1856+0245 (Hessels et al. 2008). The distance of PSR J1856+0245 was estimated as ~ 9 kpc based on its radio dispersion measure (Cordes & Lazio 2002; Rousseau et al. 2012). Molecular gas at the peak of the SCC at $\sim +34.9$ km s^{-1} is roughly surrounding the southeastern half of the PWN candidate (see left panel in Figure 15), which belongs to the $+37.7$ km s^{-1} component with corresponding broad lines detected. Nevertheless, with the kinematic distance estimated as 2.4 ± 0.2 kpc for the $+37.7$ km s^{-1} component, the radius of the surrounding molecular shell is just ~ 1.6 pc. Molecular gas at a peak of the SCC at

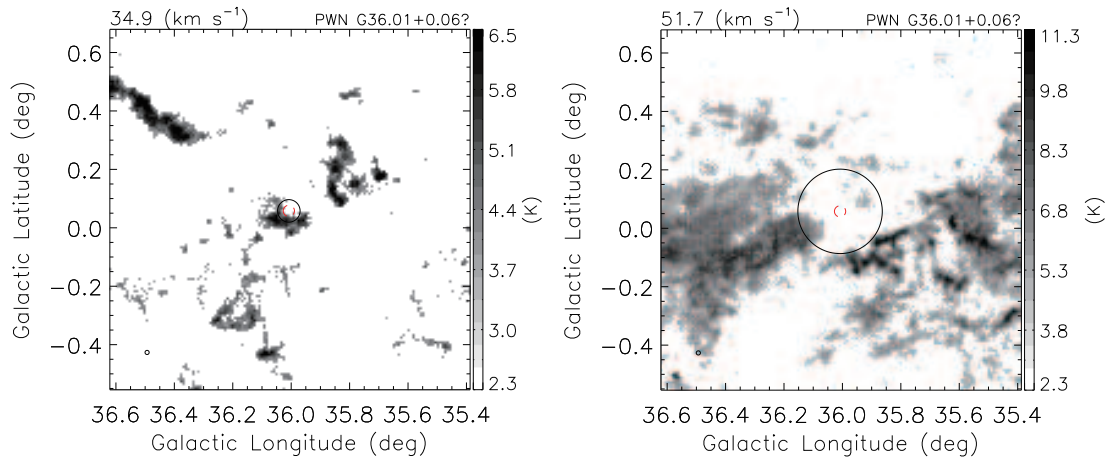


Fig. 15.— ^{12}CO ($J=1-0$) intensity maps of PWN candidate G36.01+0.06, at $+34.9 \text{ km s}^{-1}$ (left) and $+51.7 \text{ km s}^{-1}$ (right) velocity channels. Minimum values of ^{12}CO emission intensity shown in colorbars are at 5σ confidence level. Red dashed circles denote the extent of the PWN. Black solid circles delineate edges of surrounding MCs.

$\sim+51.7 \text{ km s}^{-1}$ is also distributed around the PWN candidate (see right panel in Figure 15), which seems to be spatially correlated with very-high-energy γ -ray emission (see Figure 7 in Aharonian et al. 2008b). It belongs to the $+58.1 \text{ km s}^{-1}$ component with corresponding broad lines identified. If this source is associated with the $+58.1 \text{ km s}^{-1}$ component, its kinematic distance can be estimated as $9.5\pm 0.5 \text{ kpc}$, and the distance to the edge of surrounding MCs is $\sim 24 \text{ pc}$. It is consistent with the dispersion measure distance of the associated pulsar.

G47.38-3.88: The distance of PSR J1932+1059 (i.e. PSR B1929+10) was determined as $0.361^{+0.010}_{-0.008} \text{ kpc}$ based on parallax measurements (Chatterjee et al. 2004). Molecular gas at the peak of the SCC at $\sim+6.7 \text{ km s}^{-1}$ is roughly surrounding the PWN in the north at a radius of about $2.^{\circ}3$. We identify no broad line emission around this PWN even by partial criteria. If the PWN is associated with molecular gas at $\sim+6.7 \text{ km s}^{-1}$, its near and far kinematic distances can be estimated as 0.16 ± 0.54 and $10.8\pm 0.6 \text{ kpc}$, respectively. The near kinematic distance is consistent with the parallax distance of the associated pulsar. The radius of the $\sim+6.7 \text{ km s}^{-1}$ diffuse shell-like structure at 0.361 kpc is $\sim 14 \text{ pc}$.

G59.2-4.70: The distance of the associated pulsar was derived as $2.5\pm 1.0 \text{ kpc}$ based on its radio dispersion measure (Cordes & Lazio 2002; Huang et al. 2012). ^{12}CO ($J=1-0$) emission is very weak toward this PWN, and we found no clear shell or cavity-like structure in its vicinity.

G63.7+1.1: This PWN candidate may be powered by the neutron star candidate 3XMM J194753.4+274357 (CXO J194753.3+274351; Matheson et al. 2016). Wallace et al. (1997) suggested that the PWN candidate is associated with an MC at the systemic velocity of $+21 \text{ km s}^{-1}$. However, as noted by Matheson et al. (2016), R. Kothes et al. (2016, in preparation) suggested an association with the $+13 \text{ km s}^{-1}$ MC. Here, indicated by the SCC, we detect a double shell structure at $\sim+4.0 \text{ km s}^{-1}$ (see Figure 16), which seems to be associated with the PWN candidate. It belongs to the $+5.6 \text{ km s}^{-1}$ component that is the only component with broad line candidates identified by partial criteria. If the PWN candidate is associated with the $+5.6 \text{ km s}^{-1}$ component, its kinematic distance can be estimated as $7.2\pm 0.7 \text{ kpc}$. Radii of the double shell structure are ~ 88 and $\sim 176 \text{ pc}$.

CTB 87: Based on H I absorption measurements and CO observations of nearby MCs, the PWN was suggested to be associated with $\sim-58 \text{ km s}^{-1}$ MC, and its distance was estimated to be 6.1 kpc (Kazes & Caswell 1977; Huang & Thaddeus 1986; Cho et al. 1994; Kothes et al. 2003; Liu et al. 2018, see Table 3 for more information). Here, the SCC peaks at $\sim+5.4 \text{ km s}^{-1}$; however, surrounding molecular gas shows no clear cavity or shell-like structure (see right panel in Figure 17). It belongs to the $+0.5 \text{ km s}^{-1}$ component with corresponding broad line points identified in the southwest. Nevertheless, a shell-like structure surrounding the PWN is found at a peak of the SCC at $\sim-55.9 \text{ km s}^{-1}$, with the center shifted a little to the south (see left panel in Figure 17). Molecular gas at $\sim-55.9 \text{ km s}^{-1}$ belongs to the -51.6 km s^{-1} component, of which broad line candidates are identified by partial criteria to be located a little farther to the northwest. The northern part of the shell-like structure was detected by Liu et al. (2018). Based on these evidences, the PWN is probably associated with the -51.6 km s^{-1} component. This is consistent with results in previous works, and the corresponding kinematic distance estimated in previous work is 6.1 kpc (Foster & Routledge 2002; Kothes et al. 2003). The radius of the entire shell-like structure around the PWN is $\sim 13 \text{ pc}$ at the distance of 6.1 kpc .

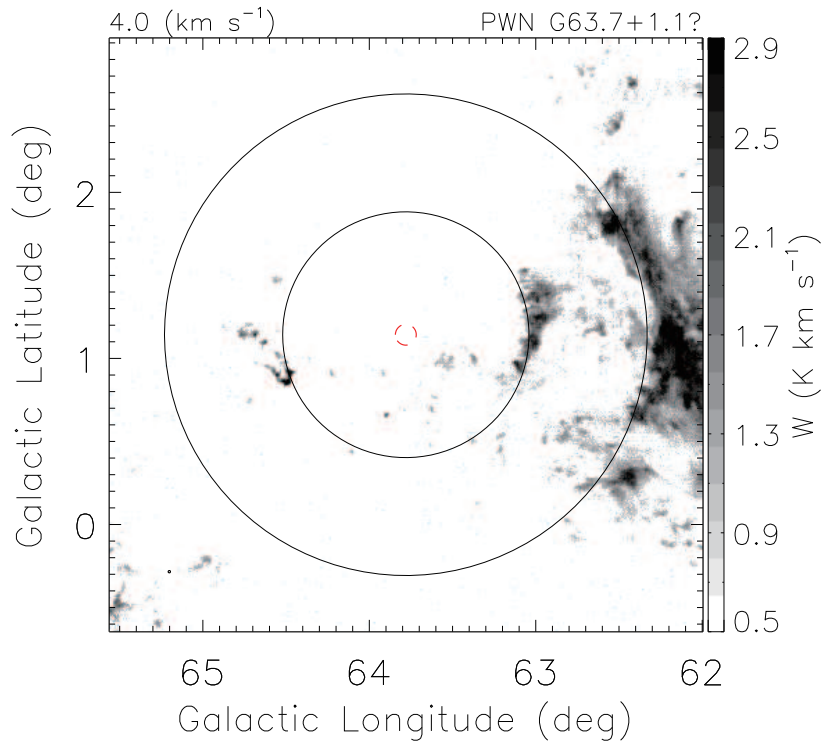


Fig. 16.— ^{12}CO ($J=1-0$) intensity map of PWN candidate G63.7+1.1, at the $+4.0 \text{ km s}^{-1}$ velocity channel. The minimum value of ^{12}CO emission intensity shown in the colorbar is at 5σ level. The extent of the PWN is denoted by a red dashed circle. Black solid circles delineate surrounding shell-like structures, with radii of $0.^{\circ}74$ and $1.^{\circ}45$.

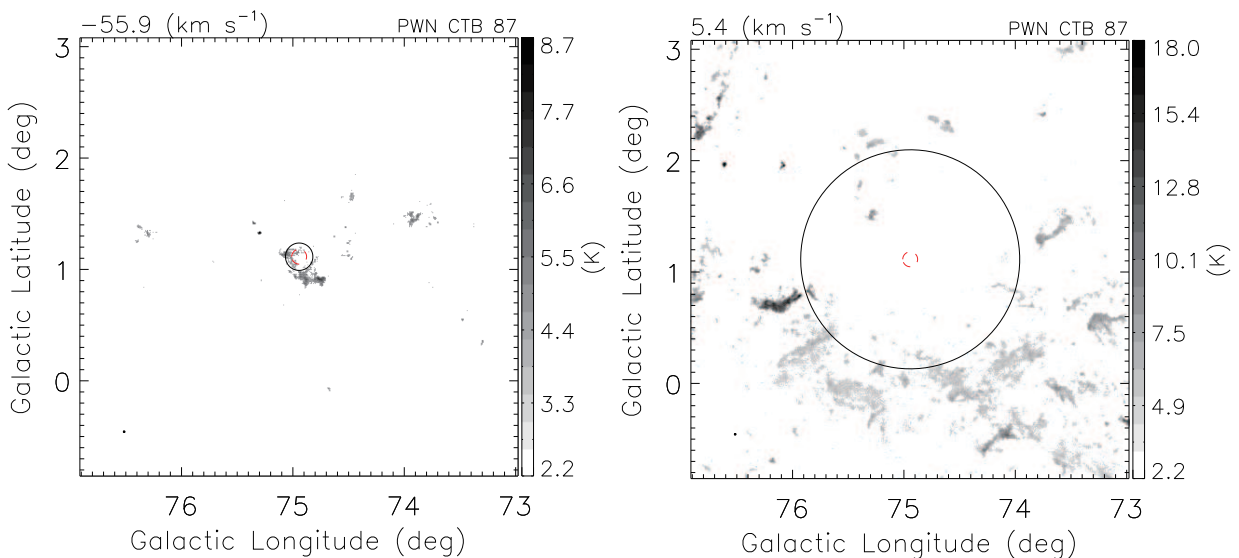


Fig. 17.— ^{12}CO ($J=1-0$) intensity maps of PWN CTB 87, at -55.9 km s^{-1} (left) and $+5.4 \text{ km s}^{-1}$ (right) velocity channels. Minimum values of ^{12}CO emission intensity shown in colorbars are at 5σ confidence level. Red dashed circles denote the extent of the PWN. Black solid circles delineate the surrounding shell-like (left) and cavity-like (right) structures.

G75.23+0.12: The distance to PSR J2021+3651 is controversial, different distance estimations gave different results, e.g., $1.8_{-1.4}^{+1.7}$ kpc by hydrogen absorbing column density measurements on X-ray observations and an adopted N_{H} -D relation (Kirichenko et al. 2015), ~ 12 kpc by the pulsar’s dispersion measure (e.g., Roberts et al. 2002), 3–4 kpc by comparing X-ray absorption column density with the total Galactic H I column density (Van Etten et al. 2008), and ~ 1 kpc by using the empirical γ -ray ”pseudo-distance” relation (e.g., Saz Parkinson et al. 2010). We find that molecular gas at the peak of the SCC at $\sim +5.6$ km s^{-1} is distributed around the PWN; however, it shows no clear shell or cavity-like structure. It belongs to the $+6.0$ km s^{-1} component with corresponding broad line candidates identified only by partial criteria, which are at a distance from the PWN. If the PWN is associated with the $+6.0$ km s^{-1} component, its kinematic distance can be estimated as 3.4 ± 0.4 kpc.

G80.22+1.02: Camilo et al. (2009) derived the dispersion measure distance of PSR 2032+4127 as ~ 3.6 kpc using the electron density model of Cordes & Lazio (2002); however, they suggested that the actual distance to the pulsar is ~ 1.8 kpc based on a detailed γ -ray flux estimate. We find that molecular gas at the peak of the SCC at ~ -2.9 km s^{-1} is distributed around the PWN at a radius of ~ 0.29 . It belongs to the -3.0 km s^{-1} component with corresponding broad lines identified. Note that some broad lines may be originated from overlapped H II regions. If the PWN is associated with the -3.0 km s^{-1} component, its kinematic distance can be estimated as 2.6 ± 0.3 kpc. The distance to the edge of surrounding molecular gas is ~ 13 pc.

3C 58: The minimum velocity of H I absorption features toward 3C 58 inferred a systemic velocity of

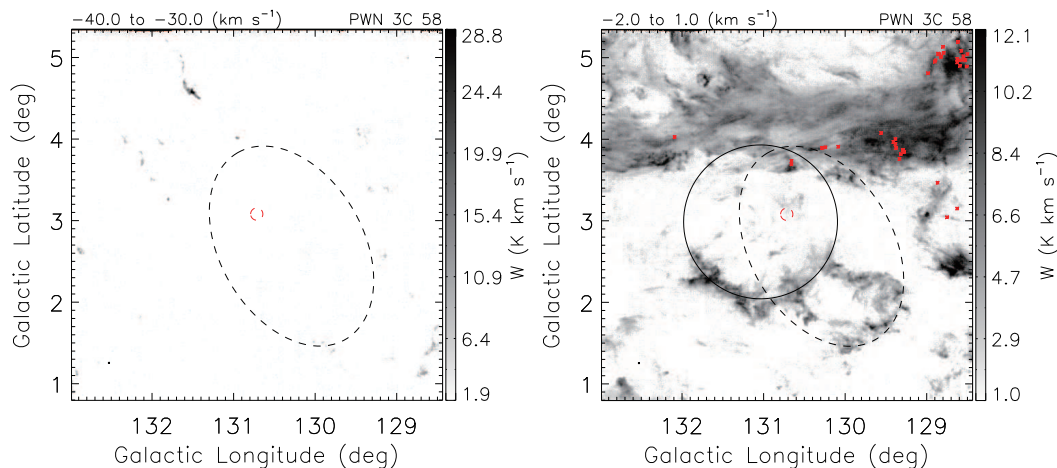


Fig. 18.— ^{12}CO ($J=1-0$) intensity maps of 3C 58, integrated over velocity ranges of -40 to -30 km s^{-1} (left) and -2.0 to $+1.0$ km s^{-1} (right). Minimum values of ^{12}CO emission intensity shown in colorbars are at 3σ confidence level. Red tiny stars denote locations of broad lines at -2.5 km s^{-1} identified by full criteria. Red dashed circles denote the extent of the PWN. The black solid circle in the right panel delineates the CO shell, and black dashed ellipses delineate the H I bipolar shell found by (Wallace et al. 1994).

~ -36 km s^{-1} (Green & Gull 1982; Roberts et al. 1993; Kothes 2013), correspondingly, the kinematic distance was estimated as ~ 2 kpc (Kothes 2013). A large bipolar shell structure was detected in H I observations around ~ -36 km s^{-1} , which was suggested to be associated with the PWN (Wallace et al. 1994; Kothes 2013). As shown in Figure 18, we detect very little CO emission associated with the H I bipolar shell around -36 km s^{-1} . However, more CO emission was detected along the H I bipolar shell around -2.5 km s^{-1} , and there are broad lines at -2.5 km s^{-1} identified on its northern part. The SCC peaks at ~ -7.3 km s^{-1} that belongs to the -2.5 km s^{-1} velocity component. The -2.5 km s^{-1} component also presents a clear CO shell structure accompanied with some inward filaments and outward protrusions. The kinematic distance of the -2.5 km s^{-1} component is estimated as 0.49 ± 0.18 kpc, hence, located in the Local Arm. The radius of the -2.5 km s^{-1} CO shell is about $56'$, i.e. ~ 8 pc at the distance of 0.49 kpc, and the offset of its center from 3C 58 is about $20'$ (i.e. ~ 2.9 pc). Considering the H I absorption results, the CO shell is probably not associated with the PWN. The CO shell of such size may originate from a wind-blown bubble of an O- or B-type star. Further analysis is needed to better understand the distribution of MCs in this region.

G141.2+5.0: The kinematic distance of this PWN was determined as 4.0 ± 0.5 kpc, based on the association with a broken H I shell at a systemic velocity of -53 km s^{-1} , which expands at $+6$ km s^{-1} and with a radius of about $6'$ (Kothes et al. 2014). We detect no significant $^{12}\text{CO}(J=1-0)$ emission associated with the H I shell here. We also find no significant spatial correlation result and identify no broad line near the PWN even by partial criteria.

Crab: As the distance to the Crab is not well constrained, a nominal distance of 2 kpc was commonly adopted

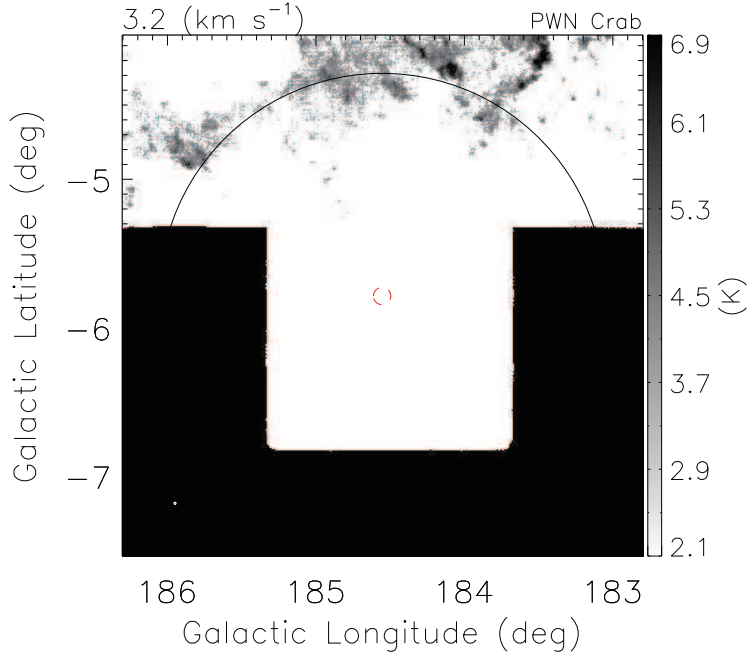


Fig. 19.— ^{12}CO ($J=1-0$) intensity map of the Crab, at the $+3.2 \text{ km s}^{-1}$ velocity channel. The minimum value of ^{12}CO emission intensity shown in the colorbar is at 5σ level. The extent of the PWN is denoted by a red dashed circle. The black solid circle delineates the diffuse shell-like structure.

(Trimble 1968), but recent GAIA studies of the central pulsar suggested that this distance might be greater (Bailer-Jones et al. 2018; Fraser & Boubert 2019). In our observation, molecular gas as the peak of the SCC at $\sim+3.2 \text{ km s}^{-1}$ is roughly surrounding this PWN in the north, of which the radius is $\sim 1.5^\circ$ (see Figure 19). No corresponding broad line is identified even by partial criteria. Note that the south of the region near the PWN, where the opposite part of the northern molecular shell might be, is not fully covered here. The PWN may be associated with molecular gas at $\sim+3.2 \text{ km s}^{-1}$. Since the direction of the PWN is toward the anti-Galactic center, its kinematic distance cannot be determined well. Nevertheless, the kinematic distance of molecular gas at $\sim+3.2 \text{ km s}^{-1}$ is estimated as $1.59 \pm 0.03 \text{ kpc}$, correspondingly, the radius of the surrounding shell-like structure is $\sim 42 \text{ pc}$.

Geminga: The distance to the Geminga pulsar by a latest parallax measurement was given as $250_{-62}^{+120} \text{ pc}$ (Faherty et al. 2007). Here, the SCC indicates a possible association between the PWN and molecular gas at $\sim-10.8 \text{ km s}^{-1}$, which presents a shell-like structure surrounding the PWN as shown in Figure 20. This shell-like structure seems to be a curved section of a long molecular filament that spreads from the northeast to the southwest. If the PWN and molecular gas at $\sim-10.8 \text{ km s}^{-1}$ are associated and both locate at the parallax distance of 250 pc, the radius of the shell-like structure would be only $\sim 0.7 \text{ pc}$.

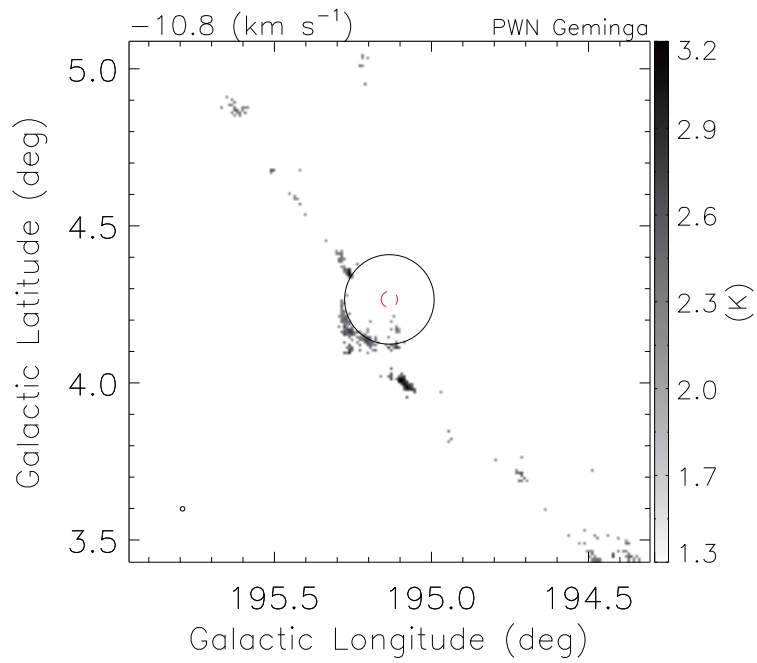


Fig. 20.— ^{12}CO ($J=1-0$) intensity map of the Geminga, at the -10.8 km s^{-1} velocity channel. The minimum value of ^{12}CO emission intensity as shown in the colorbar is at 3σ level. The extent of the PWN is denoted by a red dashed circle. The black solid circle delineates the shell-like structure.